Spring 1-1-2011

GPS-based Sub-Hourly Polar Motion Estimates: Strategies and Applications

Aurore Eglantine Sibois
University of Colorado at Boulder, aurore.sibois@gmail.com

Recommended Citation

Sibois, Aurore Eglantine, "GPS-based Sub-Hourly Polar Motion Estimates: Strategies and Applications" (2011). *Aerospace Engineering Sciences Graduate Theses & Dissertations*. 30.
https://scholar.colorado.edu/asen_gradetds/30

GPS-based Sub-Hourly Polar Motion Estimates: Strategies and Applications

by

Aurore E. Sibois

M.S., Telecommunications and Signal Processing, ESIEE Paris, 2005

M.S., Advanced Techniques in Radio Astronomy and Space Science,

Chalmers University of Technology, 2007

A thesis submitted to the

Faculty of the Graduate School of the

University of Colorado in partial fulfillment

of the requirements for the degree of

Doctor of Philosophy

Department of Aerospace Engineering Sciences

2011

This thesis entitled:
GPS-based Sub-Hourly Polar Motion Estimates: Strategies and Applications
written by Aurore E. Sibois
has been approved for the Department of Aerospace Engineering Sciences

George Born

Shailen Desai

Bruce Haines

John Wahr

Date ____________________

The final copy of this thesis has been examined by the signatories, and we find that both the content and the form meet acceptable presentation standards of scholarly work in the above mentioned discipline.

Sibois, Aurore E. (Ph.D., Aerospace Engineering Sciences)

GPS-based Sub-Hourly Polar Motion Estimates: Strategies and Applications

Thesis directed by Professor George Born

Since their advent in the late 1970's, satellite geodetic techniques have revolutionized the monitoring of the Earth's orientation in inertial space and significantly contributed to advances in geodynamics. Long- and mid-term features manifesting in the Earth Rotation Parameters power spectra are, in general, accurately determined and explained. In contrast, sub-daily fluctuations affecting polar motion and length-of-day are not known as precisely. The lack of highly-resolved time series is currently a strong limiting factor for gaining more insight into rapid polar motion - the parameter of interest here - and its geophysical implications. This thesis was aimed at customizing an estimation strategy targeting the recovery of polar motion at very high temporal resolution based on GPS ground observations only. To this end, the trade-space existing between the precise determination of the GPS satellite orbits and clocks themselves and the retrieval of the Earth's pole coordinates at sufficient accuracy for geodetic purposes was extensively investigated. The strategy design and underlying rationale are described. Candidate strategies are presented and results obtained from the reanalysis of one year of data are shown and analyzed. The challenges associated with the determination of ultra-rapid polar motion are discussed. In particular, mathematical singularities stemming from various sources are emphasized and handling techniques proposed. Difficulties inherent to the quality assessment of the estimates are stressed and the methodology employed for conducting relevant performance analyses is detailed. The validity of the solutions generated is demonstrated through the recovery of geophysical signals such as the major semi-diurnal and diurnal ocean tides and large-scale oceanic and atmospheric circulations. Among other geophysical applications, preliminary results for the detection of so-called megaquakes are shown based on the 2011 M9.0 Honshu earthquake event. Recommendations and guidelines for the determination of polar motion at high frequencies are formulated based on the numerous test cases

studied.

Dedication

To my parents,

for their constant support and unconditional love

Acknowledgements

First of all, I would like to extend my sincere gratitude to my advisor, Dr. George Born, for his support and guidance throughout the past three and a half years. I thank him for his encouragements when I needed them and for sharing his tremendous knowledge of statistical parameter estimation and many other fields. I learnt a lot from his Statistical Orbit Determination classes and their content was extremely valuable to my research. I am also very thankful to Dr. Shailen Desai and Dr. Bruce Haines of the Jet Propulsion Laboratory for their direction and technical contributions as well as for providing me with this particular research topic. I am grateful to them for offering to fund my Ph.D. at the University of Colorado at Boulder and welcoming me back at JPL every summer for the past three years. I am grateful as well to Dr. John Wahr and Dr. Richard Gross for their clear explanations of geophysical phenomena, which I hopefully did not distort too much in this dissertation, and for sharing their expertise in the fields of Earth rotation, oceanography and atmospheric science. I would also like to thank Dr. Steve Nerem and Dr. Hanspeter Schaub for agreeing to be part of my Ph.D. committee.

I wish to thank the people in the Tracking Systems and Applications division and Orbiter and Radio Metric Systems group at JPL who have helped and supported me in one way or another. In particular, I'd like to thank Dr. Jan Weiss, Dr. Kevin Miller, Dr. Da Kuang, Dr. Susan Owen, Joanne Nakayama and Allyson Beatrice. A special thanks goes to Dr. Willy Bertiger for his valuable advice as well as for patiently answering my many questions and challenging me with new ones for the past five years. I am deeply indebted to Dr. Frank Webb for offering me the opportunity to spend some time at JPL five years ago and to Dr. Jan Johansson, professor at Chalmers University of Technology, for believing in me enough to initiate my visit there.

I wish to thank my office mates in Boulder, Xianjing Liu, Ben Bradley and Vicki Hsu as well as Dr. Mike Chin at JPL for providing very pleasant working environments in both places and welcome distraction when needed. I have had the pleasure to meet incredible people while at CU and during my time at JPL; their support and friendship are truly appreciated. In particular, I am very thankful to Dr. Jill Tombasco and Carl Seubert for standing by me and being such wonderful friends since my first day at the Colorado Center for Astrodynamics Research. Last but certainly not least, I have no words to express how grateful I am to my family for their continuous support through the years and time zones and for their frequent visits in California and Colorado. This dissertation is dedicated to them.

To conclude, I would like to acknowledge that this research was generously funded by the Orbiter and Radio Metric Systems group at the Jet Propulsion Laboratory. The Zonta International organization also contributed to making my life easier while working on my thesis thanks to their Amelia Earhart fellowship program. The access to the supercalculator located at the California Institute of Technology was graciously granted by Dr. Mark Simons.

Contents

Chapter

Appendix

Tables

Table

Figures

Figure

Chapter 1

Introduction

1.1 Context of the study

The Earth's rotational motion and position in space are characterized by multi-scale variations in both the location of the Earth's spin axis (referred to as polar motion) and its rotational speed (length-of-day). Fluctuations in the orientation of the Earth are induced by external torques exerted on the planet as well as exchanges of angular momentum within the so-called Earth system, composed of the solid Earth (comprised of the crust and the mantle), its core (inner and outer), the hydrosphere (encompassing the oceans, ground water reservoirs and the cryosphere) and the atmosphere.

Because part of the variability of the Earth's rotation vector is caused by internal torques, monitoring the rapid and ultra-rapid (sub-daily) changes in its orientation is relevant to a variety of scientific fields, among which are geomagnetism, oceanography and meteorology for instance. As a result, the study of the Earth's rotation is deemed one of the most interdisciplinary of geosciences.

The determination of highly resolved, high-precision Earth rotation parameters has the potential to fulfill the three objectives of the study of the Earth's rotation identified by Dickey in [62]. Improved estimates of the polar motion and Earth's rotation rate could provide new insight into the dynamics of the Earth's interior and contribute to advancing the knowledge of the interactions and coupling between the various layers of the Earth system. In addition, identifying with increased precision the causes of observed rotational irregularities would help constrain and refine the modeling of the geophysical processes involved, which would subsequently result in more accurate estimates.

Beside their geophysical significance, the Earth orientation parameters (EOP) essentially provide the transformation between the celestial inertial and Earth-fixed re-ference frames. Because errors in timing and polar motion estimates directly map into spacecraft angular position errors, precise knowledge of the Earth's rotation and orientation in space is crucial in the context of interplanetary navigation. Increasingly stringent tracking accuracy and navigation requirements are imposed on interplanetary missions. EOP accuracy specifications are typically formulated in terms of equivalent displacement on the Earth's surface. Back in 1997, the Mars Pathfinder mission, which involved a landing phase, required 5-cm calibration accuracy (translating into an accuracy level of 1.67 milliarcseconds in polar motion) three weeks after the observations [185]. Recent missions have placed stronger constraints on the quality of the measurements; thus stressing the need for more accurate and more frequent EOP estimates.

For all the reasons cited above, the accurate determination of the EOP is fundamental to both geodesy and navigation. As such, the EOP have been the subject of intensive investigation ever since the advent of space geodesy.

1.2 Historical perspective and state-of-the-art performance

EOP series arise from two sources: classical techniques (optical astrometry and lunar occultation) and modern space geodetic techniques (VLBI, SLR, LLR, DORIS, GNSS). Changes in the Earth's orientation have been routinely observed and documented by optical astrometry since the late 19th century. Reviews of historical Earth orientation monitoring by means of astrometric observations can be found in [127], [147] and [148] for example. Beginning in the 1970s, the classical techniques have been gradu-ally replaced by space-based observational techniques which are particularly suited to the survey of large-scale geophysical phenomena. Lunar and Satellite Laser Ranging (LLR, SLR) were the first two techniques to assist in the Earth Rotation Parameters (ERP) monitoring, soon followed by Very Long Baseline Interferometry (VLBI) and the Global Positioning System (GPS) [172]. The potential of the GPS technology to recover precise ERP was detected by Freedman in the early years of the system [73] and the generation of daily-resolved solutions started in 1992. The Center for Orbit Determination in Europe (CODE) pioneered the production of sub-daily ERP series based solely on GPS data in 1994 [104]. Several centers have been working on specialized estimation techniques ever since (e.g. [179], [162] and [69]).

Historically, the interferometric and laser ranging techniques (VLBI, SLR and LLR) have provided the most accurate ERP estimates and EOP estimates in the case of VLBI. However, at high frequencies, these systems suffer from cost and computational limitations. In these conditions and owing to the relatively low cost, high reliability, global coverage and ever-increasing precision of the system, it is believed that GPS has the potential to outperform all other geodetic techniques at high temporal resolution as far as polar motion is concerned.

Each of the aforementioned space-geodetic techniques has its own unique strengths and weaknesses with regard to the determination of the EOP. Each technique is sensitive to a different subset and/or linear combination of the Earth orientation parameters. The heterogeneity observed in the EOP products delivered by each technology also originates in different temporal resolutions, temporal lengths, tracking data quality, abundance and latency and inherent maximum reachable levels of precision. Based on complementarity and redundancy considerations, Gambis [79] claims that the production of high-quality EOP series necessitates combining at least three independent techniques.

The International Earth Rotation Service (IERS) provide EOP series in the form of bulletins and, more recently, in the form of so-called EOPC04 files. Bulletin A, issued by the IERS Rapid Service, contains a rapid determination of the EOP and their formal errors at daily intervals along with predictions for one year into the future. In contrast, Bulletin B reports the so-called final determinations of EOP series at 5-day intervals. The EOPC04 series were meant as a continuous version of Bulletin B (e.g. [122]) but differ in the sense that they were recently made consistent with specific realizations of the International Terrestrial Reference Frame (ITRF) (see [19] and [20]). In all three cases, the EOP series are based on a combination of individual analysis results using data from VLBI, SLR, GPS and LLR [112]. The reader is referred to [79] and [183] for a detailed description of the combination techniques operationally run by the IERS and other analysis centers.

As defined by Gambis et al. in [77], the precision of a particular EOP solution directly relates to its agreement with a combined solution while accuracy reflects ”the real uncertainties of a solution taking into account the inconsistency and systematic errors of the EOP system with respect to terrestrial and celestial frames”. A literature review reveals discrepancies in the report of state-of-the-art performances of currently available EOP time series. Thus, in 2004, the level of precision for polar motion was believed to amount to 50-100 microarcseconds and to be of the order of 4-10 microseconds for UT1. Meanwhile, the accuracy level then ranged between 150 and 200 microarc-seconds for polar motion and from 15 to 25 microseconds in UT1 [77]. The nominal figure published on the IERS webpage is a precision of 200 microarcseconds for GPS-derived, daily-resolved polar motion times series and 60 microseconds for corresponding UT1 series. In late 2009 however, the International GNSS Service (IGS) claimed their ultra-rapid (6-hourly updated) polar motion series were accurate to less than 50 microarcseconds. As of 2010, several sources mention 50 microarcseconds to be the current level of accuracy of polar motion estimates, therefore this value is considered nominal. Performance comparisons in terms of precision and accuracy relative to the results published by different groups around the globe remain challenging due to the multiplicity of definitions that seem to exist for both terms as well as a confusion in the terminology and a lack of information on the performance metrics used in each case.

1.3 Research Overview

The research conducted for this thesis is part of a larger effort led by the Orbiter and Radiometric Systems (ORMS) group at the Jet Propulsion Laboratory (JPL) to significantly improve the accuracy of various geodetic parameters estimated from GPS observations. This goal is pursued by refining the estimation strategies and dynamic models tailored for the GPS satellite constellation while taking advantage of the high reliability of the GPS tracking data.

In the frame of that project, this work focuses on the development and optimization of an estimation strategy specifically targeting the recovery of the Earth’s pole coordinates at very high (sub-hourly) temporal resolution. Aside from the fact that no space-borne technique can compete with VLBI as far as the determination of UT1-UTC is concerned, the reasons for concentrating exclusively on polar motion are exposed in section 2.2.1.

The motivation for this study, along with the challenges and objectives it carries, are addressed in the sections that follow.

1.3.1 Motivation

As highlighted in section 1.1, an improved representation of the rapid changes in the ERP would benefit both the aerospace engineering and scientific communities. From a scientific standpoint, it would enhance our understanding of the rotational response of the Earth to sub-daily non-tidal excitations such as those caused by atmospheric and oceanic forcings. In this context, the effects of natural hazards, such as tsunamis or earthquakes, on the rotational dynamics of the Earth are also of great interest. Simulations show that earthquakes and, in some cases, the transport of water mass generated by subsequent tsunamis have the potential to cause rapid and permanent changes in the polar wobble and length-of-day. It is believed that such changes could be observable from space-based measurements. However it has been demonstrated by Gross and Chao in [92] and Gross in [89] that the most recent largest seismic events (the Sumatra and Chile earthquakes that occurred in 2004 and 2010, respectively) cannot be detected in currently produced observational time series. They estimate that the noise level is about three times greater than the estimated change in polar motion induced by those two seismic episodes. No results have been published yet, relative to the observation of anomalous behavior in polar motion directly linked to the earthquake that hit Japan in 2011, to the best of our knowledge. This cataclysm is believed to have the potential of being the first event detectable.

Our current knowledge of the variations in the Earth's orientation at sub-daily periods suffer from deficiencies that are principally due to two factors:

- The lack of sub-daily Earth orientation measurements constitutes the first and foremost limitation to the investigation of the short-term perturbations affecting the EOP. As highlighted in section 1.2, the standard time series delivered by the IERS are resolved on a daily basis and higher-resolution estimates obtained by indivi-dual research institutions remain experimental and, as such, are not necessarily publicly available.

- The issue is further complicated by the fact that geophysical processes typically manifest as red noise signals. Hence, detecting the small-amplitude signals occurring at high frequencies requires increasing the signal-to-noise ratio currently achieved rather significantly.

In addition, while it is true that other research groups have been designing estimation procedures for the past decade, the topic is still very much under investigation. In particular, methods for determining high-frequency ERP estimates using JPL's GIPSY/OASIS II software package have never been implemented operationally. Moreover, due to computational limitations and constant experimenting of new models and paramete-rization methods, there exist no homogeneous time series spanning multiple years as stressed in [179].

1.3.2 Objectives and Challenges

As stated above, the ultimate goal of this work is to establish a routine estimation strategy to monitor polar motion at sub-hourly intervals. This is accomplished by investigating the trade-space for optimal pole coordinates and precise GPS orbit determination (GPS POD).
The research presented in this dissertation provides answers to the following questions:

- What is the optimal estimation interval for the recovery of precise, useful polar motion data?

- What is the optimal orbit determination arc length in terms of balancing the orbit determination accuracy with the quality of the polar motion estimates?

- To what extent does the polar motion-tailored estimation strategy improve or degrade the accuracy of the GPS satellites precise orbit determination, possibly as a function of arc length and estimation interval?

- Are the polar motion estimates retrieved meaningful? What is the accuracy limit or internal precision reached?
- Based on the estimated noise level, what kind of geodetic signals can be observed?

Several challenges were identified along the way, among which the most critical ones to the determination of precise pole coordinates are listed below and commented on in the paragraphs following.

- the nutation handling,
- the dynamic modeling of the GPS satellites at tidal periods,
- the quality assessment of the solutions.

The term nutation handling refers to the various singularities connected to the estimation of daily and sub-daily polar motion. These singularities arise from separability issues affecting the orbital elements of the GPS satellites and the pole coordinate themselves as well as from the intrinsic dualism between the motions of nutation and polar motion in the frequency band of interest. The mathematical formulations and approaches taken to mitigate the effects of the degeneracy are extensively discussed in sections 2.1.4 and 2.2.2.

Because of the 2:1 resonant nature of the GPS orbits with the rotation of the Earth about its axis and the sidereal GPS constellation repeat period, accurate dynamic modeling is critical to correctly separate the diurnal and semi-diurnal tidally-induced variations in polar motion. In addition, in the context of atmospheric and oceanic circulation recovery, the Sun-synchronous diurnal frequency gives rise to thermal tides, i.e. tides generated by solar heating and thus changing the dynamics of the atmosphere, while impacting the GPS constellation orbit determination through systematic errors caused by deficiencies in the solar radiation pressure model.

Assessing the quality of a GPS-derived polar motion solution is challenging in the absence of a known true solution or perfect geophysical models. Although a varied set of external and internal performance metrics can be used, distinguishing between strategy artifacts and real signal remains difficult, especially in the diurnal frequency band and above, when geophysical processes are less well known and their associated models are less reliable.

1.3.3 Methodology

The work was organized into three distinct phases:

1. the modification of JPL's GIPSY/OASIS II software package;
2. the development, testing and tuning of estimation strategies;
3. the validation of the strategies through comparisons with the model officially recommended by the IERS to predict the impact of ocean tides on the pole coordinate variability in addition to comparisons with Atmospheric Angular Momentum (AAM) and Oceanic Angular Momentum (OAM) time series produced by the European Center for Medium-range Weather Forecast (ECMWF).

The first phase consisted in adding the capability to estimate the Earth Rotation Parameters as stochastic processes in the GIPSY/OASIS II software package. Due to the limited length of the EOP file format in the current version of the software, the estimation of the EOP were operationally limited to their modeling as biases and the solution interval was restricted as well to comply with the number of entries in the file. To be more specific, in the case of the pole coordinates, the issue was not related to the high-frequency estimation of the parameters itself but to its application.

The second phase constituted the core of the research completed. It included deve-loping, testing and tuning different estimation strategies. The quality of the solutions generated was then evaluated based on spectral and covariance analyses in particular. The trade-space between the precision of the solutions classically retrieved from GPS POD (i.e. orbits, clocks, station coordinates) and the quality of the pole coordinate solutions obtained was carefully analyzed at this stage of the work.

The third and last phase corresponded to the ultimate validation of the solution strategies. It was based on the comparison of the estimated time series with geophysical quantities. In particular, the compliance, to a satisfactory level, of any non-tidal signal present in the estimate time series with the atmospheric and oceanic angular momenta was verified. As expected, the steps taken in the performance assessment of the candidate strategies facilitated the selection of one of the candidate strategies as the optimal one, at least relative to the other two strategies considered. The residual polar motion time series were also analyzed in search of potentially real signal and detectable strategy artifacts. The procedures used were also applied to the detection of the 2011 Honshu major earthquake in order to provide some insight into the current limitations hindering the detection of earthquake signals buried within the polar motion residual series. This last application also offered some prospective on the strengths and shortcomings of the methods employed along the course of this research work.

1.3.4 Research Contributions

The primary contributions of this dissertations are listed below. They are synthesized in the paragraphs that follow and discussed in more details in the concluding chapter of the dissertation.

1. the implementation in the GIPSY/OASIS II software package of models and upgrades enabling the stochastic determination of the Earth rotation parameters,

2. the design and optimization of estimation strategies aiming at the recovery of polar motion at very high temporal resolution,

3. a set of guidelines for the determination of polar motion at high frequencies based on GPS ground data alone.

The major contribution of this work consists in the upgrade of the GIPSY/OASIS II software package. In particular, the capability of estimating the pole coordinates as highly resolved stochastic processes was added to the software. Moreover, models were added or updated to enhance the accuracy of the pole coordinate solutions. The GPS data processing performed for this work led to contributions in the development of the Long Arc Processing software.

Rapid and ultra-rapid polar motion can now be estimated and analyzed using the GIPSY/OASIS software and specialized estimation procedures. The levels of accuracy and precision reached are shown to be competitive with those reached by other research centers. Post-processing tools specialized for the analysis of polar motion were also implemented, although not necessarily in the software packages cited earlier.

Finally, the extensive testing and careful investigation of the trade-space between the temporal resolution and the accuracy of the solution among others, provides a set of guidelines for the determination of polar motion at periods up to a few weeks. Factors such as the parameterization and selection of the ground network, the data sampling rate, the orbit determination arc length, the parameterization of the pole coordinate stochastic estimation, the antenna calibration and the formulation of non-gravitational forces were considered among others.

1.4 Dissertation Overview

This dissertation is outlined as follows. Chapters 2 and 3 provide the necessary background on the Earth's rotation and its multi-scale variations. Chapter 4 synthesizes the statistical parameter estimation problem and is tailored towards the description of the algorithms implemented in the software package employed throughout this research. Chapter 6 describes the software packages this work heavily relied on and details the modifications brought to the GIPSY/OASIS II software. The estimation strategy design and implementation are discussed in Chapters 5 and 7, respectively. Preliminary results based on covariance analyses are shown, analyzed and discussed in Chapter 8. A more extensive performance analysis is conducted in Chapter 9 where the candidate strategies are evaluated depending on how well geodetic signals are recovered. To conclude, Chapter 10 synthesizes the contributions made through this research and presents guidelines for the precise determination of the Earth's pole coordinates at high temporal resolution. Ideas for future work on the topic are also outlined; the motivation for each of the follow-on research tasks suggested is briefly presented.

Chapter 2

The Earth's Rotation

2.1 The Earth Orientation Parameters

In principle, the orientation of the Earth in inertial space can be fully characte-rized by three angles, assuming the origins of the celestial and terrestrial reference frames to be aligned. By convention however, the Earth's rotational behavior is separated into the motion of the rotation axis in the solid Earth and its motion in space through the introduction of intermediate reference frames defined by a common reference pole, the Celestial Intermediate Pole (CIP). This convention originates in the fact that whether the rotation of the Earth is studied from a kinematic standpoint or from a dynamical point of view, both approaches naturally lead to this decomposition of the rotational motion of the Earth. Indeed, the motions of precession and nutation describe the kinematics of the Earth with respect to the quasi-inertial celestial reference frame and arise from the action of torques external to the Earth system. In contrast, polar motion and the Earth's proper rotation reflect the dynamics of the Earth system itself.

The orientation of the Earth can be described as the sum of predictable components and others that need to be determined through estimation procedures. The motions of precession and nutation can be accurately modeled unlike the variations in the rotational speed of the Earth or the exact position of the CIP with respect to the geodetic rotational axis. As a consequence, the Earth orientation is traditionally specified by a set of five variable and observable angular quantities commonly referred to as the Earth Orientation Parameters (EOP). These angles are:

- θ, or $UT1-UTC$ where $UT1$ is the time scale associated to the total rotational phase angle of the Earth and UTC is the Universal Time Coordinated.

$UT1 - UTC$ is connected to the angular velocity of the Earth;

- (x_p, y_p), the coordinates of the Celestial Intermediate Pole (CIP) relative to the Conventional Terrestrial Pole (CTP), the Earth's actual rotation axis and geodetic North pole;

- ($\delta\Delta\varepsilon$, $\delta\Delta\psi$), the celestial pole offsets in obliquity and in longitude respectively. These two variables correct the deficiencies of the IAU precession and nutation models adopted.

The EOP are all expressed relative to the CIP, which coincides with the average pole over long periods of time. The motion of the CIP in space is composed of a combined motion of precession and nutation. Its location is therefore determined by the application of a precession-nutation model. The rotational behavior of the Earth is described by $UT1-UTC$ and the trajectory followed by the pole coordinates. This subset of parameters form the Earth Rotation Parameters (ERP), sometimes referred to as the UTPM parameters. A sketch of the ERP is included in Fig. 2.1, where GAST (Greenwich Apparent Sidereal Time) is a synonym for $UT1 - UTC$. It is noteworthy that Fig. 2.1 employs the nomenclature and concepts related to the classical formulation of the orientation of the Earth. The differences between the classical and modern paradigms of Earth orientation are treated in detail in this chapter.

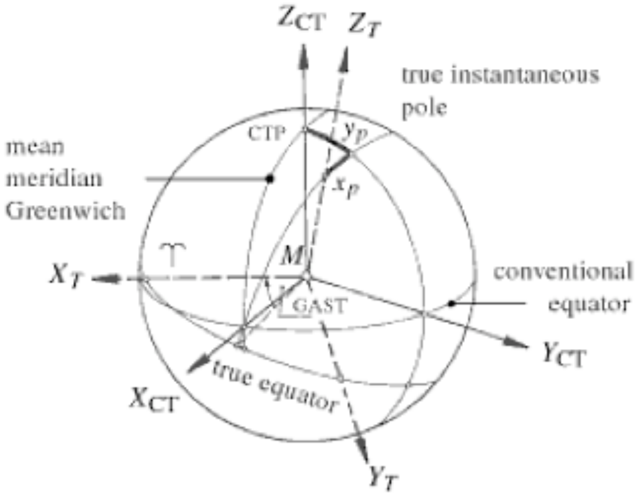

Figure 2.1: Earth Rotation Parameters, taken from [171]

The complexity of the Earth's rotational behavior due to the superposition of several motions is illustrated in Fig. 2.2. The motion amplitudes are given in minutes and seconds of arc. The characteristics indicated for polar motion correspond to the amplitude and period of the Chandler wobble, discussed in Chapter 3.

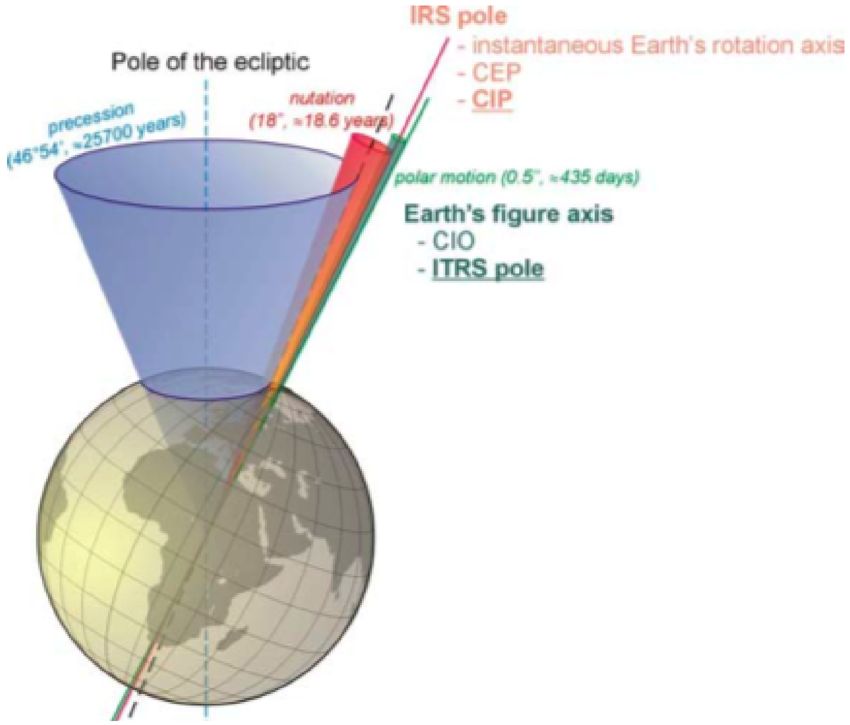

Figure 2.2: Motions undergone by the Earth's rotational axis, from [124]

The four different types of motion the Earth orientation model accounts for are discussed in the sections that follow, with an emphasis on polar motion as well as on precession and nutation. The parameters connected to the rotational speed of the Earth are only briefly addressed since they were not dealt with directly during this research work unlike the other three motions.

2.1.1 Rotation rate

UT1 is a time scale connected with the diurnal rotation of the Earth. It de-signates the Universal Time scale after it has been corrected for the shift in longitude caused by polar motion. Hence, UT1 is independent of station locations and is linearly proportional to the Earth's rotation angle (ERA) with respect to the International Celestial Reference Frame (ICRF). Its rate is chosen so that the day of UT1 is close to the mean duration of the solar day. Additionally, the phase of UT1 is chosen so that 12^h00 UT1 corresponds approximately to the instant when the Sun crosses the Greenwich meridian.

Fluctuations in UT1 are connected to changes in the C_{20} coefficient of the geopotential and are typically expressed in terms of (excess of) length of the day (LOD), which is defined as the negative of the time derivative of UT1.

The actual observable is $UT1 - UTC$ which can be viewed as the angle of rotation of the Earth relative to a mean rotation angle. UTC is designed to closely follow UT1 by the introduction of leap seconds released by the IERS in their Bulletin D.

2.1.2 Polar motion

- Definition

Polar motion, or polar wobble, is defined as the trajectory traced by the true pole at the surface of the Earth around the mean pole and in the direction of the Earth's rotation. It results from the variations occurring in the coordinates characterizing the orientation of the Earth's spin axis relative to the Earth's crust. These angular coordinates are called the polar coordinates x_p and y_p and form a left-handed system; the x-coordinate being measured along the Greenwich meridian while the y-coordinate is taken along the 90° West longitude. Variations in the polar coordinates are caused by the departure of the figure axis of the Earth from the instantaneous pole of rotation (IRP) as seen from a body-fixed reference frame attached to the solid Earth. Three types of axes are involved in the rotation of the Earth around its center of mass:

(1) the figure axis of the Earth, defined as its axis of symmetry or, more generally, as its instantaneous principal axis of maximum inertia,

(2) the Earth's instantaneous spin axis, which is the axis crossing the center of mass of the Earth and about which the Earth rotates at each instant,

(3) the axis defined by the direction of the angular momentum vector of the Earth.

Over long time periods (typically longer than 10 days, according to the IERS) these axes are all coincident. However, the distinction becomes critical in frequency bands close to the diurnal frequency. Hence, polar motion specifically refers to the wobble of the spin axis of the Earth about its figure axis [87]. Consequently, the coordinates x_p and y_p are connected to the C_{21} and S_{21} coefficients of the geopotential, themselves related to the position of the figure axis.

In addition to these three natural axes, a fourth, conventional one, is introduced in the decomposition of the motion of the Earth in space, the CIP, defined in section 2.3.5. It is critical to note that the pole coordinates reported by the IERS designate the location of the CIP, an axis that is closer to the Earth's figure axis than to the instantaneous Earth's rotation or angular momentum axes. The reasons for referring observed polar motion to the CIP are detailed by Gross in [87].

- Prograde and Retrograde Polar Motion

Since the pole describes an elliptical trajectory around the figure axis of the Earth, the polar motion vector can be expressed in the complex plane as shown in Eq. 2.1.

$$\vec{p} = p_x - ip_y \tag{2.1}$$

Starting from Eq. 2.1, polar motion is conveniently separated into the sum of a prograde (eastward motion) and a retrograde (westward motion) component, as shown in Eq. 2.2.

$$\vec{p} = A_p e^{i\phi_p} e^{i\alpha(t)} + A_r e^{i\phi_r} e^{-i\alpha(t)} \tag{2.2}$$

In Eq. 2.2, (A_p, ϕ_p) denote the amplitude and phase of the prograde component while (A_r, ϕ_r) are the equivalent quantities for the retrograde component. The parameter $\alpha(t)$ represents frequency.

The amplitudes and phases of the prograde and retrograde components of the motion can be derived analytically as follows. Beginning with Eq. 2.1, the coordinates of the pole are expressed as shown in Eqs. 2.3. In the case of tides, $\alpha(t)$ denotes the astronomical fundamental argument, sometimes referred to as $\varphi(t)$ and defined in Eq. 3.1 of Chapter 3. The variables $C_{x,y}$ and $S_{x,y}$ represent the amplitudes of the cosine and sine components of the x- and y-coordinates of the pole.

$$\begin{cases} p_x = C_x \cos(\alpha(t)) + S_x \sin(\alpha(t)) \\ p_y = C_y \cos(\alpha(t)) + S_y \sin(\alpha(t)) \end{cases} \tag{2.3}$$

Proceeding by identification between the expanded version of Eq. 2.2 and Eqs. 2.3, the coefficients of the cosine and sine components of the prograde and retrograde polar motion can be determined.

The prograde amplitude and phase are then computed as shown in Eqs. 2.4.

$$\begin{cases} A_p & = \frac{1}{2}\sqrt{(C_x - S_y)^2 + (S_x + C_y)^2} \\ \Phi_p & = \arctan\left(\frac{(S_x + C_y)^2}{(C_x - S_y)^2}\right) \end{cases} \tag{2.4}$$

Likewise, the amplitude and phase of the retrograde term are calculated using Eqs. 2.5.

$$\begin{cases} A_r & = \frac{1}{2}\sqrt{(C_x + S_y)^2 + (S_x - C_y)^2} \\ \Phi_r & = \arctan\left(\frac{(S_x - C_y)^2}{(C_x + S_y)^2}\right) \end{cases} \tag{2.5}$$

The distinction between prograde and retrograde polar motion is particularly important for the recovery of the pole coordinate fluctuations induced by the diurnal and semi-diurnal ocean tides. Indeed, the impact of tides on the variability of polar motion is traditionally expressed in terms of prograde and retrograde variations. This convention is explained by Mathews and Bretagnon in [137] by the fact that the prograde and retrograde motions originate in the action of the same potential on different geopotential coefficients. Due to the ambiguous definitions of nutation and polar motion in the diurnal band, it is expected that prograde polar motion can be retrieved more accurately than the retrograde motion in that frequency band. This is verified when spectral analyses of the estimates are performed (see Chapter 8).

2.1.3 Precession and Nutation

Unlike the ERP that must be determined through actual observations, precession and nutation can be mostly described through theory as pointed out earlier. Indeed, because nutation and precession are primarily products of torques acted upon the Earth by the surrounding celestial bodies, these types of motions are largely periodic and predictable. Therefore, the celestial pole offsets $\delta\Delta\varepsilon$ and $\delta\Delta\psi$ actually represent corrections in obliquity and longitude to be applied to the position of the celestial intermediate pole predicted by the precession and nutation models. These corrections to the conventional models are determined by VLBI processing and reported by the IERS in Bulletins A and B (c.f. section 1.2). The motions of precession and nutation arise from the same torques and are of the same nature; nutation being a by-product of the precession of the equator as explained by Kovalevsky and Seidelmann in [123].

The precessional motion of the Earth is composed of three kinds of periodic motion: the precession of the ecliptic, the precession of the equator (also known as planetary precession) and the geodesic precession induced by relativistic effects. On the one hand, the ecliptic moves under the influence of the gravitational force created by the surrounding planets and acting upon the Earth's orbit. On the other hand, the equator moves under the influence of the Sun, Moon and planet torques on the dynamical figure of the Earth, in a motion called luni-solar precession. Thus the term luni-solar precession denotes the smooth $\sim 26,000$-year period motion of the mean pole of the equator about the pole of the ecliptic. In addition, a short-period motion of the true pole around the mean pole, resulting from the combination of a variety of short-periodic motions and referred to as nutation, occurs as part of the precession of the ecliptic [123]. The nutation of the Earth's axis is made of a combination of periodic motions, the largest component being characterized by a period of 18.6 years, similar to that of the precession of the lunar orbital nodes.

2.1.4 Nutation and Polar Motion

Nutation and polar motion are two very intertwined notions, artificially separated in the conventional parameterization of the Earth orientation. Both terms represent the same motion only seen from two different viewpoints. While polar motion describes the motion of the Earth's spin axis with respect to the Earth's crust, nutation refers to the same motion relative to inertial space. For this reason, polar motion and nutation always occur simultaneously; the frequency of nutation being higher than the corresponding polar motion frequency by 1 cycle per sidereal day (the mean rate of the Earth rotation or cpsd) relative to the space-fixed frame. As a consequence, and as explained by Wahr in [194], the distinction between the two concepts can be operated considering the time scale at which the underlying excitation processes occur. Excitations at periods much longer than one day as seen from the Earth cause polar motion while nutation is associated to nearly diurnal excitations, again as seen from the Earth. This distinction stresses the relevance of polar motion monitoring for geodetic purposes since processes originating in the Earth and capable of influencing the rotation of the Earth occur over long time scales [194].

By convention, the arbitrariness in the definition of nutation and polar motion is formally resolved by imposing two constraints on the frequency contents of polar motion and nutation. These constraints are:

1. there is no retrograde diurnal component to polar motion;
2. reciprocally, there are no prograde diurnal nutation terms.

Figure 2.3 summarizes the conventions adopted by the IERS to distinguish between polar motion and nutation depending on the period considered.

From a purely observational standpoint, separating nearly diurnal polar motion from long-period nutations remains challenging however, as emphasized by Gross in [87] and verified along the course of this thesis.

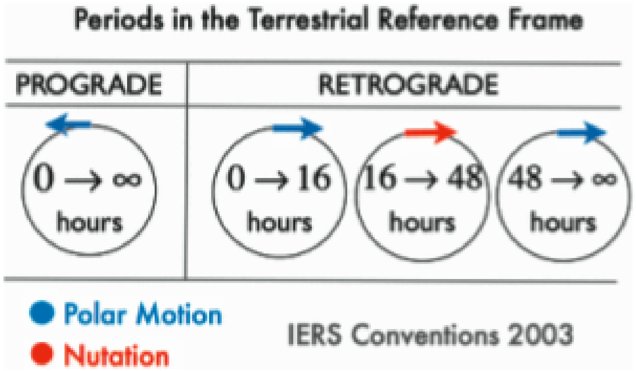

Figure 2.3: Dualism between Polar Motion and Nutation [44]

2.2 Singularities associated with space-borne EO monitoring

As mentioned in section 1.2, not all space geodetic technologies have access to the same subset of EOP nor contribute the same amount to the IERS official combined solutions. Table 2.2 displays a rough estimation of the weight the individual observational techniques are allocated in those combined solutions. The table is adapted from [77] and [69]. The stars denote the observability of the geodetic parameter considered on a given line of the table using the geodetic technique specified by the column number. The number of stars reflects the relative contribution of each technique to the products derived by the IERS. An empty star reflects the fact that, while a parameter is observable, its determination through the technique is not included in the IERS combined solution.

Geodetic parameters	VLBI	GNSS	DORIS	SLR	LLR
UT1	★★★				★
LOD	★★★	★★	★	★	★
Polar Motion	★★★	★★★	★	★★	☆
Nutation	★★★	★ (rates)		★ (rates)	★★

Table 2.1: Contributions of space geodetic techniques to the monitoring of the EOP, adapted from [77] and [69]

Obviously, due to the over-determination of the Earth orientation parameter set, at most three parameters can be estimated simultaneously unless special constraints are imposed. Additional observability and parameter separability issues are discussed in the next two sections.

2.2.1 UT1-UTC, Precession and Nutation

No satellite technique can observe absolute UT1-UTC or celestial pole offsets. The satellite orbital elements, in particular the inclination, right ascension of the ascending node (RAAN) and argument of latitude, are indeed fully correlated with each of the former three angles, as demonstrated in Eqs. 2.6.

$$\begin{aligned} \Delta(UT1-UTC) &= -\left(\Delta\Omega + \cos(i)\,\Delta u_0\right)/k \\ \delta\Delta\varepsilon &= \cos(\Omega)\,\Delta i + \sin(i)\,\sin(\Omega)\,\Delta u_0 \\ \delta\Delta\psi\,\sin(\varepsilon_0) &= -\sin(\Omega)\,\Delta i + \sin(i)\,\cos(\Omega)\,\Delta u_0 \end{aligned} \tag{2.6}$$

In the set of Eqs. 2.6, Ω is the right ascension of the ascending node (RAAN) of the satellite, u_0 is the argument of latitude at the osculating epoch, i denotes the inclination of the orbit, and k the ratio of universal time to sidereal time. The parameter ε_0 is the mean obliquity of the ecliptic. The analytical derivation of this set of equations can be found in [161] and is not reproduced here.

VLBI is actually the only observational technique capable of a direct determination of the Earth's rotational phase angle and celestial pole offsets. The space-borne techniques have access to the time derivative of the former quantity, which corresponds to the (negative) length-of-day (LOD). The system can nonetheless be made obser-vable provided a priori information is available. Namely, UT1-UTC can be determined by satellite techniques by tightly constraining the parameter at the first epoch of the observation arc to its a priori value at the time. This statement holds for the nutation corrections in longitude and obliquity.

Despite the possibility to estimate the Earth's rotation rate using GPS under certain, seemingly easily fulfilled, conditions, this work deals solely with the determination of the Earth's pole coordinates. The decision to ignore the third component of the ERP set was motivated by several factors:

- First, GPS-based series for UT1-UTC are unlikely to demonstrate a precision level of the order of that guaranteed by the VLBI products.
- Then, UT1-UTC varies more rapidly and more erratically than polar motion, as a result the short-term oscillations are more difficult to model and capture than those affecting the pole position. Using GPS, correlations of unidentified origin are introduced when UT1-UTC is estimated simultaneously to polar motion, weakening the overall ERP solution.
- Finally, LOD cannot be estimated as a stochastic parameter in the software package used for this work, which prevents its inclusion in the strategy and determination at high temporal resolution.

2.2.2 Sub-daily Polar Motion

Polar motion is directly accessible to all space geodetic techniques. Yet, the determination of the pole coordinates at sub-daily intervals is complicated by the combination of two different singularities.

As mentioned in section 2.1.3, polar motion and the nutation of the Earth are fully degenerate due to the over-determination of the Earth orientation through five parameters instead of the three sufficient and necessary.

In [30], Brzeziński and Capitaine mathematically model this degeneracy as follows:

$$\begin{aligned} p &= N e^{-\mathrm{i}\theta} \\ \text{where } p &= x_p - \mathrm{i}\, y_p \\ \text{and } N &= X + \mathrm{i}\, Y = \sin(\varepsilon_0)\,\Delta\psi + \mathrm{i}\,\Delta\varepsilon \end{aligned} \tag{2.7}$$

In Eqs. 2.7, p denotes the polar motion vector expressed in the complex plane while N symbolizes the nutation vector. The complex formulation of the nutation vector is derived in [30].

The fact that the non-uniqueness of the set of ERP results in the strict equivalence between a prograde diurnal nutational motion and retrograde diurnal polar motion can be proven by expanding

Eqs. 2.7. Doing so yields Eqs. 2.8, in which the polar motion coordinates are formulated as nonlinear combinations of the nutation parameters and rotational phase angle of the Earth.

$$\begin{cases} x_p = -\Delta\psi \sin(\varepsilon_0) \cos(\theta) - \Delta\varepsilon \sin(\theta) \\ \quad = -\Delta\psi \sin(\varepsilon_0) \sin\left(\frac{\pi}{2} - \theta\right) - \Delta\varepsilon \cos\left(\frac{\pi}{2} - \theta\right) \\ y_p = -\Delta\psi \sin(\varepsilon_0) \sin(\theta) + \Delta\varepsilon \cos(\theta) \end{cases} \tag{2.8}$$

The polar motion appearing in Eqs. 2.8 can be interpreted as diurnal due to the presence of the GAST angle θ. In addition, the motion is considered retrograde given that the x_p component precedes the y_p component by 90°.

Because the nutation correction terms are correlated with the orbital elements of the satellites through Eqs. 2.6, retrograde diurnal polar motion becomes correlated as well with the orbital elements as a secondary effect of Eqs. 2.8. Hence, issues arise even when the celestial pole offsets are not estimated in the final solution and the determination of polar motion at sub-daily intervals leads to the estimation of large retrograde diurnal terms. A geometrical interpretation of this singularity in the case of the GPS constellation is proposed by Eubanks in [70] and was adapted to the GPS constellation by Rothacher et al. in [162]. Fundamentally, the source of the singularity can be viewed as the impossibility to separate rotations of the Earth from rotations of the entire network of satellites when many satellites are tracked simultaneously and as viewed from inertial space [70]. In the particular case of GPS, this separability issue stems from the fact that a common tilting of all six orbital planes in the inertial frame can be entirely compensated by an exact retrograde diurnal polar motion signal [162].

Dealing with the singularities defined in sections 2.1.4 and 2.2.2 is commonly referred to as nutation handling in the literature. That terminology is employed in the remainder of this document. Two main approaches were briefly considered at some point of this research. First, the retrograde diurnal signal could be mostly eliminated by introducing an a priori model. This solution did not seem very practical however because it requires an accurate knowledge of the effects of the singularity on the estimates, effects that are difficult to quantify and predict. Second, an estimation strategy could possibly be developed to minimize the amplitude of the retrograde polar motion signal in the diurnal band. A shortcoming of this technique resides in the resulting mitigation of potentially real and useful geophysical information contained in the retrograde diurnal part of the polar motion spectrum. In particular, the Nearly Diurnal Free Wobble (NDFW), corresponding to the Free Core Nutation (FCN) mode as seen from the terrestrial frame, is a retrograde process exhibiting a nearly diurnal frequency as seen from the Earth, as discussed in Chapter 3. Fortunately, the implementation of the latest International Astronomical Union (IAU) models of precession and nutation [152] significantly reduced the need for proper nutation handling. Ultimately, no specific constraints were applied to block the retrograde diurnal signal out during the estimation procedure.

2.3 Evolution of the Conventional Theory of Earth Orientation

2.3.1 Introduction

Over the past decade, the conventional theory of Earth orientation has evolved from a representation derived solely from the dynamics of the solar system to a purely kinematic representation. This has resulted in significant changes in the formulation of the attitude of the Earth and hence in the related nomenclature. The modifications to the conventions are listed and briefly justified in a series of Resolutions adopted by the International Astronomical Union (IAU) and by the International Union of Geodesy and Geophysics (IUGG). The need for the transition between the old and the new sets of concepts and parameters as well as the differences between these two sets are fully detailed and discussed in the papers compiled in the IERS Technical Note 29 [43]. The purpose of this section is to offer a background on the Earth's rotation by synthesizing the main implications of the evolution of the conventions, especially regarding their implementation. Thus, it provides insight into the part of the thesis devoted to the upgrade of the software package used, further detailed in Chapter 6.

2.3.2 Reference frames and systems involved

Models and theories of the Earth orientation are needed to accurately transform vectors from an inertial reference frame to a terrestrial reference frame. Such transformations require the use of a space-fixed reference frame, the so-called conventional celestial reference frame, an Earth-fixed reference frame, the so-called conventional terrestrial frame, and the introduction of two moving reference frames of date that serve as intermediate reference frames. Figure 2.4 displays the various frames at play, together with their defining parameters. The type of motion relating one reference system to the next is also indicated.

As visible in Fig. 2.4, the Celestial Intermediate Reference System (CIRS) and its Terrestrial counterpart, the TIRS, are the two intermediate reference systems involved in the procedure transforming between the Geocentric Celestial Reference System (GCRS) and the International Terrestrial Reference System (ITRS). Note that although a re-ference system is rigorously defined as a specific realization of a reference frame, it is possible that in this document the terms system and frame are used indifferently at times.

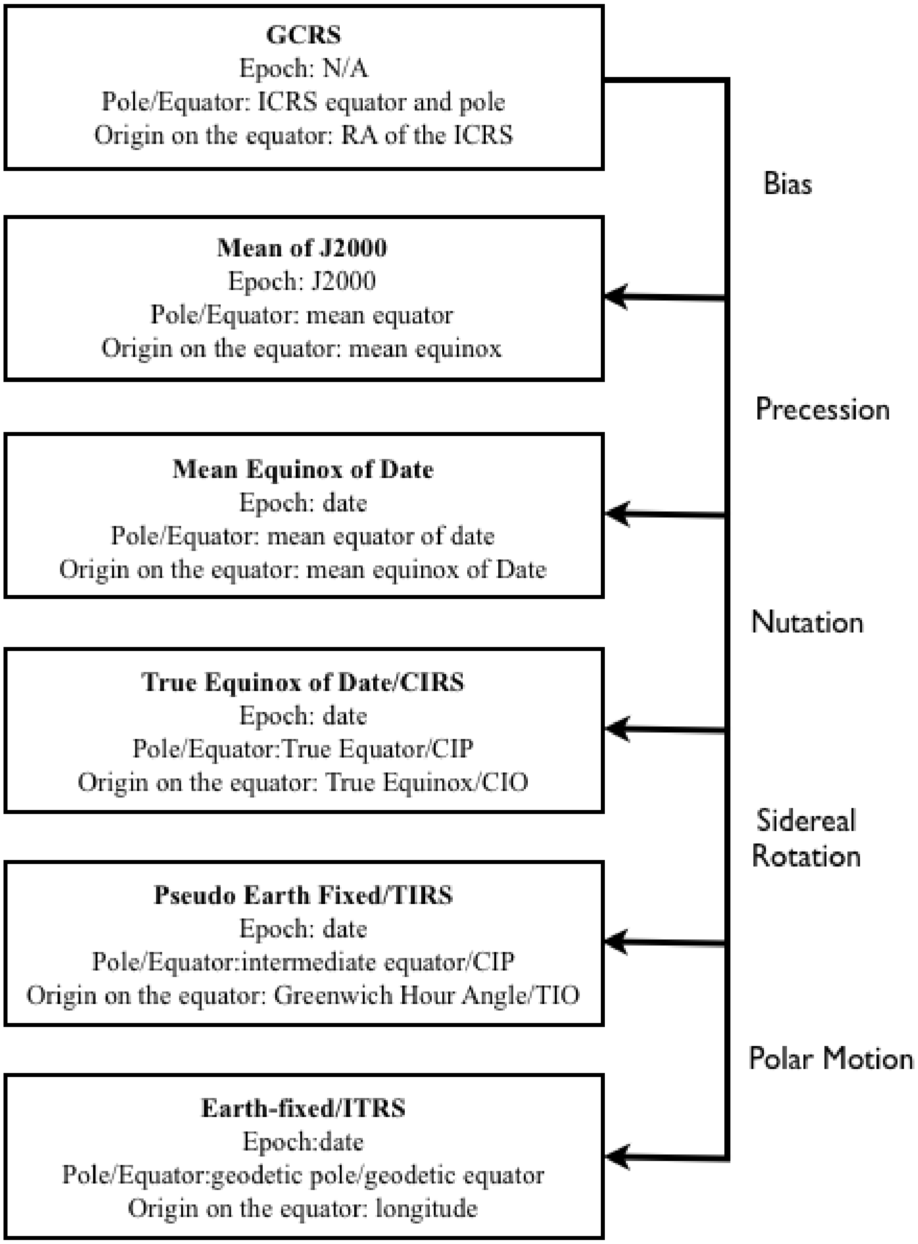

Figure 2.4: The Celestial, Intermediate and Terrestrial Frames and their descriptors

In practice, the instantaneous transition from the ICRS to the ITRS is realized through a sequence of rotations represented in matrix form in Eq. 2.9.

$$[GCRS] = BPN(t)\ \underbrace{R(t)\ \underbrace{W(t)\,[ITRS]}_{=[TIRS]}}_{=[CIRS]} \tag{2.9}$$

The combined Bias/Precession/Nutation matrix, $BPN(t)$, relates the GCRS to the CIRS. The sidereal rotation matrix $R(t)$ about their common axis, the Celestial Intermediate Pole (CIP), connects the CIRS and the TIRS and describes the proper rotational motion of the Earth. Finally, the polar motion matrix $W(t)$ provides the transition from the TIRS to the ITRS. The full procedure enabling the reduction of celestial coordinates into terrestrial coordinates is detailed in the Astronomical Almanac [164] and its explanatory supplement [172] among others. Its implementation in the software package used for this work is detailed in section 2.4. All the rotational motions involved in the transformation were discussed in section 2.1.

Both the classical and modern formulations of the Earth's orientation in space are briefly described in the sections following. The need for the modernization of the parameterization is also addressed.

2.3.3 Classical paradigm

The parameterization of the orientation of the Earth in inertial space is based on the rule that any reference frame can be defined by an origin, a reference plane determined by two axes and a fiducial direction that defines one axis in the plane. The fundamental difference between the classical and the modern paradigms lies in the definition of the fiducial point or origin of the right ascension in this context.

Until January 1, 1998 and the introduction of the International Celestial Refe-rence System and Frame (ICRS/ICRF), the realization of the celestial reference frame relied entirely on the theoretical equations of motion of the planets and Moon. The fixed directions of the celestial reference frame were defined by the mean equator and equinox for a reference epoch (e.g. J2000.0) at which this specific realization held true. Thus, the ecliptic and equatorial planes served as the two planes of reference while their intersection determined the frame's fiducial point. This parameterization of the ICRF consequently necessitated the dynamical modeling of the Earth's orbital motion to determine the positions of the vernal equinox and ecliptic.

In addition, the reference pole for nutation and polar motion, common to both intermediate frames, was the Celestial Ephemeris Pole (CEP) - or true celestial pole of date. The CEP was chosen to be aligned with the figure axis of the mean surface of the Earth and to remain fixed in both the celestial and the terrestrial reference frames. The position of the CEP was determined using the combination of the IAU 1980 Theory of Nutation derived by Wahr [190] and the IAU 1976 Precession model developed by Lieske et al. [132]. The precession model provided the mean equator and equinox while the nutation model yielded their true positions. In addition, the IAU 1982 expressions for the Greenwich Mean Sidereal Time (GMST) and Hour Angle, consistent with the aforementioned precession and nutation models, were used to describe the Earth's proper rotation.

2.3.4 Limitations of the classical formulation and motivations for a new paradigm

Overall, the motivations for the re-parameterization of the models for the Earth orientation and the reformulation of the associated theories resulted from the need to simplify these theories while reducing the number of error sources that could potentially affect the reduction of observational data. There were two major limitations in the former formulation. First, owing to significant progress achieved in observational capabilities and measurement accuracy as well as improvements in astronomical and geophysical modeling, a clear separation between all motions was needed to avoid the potential propagation of errors or inconsistencies due to interactions between motions. In particular, dealing with the intrinsic dualism between polar motion and nutation in the high-frequency domain had become critical. In addition, the coupling between the GST and the precessional and nutational motions, highlighted in Eq. 2.22, needed to be removed. The second critical issue originated in the choice of a geometric definition for the origin of the right ascension. Indeed, the vernal equinox is defined as the intersection of the ecliptic and equatorial planes which are both moving under the effects of general precession. This definition imposes the parameterization to be time-dependent and implies limits on its domain of validity. The matter was further complicated with the multiplicity of realizations of the equinox.

2.3.5 Modern representation

The modifications to the classical paradigm relevant to this work are enumerated and described below. The corresponding implementation procedures are detailed in the IERS Technical Note 36 [152]. Furthermore, the practical consequences of these changes on data analysis are addressed by McCarthy and Capitaine in [143].

(1) Adoption of the International Celestial Reference Frame

The first step taken in the reformulation of the theory of Earth orientation was the adoption of the ICRF as the conventional celestial reference frame. The ICRF is a purely kinematic, quasi-inertial frame defined by its ties to 212 extragalactic radio sources whose proper motion can be neglected considering the current reachable level of accuracy. The introduction of the ICRF marked the switch from a dynamical representation of the celestial frame to a parameterization that is entirely determined by observations and relies exclusively on VLBI observations. The directions of the ICRF axes remain fixed relative to the defining quasars. In addition, to ensure the continuity between the old and the new systems, the pole and origin of the right ascension of the ICRS are kept close to those of the former FK5/J2000.0 celestial reference frame. The ICRF also offers the advantage of being epoch-less.

(2) Introduction of the Celestial and Terrestrial Intermediate Origins

The fundamental change implemented in the revised formulation consists in its complete independence from the equinox. This was achieved by the substitution of the equinox as the origin of right ascension on the true celestial equator by the so-called Celestial Intermediate Origin (CIO). The CIO is independent from the position of the ecliptic and is determined based solely on observations of the Celestial Intermediate Pole (CIP), which itself replaces the CEP. The determination of the CIO relies on the notion of non-rotating origin introduced by Guinot in [94]. It is defined such as not to have any instantaneous motion along the equator of the celestial sphere and so that its motion relative to the GCRS is practically theory-independent. The counterpart of the CIO on the terrestrial sphere is the so-called TIO (Terrestrial Intermediate Origin). Similar to the CIO, the TIO is based on the concept of the non-rotating origin.

(3) Substitution of the Celestial Ephemeris Pole by the Celestial Intermediate Pole

As mentioned earlier, the CEP is replaced by the CIP in the revised formulation of the Earth orientation. The CIP is merely an extension of the CEP in the high-frequency domain meant to resolve the singularity arising in the diurnal band between polar motion and nutation. Therefore, the CIP coincides with the CEP in the low-frequency domain.

(4) Introduction of the Earth Rotation Angle (ERA)

Due to the drop of the equinox as the celestial fiducial point, the rotation of the Earth is no longer determined in terms of the Greenwich Sidereal Time. Instead, the so-called Earth Rotation Angle (ERA) is measured from the CIO.

(5) Update of the precession and nutation models

To simplify the theory, the distinction between the mean and true equator and equinox is eliminated by applying the precession and nutation models together. In addition, the IAU 1980 Theory of Nutation has been replaced by the IAU 2000A model developed by Mathews, Buffet and Herring. The IAU2000A nutation model provides the direction of the celestial pole in the GCRS with an accuracy of 0.2 mas [144]. The model corrects for errors in the IAU1980 Theory of Nutation by accounting for effects of ocean tides, mantle anelasticity and electromagnetic couplings produced within the solid Earth on nutation. Parallel to the evolution in nutation modeling and accuracy, the IAU 1976 precession model has been replaced by a revised precession model, the P03 model, later officially recognized by the IAU as the IAU 2006 precession model. This precession model is to be used in conjunction with the IAU 2000A Theory of Nutation. The need for a new precession model arose from the fact that the IAU 1976 theory of general precession was shown to be in error by approximately 300 mas per century. For more information on the limitations of the IAU 1976 precession model, the reader is referred to [42]. The IAU 2006 (or P03) model was made consistent with the dynamical theory by inclusion of higher order terms in the theory that was previously limited to the zeroth and first order terms. The IAU 2006 model was also slightly modified to comply with the IAU 2000A theory of nutation. According to [108], this new precession theory is accurate to approximately 2 mas per century. It is important to point out that in the state-of-the-art IAU2000A/IAU2006 nutation-precession model, the ecliptic is redefined as the mean orbital angular momentum vector of the Earth-Moon barycenter in the Barycentric Celestial Reference System (BCRS), as recommended by the IAU Working Group on Precession and the Equinox in [108].

2.3.6 Impact of the precession/nutation models on the estimation of tidally-driven polar motion variability

Figures 2.5 to 2.7 show the impact the precession/nutation model has on the recovery of tidally-induced polar motion. Each figure corresponds to one of the three estimation strategies customized for the recovery of polar motion. The strategies as well as explanations for the differences are detailed in Chapters 5 and 7. The three models tested for this analysis are the obsolete IAU1980/IAU1976 (referred to as IAU1980 in the legend), the IAU2000A model officially recommended for use by the IERS starting on Jan. 1, 2006 and the IAU2000A/IAU2006 (or IAU2006A) precession-nutation model officially recommended for use starting on Jan. 1, 2009. The four subplots show Lomb-Scargle periodograms of the pole coordinate estimates recombined to form the prograde and retrograde components of polar motion.

As observed on this set of plots, switching from one model to the other significantly impacts the recovery of the diurnal retrograde motion of the pole. This result is expected since the IAU 2000A nutation model includes the effects of ocean tides on nutation unlike the IAU 1980 nutation model. In contrast, retrograde semi-diurnal polar motion is not impacted. Prograde polar motion is affected neither in the semi-diurnal band nor in the diurnal band. Note that the signal contained in the retrograde diurnal band most likely corresponds to residual nutation contaminating the polar motion estimates due to the nutation handling issue addressed in section 2.2.2. Indeed, as stated in section 2.1.4, there should be no polar motion content in that spectral band.

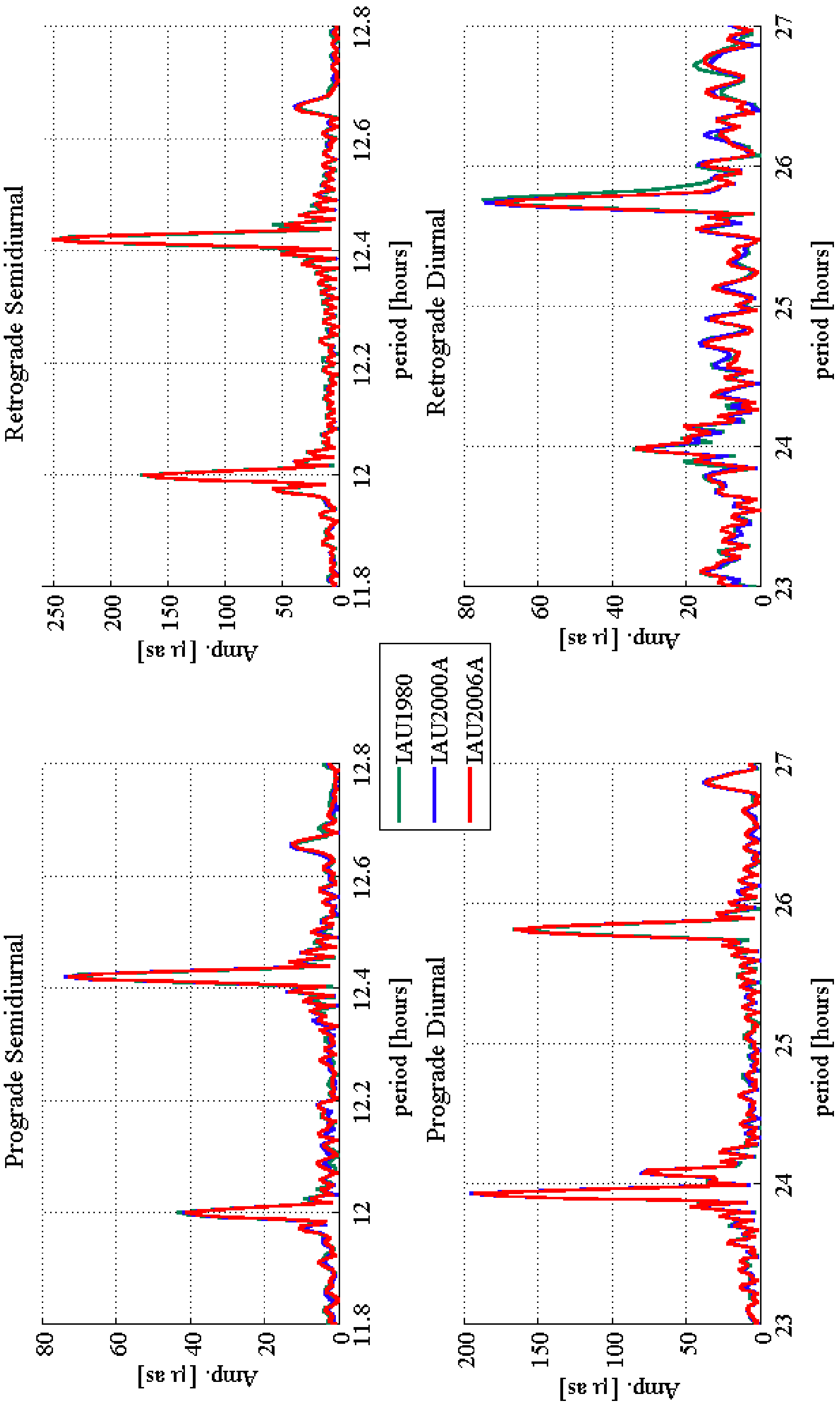

Figure 2.5: Impact of the precession/nutation model on the recovery of tidally-induced polar motion: Flinn-like Strategy

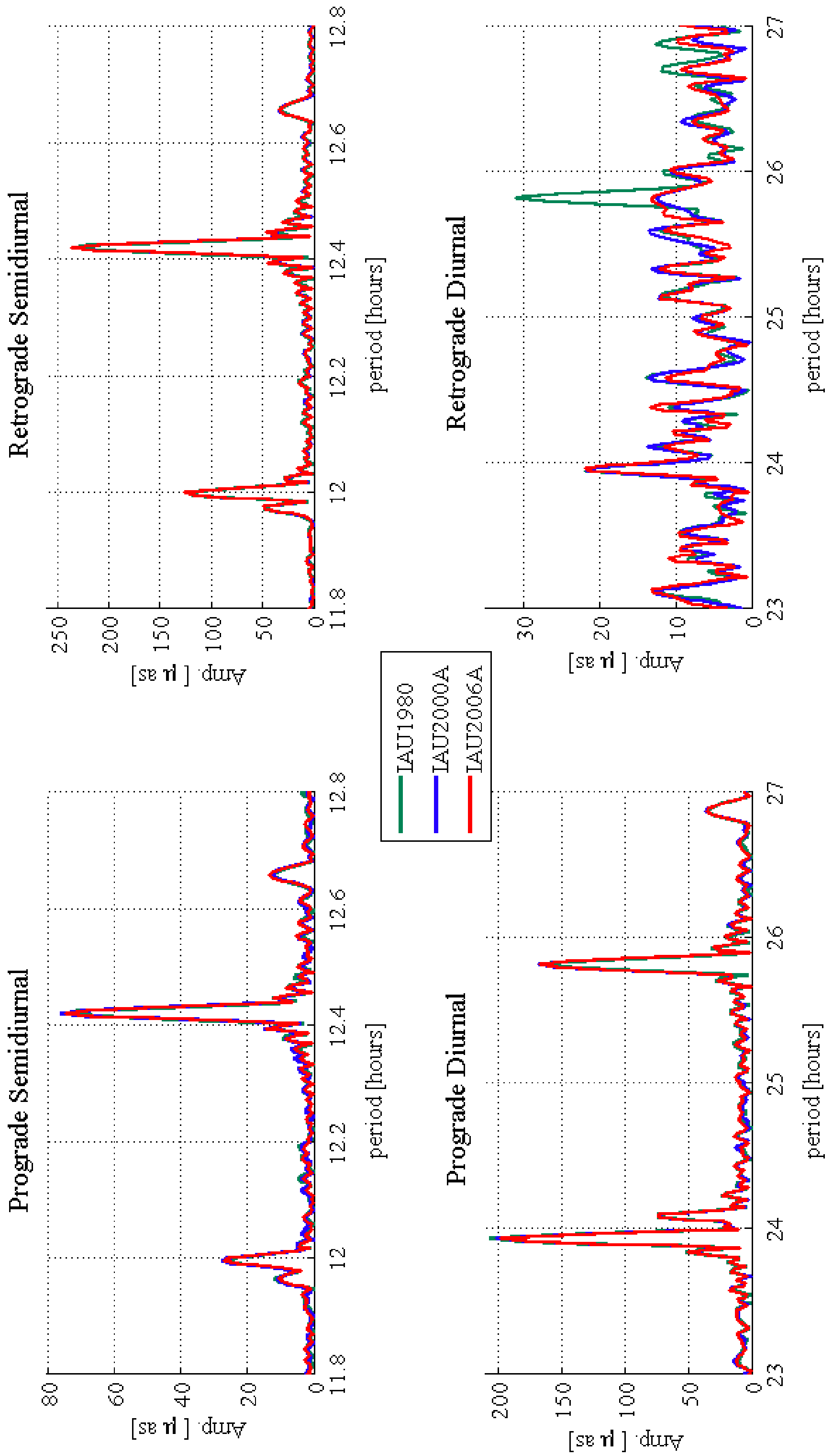

Figure 2.6: Impact of the precession/nutation model on the recovery of tidally-induced polar motion: 3-day Strategy

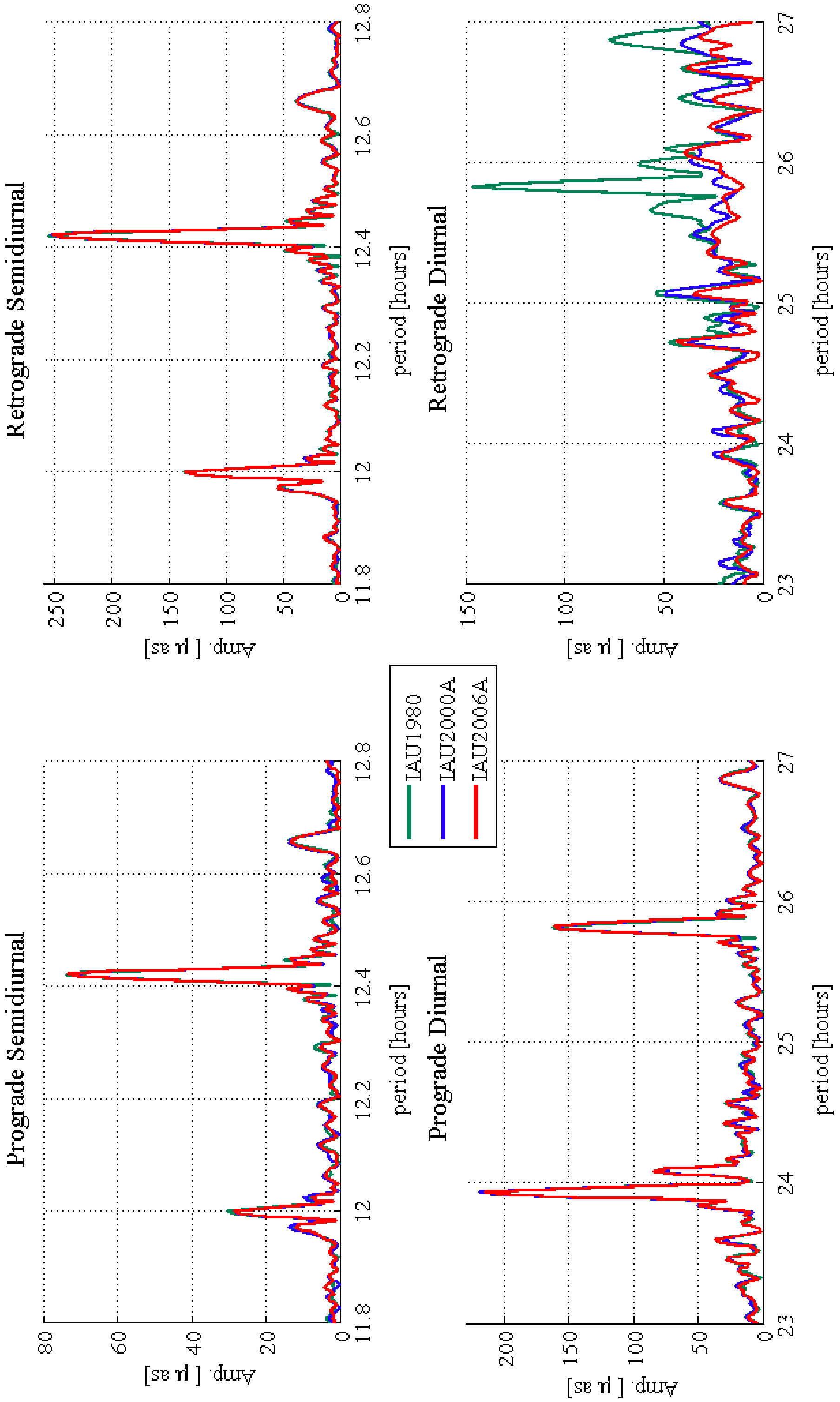

Figure 2.7: Impact of the precession/nutation model on the recovery of tidally-induced polar motion: 9-day Strategy

2.4 Numerical implementation of the Inertial-to-Earth-fixed transformation

This section describes the Earth-centered Earth-fixed (ECEF) coordinate system and the rotation matrix that transforms it into Earth-centered inertial (ECI) coordinates. The general equation to transform a position vector $\vec{r}_{ITRF}$ expressed in ECEF coordinates into the corresponding vector $\vec{r}_{ICRF}$ in inertial coordinates at time t_i is written:

$$\vec{r}_{ICRF} = [B]\,[P(t_i, t_0)]\,[N(t_i)]\,[U(t_i)]\,[W(t_i)]\,\vec{r}_{ITRF} \tag{2.10}$$

where $[B]$ is the frame-bias matrix accounting for the constant offset between the direction of the CIP at J2000.0 and the direction of the pole of the GCRS, $[P(t_i, t_0]$ is the rotation due to precession, $[N(t_i)]$ is the rotation due to nutation, $[U(t_i)]$ is the hour-angle rotation and $[W(t_i)]$ is the rotation due to polar motion. These rotation matrices are defined by a set of models and measurements adopted from the IERS Conventions [152]. Further details on each step of the transformation are given in the paragraphs that follow.

Two different sets of models and approaches are supported by the GIPSY/OASIS software package for the computation of Eq. 2.10. The most recent precession-nutation model, hereafter referred to as the IAU06A model, was included in the software as part of this thesis work. The out-of-date model, referred to as the IAU80 model, remains available as well. The implementation of the latest IERS-recommended models follow the so-called equinox-based procedure, also designated as ”improved classical system” procedure by Kovalesky and Seidelman in [123]. It uses the CIP as determined by the IAU 2000A nutation and IAU 2006 precession models along with an improved expression to relate the GMST to UT1.

2.4.1 Bias, Precession and Nutation matrices

- Classical representation

When the IAU80 precession/nutation models are used, the precession and nutation matrices are computed independently from each other. The precession motion is characterized by the three

Euler angles ζ_A, Θ_A and z_A represented in Fig. 2.8. Accor-ding to the IAU 1976 precession model, the precession angles (ζ_A, Θ_A, z_A) are computed by means of the following polynomials:

$$\zeta_A = 2306.2181'' \, t + 0.30188'' \, t^2 + 0.017998'' \, t^3 \tag{2.11a}$$

$$\Theta_A = 2004.3109'' \, t - 0.42665'' \, t^2 - 0.041833'' \, t^3 \tag{2.11b}$$

$$z_A = 2306.2181'' \, t + 1.09468'' \, t^2 + 0.018203'' \, t^3 \tag{2.11c}$$

The associated rotation matrix corresponds to the matrix of a 3-2-3 Eulerian rotation and is written:

$$P = R_3(\zeta_A) \, R_2(-\Theta_A) \, R_3(z_A) \tag{2.12}$$

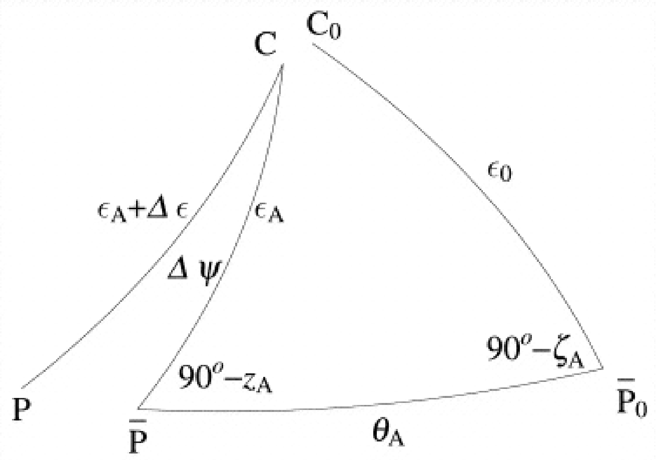

Figure 2.8: Schematic of the Precession Angles [76]

In Fig. 2.8, excerpted from [76], the points $\bar{P}$ and $\bar{P}_0$ stand for the mean equatorial poles of date and of epoch, respectively. Likewise, the points C and C_0 denote the ecliptic poles of date and of epoch, respectively. The point P represents the true equatorial pole of date, connected to the mean equatorial pole of date and ecliptic pole of date through the nutation angles $\Delta\psi$ and $\Delta\varepsilon$. Following the rotation, the x-axis of the coordinate system is aligned with the mean equinox of date while the z-axis is aligned to the mean equatorial pole of date.

In the GIPSY/OASIS II software, the nutation parameters $\Delta\psi$ and $\Delta\varepsilon$, represented in Figs. 2.8 and 2.9, are not actually computed based on the IAU 1980 Theory of Nutation. For simplicity and to speed up the computation, they are readily extracted from the planetary ephemerides.

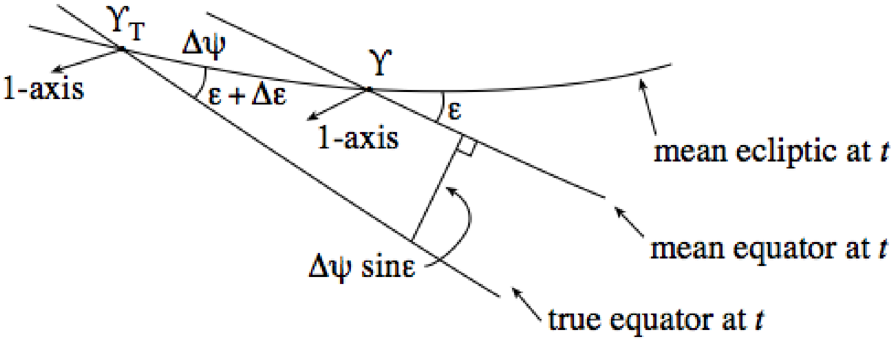

Figure 2.9: Schematic of the Nutation Angles [76]

The nutation matrix is then formed through Eq. 2.13 which corresponds to a 1-3-1 Eulerian rotation.

$$N = R_1(-\bar{\varepsilon})\, R_3(\Delta\psi)\, R_1(\varepsilon) \tag{2.13}$$

where

$$\bar{\varepsilon} = 84381.448'' - 46.8150''\, t - 0.00059''\, t^2 + 0.001813''\, t^3 \tag{2.14}$$

and

$$\varepsilon = \bar{\varepsilon} + \Delta\varepsilon \tag{2.15}$$

Following the nutation rotation, the mean equator and equinox of date are transformed into the true equator and equinox of date P and C.

- <u>Modern representation</u>

Various implementation approaches are documented (see [144], [42] or [114]) for the computation of the bias, precession and nutation matrices using the IAU2006A precession-nutation model. For simplicity and as mentioned in the introduction of this section, we chose to follow the improved classical, equinox-based formulation.

In this approach the nutations in longitude and in obliquity, resp. $\Delta\psi$ and $\Delta\varepsilon$, are calculated based on the full IAU 2000A Nutation model developed by Mathews, Herring and Buffet in their series of papers [140], [107] and [34]. The two nutation parameters are computed from series of 678 lunisolar terms and 687 planetary terms stored in tables directly provided by the IAU "Standards of Fundamental Astronomy" (SOFA) initiative. Their mathematical formulations are given by Eqs. 2.16 and 2.17.

$$\begin{cases} \Delta\psi = \sum_{i=1}^{N} (A_i + A_i' t)\,\sin(arg) + (A_i'' + A_i''' t)\,\cos(arg) & (2.16) \\ \Delta\varepsilon = \sum_{i=1}^{N} (B_i + B_i' t)\,\cos(arg) + (B_i'' + B_i''' t)\,\sin(arg) & (2.17) \end{cases}$$

In Eq. 2.16 A_i and A_i' denote the in-phase coefficients for the nutation in longitude and their time variations, respectively. A_i'' and A_i''' are the out-of-phase coefficients and their time variations. B_i, B_i', B_i'' and B_i''' represent the same quantities for the nutation in obliquity. The upper limit of the summations, N, is equal to 678 for the lunisolar contribution to nutation and 687 for the planetary nutation terms. The time variable t is measured in Julian centuries from J2000.0. The argument arg of the trigonometric functions represents linear combinations of fundamental arguments, the coefficients of which are specified in tables available electronically through [113]. In the case of the lunisolar terms, the fundamental arguments are the 5 Delaunay arguments, defined in the next chapter of this dissertation (see section 3.2.2). In the case of the planetary nutation terms, they correspond to the mean longitudes of the planets. The expressions for the fundamental arguments of nutation (lunisolar as well as planetary) are developed in the IERS Conventions 2003 [144].

The nutation parameters $\Delta\psi$ and $\Delta\varepsilon$ thus obtained are then adjusted to be compatible with the IAU 2006 Precession model following Eq. 5 of [195], reproduced below.

$$\begin{aligned} \Delta\psi &= \Delta\psi + (0.4697.10^{-6} + f)\,\Delta\psi \\ \Delta\varepsilon &= \Delta\varepsilon + f\,\Delta\varepsilon \qquad (2.18) \\ \text{where } f &= (\dot{J}_2/J_2)\,t = -2.7774.10^{-6}\,t \end{aligned}$$

In Eq. 2.18, t is the Terrestrial Time interval since J2000 in Julian centuries.

Once $\Delta\psi$ and $\Delta\varepsilon$ are determined as detailed above, the bias, precession and nutation matrices are computed altogether using the P03 (IAU 2006) precession model. This model was developed by Capitaine et al., discussed in [42] and recommended by the Working Group on Precession and the Ecliptic [108]. It is implemented in GIPSY/OASIS using the Fukushima-Williams (FW) parameterization explained and derived by Fukushima in [76]. This choice is justified by the various advantages offered by the FW parameterization over the other three possible formulations of precession. The benefits of the Fukushima-Williams angles are detailed in [108]. The Fukushima-Williams parameterization consists of a set of four angles: ϵ_A, $\bar{\psi}$, $\bar{\phi}$ and $\bar{\gamma}$. The FW angles are computed as polynomials based on coefficients provided in Table I of [108]. The dependent variable is Terrestrial Time expressed in Julian centuries since J2000.0. The diagram displayed in Fig. 2.10 shows how these angles are defined.

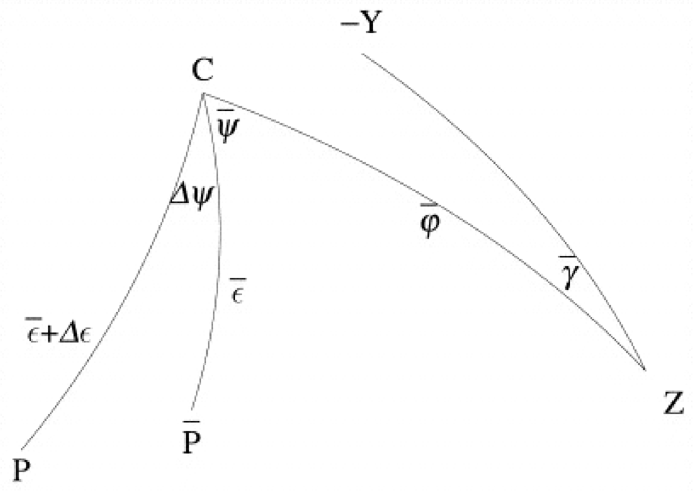

Figure 2.10: The Fukushima-Williams parameterization [76]

In the sketch above, Y and Z respectively denote the y- and z-axis of the celestial reference frame. P, $\bar{P}$ and C represent the same quantities as in Fig. 2.8.

As explained in [108], the bias matrix B is directly incorporated into the precession matrix as a result of the FW parameterization. By adding the nutation in longitude $\Delta\psi$ to the second

FW angle ψ and the nutation in obliquity $\Delta\epsilon$ to the first FW angle ϵ_A, the overall BPN matrix is formed as shown in Eq. 20 of [108], reproduced here:

$$NPB = R_1(-\epsilon_A - \Delta\epsilon)\, R_3(-\psi - \Delta\psi)\, R_1(\phi)\, R_3(\gamma) \tag{2.19}$$

2.4.2 Greenwich Sidereal Time

Because the GST formulation needs to be compatible with the precession model used, two separate formulations of sidereal time are considered depending on whether the IAU06A or the IAU80 precession-nutation model is used.

- Classical paradigm

The Hour Angle in the formulation consistent with the IAU80 precession-nutation model corresponds to the Greenwich Apparent Sidereal Time (GAST). Computing the GAST involves calculating the Greenwich Mean Sidereal Time (GMST) as well as the Equation of the Equinoxes beforehand. The equations of interest are provided on page 30 of the IERS Technical Note 13 [141]. The GMST is computed using:

$$\begin{aligned} GMST &= JDF + 67310.54841 + \dots \\ &\quad 8640184.812866\, T_u + 0.093104\, T_u^2 - 6.2.10^{-6}\, T_u^3 \end{aligned} \tag{2.20}$$

The Equation of the Equinoxes can be retrieved directly from the nutation matrix using:

$$Ee = \tan^{-1}\left(\frac{N(1,2)}{N(1,1)}\right) \tag{2.21}$$

Eventually, the GAST is obtained by summing the two previous quantities:

$$GAST = GMST + Ee \tag{2.22}$$

In Eq. 2.21, N denotes the nutation matrix. In Eq. 2.20, JDF refers to the fraction of UT1 Julian day expressed in seconds and T_u is UT1 expressed in Julian centuries. Equation 2.22 provides evidence that the motions of precession and nutation contribute to the definition of the Greenwich apparent sidereal time, as mentioned in section 2.3.4.

- Modern representation

As suggested in [195] and [114], the consistency between the Hour Angle formulation and the IAU06A precession-nutation model is ensured by computing parameters specific to the CIO-based paradigm internally prior to reverting back to the equinox-based formulation via the use of the so-called Equations of Origins. The method can be more easily understood by visualizing the diverse parameters entering the equation. Figure 2.11 is a sketch of the locations of the ICRF and ITRF origins and important angular quantities involved in the calculation of the Greenwich Sidereal Time. The notations in this figure that are relevant to the use of the equinox-based version of the modern formulation of Earth orientation are as follows: σ is the CIO, γ and γ_1 are the ascending nodes of the ecliptic of date and J2000 ecliptic, respectively.

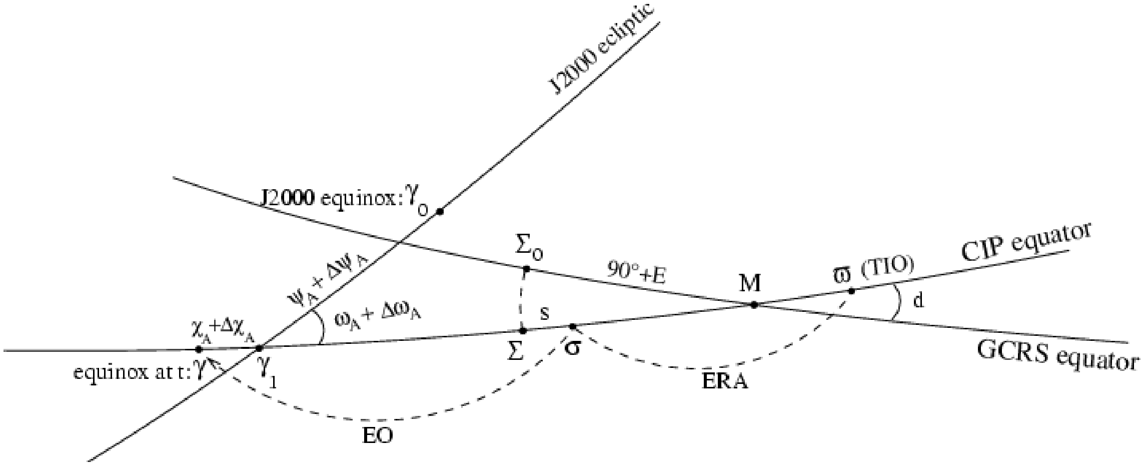

Figure 2.11: ERA, Equations of the Origins and locations of the CIO and TIO [40]

The procedure implemented in GIPSY/OASIS therefore follows the steps outlined by Wallace and Capitaine in [195] and [41]. A flow chart is given below.

- To begin with, the Earth Rotation Angle is computed. The ERA is defined as the hour angle of the CIO from the TIO meridian. It is calculated using Eq. 15 of [144].

$$\begin{aligned} ERA(T_u) = 2\pi\,(&\text{UT1 Julian day fraction} \\ &+ 0.7790572732640 + 0.00273781191135448\,T_u) \end{aligned} \tag{2.23}$$

In Eq. 2.23, T_u is the Julian UT1 date since epoch J2000 where UT1 is deduced from Eq. 2.24.

$$UT1 = UTC + (UT1 - UTC) \tag{2.24}$$

- A pre-determined Bias/Precession/Nutation matrix is then supplied and used to form the Equation of the Origins. The Equation of the Origins owes its name to the fact that it relates the CIO and the equinox, i.e. the origins of the modern and classical celestial frames.
    - ∗ The Celestial Intermediate Pole (CIP) coordinates are first extracted from the input BPN matrix. They are defined as:

$$\begin{cases} X = NPB(3,1) \\ Y = NPB(3,2) \\ Z = NPB(3,3) \end{cases} \tag{2.25}$$

    - ∗ Likewise, the three vectors $\vec{\Upsilon}$, $\vec{y}$ and $\vec{\Sigma}$, defined below, are formed based on the BPN matrix following Eqs. 13 to 15 of [195].

$$\vec{\Upsilon} = NPB(1,:) \tag{2.26}$$

$$\vec{y} = NPB(2,:) \tag{2.27}$$

$$\begin{cases} \Sigma(1) = 1 - X^2/(1+Z) \\ \Sigma(2) = -XY/(1+Z) \\ \Sigma(3) = -X \end{cases} \tag{2.28}$$

    - ∗ The so-called CIO locator s is then deduced from tabulated series of the quantity $s + XY/2$ using the X and Y coordinates computed via Eq. 2.25.

$$\begin{aligned} s = {} & 94.0 + 3808.35\,t - 119.94\,t^2 - 72574.0\,t^3 + 27.70\,t^4 + 15.61\,t^5 \\ & + \sum_{\substack{i \\ j=0,4}} [\, S_{i,j}\, t^j \sin(arg_i) + C_{i,j}\, t^j \cos(arg_i) \,] - XY/2 \end{aligned} \tag{2.29}$$

In Eq. 2.29, X and Y are the CIP coordinates calculated through Eq. 2.25. $S_{i,j}$ (resp. $C_{i,j}$) denote the coefficients for the i^{th} sine (resp. cosine) term of degree j of the $XY/2$ series. These coefficients are tabulated and are available electronically through [113].

The Equation of the Origins is finally computed as shown below and in Eq. 16 of [195].

$$EO = s - \tan^{-1}\left(\frac{\vec{y}.\vec{\Upsilon}}{\vec{\Upsilon}.\vec{\Sigma}}\right) \tag{2.30}$$

- The GST, defined as the hour angle of the equinox from the TIO meridian, is eventually obtained through Eq. 17 of [195].

$$GST = ERA - EO \tag{2.31}$$

2.4.3 Polar Motion

- Classical paradigm

In the case of the IAU80 implementation, the polar motion matrix is simply written as:

$$W = R_2(x_p)\, R_1(y_p) \tag{2.32}$$

where R_2 is a rotation about the y-axis by the angle x_p and R_1 is a rotation about the x-axis by y_p.

- Modern formulation

The polar motion matrix W is slightly modified with respect to the IAU80 model implementation when the modern approach is taken. This new formulation, shown in the equations below, results in improved accuracy.

$$W = R_3(-s')\, R_2(x_p)\, R_1(y_p) \tag{2.33}$$

In Eq. 2.33, the quantity s' refers to the TIO locator, defined in Eq. 13 of Chapter 5 in [152]. The mathematical expression can be simplified and reduced to Eq. 2.34 as explained in [152].

$$s' = -(47\mu\text{as})t \tag{2.34}$$

In the equation above, t is again expressed in Julian centuries of Terrestrial Time since J2000.0 and R_3 is a rotation about the z-axis by the angle $-s'$.

2.4.4 Models implemented in GIPSY for Polar Motion and UT1-UTC

The Hour Angle - or Greenwich Sidereal Time (GST) - matrix, U, depends both on models and on the frequent measurement of $UT1{-}UTC$. Likewise, the matrix W depends on measurements of the instantaneous position of the Earth's rotational axis as well as on models.

As mentioned for Eq. 2.23, Eq. 2.24 is used to deduce UT1 from the specified UTC epoch. In that equation the quantity $UT1 - UTC$ is computed as follows.

$$UT1 - UTC = (TAI - UTC) - (TAI - UT1) \tag{2.35}$$

In Eq. 2.35, the quantity $TAI{-}UTC$ corresponds to leap seconds, the values of which are tabulated and available through IERS Bulletins. In GIPSY, the value of $TAI{-}UT1$ at a specified UTC epoch is obtained through the cubic Hermitian interpolation of measurements. Prior to the interpolation, the measurement time series are smoothed through regularization to enhance the interpolation accuracy. Regularization is achieved by substracting the sum of 41 terms with periods ranging from 5 to 35 days from the $TAI - UT1$ series. This corresponds to the smoothing of the $TAI - UT1$ series by removing the effects of zonal tidal variations. The procedure is carried out based on models recommended by the IERS Conventions. Table 8.1 of [144] provides the coefficients for one of the zonal tide models implemented in the software. After the interpolation is performed, the model value is added back at the interpolating epoch. In addition, variations in UT1 induced by the ocean tides at semi-diurnal and diurnal periods are accounted for by means of models such as the one shown in Tables 8.3 of [144].

The rotation angles x_p and y_p are determined by measurements and models. Similar to what is done for $UT1$, observed values of the pole coordinates are interpolated to the specified UTC epoch using a cubic Hermitian scheme. Models for the variations in polar motion due to the ocean tides are implemented as well and added to the observations.

It is noteworthy that the ECEF coordinates themselves are defined by agreed upon reference coordinates and velocities that are made as self-consistent as possible with various geodetic measurement systems including Very Long Baseline Interfero-metry (VLBI), Satellite Laser Ranging (SLR) and GPS. Along with reference cartesian coordinates and velocities, a set of models describing the deformation of the Earth over time are necessary. These models include models for the solid tides, ocean tides and pole tides. Plate tectonics are accounted for in site velocities. All the geophysical models used to the end of augmenting the accuracy of the ECEF coordinates are discussed in Chapter 7.

Chapter 3

Polar Motion Temporal Variations

This chapter provides an overview of the short-term features of the polar motion spectrum as well as a mathematical description of their underlying causes. It also reviews the background needed for the geophysical analyses of the pole coordinates time series conducted in Chapter 9. Because this research is concerned only with the determination of polar motion, observed oscillations in the rotation rate of the Earth are not treated here. The reader is referred to short reviews by Wahr [194], Dickey [62] and Rochester [159] or longer ones by Munk and MacDonald [148] or Moritz and Mueller [147] among many others for information on the temporal variation of UT1 and length-of-day. This chapter is organized as follows. To begin with, the most significant long-period characteristics of polar motion are briefly acknowledged before a more detailed description of the rapid (characterized by periods ranging from 2 to 20 days) and ultra-rapid (sub-daily) constituents of the polar motion spectrum is given. Sources of excitation of polar motion are then discussed. In particular, the roles of the luni-solar torque and internal geophysical processes are detailed. To this end, the mathematical representation of the forcing mechanisms is provided by means of the linearization of the Euler-Liouville rotational equations of motion. To conclude, the relationship that links the measurable geophysical excitations to the observable pole coordinates is derived.

3.1 Overview of the frequency spectrum of polar motion variations

Figure 3.1 schematically represents the various phenomena influencing polar motion and indicates their characteristic periods. The fact that long-period nutation (as seen from the celestial frame) cannot be separated from diurnal polar motion (relative to the terrestrial frame) is illustrated.

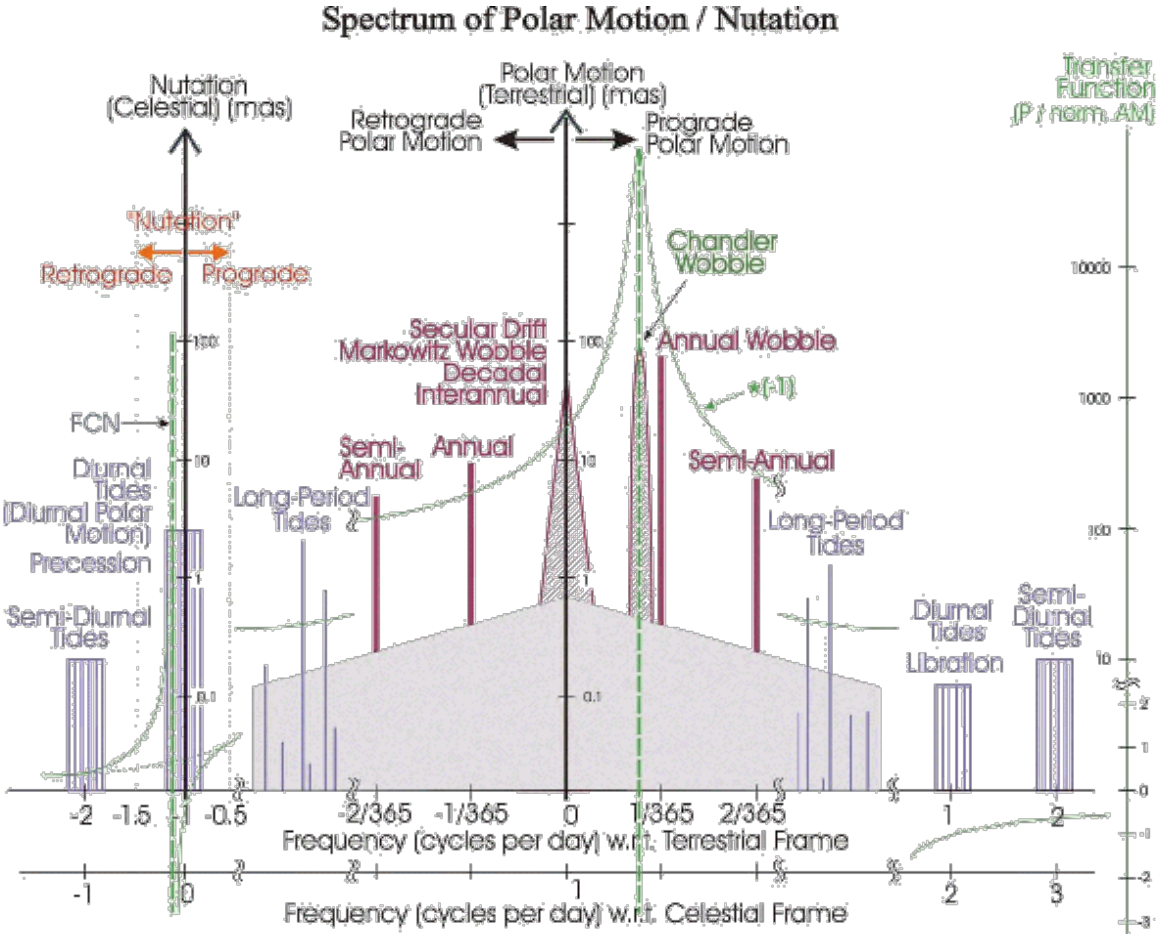

Figure 3.1: Schematic spectrum of polar motion variations, from [47]

As mentioned in Chapter 1, polar motion variations behave like red noise. Therefore, the spectrum is dominated by phenomena occurring over long periods, as clearly visible on Fig. 3.1. In fact, Bizouard and Seoane recently reported that rapid polar motion is deemed to account for less than 1% of the total power spectrum, its amplitude not exceeding 2 mas [21]. For this reason, the section following is devoted to the description of the main long-period contributors to polar motion. Since the sources of polar motion variability fall into two categories, the distinction between the free and forced wobbles is addressed next. Note that the significance of the transfer function line represented in Fig. 3.1 is dealt with in Chapter 9 of this dissertation.

3.1.1 Main contributors to polar motion

As visible on the plot shown above, the predominant features of polar motion are the annual and Chandler wobbles. These rotational motions consist of nearly-circular oscillations with amplitudes of 100 and 200 mas and periods of about one year and 433 days, respectively. The origin of the Chandler wobble, a free oscillation of the Earth, remains unclear although the main contributors to its excitation are believed to be the atmosphere and oceans. The annual wobble is also largely excited by the atmosphere and oceans along with ground water storage. In addition, a secular drift amounting to a few milliarcseconds per year contributes a significant amount to polar motion and is believed by the geophysics community to be a consequence of glacial isostatic rebound and ice cap melting. Decadal variations have also been observed with amplitudes of 50 mas and fluctuations of polar motion over time scales of a few weeks to a few months have been measured with peak-to-peak variations of less than 20 mas [62]. The cumulative effect of these relatively long-term variations produces excursions in the pole location of 10 meters over a period of one year according to [185].

3.1.2 Free wobbles

Free wobbles are rotational eigenmodes of the Earth and, as such, are resonant modes of the Earth's rotation. They are the solutions to the homogeneous Euler-Liouville rotational equations of motion derived in section 3.3.2 and are thus functions of the Earth's internal structure and composition. According to Gross, Fukumori and Menemenlis, there are three principal free wobbles: the Chandler wobble, the Nearly Diurnal Free Wobble (NDFW) and the Inner Core Wobble [93]. However, only the first two proper modes are relevant to this research for reasons exposed in Chapter 9; as a result the inner core wobble is ignored in this dissertation.

The Chandler wobble is the primary free oscillation of the Earth and was the first one to be theoretically investigated and detected. It is a prograde motion (counter-clockwise) with an average period of 435 days as derived from observations collected by various astrometric and geodetic techniques. The Chandler wobble has been the object of numerous studies in the literature and its origins are still under active investigation. The NDFW, also called the Free Core Nutation (FCN) due to the dualism between polar motion and nutation, is a retrograde process exhibiting a nearly diurnal frequency (the frequency is estimated to be -1.0023203 cpsd by Chin, Gross and Dickey in [52]) as seen from the Earth and a period of approximately 460.5 days as seen from the inertial frame, according to Hefty [103]. As suggested by its name, the FCN is due to the dynamical motion of the fluid outer core. The resonant effect associated with the FCN manifests itself in the diurnal tidal band and is therefore detected in the effects of diurnal ocean tides on polar motion. As a matter of fact, the resonance observed in the amplitudes of the diurnal Earth tides constitutes indirect evidence for the free core nutation and is considered the most convincing proof of existence of this mode [166]. Note that the FCN-induced resonant effects are removed from the IERS-recommended model used to predict tidal variations in the pole coordinates. Similar to the Chandler wobble, the NDFW has been widely studied; nevertheless its characteristic parameters (period, damping factor and excitation mechanisms) still remain to be clearly identified and determined with accuracy. The complexity of this free wobble and its geophysical interpretation and possible excitation mechanisms have been discussed in [160], [150], [103] and [166] for instance.

Both the Chandler and Nearly Diurnal Free wobbles play a critical role in the analysis and validation of series of polar motion estimates when these are used for comparison with geophysical excitations. Their importance and treatment in the context of polar motion series analysis are addressed in Chapter 9 and more specifically in section 9.2, a section dedicated to the deconvolution of polar motion estimates.

3.1.3 Forced wobbles

Forced polar motions correspond to the solutions of the inhomogeneous Euler-Liouville rotational equations of motions. They are characterized by the fact that their frequencies are the same as the frequencies of their forcing mechanisms. As represented in Fig. 3.1, there exist various classes of forced wobbles outside of the period identified with the rapid and ultra-rapid polar motions. Forced wobbles actually occur on all observable time scales and are caused by a variety of forcing mechanisms. In his review of long-period Earth rotation variations [88], Gross devotes a large section to the description of long-periodic forced polar motions, detailing their periods, amplitudes and assumed or well-known forcing mechanisms.

As mentioned in the introductory chapter of this thesis, the research presented here concentrates on the recovery and analysis of forced polar motion. In particular, the sections that follow focus on the causes of ultra-rapid and rapid polar motion. Both external and internal (i.e. internal to the Earth system) torques are at play in this case. On the one hand, the daily and sub-daily variations in polar motion (constituting ultra-rapid polar motion) are driven by the action of the luni-solar torque. On the other hand, rapid polar motion is forced by inter-exchanges of angular momentum involving all the layers of the Earth system. These excitation sources are discussed in the next sections.

3.2 The luni-solar tidal potential

3.2.1 The luni-solar gravitational torque

The gravitational attraction exerted by the Sun and Moon on the Earth causes deformations of the Earth and perturbations in its position and orientation in inertial space. The effects of the luni-solar torque on the Earth are classically separated into three types of responses [58]:

(1) the orbital motions of the Earth about the Sun and the Moon about the Earth due to the net acceleration of the Earth's (resp. Moon's) center of mass induced by the force;

(2) tides manifesting in every layer of the Earth system as an effect of the residual spatially-variable acceleration cited above;

(3) changes in the Earth orientation parameters through rotational motions of precession and nutation, forced polar motion and irregularities in the length of day.

Variations in polar motion characterized by periods of one day and shorter are essentially due to changes in the ocean heights and currents induced by the luni-solar tidal potential [162]. Even though the atmosphere and solid Earth are also subjected to these tidal forces to some extent, the influence of ocean tides clearly dominates. It is for instance believed that the influence of ocean tides is about two orders of magnitude larger than the influence of atmospheric tides in the sub-daily frequency band, as stated in [69]. The response of the oceans to these tidal effects is described in the next section. The impact of body tides, pole tides and atmospheric tides on the determination of rapid polar motion are all mentioned in Chapter 7.

3.2.2 Ocean tides and associated polar motion variations

A detailed description of the tide generating potential (TGP) and its analytical formulation are beyond the scope of this chapter. This section concentrates on the ma-thematical description of the ocean response to constituents of the TGP. The equations presented below were used for the tidal analyses carried out in Chapter 9. The thorough derivations of the equations shown here can be found in [58].

In the time domain, the tidal potential generated by the Sun and Moon is written as a function of the positions of these two celestial bodies relative to the Earth. Two sets of angular variables, each composed of six astronomical arguments, can be used to describe these geocentric positions: the Doodson arguments and the Delaunay arguments. The Delaunay arguments consist of χ, l, l', F, D and Ω. Each of these astronomical phase angles is defined below:

- $\chi = \theta + \pi$, where θ is the Greenwich Mean Sidereal Time, represents the rotation phase angle of the Earth.
- l denotes the mean anomaly of the Moon.
- l' is the mean anomaly of the Sun.

- $F = L - \Omega$, where L is the mean longitude of the Moon, is the mean argument of latitude of the Moon.
- D is the mean elongation of the Moon from the Sun.
- Ω represents the mean longitude of the ascending node of the Moon.

The calculation of the Delaunay arguments is presented in Appendix A.

In the frequency domain, the constituents of the tidal potential are expressed as spherical harmonic series characterized by their order n and degree m. The angular argument of each tidal constituent, composed of a frequency ω_{nmj} and an astronomical phase β_{nmj}, is determined by a linear combination of the Delaunay arguments. Following Woodward's convention, the coefficients involved in such linear combinations are specified by a sequence of 6 integers $(a_j, b_j, c_j, d_j, e_j, f_j, g_j)$, as shown in Eq. 3.1.

$$\omega_{nmj}\, t + \beta_{nmj} = a_j\, l + b_j\, l' + c_j\, F + d_j\, D + e_j\, \Omega + f_j\, (\theta + \pi) - \delta(n, m)\, \frac{\pi}{2} \tag{3.1}$$

In Eq. 3.1, $\delta(n, m)$ is equal to 1 when $n+m$ is odd and is null otherwise. Note that only the 8 major semi-diurnal and diurnal tides were considered in the tidal analyses conducted for this research. While $n = 2$ for all 8 tides, $m = 2$ for semi-diurnal tides and $m = 1$ for diurnal tides by definition [58].

In practice, the origin of a tide constituent can be inferred by looking at the coefficients attached to each Delaunay variable. Table 3.1 states the species of each of the eight major tides considered. The associated Delaunay coefficients are also shown in Table 3.2.

Tide symbol	**Period [hours]**	**Species**
Q1	26.87	larger lunar elliptic diurnal
O1	25.82	lunar diurnal
P1	24.07	solar diurnal
K1	23.94	lunisolar declination diurnal
N2	12.67	larger lunar elliptic semidiurnal
M2	12.42	principal lunar semidiurnal
S2	12.00	principal solar semidiurnal
K2	11.97	lunisolar semidiurnal

Table 3.1: Principal diurnal and semi-diurnal ocean tides

As formulated by Desai in [58], the ocean response $\zeta_{nmj}(\theta, \lambda, t)$ to a tidal constituent characterized by its frequency ω_{nmj} and astronomical phase β_{nmj} is expressed in terms of two location-dependent quantities: an amplitude $A(\theta, \lambda)$ and a Greenwich phase lag $G(\theta, \lambda)$. The latter parameter refers to the angle by which the maximum tidal uplift is delayed with respect to the instantaneous Earth-Moon vector due to energy dissipation occurring in the oceans. Equation 3.2 shows how the ocean tide response is then defined:

$$\zeta_{nmj}(\theta, \lambda, t) = A(\theta, \lambda)\,\cos\left(\omega_{nmj} + \beta_{nmj} - G(\theta, \lambda) + \delta_{nmj}\,\pi\right) \tag{3.2}$$

where δ_{2mj}, by definition, has a value of 1 for the K1 tide and 0 for the rest of the 8 principal diurnal and semi-diurnal ocean tides.

In practice (c.f. section 9.1.2), the amplitude and Greenwich phase lag are determined by rewriting Eq. 3.2 as:

$$\begin{aligned} \zeta_{nmj}(\theta, \lambda, t) = A(\theta, \lambda)\cos\left(G(\theta, \lambda)\right)\cos\left(\omega_{nmj} + \beta_{nmj} + \delta_{nmj}\pi\right) + \ldots \\ A(\theta, \lambda)\sin\left(G(\theta, \lambda)\right)\cos\left(\omega_{nmj} + \beta_{nmj} + \delta_{nmj}\pi\right) \end{aligned} \tag{3.3}$$

The reaction of the oceans to the luni-solar tidal potential causes periodic changes in the Earth's inertia tensor due to the massive redistribution of water induced by the tidal deformation. Because the principal moments of inertia of the Earth define its orientation in space, they are closely related to the coordinates of the pole and length-of-day. Therefore, any periodic variation in the Earth's principal moments of inertia translates into variations in polar motion of the same period.

Table 3.2 shows the effects of the eight major ocean tides on diurnal and semi-diurnal polar motion as predicted by models. The chart is excerpted from the IERS Technical Note 36 (c.f. Table 8.2 of [144]).

Tide	l	l'	F	D	Ω	χ	Doodson	Period	Δx		Δy	
									Coefficients of			
								[hrs]	Sin	Cos	Sin	Cos
Q_1	-1	0	-2	0	-2	1	135.655	26.87	6.2	26.3	-26.3	6.2
O_1	0	0	-2	0	-2	1	145.555	25.82	48.8	132.9	-132.9	48.8
P_1	0	0	-2	2	-2	1	163.555	24.07	26.1	51.2	-51.2	26.1
K_1	0	0	0	0	0	1	165.555	23.94	-77.5	-151.7	151.7	-77.5
N_2	-1	0	-2	0	-2	2	245.655	12.67	-56.9	-12.9	11.1	32.9
M_2	0	0	-2	0	-2	2	255.555	12.42	-330.2	-27.0	37.6	195.9
S_2	0	0	-2	2	-2	2	273.555	12.00	-144.1	63.6	59.2	86.6
K_2	0	0	0	0	0	2	275.555	11.97	-38.5	19.1	17.7	23.1

Table 3.2: Diurnal and sub-diurnal variations of polar motion due to oceanic tides. Units of the coefficients are μas.

Beside the tidal variations observed in sub-daily polar motion, other rapid changes are due to the interaction of the oceans and atmosphere with the solid Earth. These fluctuations observed in polar motion can be explained by corresponding changes in the Earth's inertia tensor and relative angular momentum arising from internal torques. The application of the principle of conservation of angular momentum to the non-rigid Earth and its implications for polar motion studies are detailed in the section following.

3.3 Conservation of angular momentum in the deformable Earth system

3.3.1 Motion of a deformable body

This subsection aims at introducing some of the quantities and terminology that will be used not only in the remainder of this chapter but also in the sections of Chapter 9 dedicated to the comparison of the estimated time series with effective angular momentum functions. The full mathematical analysis is not presented here but can easily be derived and is detailed in [147] for example.

The motion of a deformable body is characterized by the combination of motions of translation, rotation and deformation. Similar to the case of a rigid body, the translational motion can readily be isolated from the two other types of motions by placing the origin of the reference frame attached to the body at its center of mass. The rotational and deformational parts of the overall motion are then separated by choosing a proper reference frame, known as a Tisserand frame.

The angular momentum vector about the center of mass of the body is the quantity of interest when studying the variability of the Earth's rotation parameters caused by internal torques. The distinction between the three kinds of motions directly translates into the equation for the angular momentum of a deformable body. Indeed, three components can be identified: the translational (or orbital) angular momentum, the rotational angular momentum and the deformational (or relative) angular momentum. More information on the distinction between each of the components of motion is given in the paragraphs that follow. For the sake of simplicity, the time-dependency of all parameters has been dropped in the equations shown below.

Considering a deformable body rotating with the angular velocity $\vec{\omega}$ relative to inertial space, an infinitesimal element of mass dm is defined by its inertial position vector $\vec{R}$ and its internal position vector relative to the body's center of mass O denoted as $\vec{r}$ so that:

$$\vec{R} = \vec{R}_o + \vec{r} \tag{3.4}$$

where $\vec{R}_o$ is by definition the center of mass position vector. Taking the time derivative, as seen from the inertial frame, of Eq. 3.4 gives:

$$\dot{\vec{R}} = \vec{V} + \vec{\omega} \times \vec{r} + \vec{v} \tag{3.5}$$

In Eq. 3.5:

- $\vec{V} = \dfrac{\mathrm{d}\vec{R}_o}{\mathrm{dt}}$ is the translational velocity of the body;
- the term $\vec{\omega} \times \vec{r}$ represents its rotation and arises from the application of the transport theorem to the inertial derivative of the vector $\vec{r}$;
- $\vec{v} = \dfrac{\mathrm{d}\vec{r}}{\mathrm{d}t}$ denotes the deformational velocity of the body.

Computing the angular momentum vector of the body about the origin of the reference frame, one obtains, after expansion of all the terms:

$$\begin{aligned}\vec{H} &= \iiint\limits_B \vec{R} \times \dot{\vec{R}}\,\mathrm{d}m \\ &= \underbrace{\iiint\limits_B \vec{r} \times \dot{\vec{r}}\,\mathrm{d}m}_{\vec{H}_{internal}} + \underbrace{\left[\iiint\limits_B \vec{r}\,\mathrm{d}m\right] \times \vec{V}}_{\vec{H}_{interactional}} + \underbrace{\vec{R}_o \times \iiint\limits_B \dot{\vec{R}}\,\mathrm{d}m}_{\vec{H}_{orbital}} \end{aligned} \tag{3.6}$$

The so-called interactional angular momentum term is cancelled by placing the origin of the reference frame at the center of mass of the body. The translational angular momentum is ignored hereinafter because it translates into the orbital angular momentum of the Earth around the Sun. Instead, we focus on the term corresponding to the internal angular momentum vector with respect to the body frame. This term contains the contributions of both the rotation and deformation of the body. It can be re-written using the transport theorem once again to give Eq. 3.7.

$$\vec{H}_{internal} = \underbrace{\iiint\limits_B \vec{r} \times \vec{\omega} \times \vec{r}\,\mathrm{d}m}_{I(t)\,\vec{\omega}} + \underbrace{\iiint\limits_B \vec{r} \times \vec{v}\,\mathrm{d}m}_{\vec{h}} \tag{3.7}$$

In Eq. 3.7, $\vec{h}$ represents the so-called relative angular momentum. The quantity $I(t)$ represents the inertia tensor of the body and is a function of time because the body deforms through time. It is clear from Eq. 3.7 that the separation between rotation and deformation is dependent on the reference frame tied to the body.

The convention in geophysics is to use a Tisserand frame as the reference frame attached to the body. The Tisserand axes are defined such as to globally minimize the deformation in a least-squares sense, which is equivalent to minimizing the kinetic energy of the deformation undergone by the body [147]. Such frames also offer the advantage of allowing the complete separation of the motions of rotation, deformation and translation as mentioned earlier. Indeed, the frame can be specified so that the relative angular momentum term $\vec{h}$ becomes null. In the particular case of the multi-layered Earth, the reference frame traditionally picked is referred to as the mean-mantle Tisserand frame. The axes of this frame are determined so that the relative angular momentum vector of the mantle vanishes.

3.3.2 Euler-Liouville rotational equations of motion

The rotational behavior of the non-rigid Earth is described by the Euler-Liouville rotational equations of motion. These equations are adapted from Euler's rotational equations of motion by replacing the hypothesis of a rigid body by that of a deformable one and by assuming a temporally-variable inertia tensor. The closed system under consideration for application of the principle of conservation of angular momentum is composed of the solid Earth (core and mantle), the oceans and atmosphere. It is hereinafter referred to as the deformable Earth.

The development of the Euler-Liouville rotational equations of motion is shown below and can be found in extenso in [126]. It is based on a perturbation method. The main steps and equations are reproduced here employing the nomenclature introduced by Desai in [58].

The equilibrium state of the system is defined by its angular velocity vector $\vec{\omega}_0$ and inertia tensor I_0:

$$\begin{cases} \vec{\omega}_0 = \begin{bmatrix} 0 & 0 & \Omega \end{bmatrix}^T & (3.8a) \\ I_0 = \begin{bmatrix} A & 0 & 0 \\ 0 & B & 0 \\ 0 & 0 & C \end{bmatrix} & (3.8b) \end{cases}$$

where Ω denotes the mean rotation rate of the Earth, A and B the equatorial moments of inertia and C the polar moment of inertia.

By definition, the angular momentum at equilibrium is:

$$\vec{H}_0 = I_0\,\vec{\omega}_0 = C\,\Omega\,\hat{z} \tag{3.9}$$

Excluding the action of external torques, the angular momentum vector of the Earth, shown in Eq. 3.9, can be perturbed either by a change in the Earth's inertia tensor or by inducing a motion in the fluid portions of the Earth, thus giving rise to a relative angular momentum vector $\vec{h}$ defined in section 3.3.

Applying both types of perturbations simultaneously yields the instantaneous angular velocity vector $\vec{\omega}(t)$ on the one hand:

$$\vec{\omega}(t) = \vec{\omega}_0(t) + \delta\vec{\omega}(t) \tag{3.10a}$$

$$\text{where } \delta\vec{\omega} = \Omega\,[m_1\ m_2\ m_3] \tag{3.10b}$$

$$\text{with } m_i \ll 1 \text{ for j=1..3} \tag{3.10c}$$

and the Earth's instantaneous tensor of inertia $I(t)$ on the other hand:

$$I(t) = I_0(t) + \delta I(t) \tag{3.11a}$$

$$\text{where } \delta I(t) = \begin{bmatrix} c_{11}(t) & c_{12}(t) & c_{13}(t) \\ c_{21}(t) & c_{22}(t) & c_{23}(t) \\ c_{31}(t) & c_{32}(t) & c_{33}(t) \end{bmatrix} \tag{3.11b}$$

$$\text{with } c_{ij}(t) \ll C \text{ for i, j = 1...3 at all times} \tag{3.11c}$$

In Eq. 3.10b, the parameters $(m_1,\, m_2)$ define the slight deviation in the orientation of the Earth's rotation axis caused by the perturbation in equilibrium and are therefore connected to the coordinates of the pole $(x_p,\, y_p)$. The exact relationship between $(m_1,\, m_2)$ and $(x_p,\, y_p)$ is derived in section 3.4.4 and Appendix C. Likewise, m_3 is directly related to the change in length-of-day by $LOD = -\dfrac{m_3 \times 2\pi}{\Omega}$.

Starting from the sets of Eqs. 3.10 and Eqs. 3.11, the angular momentum of the slightly perturbed Earth becomes:

$$\vec{H}(t) = \vec{H}_0(t) + \delta\vec{H}(t) \tag{3.12a}$$

$$\text{where: } \delta\vec{H}(t) = I_0\, \delta\vec{\omega}(t) + \delta I(t)\, \vec{\omega}_0 + \vec{h}(t) \tag{3.12b}$$

Equation 3.12a is equivalently expressed as Eq. 3.7 or Eq. 3.13 below.

$$\vec{H}(t) = I(t)\, \vec{\omega}(t) + \vec{h}(t) \tag{3.13}$$

Taking the inertial time derivative of the angular momentum of the perturbed Earth and then applying the transport theorem yields:

$$\dot{\vec{H}}(t) = \frac{{}^{N}\mathrm{d}}{\mathrm{d}t}\vec{H}(t) = \frac{{}^{B}\mathrm{d}}{\mathrm{d}t}\vec{H}(t) + \vec{\omega}(t) \times \vec{H}(t) \tag{3.14}$$

In Eq. 3.14, the superscript N and B indicate that the derivative is computed as seen from the inertial frame and body frame, respectively. By expanding its right-hand side, the equation becomes:

$$\dot{\vec{H}}(t) = \frac{{}^{B}\mathrm{d}}{\mathrm{d}t}I(t)\vec{\omega}(t) + I(t)\frac{{}^{B}\mathrm{d}}{\mathrm{d}t}\vec{\omega}(t) + \frac{{}^{B}\mathrm{d}}{\mathrm{d}t}\vec{h}(t) + \vec{\omega}(t) \times [I\vec{\omega}(t) + \vec{h}(t)] \tag{3.15}$$

Eventually, the Euler-Liouville rotational equations of motion are obtained by making use of the law of dynamics stating that the inertial time derivative of the angular momentum vector equals the applied torque. Thus Eq. 3.15 becomes:

$$\vec{L}(t) = \frac{{}^{B}\mathrm{d}}{\mathrm{d}t}I(t)\, \vec{\omega}(t) + I(t)\frac{{}^{B}\mathrm{d}}{\mathrm{d}t}\vec{\omega}(t) + \frac{{}^{B}\mathrm{d}}{\mathrm{d}t}\vec{h}(t) + \vec{\omega}(t) \times [I(t)\, \vec{\omega}(t) + \vec{h}(t)] \tag{3.16}$$

The series of equations that follow consist in the expansion of each of the terms forming the Euler-Liouville equation, Eq. 3.16.

$$\frac{\mathrm{d}}{\mathrm{d}t}[\delta I(t)]\,\vec{\omega}(t) = \begin{bmatrix} \Omega\, m_1\, \dot{c}_{11} + \Omega\, m_2\, \dot{c}_{12} + \Omega\, m_3\, \dot{c}_{13} + \Omega\, \dot{c}_{13} \\ \Omega\, m_1\, \dot{c}_{21} + \Omega\, m_2\, \dot{c}_{22} + \Omega\, m_3\, \dot{c}_{23} + \Omega\, \dot{c}_{23} \\ \Omega\, m_1\, \dot{c}_{31} + \Omega\, m_2\, \dot{c}_{32} + \Omega\, m_3\, \dot{c}_{33} + \Omega\, \dot{c}_{33} \end{bmatrix} \tag{3.17}$$

$$I(t)\,\Omega\,\frac{{}^{B}\mathrm{d}}{\mathrm{d}t}\,\vec{m}(t) = \begin{bmatrix} A\,\Omega\,\dot{m}_1 + c_{11}\,\Omega\,\dot{m}_1 + c_{12}\,\Omega\,\dot{m}_2 + c_{13}\,\Omega\,\dot{m}_3 \\ c_{21}\,\Omega\,\dot{m}_1 + B\,\Omega\,\dot{m}_2 + c_{22}\,\Omega\,\dot{m}_2 + c_{23}\,\Omega\,\dot{m}_3 \\ c_{31}\,\Omega\,\dot{m}_1 + c_{32}\,\Omega\,\dot{m}_2 + C\,\Omega\,\dot{m}_3 + c_{33}\,\Omega\,\dot{m}_3 \end{bmatrix} \tag{3.18}$$

$$\vec{\omega}(t){\times}I(t)\,\vec{\omega}(t) = \Omega^2 \begin{bmatrix} m_1\, m_2\, c_{31} + m_2^2\, c_{32} + m_2\, C + m_2\, m_3\, C + m_2\, c_{33} + m_2\, m_3\, c_{33} - m_1\, c_{21} \dots \\ -m_1\, m_3\, c_{21} - B\, m_2 - c_{22}\, m_2 - B\, m_2\, m_3 - c_{22}\, m_2\, m_3 - c_{23} - 2m_3\, c_{23} - m_3^2\, c_{23} \\ A\, m_1 + c_{11}\, m_1 + c_{12}\, m_2 + c_{13} + 2m_3\, c_{13} + A\, m_1\, m_3 + c_{11}\, m_1\, m_3 + c_{12}\, m_2\, m_3 \dots \\ +m_3^2\, c_{13} - m_1^2\, c_{31} - m_1\, m_2\, c_{32} - m_1\, C - m_1\, m_3\, C - m_1\, c_{33} - m_1\, m_3\, c_{33} \\ m_1^2\, c_{21} - m_2^2\, c_{12} - m_2\, c_{13} + m_1\, c_{23} - A\, m_1\, m_2 + B\, m_1\, m_2 \dots \\ -c_{11}\, m_1\, m_2 + c_{22}\, m_1\, m_2 - c_{13}\, m_2\, m_3 + c_{23}\, m_1\, m_3 \end{bmatrix} \tag{3.19}$$

$$\vec{\omega}(t) \times \vec{h}(t) = \begin{bmatrix} h_3\, m_2\, \Omega - h_2\, \Omega - h_2\, m_3\, \Omega \\ h_1\, \Omega + h_1\, m_3\, \Omega - h_3\, m_1\, \Omega \\ h_2\, m_1\, \Omega - h_1\, m_2\, \Omega \end{bmatrix} \tag{3.20}$$

According to Gross in [88], the rotation axis of the Earth deviates from its equilibrium position with respect to the Earth's crust by about a part in a million only, which justifies the linearization to the first order of all the equations shown above using the following set of assumptions:

$$\begin{cases} m_i \ll 1 & (3.21a) \\ c_{ij} \ll C & (3.21b) \\ h_i \ll \Omega C & (3.21c) \end{cases}$$

Note that the first two hypotheses were already posed in the definition of the perturbations. After linearization, the Euler-Liouville equations are written:

$$\vec{L} = \begin{bmatrix} \Omega \dot{c}_{13} + A\,\Omega\,\dot{m}_1 + \dot{h}_1 + \Omega^2\,m_2(C-B) - c_{23}\,\Omega^2 - h_2\,\Omega \\ \Omega \dot{c}_{23} + B\,\Omega\,\dot{m}_2 + \dot{h}_2 - \Omega^2\,m_1(C-A) + c_{13}\,\Omega^2 + h_1\,\Omega \\ \Omega \dot{c}_{33} + C\,\Omega\,\dot{m}_3 + \dot{h}_3 \end{bmatrix} \tag{3.22}$$

A consequence of the linearization to the first order of the Euler-Liouville equations is the decoupling between the equatorial deformation components (m_1, m_2) and the polar component m_3 visible in Eq. 3.22. Because this research is focused on polar motion only, the third equation of motion is ignored from this point forward.

To comply with the assumption of conservation of angular momentum, the motion is made torque-free. After setting $\vec{L} = \vec{0}$, the linearized, homogeneous Euler-Liouville equations associated with polar motion become:

$$\begin{cases} A\,\Omega\,\dot{m}_1 + \Omega^2\,(C-B)\,m_2 = c_{23}\,\Omega^2 + h_2\,\Omega - \dot{c}_{13}\,\Omega - \dot{h}_1 \\ B\,\Omega\,\dot{m}_2 - \Omega^2\,(C-A)\,m_1 = -c_{13}\,\Omega^2 - h_1\,\Omega - \dot{c}_{23}\,\Omega - \dot{h}_2 \end{cases} \tag{3.23}$$

3.4 Equatorial Excitation and Angular Momentum Functions

3.4.1 Excitation functions

Excitation functions are defined by Gőttl and Seitz in [84] as the "mathema-tical description of the geophysical effects on the Earth's rotation". They represent the forcing mechanisms governing the variations in the Earth's rotation and arising from internal dynamics of the Earth system. All the geophysical excitations originate in internal processes occurring within the various layers of the Earth as well as from interactions between the different subsystems of the Earth. They include but are not limited to large-scale mass redistribution due for instance to the global atmospheric and oceanic circulations as well as to convection in the mantle and electromagnetic coupling between the core and the mantle.

Figure 3.2 illustrates the main known mechanisms acting on the Earth and contributing to the deformations of its figure.

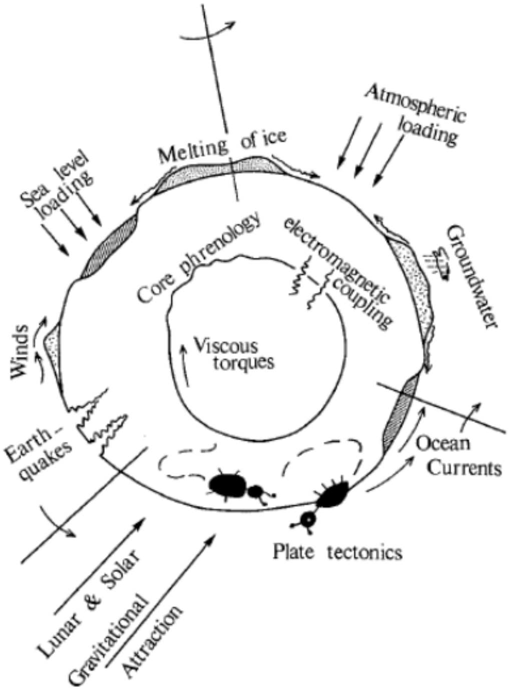

Figure 3.2: Schematics of forces perturbing the rotational behavior of the deformable Earth, from [127]

In the context of polar motion estimation, Eqs. 3.23 are conventionally reformulated to include the so-called equatorial excitation functions denoted by the complex parameter $\vec{\psi} = \psi_1 + \mathrm{i}\,\psi_2$. In the absence of any external torque, the ψ_i are functions of the perturbations to the inertia tensor and the relative angular momentum as well as their time derivatives. Equations 3.23 reveal that the observed variations in polar motion are excited by the first and second components of the relative angular momentum and by the small changes in the mass distribution of the Earth, represented by the two equatorial components of the differential inertial tensor of the Earth.

The introduction of the excitation functions into Eqs. 3.23 is accomplished by multiplying the first and second linearized, homogeneous Euler-Liouville equations by the factors $\sqrt{\dfrac{B(C-B)}{A(C-A)}}$ and $\sqrt{\dfrac{A(C-A)}{B(C-B)}}$ respectively, after both sides of each equation have been dividing by $\Omega\,(C-B)$ and $\Omega\,(C-A)$, respectively.

Doing so yields:

$$
\begin{aligned}
\sqrt{\frac{AB}{\Omega^2(C-B)(C-A)}}\,\dot{m}_1 + \sqrt{\frac{B(C-B)}{A(C-A)}}\,m_2 \quad = \quad & \sqrt{\frac{B}{A}}\frac{c_{23}}{\sqrt{(C-B)(C-A)}} \\
& + \sqrt{\frac{B}{A}}\frac{h_2}{\Omega\sqrt{(C-B)(C-A)}} \\
& - \sqrt{\frac{B}{A}}\frac{\dot{c}_{13}}{\Omega\sqrt{(C-B)(C-A)}} \\
& - \sqrt{\frac{B}{A}}\frac{\dot{h}_1}{\Omega^2\sqrt{(C-B)(C-A)}}
\end{aligned}
$$

$$
\begin{aligned}
\sqrt{\frac{AB}{\Omega^2(C-B)(C-A)}}\,\dot{m}_2 - \sqrt{\frac{A(C-A)}{B(C-B)}}\,m_1 \quad = \quad & -\sqrt{\frac{A}{B}}\frac{c_{13}}{\sqrt{(C-B)(C-A)}} \\
& - \sqrt{\frac{A}{B}}\frac{h_1}{\Omega\sqrt{(C-B)(C-A)}} \\
& - \sqrt{\frac{A}{B}}\frac{\dot{c}_{23}}{\Omega\sqrt{(C-B)(C-A)}} \\
& - \sqrt{\frac{A}{B}}\frac{\dot{h}_2}{\Omega^2\sqrt{(C-B)(C-A)}}
\end{aligned}
$$

The set of equations above are simplified by using the definition of the Euler frequency given below and by neglecting the ellipticity of the equator, so that $A = B$.

$$\sigma_E^2 = \frac{\Omega^2}{AB}(C - A)^2 \tag{3.24}$$

The excitation functions are finally expressed in the complex plane as a function of $\vec{m}(t)$ as shown below:

$$\vec{m}(t) + \frac{\mathrm{i}}{\sigma_E}\frac{\mathrm{d}}{\mathrm{d}t}\vec{m}(t) = \vec{\psi} \tag{3.25}$$

In Eq. 3.25, the ψ_i functions are equal to:

$$\begin{cases} \psi_1 = \dfrac{c_{23}}{C - A} + \dfrac{h_2}{\Omega\,(C - A)} - \dfrac{\dot{c}_{13}}{\Omega\,(C - A)} - \dfrac{\dot{h}_1}{\Omega^2\,(C - A)} \\ \psi_2 = -\dfrac{c_{13}}{C - A} - \dfrac{h_1}{\Omega\,(C - A)} - \dfrac{\dot{c}_{23}}{\Omega\,(C - A)} - \dfrac{\dot{h}_2}{\Omega^2\,(C - A)} \end{cases} \tag{3.26}$$

The left-hand side of Eq. 3.25 is associated with the geodetic observation of polar motion while the right-hand side consists of the geophysical excitation function responsible for the observed response. Excitation functions can be decomposed into three components: a mass term, a motion term and a torque term [127]. Those three terms reflect the three types of mechanisms through which angular momentum is exchanged between the various subsystems of the Earth. The mass term is in general related to pressure terms: surface air pressure in the case of atmospheric excitation functions and ocean bottom pressure in the case of oceanic forcing. The motion term is associated with atmospheric winds and oceanic currents. In the absence of external body force, the torque term relates to surface torques. As a consequence, it includes friction torques arising between the crust and the oceans as well as the mountain torque for instance. The torque terms result from the interaction of the matter and motion terms.

3.4.2 Angular Momentum Functions

The notion of angular momentum function was introduced by Barnes et al. in [10] to simplify the excitation functions. The equatorial angular momentum functions are defined by Eqs. 3.27:

$$\begin{cases} \chi_1(t) = \dfrac{h_1(t) + \Omega\, c_{13}(t)}{\Omega\,(C - A)} \\[2ex] \chi_2(t) = \dfrac{h_2(t) + \Omega\, c_{23}(t)}{\Omega(C - A)} \end{cases} \tag{3.27}$$

Equations 3.25 are re-formulated in terms of the angular momentum functions as:

$$\begin{cases} \dfrac{1}{\sigma_E}\dfrac{\mathrm{d}}{\mathrm{d}t} m_1(t) + m_2(t) = -\dfrac{1}{\Omega}\dfrac{\mathrm{d}}{\mathrm{d}t}\chi_1(t) + \chi_2(t) \\[2ex] \dfrac{1}{\sigma_E}\dfrac{\mathrm{d}}{\mathrm{d}t} m_2(t) - m_1(t) = -\dfrac{1}{\Omega}\dfrac{\mathrm{d}}{\mathrm{d}t}\chi_2(t) - \chi_1(t) \end{cases} \tag{3.28}$$

The relationship between the geophysical forcing and the associated response is esta-blished by defining the set of complex functions shown in Eqs. 3.29.

$$\begin{aligned} \vec{m}(t) &= m_1(t) + \mathrm{i}\, m_2(t) \\ \vec{c}(t) &= c_{13}(t) + \mathrm{i}\, c_{23}(t) \\ \vec{h}(t) &= h_1(t) + \mathrm{i}\, h_2(t) \end{aligned} \tag{3.29}$$

Using the complex notations defined above, one finally obtains:

$$\vec{m}(t) + \frac{\mathrm{i}}{\sigma_E}\frac{\mathrm{d}}{\mathrm{d}t}\vec{m}(t) = \vec{\chi}(t) - \frac{\mathrm{i}}{\Omega}\frac{\mathrm{d}}{\mathrm{d}t}\vec{\chi}(t) \tag{3.30}$$

The excitation functions are easily defined in terms of the angular momentum functions by means of Eq. 3.31.

$$\vec{\psi}(t) = \vec{\chi}(t) - \frac{\mathrm{i}}{\Omega}\frac{\mathrm{d}}{\mathrm{d}t}\vec{\chi}(t) \tag{3.31}$$

Similar to the excitation functions, the angular momentum functions can be decomposed into a motion term and a mass term. The distinction between these two terms is essential in the computation of the so-called effective angular momentum functions (EAMF). These functions and their significance are the object of the section that follows.

3.4.3 Effective Angular Momentum Functions

The effective angular momentum functions (EAMF) $\tilde{\chi}_i$ were first introduced by Barnes et al. in [10] to express the atmospheric effects on the rotation of the Earth. They were then extended and adapted to the case of the oceanic effects by Ponte and Stammer who showed in [153] that the concept of EAMF can be applied to any geophysical fluid.

The EAMF include the effects of the rotational deformation of the Earth and the surface loading effects by means of Love numbers, as well as the presence of a fluid core and the degree of decoupling of its motion relative to the mantle. Each of these factors is accounted for in the EAMF equations shown in Eqs. 3.32.

There are a number of formulations for the effective angular momentum functions in the literature. A review of the different equations and numerical values employed is available in [65]. The expressions given below correspond to the formulation used by the GFZ IERS Associated Product Center in Postdam to compute their series of effective angular momentum functions based on ECMWF collected and simulated atmospheric and oceanic data [66]. These expressions are relevant to this research because the operational GFZ ECMWF series were used extensively in Chapter 9.

$$\begin{cases} \tilde{\chi}_1(t) = \underbrace{\dfrac{1}{1-\dfrac{k_2}{k_s}}}_{\substack{\text{rotational}\\ \text{deformation}}} \quad \dfrac{1}{\Omega^2\,\underbrace{(C_m - A_m)}_{\text{core decoupling}}}\left[\,\underbrace{(1+k_l)}_{\text{loading}}\,\Omega^2\,c_{13}(t) + \Omega\,h_1(t)\,\right] \\ \tilde{\chi}_2(t) = \underbrace{\dfrac{1}{1-\dfrac{k_2}{k_s}}}_{\substack{\text{rotational}\\ \text{deformation}}} \quad \dfrac{1}{\Omega^2\,\underbrace{(C_m - A_m)}_{\text{core decoupling}}}\left[\,\underbrace{(1+k_l)}_{\text{loading}}\,\Omega^2\,c_{23}(t) + \Omega\,h_2(t)\,\right] \end{cases} \tag{3.32}$$

Each of the effects arising from the non-rigidity of the Earth-Oceans-Atmosphere system is briefly described hereafter. However, an in-depth explanation of the geophysical parameters involved and a thorough discussion of the various hypotheses formulated regarding the core-mantle decoupling are beyond the scope of this work. For more information on the latter, the reader is referred to the reviews by Dickman [65] and Gross [88] for instance. Details on the Love numbers and thorough derivations of the loading and elastic Earth yielding effects can be found in the book by Moritz and Mueller [147] or the monographs by Munk and MacDonald [148] and Lambeck [127].

- Rotational deformation effects

The rotational deformation effects are caused by the variable centrifugal forces arising from the rotation of the Earth about an axis slightly deviating from its axis of symmetry. These forces tend to distort the Earth through the phenomenon of elastic yielding. The magnitude of the deformation undergone by the Earth depends on its coefficients of elasticity and anelasticity. The factor accounting for these effects is given by:

$$\alpha_{\substack{\text{rotational}\\ \text{deformation}}} = \frac{1}{1-\dfrac{k_2}{k_s}} \tag{3.33}$$

where k_2 is the degree 2 rotational Love number and k_s is the secular or fluid Love number.

- Loading effects

Loading effects refer to the deformations caused by surface loading. Pressure terms correspond to mass redistribution and are therefore loading effects. On the contrary, motion terms represent the dynamical effects of mass motions and, as such, do not load the Earth. The loading effect factor is equal to:

$$\alpha_{\text{loading}} = (1 + k_l) \tag{3.34}$$

where k_l is the load Love number of degree 2.

The rotational deformation and surface loading effects are corrected for in the effective angular momentum functions by superposition to the angular momentum functions characteristic of an ideal rigid body, so that: $\chi_{\text{effective}} = \chi_{\text{rigid}} + \chi_{\substack{\text{rotational}\\ \text{deformation}}} + \chi_{\text{loading}}$.

- Core-mantle decoupling

The effects of the core-mantle decoupling are a delicate matter and the degree of coupling between the two shells as well as the inclusion of these effects in the case of polar motion excitation remain controversial. The coefficients appearing in Eqs. 3.32 are somewhat dependent on the assumed degree of core-mantle decoupling in addition to other Earth parameters. The implications of several different hypotheses regarding this coupling are discussed in details by Dickman in [65] for example.

In practice, the effective angular momentum functions are evaluated using nume-rical weather models and general circulation models fed with meteorological and oceanographic data such as atmospheric pressure and temperature, ocean bottom pressure as well as wind and oceanic current velocities measurements. The practical computation methods and approaches are reviewed in [192] and [117]. The equations relating the variations in inertia tensor coordinates and relative angular momenta along the x- and y-axis are shown below.

$$\begin{cases} c_{13} = -R^2 \displaystyle\int\limits_{\phi=-\frac{\pi}{2}}^{\frac{\pi}{2}} \int\limits_{\lambda=0}^{2\pi} p_s \cos(\phi)^2 \sin(\phi) \cos(\lambda)\,\mathrm{d}\lambda\,\mathrm{d}\phi \\ \\ c_{23} = -R^2 \displaystyle\int\limits_{\phi=-\frac{\pi}{2}}^{\frac{\pi}{2}} \int\limits_{\lambda=0}^{2\pi} p_s \cos(\phi)^2 \sin(\phi) \sin(\lambda)\,\mathrm{d}\lambda\,\mathrm{d}\phi \end{cases} \tag{3.35}$$

$$\begin{cases} h_1 = -R \displaystyle\int\limits_{p_{min}}^{p_{max}} \int\limits_{\phi=-\frac{\pi}{2}}^{\frac{\pi}{2}} \int\limits_{\lambda=0}^{2\pi} (u \sin(\phi) \cos(\lambda) - v \sin(\lambda)) \cos(\phi)\,\mathrm{d}\lambda\,\mathrm{d}\phi\,\mathrm{d}p \\ \\ h_2 = -R \displaystyle\int\limits_{p_{min}}^{p_{max}} \int\limits_{\phi=-\frac{\pi}{2}}^{\frac{\pi}{2}} \int\limits_{\lambda=0}^{2\pi} (u \sin(\phi) \sin(\lambda) + v \cos(\lambda)) \cos(\phi)\,\mathrm{d}\lambda\,\mathrm{d}\phi\,\mathrm{d}p \end{cases} \tag{3.36}$$

In Eqs. 3.35 and 3.36, R denotes the mean radius of the Earth, ϕ, λ and p denote latitude, longitude and pressure, respectively. The variable $u(\phi, \lambda, p, t)$ and $v(\phi, \lambda, p, t)$ are the eastward and northward components of motion and $p_s(\phi, \lambda, t)$ is the surface pressure.

3.4.4 Relationship between geophysical excitations and observed polar motion variations

The equations shown above relate the geophysical excitations and angular momentum functions to the variations in the location of the figure axis of the Earth specified by the coordinates (m_1, m_2). Indeed, according to [147], the figure axis is defined by Eq. 3.37, which can be identified with the mass term of the angular momentum functions.

$$f = f_1 + \mathrm{i}\, f_2 = \frac{c}{C - A} = \frac{c_{13} + \mathrm{i}\, c_{23}}{C - A} \tag{3.37}$$

Because, as discussed in Chapter 2, space-geodetic techniques observe the variations in the location of the CIP rather than the changes in the location of the figure axis of the Earth, the two quantities need to be related in order to subsequently connect the excitation functions to the observed polar motion variations.

The transformation properties characterizing the transition from the analytical to the observable pole coordinates are developed by Gross in [87]. Its treatment relies on the use of the rotation matrix mapping. For clarity, the full derivation is placed in Appendix C and only the results are shown here in Eq. 3.39. The actual modified set of equations referring the angular momentum functions to the CIP instead of the instantaneous rotation pole was originally derived by Brzeziński [29]. The result is shown in Eq. 3.38.

$$\vec{p}(t) + \frac{\mathrm{i}}{\sigma_{cw}} \frac{\mathrm{d}}{\mathrm{d}t}\vec{p}(t) = \vec{\chi}(t) \tag{3.38}$$

It is obtained by combining the two equations below:

$$\vec{m}(t) = \vec{p}(t) - \frac{\mathrm{i}}{\Omega} \frac{\mathrm{d}}{\mathrm{d}t}\vec{p}(t) \tag{3.39}$$

$$\vec{m}(t) + \frac{\mathrm{i}}{\sigma_{cw}} \frac{\mathrm{d}}{\mathrm{d}t}\vec{m}(t) = \vec{\chi}(t) - \frac{\mathrm{i}}{\Omega} \frac{\mathrm{d}}{\mathrm{d}t}\vec{\chi}(t) \tag{3.40}$$

In the equations above, the Euler angular frequency σ_E has been replaced by the Chandler wobble frequency σ_{cw} that includes the effects mentioned in section 3.4.3. The Chandler frequency is given by Eq. 3.41.

$$\sigma_{cw} = \left(1 - \frac{k_2}{k_s}\right) \frac{(C_m - A_m)}{A_m} \Omega \tag{3.41}$$

Note that Eq. 3.38 is valid at low frequencies only; for frequencies close to the diurnal band, the resonant effect of the Nearly Diurnal Free Wobble, or FCN, must be accounted for. This special case is treated later in Chapter 9.

Chapter 4

Statistical Parameter Estimation

4.1 Introduction

4.1.1 Concept and Application to Precise Orbit Determination

Statistical parameter estimation seeks to determine the most probable estimate, at some epoch, of the state of a system whose dynamics can be modeled to some level of accuracy, based on a collection of observations of sufficient accuracy. Because the number of measurements is typically much larger than the number of parameters to estimate, the system to solve is usually over-determined and L_2-norm solution techniques are employed.

The estimation procedure can be outlined as follows. Starting from a set of a priori initial conditions, a reference trajectory is numerically integrated across the estimation arc and used to produce predicted measurements. Those predicted measurements are compared to a set of actual observations. A solution is obtained by iterative least-squares adjustment of the a priori parameters to gradually enhance the fit of the models to the observational data. This is achieved by means of the partial derivatives of both the measurement and dynamical models with respect to the parameters of interest. The optimality of a solution to a posed estimation problem is defined in a statistical sense based on a performance index.

When applied to the precision orbit determination problem, a given parameter is estimable as long as the available observations and the satellite's orbit somehow depend on that parameter. The parameter of interest must impact the measurement model or the dynamics of the spacecraft, either explicitly or implicitly. In particular, in the context of this study, that deals with the Earth's orientation and rotation, because the motion of the spacecrafts is described in the ECI frame while the coordinates of the tracking stations are expressed in the ECEF frame, the ERP appear in both the pseudorange and carrier-phase GPS measurements. In practice, for most applications and in particular in the case of POD, the convergence of the least-squares process often relies on the linearization of both the state and measurement vectors since the equations of motion of a satellite, along with the observation-state relationship, include highly non-linear terms.

4.1.2 Minimum Variance Estimate with A Priori Information

The minimum variance criterion is often selected as the aforementioned performance index. The goal then is to find the linear, unbiased and minimum variance estimate $\hat{x}_k$ of the (often linearized) state vector $\vec{x}_k$ at some given epoch t_k [182]. This approach takes advantage of the a priori knowledge of the statistical characteristics of both the observation errors and state estimation errors.

The performance index is usually reformulated mathematically by stating that the (weighted) sum of the norm of the postfit observation residuals and the norm of the estimation errors needs to be minimized. Indeed, at each observation epoch, the measurements are assumed to be contaminated by random and systematic errors. The vector of random errors, or noise, is denoted $\vec{\varepsilon}$ and obeys a Gaussian distribution cha-racterized by $\vec{\varepsilon} \sim \mathcal{N}(\bar{\varepsilon}, R)$ where R, the observation error covariance matrix, is defined by $R = E\left[\vec{\varepsilon}.\vec{\varepsilon}^T\right]$, assuming potential biases on the observational series have been removed (i.e. $\bar{\varepsilon} = 0$). Similarly, it is assumed that the estimate of the state deviation vector will be corrupted by errors forming the vector $\vec{\eta}$ obeying a Gaussian distribution characterized by $\vec{\eta} \sim \mathcal{N}(\bar{\eta}, P)$ where the matrix P, the estimation error covariance matrix, characte-rizes the uncertainties on the state parameters and is defined by $P = E\left[\vec{\eta}.\vec{\eta}^T\right]$ assuming again that $\bar{\eta} = E[\vec{\eta}] = 0$.

In addition to the various errors that distort the estimate of the state, difficulties arise due to non-linearities involved in the dynamics governing the motion of the satellite as well as in the measurement models that relate the state variables to the observables. As a consequence, a linearization procedure necessitating a reference trajectory needs to be applied prior to any data processing. The linearization procedure consists in computing deviation vectors for both the state and the measurements (unless only one data type is considered, in which case the observation deviation is a scalar at each epoch of observation). This is achieved by performing a Taylor's series expansion to the first-order of the actual trajectory about a nominal trajectory that needs to be close enough to the true trajectory in order to guarantee the convergence to the correct solution.

Letting $\dot{\vec{X}} = \vec{F}(\vec{X}, t)$ be the non-linear state equations of the system, the state deviation vector is obtained through:

$$\begin{gathered} \vec{x}(t) = \vec{X}(t) - \vec{X}^*(t) \\ \Downarrow \; A(t) = \left[\frac{\partial \vec{F}(\vec{X}(t), t)}{\partial \vec{X}(t)} \right]^* \\ \dot{\vec{x}}(t) = A(t)\,\vec{x}(t) \end{gathered} \tag{4.1}$$

In Eqs. 4.1, $\vec{F}(\vec{X}, t)$ represents the dynamical model and $A(t)$ is the model sensitivity matrix (or design matrix), a matrix composed of the partial derivatives of the dynamical model with respect to the state vector. The star superscript indicates that the quantities are evaluated along the reference trajectory.

Likewise, the measurements are modeled and linearized as shown in the set of equations below. Note that it is assumed that more than one data type is used, so that the quantities appearing in Eqs. 4.2 are vectors rather than scalars.

$$\begin{gathered} \vec{Y}(t) = \vec{G}(\vec{X}, t) + \vec{\varepsilon}(t) \\ \Downarrow \; \tilde{H}(t) = \left[\frac{\partial \vec{G}(\vec{X}(t), t)}{\partial \vec{X}(t)} \right]^* \\ \vec{y}(t) = \tilde{H}(t)\,\vec{x}(t) + \vec{\varepsilon}(t) \end{gathered} \tag{4.2}$$

The observation deviation vector - or vector of observation residuals - is obtained through the linearization of the actual observation vector about the predicted observation vector evaluated from the observation model $\vec{G}(\vec{X}, t)$ along the propagated reference trajectory as shown in Eqs. 4.2.

After linearizing both the state and the observation vectors, the system of state-propagation and observation-state equations can be written in discrete form as shown in Eqs. 4.3.

$$\vec{x}_k = \Phi(t_k, t_i)\,\vec{x}_i \tag{4.3a}$$

$$\vec{y}_k = \tilde{H}_k\,\vec{x}_k + \vec{\varepsilon}_k \tag{4.3b}$$

Equation 4.3b is referred to as the ”data equation” later in this document. The index k denotes the epoch.

The optimal solution, in a least-squares sense, to the orbit determination problem is the solution that minimizes the minimum variance performance index, which is the L_2 norm defined as the sum of squares of the observation residuals. It can therefore be analytically derived starting from the definition of this criterion (c.f. [182]). It consists of the best estimate of the epoch state vector $\hat{x}_k$ and its associated variance-covariance estimation error matrix P_k. Both quantities are determined using Eqs. 4.4.

$$\hat{x}_k = \left(\tilde{H}_k^T R_k^{-1} \tilde{H}_k + \bar{P}_k^{-1}\right)^{-1} \left(\tilde{H}_k^T R_k^{-1} y_k + \bar{P}_k^{-1} \bar{x}_k\right) \tag{4.4a}$$

$$P_k = \left(\tilde{H}_k^T R_k^{-1} \tilde{H}_k + \bar{P}_k^{-1}\right)^{-1} = \Lambda_k^{-1} \tag{4.4b}$$

The sections that follow provide an overview of the data processing tools relevant to this work. In particular, in spite of the myriad of estimators and processors discussed in the literature, the scope is restricted to the algorithms implemented in the GIPSY/OASIS II software package. The functioning and flow chart of the software package itself are detailed in Chapter 6. The reader is referred to [17], [182], [118], [36], [130] and [129] for thorough derivations of the algorithms depicted here and extensive discussion of their merits and shortcomings.

4.2 Batch Processor

The batch processor is a direct implementation of the minimum variance estimator. It is an epoch-state filter, so that it requires that all the observations be processed before an estimate can be calculated. For this reason, the batch processor is typically used to iterate on a spacecraft's initial state vector in the context of orbit determination. The version of the algorithm presented below corresponds to the implementation of a weighted least-squares filter with a priori information. The weighting is operated by means of the inverse of the observation-error covariance matrix R which reflects the confidence placed on the precision of the observations or their data types.

As mentioned in section 4.1.1, the performance index to minimize in this case is written:

$$J(\vec{x}) = \frac{1}{2}\vec{\varepsilon}^{T}\, R^{-1}\,\vec{\varepsilon} + \frac{1}{2}\vec{\eta}^{T}\,\bar{P}\,\vec{\eta} \tag{4.5}$$

The filter is initialized based on a nominal trajectory $\vec{X}^*$ and available a priori information in the form of the a priori estimate-error covariance matrix $\bar{P}_0$ and state deviation vector $\bar{x}_0$, both given at the epoch time, as shown in Eqs. 4.6 through 4.10

$$k = 1: \qquad t_{k-1} = t_0 \tag{4.6}$$

$$\vec{X}^*(t_{k-1}) = \vec{X}_0^* \tag{4.7}$$

$$\Phi(t_{k-1}, t_0) = I \tag{4.8}$$

$$\Lambda = \bar{P}_0^{-1} \tag{4.9}$$

$$N = \bar{P}_0^{-1}\bar{x}_0 \tag{4.10}$$

In the set of equations placed above, Φ represents the state transition matrix introduced in the previous section, Λ is the information matrix and Λ and N form the so-called normal equations. The state deviation vector $\vec{x}$ results from the linearization of the observed trajectory around the reference trajectory $\vec{X}^*$.

Following the initialization phase, the observations are processed one by one through a loop. Three stages can be identified for each step of the loop.

First, both the state transition matrix and the reference trajectory are propagated from the current epoch to the next by numerical integration of their respective dynamics, as shown in Eqs.

4.11 and 4.12.

$$\dot{\vec{X}}_k = \vec{F}(\vec{X}_k, t_k) \tag{4.11}$$

$$\dot{\Phi}(t_k, t_0) = A(t_k)\,\Phi(t_k, t_0) \tag{4.12}$$

Equation 4.12 is often referred to as the variational equations of the observed system. In the case of the batch processor, because it is an epoch-state vector, the variational equations represent the sensitivity of the state vector, in particular the dynamical portion of it, to the initial conditions.

The measurement sensitivity matrix $\tilde{H}$ is then evaluated and mapped to the epoch time by means of the state transition matrix as shown in Eqs. 4.13.

$$\tilde{H}(t_k) = \left[\frac{\partial \vec{G}(\vec{X}(t_k), t_k)}{\partial \vec{X}(t_k)}\right]^* \Rightarrow H_0 = \tilde{H}(t_k)\,\Phi(t_k, t_0) \tag{4.13}$$

Finally, the matrices characterizing the normal equations, namely the information matrix Λ and the matrix N, are accumulated after the observation deviation vector is computed. The accumulated matrices are presented in Eqs. 4.14a and 4.14b.

$$\begin{cases} \Lambda = \Lambda + H_k^T\, R_k^{-1}\, H_k & (4.14a) \\ N = N + H_k^T\, R_k^{-1}\, \vec{y}_k & (4.14b) \end{cases}$$

Once all the observations have been read, the normal equations are solved to yield $\hat{x}_0$, the best estimate of the state deviation vector at the epoch time and the associated estimation error variance-covariance matrix P_0.

$$\begin{cases} \hat{x}_0 = \Lambda^{-1}\, N & (4.15a) \\ P_0 = \Lambda^{-1} & (4.15b) \end{cases}$$

The initial guess is updated by inclusion of the best estimate of the state deviation vector. The whole process can be iterated upon until a convergence tolerance is reached. A flowchart of the batch processor is included in Fig. 4.1.

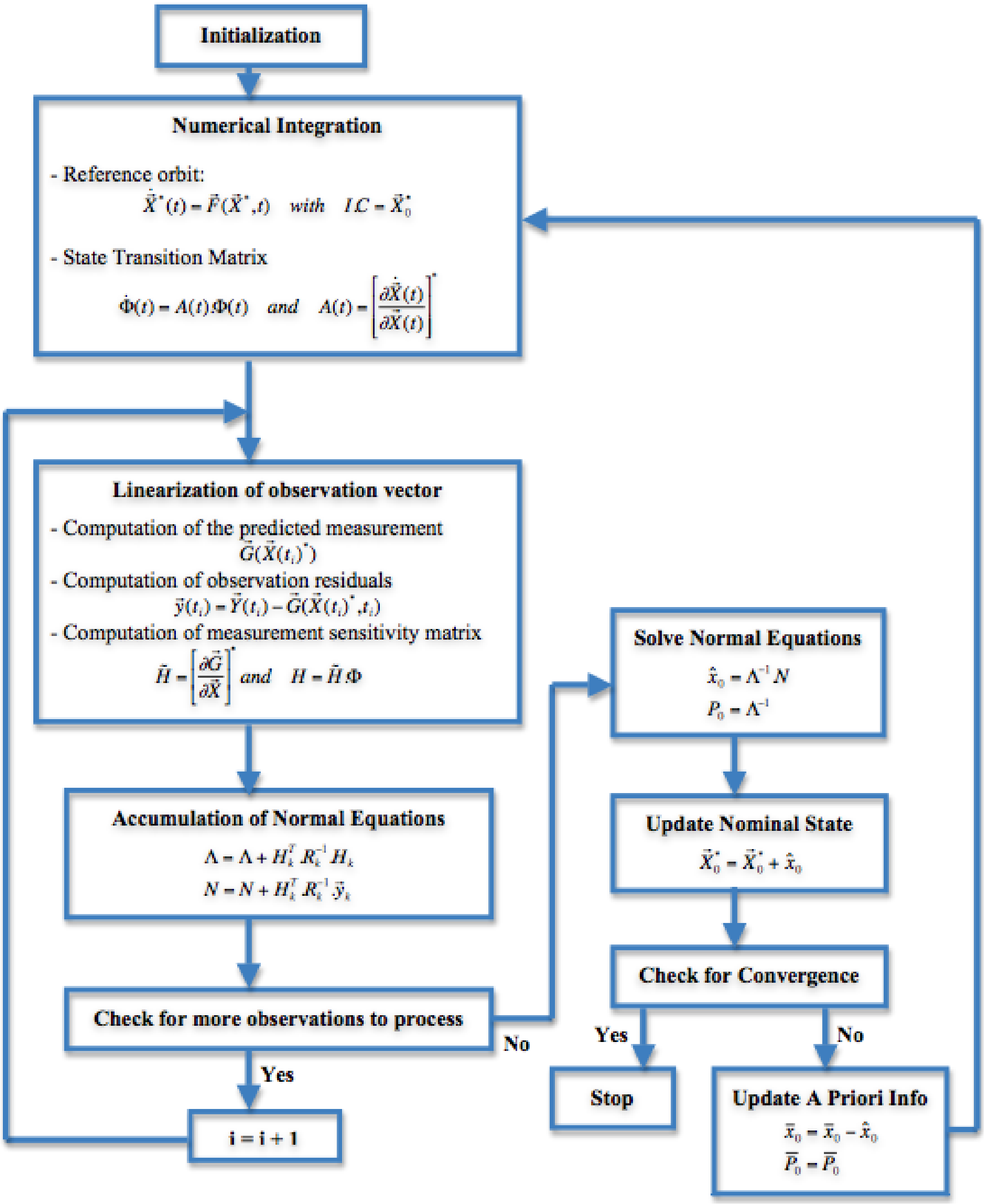

Figure 4.1: Flowchart of the batch processor

4.3 Process Noise

4.3.1 Concept of Dynamic Model Compensation

Dynamic Model Compensation (DMC) is a way to accommodate unmodeled or mismodeled dynamics in a filter. Doing so prevents the filter from saturating and the solution from diverging. The unknown behavior of the state is modeled in the filter as a stochastic process and is added to the purely deterministic dynamic model previously used to represent the evolution of the true state. As explained by Yunck in [204], through the use of process noise, the filter estimates at each time step a local correction to the dynamic model valid over a pre-defined update interval only. As it proceeds through the data, the filter thus generates a sequence of local corrections; hence improving the fit of the final solution to the observations and enabling the recovery of un-modeled perturbations.

Process noise is accounted for in the dynamics of a linear or linearized system through:

$$\dot{\vec{x}}(t) = A(t)\vec{x}(t) + B(t)\vec{u}(t) \tag{4.16}$$

In Eq. 4.16, the variable $\vec{u}(t)$ represents the process noise vector. It obeys a normal distribution such that $\vec{u} \sim \mathcal{N}(\bar{u}, Q\delta_{ij})$

In practice, the estimation arc is divided into discrete time intervals (so-called batches) and the process noise parameters are included in the state vector to be estimated (see section 4.4.2). Over the duration of each batch, the process noise parameters are considered piecewise constant. The uncertainties on their estimated values are inflated or reset at the end of each batch based on the model employed for the process noise. The time-varying behavior of the stochastic parameters is therefore a consequence of the variations affecting the associated covariance matrix through successive batches. Under the influence of process noise, the true state propagates as:

$$\vec{x}(t) = \Phi(t, t_0)\,\vec{x}_0 + \int_{t_0}^{t} \Phi(t, \tau)\,B(\tau)\,\vec{u}(\tau)\,\mathrm{d}\tau \tag{4.17}$$

The inclusion of a measurement in the filter (the so-called measurement update stage in the case of sequential filters) is not impacted by the use of process noise. However, the mapping from one epoch to the next, referred to as the time update stage for sequential filters, is affected by it. Thus, the time update equations in the discrete time domain become:

$$\bar{x}_{k+1} = \Phi(t_{k+1}, t_k)\, x_k + \Gamma(t_{k+1}, t_k)\, u_k \tag{4.18a}$$

$$\bar{P}_{k+1} = \Phi(t_{k+1}, t_k)\, P_k\, \Phi(t_{k+1}, t_k)^T + \Gamma(t_{k+1}, t_k)\, Q_k\, \Gamma(t_{k+1}, t_k)^T \tag{4.18b}$$

where the process noise transition matrix, Γ is defined as:

$$\Gamma(t_{k+1}, t_k) = \int_{t_k}^{t_{k+1}} \Phi(t_{k+1}, \tau)\, B(\tau)\, \mathrm{d}\tau \tag{4.19}$$

The stochastic processes used for dynamic model compensation are often modeled as first-order Gauss-Markov random processes, to reflect the fact that the signal can be decomposed into two distinct components.

4.3.2 Gauss-Markov processes

A Gauss-Markov process of the first order consists of a deterministic part and a random part. The time evolution of such a process, designated as η here and in [182], is of the form presented in Eq. 4.20.

$$\eta(t_j) = e^{-\beta(t_j - t_i)}\, \eta(t_i) + u_k(t_i) \sqrt{\frac{\sigma^2}{2\beta} \left(1 - e^{-2\beta(t_j - t_i)} \right)} \tag{4.20}$$

β is the inverse of the process correlation time τ and u is white Gaussian noise such that $u \sim \mathcal{N}(0, \sigma^2)$.

Considering a vector $\vec{p}$ of Gauss-Markov processes of the 1^{st} order and writing Eq. 4.20 in matrix form yields:

$$\vec{p}_{j+1} = M_j\, \vec{p}_j + \vec{w}_j \tag{4.21}$$

In Eq. 4.21, M_j is a diagonal matrix with entries such that $m_{ii} = e^{-\Delta t_j / \tau_i}$. The letters i and j respectively denote the i^{th} stochastic parameter and j^{th} batch, so that τ_i denotes the time constant of the i^{th} parameter while Δt_j represents the duration of the j^{th} batch

The vector $\vec{w}$ contains the driving noise obeying a probability law $\mathcal{N}(0, Q\, \delta_{ij})$ where Q, the process noise covariance matrix, is a diagonal covariance matrix such that $Q_{ii} = (1 - m_{ii}^2)\,\sigma_{ss_i}^2$. The symbol δ_{ij} denotes the Kronecker delta function. The term σ_{ss_i} is the steady-state standard deviation of the i^{th} Gauss-Markov process. It is defined as the noise level that could be reached if the system were left undisturbed for a time period much greater than τ. Comparing Eqs. 4.20 and 4.21, the steady-state variance is defined as:

$$\sigma_{ss}^2 = \frac{\sigma^2}{2\beta} \tag{4.22}$$

Gauss-Markov processes of the first order are also referred to as colored noise. A broad spectrum of exponentially-correlated random functions can be generated based on the choice of the σ and β parameters. White noise and random walk processes are the two opposite limiting cases.

- White noise is characterized by: $\sigma_{ss} = 0, \tau = 0 \Rightarrow M = 0$

White noise processes are typically selected in the context of DMC when the error in the dynamic model is regarded as uncorrelated from batch to batch. In practice, this model is useful in cases where there are no specific expectations on the behavior of the parameter to estimate. Every time a white noise reset occurs, the Q matrix is redefined and made diagonal again by resetting the off-diagonal terms to 0. Over a batch, the noise grows; it is then reset to a small value between successive update intervals. In the absence of data, the white noise parameters remain 0 with a constant assumed variance. In the case of GPS data processing the white noise model is widely used in substitution for transformations to remove ”nuisance parameters” such as ionospheric delay and clock errors. Indeed, as highlighted in [121], estimating ionospheric delay as white noise for each observation would be equivalent to performing the more commonly used (e.g. in GIPSY/OASIS) ionospheric linear combination of data. In addition, clock errors are dealt with by estimating the clock parameters as white noise instead of using a classical double-differencing transformation.

- Random Walk processes are such that: $\tau \to \infty, \sigma_{ss} \to \infty \Rightarrow M = I$

The random walk model is mathematically equivalent to an integrated white noise model. When a stochastic parameter is modeled as a random walk process, a steady state is never reached.

The uncertainty on the estimate increases proportionally to the square-root of the batch duration. Therefore, in contrast to the white noise model, when a random walk model is used and in the absence of measurements, the estimated parameter retains its last value while its variance increases linearly in time. The random-walk model is of particular importance in the estimation of geophysical parameters such as the EOP or meteorological quantities for which small variations in time are expected.

A shortcoming of batch least-squares filters is that including process noise in the algorithm significantly complicates the resolution of the normal equations. For this reason, dynamic model compensation is hardly ever accomplished by means of batch processors. Because precise orbit determination requires mitigating errors and/or deficiencies in the dynamical and/or measurement models, a sequential filter is often preferred. A sequential filter is the equivalent alternate approach to the batch processor. In practice, the two types of filters are often used in association with each other. Typically, the observations are processed individually at the current time (rather than as a set at the epoch time) and compared to predicted observations modeled based on a set of initial conditions adjusted beforehand in the batch processor. The GIPSY/OASIS II software package implements this configuration as further detailed in Chapter 6.

The next section describes the sequential filter used for data processing in that software. The inclusion and treatment of process noise in the filter are treated.

4.4 Square Root Information Filter

The Square Root Information Filter (SRIF) is a sequential filter based on the direct use of the information matrix Λ. Specifically, the filter operates on R, the square-root of the information matrix. R is related to the covariance matrix P introduced in section 4.2 through $P = R^{-1}R^{-T}$. Such factorized filters offer the advantages of being fast and extremely robust to computer precision errors by decreasing the condition number of the matrices manipulated. Information filters themselves offer several advantages over the more conventional covariance sequential filters such as the Kalman filter. They prove especially useful when a large number of very accurate observations need to be processed. In addition, unlike covariance filters in which the data contribution tend to get ignored in such situations, information filters can be initialized with infinite or singular a priori estimation-error covariance matrix $\bar{P}_0$.

The principle underlying the SRIF is the reformulation of the normal equations into the form shown in Eq. 4.23.

$$\Lambda\hat{x} = N \xRightarrow[transformation]{orthogonal} R\hat{x} = b \tag{4.23}$$

In Eq. 4.23, R, the square-root of the information matrix Λ, is an upper triangular matrix and $\hat{x}$ can be retrieved through a backward-substitution scheme once the normal equations have been re-written via a sequence of orthogonal transformations. The SRIF mechanization discussed here, developed by Bierman [17], corresponds to the one implemented in the GIPSY/OASIS II software, introduced in Chapter 6 (see [130] and [118]). It corresponds to the case of the SRIF with a priori information and in the presence of exponentially-correlated process noise. The main governing equations are reproduced here from the cited sources.

4.4.1 Change of variables

To begin with and for simplicity, the parameters to estimate are grouped into three classes:

- the dynamic model parameters, forming the vector $\vec{x}$,
- the process noise parameters represented as $\vec{p}$,
- the constant parameters, or biases, gathered in $\vec{b}$.

The overall state vector $\vec{X}$ then becomes:

$$\vec{X} = \begin{bmatrix}\vec{x} & \vec{p} & \vec{b}\end{bmatrix}^T \tag{4.24}$$

A specificity of the SRIF is that all the a priori information is reformulated in the form of data equations similar to Eq. 4.3b. For instance, the dynamic model parameters are characterized by a priori values such that:

$$\bar{x} = \vec{x} + \vec{\eta} \text{ with } E\left[\vec{\eta} \,.\, \vec{\eta}^T\right] = \bar{P} = \bar{\Lambda}^{-1} \tag{4.25}$$

In Eq. 4.25, the bar above the parameters indicates a priori values. This convention is respected in the remainder of this chapter. Using $\bar{\Lambda} = \bar{R}^T \bar{R}$ and multiplying both sides by $\bar{R}_x$, the block of the square-root of the a priori information matrix specific to $\vec{x}$, one writes:

$$\bar{b} = \bar{R}_x \, \vec{x} + \bar{\eta} \text{ where } \bar{b} = \bar{R}_x \, \bar{x} \text{ and } \bar{\eta} = \bar{R}_x \, \vec{\eta} \tag{4.26}$$

This procedure is repeated for the vectors containing the Gauss-Markov processes and the constant parameters. The equations obtained are identical to Eq. 4.26 except for the subscript that changes accordingly from x to p and b respectively.

The driving noise affecting the Gauss-Markov processes and defined in Eq. 4.21 as $\vec{\omega}$ needs to be included in the performance index to be minimized as well. It is itself characterized by the a priori error on its estimate, $\vec{\gamma}$, such that:

$$\bar{\omega} = \vec{\omega} + \vec{\gamma} \tag{4.27}$$

and a covariance matrix Q described in section 4.3.2 and that can be factorized into:

$$Q = R_w^{-1} \, R_w^{-T} \tag{4.28}$$

4.4.2 Observation and State Dynamics Modeling

Following the conventions and notations of section 4.4.1, the models for both the observations and the state dynamics are modified to explicitly contain the three classes of parameters.

- The measurement equation initially presented in Eq. 4.3b becomes Eq. 4.29.

$$\vec{y} = H_x^c \, \vec{x}(t_j) + H_p^c \, \vec{p} + H_b^c \, \vec{b} + \vec{\varepsilon} \tag{4.29}$$

The superscript c denotes the fact that the matrices are valid at the current epoch. The subscript on the H matrix indicates the vector with respect to which the partials are computed.

Note that in order to use the SRIF, the observations need to be pre-whitened prior to being processed. This is achieved by multiplying both sides of the original data equation by the square-root of the observation-error covariance matrix. After the pre-whitening stage, the observation errors obey a normal distribution law similar to that governing the distributions of the estimation errors $\bar{\eta}$ and $\bar{\gamma}$ and shown in Eq. 4.30.

$$\varepsilon \sim \mathcal{N}(0, I) \tag{4.30}$$

- The dynamics of the satellite state from Eq. 4.3a are transformed into:

$$\vec{x}(t_{k+1}) = \Phi_x(t_{k+1}, t_k)\,\vec{x}(t_k) + \Phi_p(t_{k+1}, t_k)\,\vec{p} + \Phi_b(t_{k+1}, t_k)\,\vec{b} \tag{4.31}$$

Each of the Φ matrices appearing in Eq. 4.31 is the state transition matrix associated with the set of parameters belonging to the class denoted by the subscript. Recalling Eq. 4.21, the discrete-time model of the filter dynamics is then written in matrix form as shown in Eq. 4.32.

$$\begin{bmatrix} \vec{x} \\ \vec{p} \\ \vec{b} \end{bmatrix}_{k+1} = \begin{bmatrix} \Phi_x(t_{k+1}, t_k) & \Phi_p(t_{k+1}, t_k) & \Phi_b(t_{k+1}, t_k) \\ 0 & M_k & 0 \\ 0 & 0 & I \end{bmatrix} \cdot \begin{bmatrix} \vec{x} \\ \vec{p} \\ \vec{b} \end{bmatrix}_k + \begin{bmatrix} 0 \\ \vec{w}_k \\ 0 \end{bmatrix} \tag{4.32}$$

In this equation, $\vec{x}$ represents the vector of current state dynamic parameters, $\vec{p}$ is a vector of colored noise components and $\vec{b}$ is a vector of parameters that will be adjusted as constants. The matrix M and vector $\vec{w}$ were both defined in section 4.3 of this dissertation.

4.4.3 Performance index

The filtering procedure using the square-root information matrix (SRI) is entirely based on the manipulation of the performance index J. This criterion defined in

Eq. 4.33 for the epoch t_{k-1} is re-formulated using Eqs. 4.26. This yields:

$$\hat{J}_{k-1}(X) = ||\bar{\eta}_{x_{k-1}}||^2 + ||\bar{\eta}_{p_{k-1}}||^2 + ||\bar{\eta}_{b_{k-1}}||^2 + ||\bar{\gamma}_{k-1}||^2 + ||\bar{\varepsilon}_{k-1}||^2 \tag{4.33}$$

The final expression is shown in Eq. 4.34.

$$\begin{aligned}\hat{J}_{k-1}(X) \;=\; & ||\bar{R}_x\,\vec{x} - \bar{b}_{x_{k-1}}||^2 + ||\bar{R}_p.\vec{p} - \bar{b}_{p_{k-1}}||^2 + ||\bar{R}_b\,\vec{x} - \bar{b}_{b_{k-1}}||^2 \\ & + ||R_w\,(\vec{p}_k - M_k\,\vec{p}_{k-1}) - \bar{\vec{b}}_{w_{k-1}}||^2 \\ & + \left(\begin{bmatrix} H_x & H_p & H_b \end{bmatrix} \cdot \begin{bmatrix} \vec{x} \\ \vec{p} \\ \vec{b} \end{bmatrix} - y \right)^2_{k-1}\end{aligned} \tag{4.34}$$

4.4.4 Pseudo-Epoch State

To reduce the computational loads and memory allocation requirements, both in the filter propagation stage and especially in the smoother, the SRIF algorithm is usually implemented in terms of pseudo-epoch state variables instead of the current state variables typically used in sequential filters. Extra computation is however needed since the pseudo-epoch state must always be referred to the true epoch time. Again, this approach is implemented in the GIPSY/OASIS II software package.

A pseudo-epoch state filter can be viewed as a hybrid between the batch processor and a sequential filter. It represents a way of getting around the difficulty hindering the inclusion of process noise in a batch processor. Indeed, this formulation of a sequential filter allows the use of DMC while preserving the epoch-state property of the batch formulation since the filter outputs an estimate of the epoch state.

The current time state vector $\vec{x}$ at time t_j is related to the pseudo-epoch state vector $\vec{x}_j$ through Eq. 4.35.

$$\vec{x}(t_j) = \Phi_x(t_j, t_0)\,\vec{x}_j + \Phi_b(t_j, t_0)\,\vec{b} \tag{4.35}$$

In Eq. 4.35, t_0 is the epoch time and t_j is the current epoch.

Reciprocally, the pseudo-epoch state vector at time t_j is defined as:

$$\vec{x}_j = \Phi_x^{-1}(t_j, t_0)\left[\vec{x}(t_j) - \Phi_b(t_j, t_0)\,\vec{b}\,\right] \tag{4.36}$$

From Eq. 4.36 it is clear that the pseudo-epoch state vector is strictly equivalent to the epoch state in the absence of process noise. Therefore, x_j, the pseudo-epoch state, is defined as the pseudo initial conditions that compensate for the presence of process noise. Equation 4.36 also gives insight into the geometrical interpretation of the pseudo-epoch state vector shown in Fig. 4.2.

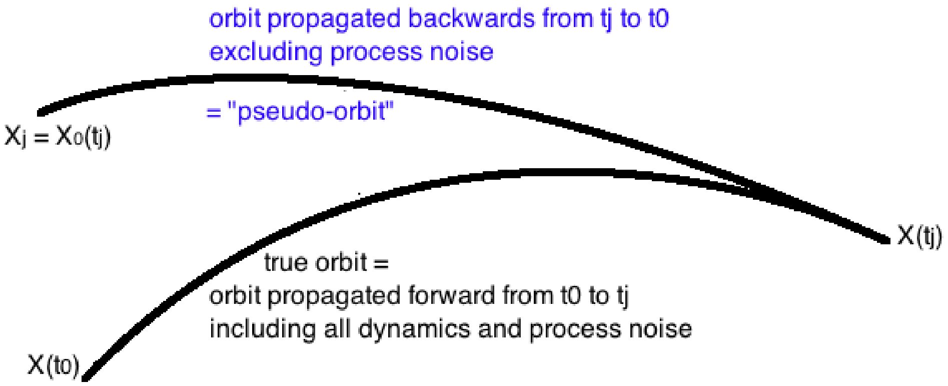

Figure 4.2: Illustration of the pseudo-epoch orbit (adapted from [118])

The overall state transition matrix, Φ, is greatly simplified when expressed in terms of the pseudo-epoch state. The system dynamical equations can be reformulated in terms of the pseudo-epoch state as shown in Eq. 4.37. The matrix manipulations yielding this equation are detailed in [118].

$$\begin{bmatrix} \vec{x} \\ \vec{p} \\ \vec{b} \end{bmatrix}_{k+1} = \begin{bmatrix} I & V_p(k) & 0 \\ 0 & M_k & 0 \\ 0 & 0 & I \end{bmatrix} \begin{bmatrix} \vec{x} \\ \vec{p} \\ \vec{b} \end{bmatrix}_k + \begin{bmatrix} \vec{0} \\ \vec{w} \\ \vec{0} \end{bmatrix}_k \tag{4.37}$$

In Eq. 4.37, V_p accounts for a potential dynamic coupling between the process noise parameters and the dynamical parameters. It represents the deterministic portion of the time update while

M_k contains the stochastic portion. V_p is defined in Eq. 4.38.

$$V_p(k) = [\Phi_x(t_{k+1}, t_0)]^{-1}\,\Phi_p(t_{k+1}, t_0) - [\Phi_x(t_k, t_0)]^{-1}\,\Phi_p(t_k, t_0) \tag{4.38}$$

The measurement equation, Eq. 4.29, is modified by the change of variables as follows:

$$\vec{y} = H_x^0\,\vec{x}_k + H_p\,\vec{p} + H_b^0\,\vec{b} + \vec{\varepsilon} \text{ where } H_p = H_p^0 - H_x^0\,\Phi_x^{-1}(t_k, t_0)\,\Phi_p(t_k, t_0) \tag{4.39}$$

In Eq. 4.39, the variables $H_{x/p/b}^0$ denote the measurement partials with respect to the epoch time values of the vectors $\vec{x}$, $\vec{p}$ and $\vec{b}$ respectively. Note that the process noise and bias parameter vectors are given at the current time so that the process noise parameters can actually be propagated through time. Only the dynamical state vector is expressed in the pseudo-epoch state format. The second part of Eq. 4.39 is specific to the implementation setup in the GIPSY/OASIS II software. Indeed, the modules responsible for the generation of the state transition matrices Φ and the measurement sensitivity matrices H provide their values relative to the epoch time only. In this context, it becomes necessary to map both types of matrices forward from the epoch time to the current time.

4.4.5 Time Update

In a sequential filtering process, the time update stage propagates the state vector and covariance matrix from the current batch epoch to the next one. The general set of equations representing the time update mechanism is shown in Eq. 4.40.

$$\begin{cases} \vec{x}_{k+1} = \vec{x}_k + V_p(k)\,\vec{p}_k \\ \vec{p}_{k+1} = M_k\,\vec{p}_k + \vec{w}_k \\ P_{k+1} = \Phi P_k\,\Phi^T + Q \end{cases} \tag{4.40}$$

In the case of a SRIF, the deterministic and stochastic components of the state vector can either be treated separately or be updated simultaneously through matrix concatenation (see [182]). In the software package used for this work, the time update is carried out in two steps.

On the one hand, the deterministic time update is performed through the matrix multiplication shown in Eq. 4.41.

$$\bar{R}_{k+1} = \hat{R}_k \begin{bmatrix} I_x & -V_p(t_k) & 0 \\ 0 & I_p & 0 \\ 0 & 0 & I_b \end{bmatrix} \tag{4.41}$$

On the other hand, the stochastic portion of the time update uses a series of orthogonal transformations based on the square-root free Givens algorithm.

4.4.6 Measurement Update

Similar to the time update, the measurement update at time t_k is completed by applying a sequence of orthogonal transformations to the matrix form of the performance index J. Householder transformations are employed rather than Givens transformations in this case. Making use of the a priori SRI matrix and error estimates, the performance index is written as shown in Eq. 4.42.

$$\hat{J}_k = \left\| \begin{bmatrix} \bar{R}_x & 0 & 0 \\ 0 & \bar{R}_p & 0 \\ 0 & 0 & \bar{R}_b \\ H_x & H_p & H_b \end{bmatrix} \cdot \begin{bmatrix} \vec{x} \\ \vec{p} \\ \vec{b} \end{bmatrix} - \begin{bmatrix} \vec{b}_x \\ \vec{b}_p \\ \vec{b}_b \end{bmatrix} \right\|^2 + \left\| R_w \left(\vec{p}_{k+1} - M_{k+1} \vec{p}_k \right) - \bar{b}_{w_k} \right\|^2 \tag{4.42}$$

A sequence of orthogonal transformations following the Householder scheme is applied to the data equations of Eq. 4.42 to obtain Eq. 4.43.

$$\hat{J}_k = T_{H_k} \begin{bmatrix} \bar{R}_k & \bar{z}_k \\ H_k & \vec{y}_k \end{bmatrix} = \begin{bmatrix} \hat{R}_k & \hat{z}_k \\ 0 & \hat{e}_k \end{bmatrix} \tag{4.43}$$

In Eq. 4.43, T_{H_k} denotes the Householder transformation applied at time t_k. The barred quantities represent the current a priori values of these quantities while the hat symbol denotes updated quantities. H is the overall matrix of measurement partials, $\hat{e}$ is a vector containing the sum of squares of the observation residuals. Operationally, since a pre-whitening transformation is implemented prior to the processing of the data, the H matrix and $\hat{e}$ are actually normalized by the square-root of the measurement noise matrix.

The updated square-root information matrix is:

$$\hat{R}_{k-1} = \begin{bmatrix} \hat{R}_x & \hat{R}_{xp} & \hat{R}_{xb} \\ 0 & \hat{R}_p & \hat{R}_{pb} \\ o & 0 & \hat{R}_b \end{bmatrix}_{k-1} \tag{4.44}$$

The best estimates $\hat{x}$, $\hat{p}$ and $\hat{b}$ of the full state vector are obtained by means of a backward-substitution algorithm.

Figure 4.3 synthesizes the mechanization of the SRIF algorithm as implemented in the GIPSY/OASIS II software. Flow charts of algorithms for the square-root free Givens and Householder transformations are not shown here but are available in [182]. Note that because there is usually an observation at time t_0, the measurement update stage occurs prior to the time update stage.

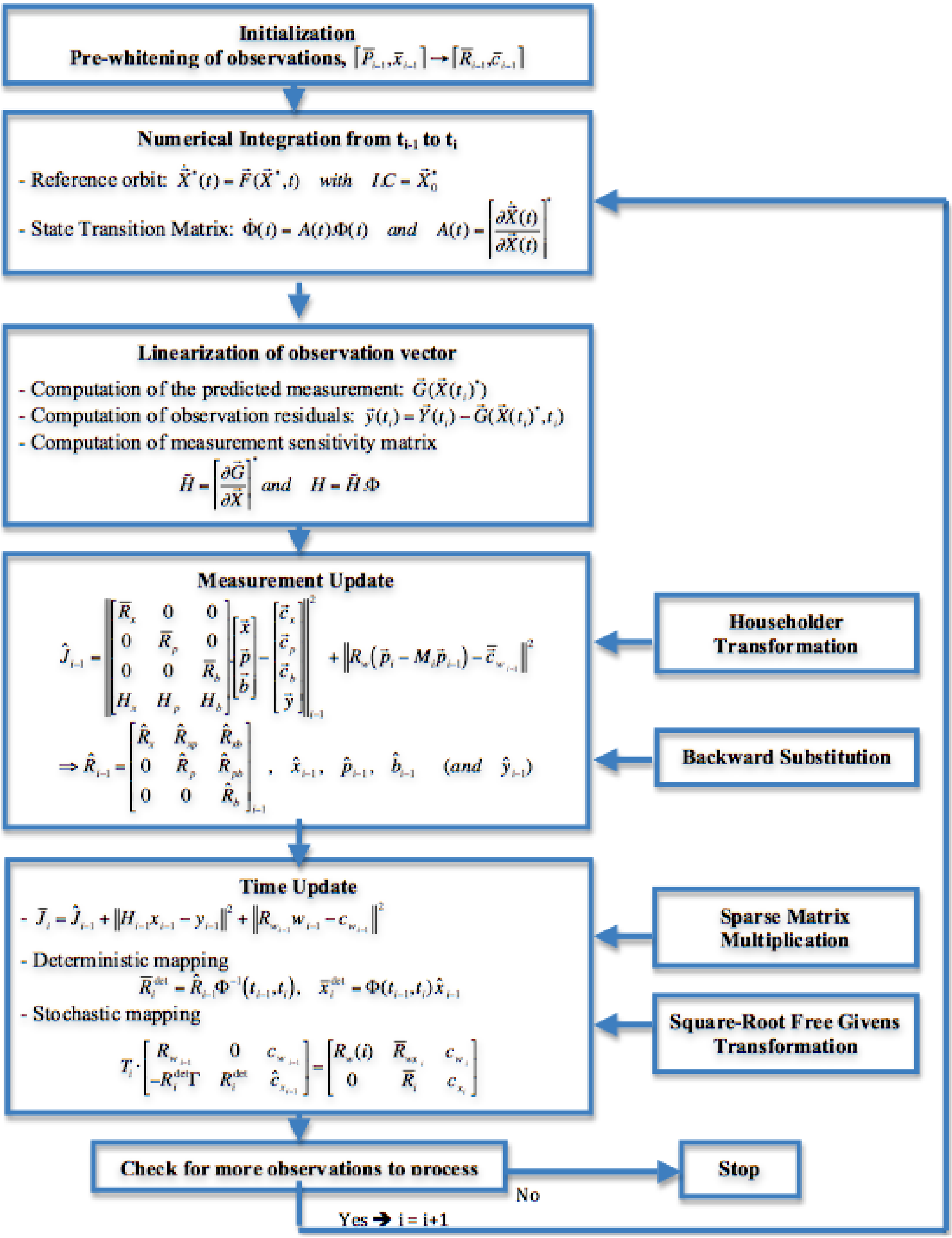

Figure 4.3: Flowchart of the SRIF

4.5 Smoother

Due to the combined use of process noise and pseudo-epoch states, the filtered data must be smoothed and mapped at all epochs. The smoothing algorithm implemented in combination to the SRI filter in the software package used corresponds to the UDU factorized covariance version introduced by Bierman in [17] and [18]. The mapping of the smoothed estimates is performed following a procedure detailed in [118].

Chapter 5

Estimation Strategy Design

5.1 Introduction

This chapter provides a description of the main characteristics of the estimation strategies developed and employed for this work. The rationale behind each of the approaches taken and each of the specialized features included in the implemented procedures is detailed.

To begin with, the concept of reduced-dynamic solution is explained.

5.2 Reduced-dynamic approach

Precise orbit determination can be carried out taking three different kinds of approaches:

- a kinematic approach,
- a dynamic approach,
- a hybrid of the former two designated as reduced-dynamic approach.

In the first case, the satellite states are estimated in a purely geometric fashion, independently of any force model. The error budget is thus dominated by random errors due to data noise, the primary error sources arising from the tracking data qua-lity and strength of the observing geometry. Systematic measurement model errors due to multipath for instance also contribute to the error budget. In practice, kinematic strategies can only be employed when the observations are of sufficient accuracy, globally distributed and available continuously. These requirements on the tracking data quality limit the implementation of the kinematic approach to GPS measurements.

In the second case, the estimation procedure relies nearly exclusively on Newton's fundamental law of dynamics for the computation of the spacecraft's acceleration over time. Such approach is supported by a wide variety of mathematical models. It necessitates the use of a nominal trajectory that serves as initial conditions in the numerical integration process. Obviously, in this case, mis-modeling errors, along with the computational stability and robustness of the orbit integrator and quality of the reference solution, are the main contributors to the error budget. The solution is iterated upon until the fit to the tracking data meets a satisfactory level.

The third possible approach results from the coupling of the first two. The two approaches depicted suffer from different kinds of limitations and complement each other that way. While a purely kinematic solution can be ridden with data noise, a dynamic solution can be corrupted by systematic errors. The reduced-dynamic approach seeks a trade-off between the contributions of a robust tracking geometry and high-fidelity force models. Achieving the optimal balance should result in the minimization of the overall error (i.e. the sum of the random and systematic errors). Such compromise is made by introducing process noise in the filter. The weight allocated to each of the two approaches is determined by the process noise parameterization.

In reality, as highlighted by Yunck in [204], reduced-dynamic strategies form a continuum bounded by fully dynamic precise orbit determination on one end and purely kinematic orbit estimation on the other end. When the correlation time of the associated Gauss-Markov process greatly exceeds the duration of a batch and the steady-state variance approaches 0, the strategy becomes fully dynamic. Conversely, a kinematic strategy corresponds to a situation in which the time constant approaches 0 while the steady-state variance is infinite.

5.3 Significance of multiple-revolution arc strategy

The estimation arcs considered in this work span many orbital revolutions of the GPS satellites. This choice is motivated by the fact that using long arcs is beneficial to the solution in three aspects:

1. The dynamics of the spacecraft are better constrained over many revolutions.

2. the final solution is less sensitive to tracking data errors. Indeed, the effects of noisy measurements are significantly reduced through averaging over long time spans.

3. The number of discontinuities occurring in a series of solutions is reduced.

Potential shortcomings of a long-arc strategy include the need for high-fidelity dynamic modeling and increased computational effort and time. The former constraint is satisfied by the set of models available in GIPSY/OASIS. The latter limitation can be easily removed by decreasing the number of stations in the tracking network. Doing so effectively results in the de-weighting of the kinematic portion of the reduced-dynamic strategy and in a shift towards a more dynamic strategy.

5.4 The once-per-revolution empirical accelerations

The tuning of the estimation strategies primarily consists in refining the paramete-rization of custom acceleration terms with a frequency of one cycle per revolution (1-cpr). The rationale for specifically targeting the orbit error exhibiting a 1-cpr signature are given in section 5.4.1. Section 5.4.2 depicts how this error is effectively mitigated by means of those 1-cpr acceleration terms.

5.4.1 Motivation

The rationale for estimating empirical accelerations with a 1-cpr signature is twofold:

- On the one hand, the residual orbit error spectrum is clearly dominated by a spectral line with a frequency of 1 cycle per revolution.

Colombo showed in [53] that resonant perturbations are responsible for long-period variations in the satellite orbital elements. In the case of the GPS constellation, the satellite orbit error tends to be dominated by slow variations in the orbital elements caused mainly by the solar radiation pressure force modeling errors but also partly by resonant gravitational forces due to the 2:1 resonant periods of the GPS satellite orbits and Earth's rotation and 12-hour periodic repeatable orientation of the spacecraft's solar panels relative to the Earth and Sun (see section 5.6).

- On the other hand, compensating for such perturbations leads to a dramatic reduction of the bow-tie effect that manifests due to the combined use of long estimation arcs and the use of the pseudo-epoch state formulation in the square-root information filter.

As discussed by Fu and Cazenave in [75], the bow-tie effect originates in secular drifts in the orbit elements of a satellite when only the initial conditions are estimated. This effect is consequently of relevance for this work due to the pseudo-epoch state formulation implemented in the SRIF.

5.4.2 Parameterization of the empirical accelerations

The empirical 1-cpr accelerations are modeled as process noise with a 12-hour update time and small a priori and steady-state variances.

A set of four parameters are estimated as random-walk processes in the orbit determination strategy to compensate for the slowly-varying orbit element errors: a sine and a cosine terms in both the cross-track and in-track directions. Alternatively, a sine and a cosine terms in the cross-track and radial directions could be estimated but solving for acceleration terms in both the radial and in-track directions simultaneously would result in a near-singular solution [75].

The set up of these 4 parameters as independent random-walk processes allows the amplitude and phase of the overall 1-cpr custom acceleration to vary slowly throughout the arc, leading to the absorption of the residual long-period orbit error.

The validity of this parameterization of the 1-cpr custom acceleration was demonstrated in [96] by Haines et al. who included these four terms in the estimation strategy they developed for the TOPEX/Poseidon POD. It has been widely used since then (e.g. by Luthcke et al. for the Jason-1 mission POD, see [133]) and is currently considered state-of-the-art.

5.5 Fiducial strategy

It is impossible to simultaneously freely estimate all satellite orbits, tracking site locations and Earth's pole coordinates without a priori information. If no a priori information were supplied, the observability of the system would be compromised and the solution would become singular. When a priori information is supplied, the ground network can be let free but the estimation process has to be followed by the fixing of the frame thus realized to some official realization of the ITRF by means of a Helmert transformation. This approach is operationally used to produce the solutions generated for JPL's FLINN products for instance. Yet, when proceeding in this manner, the formal errors associated with the pole coordinate estimates can be very large. For this work, another approach was chosen in which some of the tracking stations are readily fixed to a well-known-well-established terrestrial reference frame. In that configuration, over each estimation arc the set of fiducial sites establishes the geodetic datum in which all other quantities are determined.

Polar motion is a vectorial quantity and, as such, is frame-dependent. Consequently, any day-to-day variability in the realization of the reference frame directly translates into the estimates of the pole coordinates. This can potentially lead to inconsistencies or discontinuities in time series spanning many arcs. Therefore, not only the number of fixed stations and their global distribution but also the repeatability of the ground network arc after arc are critical factors. The ground network selection process is detailed in section 7.3.

The main shortcoming in estimating a network-fixed solution is that it is, by definition, site specific. Errors occurring at a specific site can potentially contaminate the whole network. An ill-determined network can, in turn, significantly impact and degrade the final orbit, clock and polar motion solutions. As a matter of fact, even small inaccuracies in the positions of the stations have the potential to induce significant errors in the polar motion series. Clearly, the overall quality of a solution depends on a complex interplay between the determination of the Earth orientation, the satellite states and ground receiver coordinates. Ultimately all these quantities must be determined in a fully consistent manner.

5.6 GPS Orbit Determination Error Analysis

The estimation strategy design fundamentally stems from the GPS constellation POD error analysis. The error budget associated with GPS orbit determination quickly grows due to the large number of error sources.

Error sources can be sorted into three categories:

- some errors arise from the space segment; they are due to perturbations caused by forces acting on the satellites or disturbances affecting the satellite clocks,
- others are directly related to the propagation path of the signals through the various layers of the atmosphere,
- the ground segment also contributes to the error budget with effects inherent to the location and site maintenance of the ground tracking stations as well as hardware biases in the receiver antennas and clocks.

The sections following describe the various contributors to the total GPS OD error budget. The general features of dynamic modeling and other means employed to mitigate each of the error sources are briefly mentioned.

The actual implementation is detailed in Chapter 7.

5.6.1 Forces on satellites

The forces acting on a satellite can be sorted into two main categories: gravi-tational forces and surface forces. A secondary classification distinguishes resonant and non-resonant perturbations. Each type of force acting on the GPS satellite is described in the section that follows. The resonant nature of some of these perturbations is discussed.

- Gravitational and tidal forces

Gravitational attraction exerted by the Earth, Sun, Moon and, to some lower degree, other celestial bodies, is the largest perturbing force acting on the GPS satellites.

Tidal forces arise as a secondary effect of the luni-solar gravitational force as mentioned in Chapter 3. Tidal forces include ocean tides, ocean tidal loading, pole tides as well as solid Earth tides or body tides. All these forces need to be modeled and accounted for in the context of the precise orbit determination of Earth orbiters because they affect the positions of the ground receivers and states of the spacecrafts. High-fidelity models are used (e.g. the geopotential model is derived from GRACE observations, in the case of the GGM02 gravity model), so that the errors are small compared to the errors related to the solar radiation pressure for example. The gravitational and tidal force models used for this work are described in Chapter 7.

- Radiation pressure and thermal effects

Radiation pressure forces encompass perturbing accelerations that are due not only to direct sunlight radiation but also to radiation reflected and emitted by the Earth and thermal effects originating in the heat emitted by the spacecraft itself and its antennas.

Because of the altitude at which the GPS constellation evolves, the solar radiation pressure force is the largest perturbation acting on the satellites after the gravitational forces mentioned above. It is also currently considered the largest error source in the modeling of GPS orbital dynamics. This is due to the fact that solar radiation pressure depends primarily on the shape, size and mass of the spacecraft as well as on aging effects of the satellite surfaces. Because these parameters can be very different from block to block (i.e. GPS spacecraft generation) and can also differ from satellite to satellite within the same block, modeling errors quickly grow. Besides, the solar radiation pressure force a satellite is subjected to varies following seasonal fluctuations in the solar flux and other smaller-scale and unpredictable temporal variations. Another big contributor lies in the uncertain orientation of the GPS satellites since no star tracker information is available from the GPS constellation.

The perturbing acceleration due to SRP can be modeled using two parameters: an adjustable scaling factor and the so-called Y-bias. The so-called solar scale parameter reflects the change in the solar flux constant and is related to the surface reflectivity. The Y-bias is not directly induced by the SRP force but occurs as a secondary effect of that force. It is caused by a combination of misalignments of the solar panels, solar sensors and thermal radiation vector. The Y-bias owes its name to the fact that the related perturbing acceleration lies along the Y-axis in the satellite-centered Earth-Probe-Sun (EPS) coordinate system. In that system, the Y-axis runs along the solar panels. The orbit errors associated with a mis-modeled Y-bias acceleration are mostly in the along-track direction.

The SRP and infrared thermal radiation from the Earth measurably impact the GPS satellite trajectories and must be carefully accounted for. Because there is no star tracker information from GPS as mentioned above, models of the spacecraft attitude are used. The SRP models developed at JPL by Bar-Sever et al. are documented in [8] and [9].

- Resonant disturbing forces

Due to their 12-hour orbit, the GPS satellites are in a deep 2:1 resonance with the Earth's rotation. Yet, resonant disturbances are induced not only by gravitational forces but also by non-conservative forces such as thermal radiation forces. The solar radiation pressure force tends to exhibit a nearly periodical pattern as the attitude of the spacecraft and its solar panels relative to the Earth and Sun repeats almost exactly every 12 hours, as explained in [53]. It is believed that most of the errors arising from mis-modeling of the forces acting of the satellites are of the resonant type [53].

To compensate for these resonant perturbations due to the mis-modeling of the main forces acting on the spacecrafts, a custom acceleration term is often estimated in the GPS orbit determination process as described and referred to as the 1-cpr acceleration in section 5.4.

5.6.2 Signal propagation

As they propagate through the layers of the atmosphere, the GPS signals are distorted and delayed. The ionosphere is a dispersive medium with respect to the GPS radio signals; as a result code pseudo-ranges are naturally delayed and carrier-phase measurements advanced. The effects of the ionosphere on the signals constitutes the major source of error on GPS measurements if not corrected for. The ionospheric refraction is easily mitigated through the use of a dual frequency linear combination technique.

Their passage through the neutral atmosphere also impacts the GPS signals through the tropospheric path delay. This effect adds an extra delay in the measurement of travel time from the transmitter to the receiver. This phenomenon represents a serious error source due to the strong spatial heterogeneity and temporal variability of the troposphere. Without appropriate compensation, this delay can induce a bias on the measurements ranging from 3 m at zenith to 30 m at low elevation.

Various models exist that predict the delay induced by propagation through the troposphere and estimate it at zenith angle. A mapping function is then used to apply an obliquity factor based on the line of sight. The models and mapping function used for this research are discussed in section 7.2.2.

5.6.3 Ground receivers

Several types of errors originate from the ground receiver locations. In particular, multipath effects and atmospheric effects arising from the environment surrounding the antennas can significantly corrupt the GPS signals. Hardware delays can also affect the solution. The observing geometry is also an important factor as the solution degrades with reduced strength of the line of sight. Clock errors is another problem that affects ground receivers because ground clocks are generally less stable than transmitter clocks. They can also get de-synchronized relative to the transmitter clocks. All these factors stress the need for robust, carefully selected ground networks. Clock errors are less of an issue in the actual implementation of the estimation strategy used for this work since they are estimated simultaneously to the GPS orbits and clocks.

5.6.4 Relativistic effects

General relativity affects three components of the GPS system: the satellite orbits (through the modification of their equations of motion), the propagation of the signals transmitted from space (through a space-time curvature) and the rate at which the clocks run. If some of the errors induced by relativistic effects are negligible or can be corrected beforehand, others cannot be ignored in the context of precise orbit determination. The two main error sources reside in the curvature of the signal propagation path and the Sagnac effect, arising from the Earth's rotation and affecting the receiver clocks by inducing the motion of the station while the signal propagates from the transmitter to the receiver. Those perturbations can be modeled and compensated for. In addition, a corrective term for the residual acceleration resulting from the modification of the constellation equations of motion can be computed. The treatment of relativistic effects in GPS applications is covered in [110].

5.6.5 Overview

Figure 5.1 gives an overview of the effects of each type of perturbations on the accuracy of the orbit determination of the GPS constellation. The table shown in this figure is excerpted from [178]. The values printed correspond to the root-mean-squares of the difference between GPS orbits estimated while including a dynamic model for each perturbing acceleration and the GPS orbits estimated turning off a specific force model at a time. The orbit determination procedure employed by Springer to obtain the results gathered in Fig. 5.1 corresponds to the orbit determination procedure setup at CODE at the time of publication, i.e. in 1999. This table gives a rough idea of the orders of magnitude of the various forces acting on the GPS satellites over 3 days.

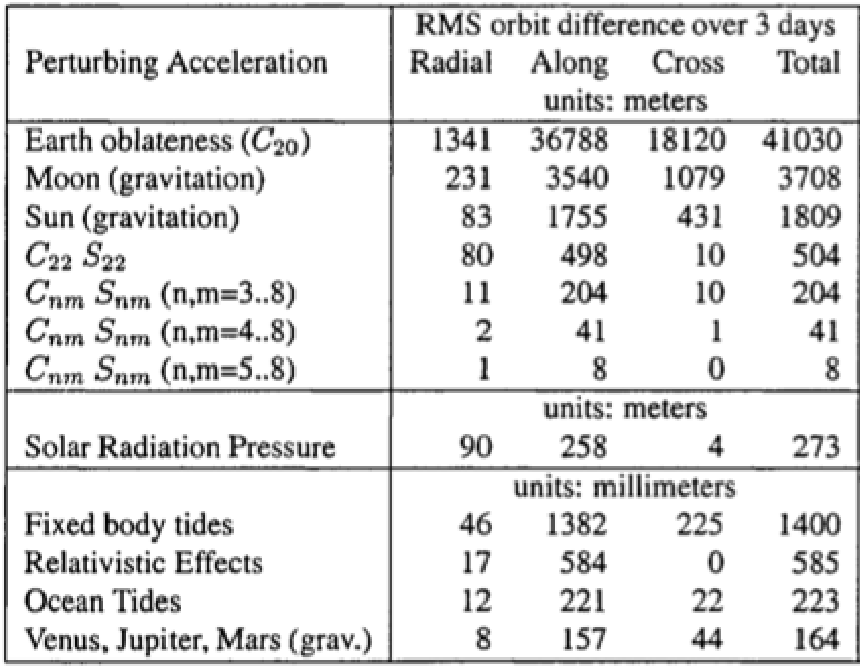

	RMS orbit difference over 3 days			
Perturbing Acceleration	Radial	Along	Cross	Total
	units: meters			
Earth oblateness (C_{20})	1341	36788	18120	41030
Moon (gravitation)	231	3540	1079	3708
Sun (gravitation)	83	1755	431	1809
C_{22} S_{22}	80	498	10	504
C_{nm} S_{nm} (n,m=3..8)	11	204	10	204
C_{nm} S_{nm} (n,m=4..8)	2	41	1	41
C_{nm} S_{nm} (n,m=5..8)	1	8	0	8
	units: meters			
Solar Radiation Pressure	90	258	4	273
	units: millimeters			
Fixed body tides	46	1382	225	1400
Relativistic Effects	17	584	0	585
Ocean Tides	12	221	22	223
Venus, Jupiter, Mars (grav.)	8	157	44	164

Figure 5.1: Impact of the main perturbations on a GPS satellite orbit determination over a 3-day arc, from [178]

Chapter 6

Software packages

This chapter gives a broad description of the software packages used for this work, namely the GIPSY/OASIS II software along with higher-level software packages providing an interface to the main piece of software.

As mentioned in section 1.3.3, the first phase of the work presented in this dissertation consisted in modifying the GIPSY/OASIS II software to enable the estimation of the Earth Rotation Parameters as stochastic processes at high temporal resolution. The last section of this chapter describes the upgrades implemented into the current software version and the testing procedure employed to validate the changes.

6.1 Overview of GIPSY/OASIS II

6.1.1 Introduction

The GIPSY/OASIS II software package was developed by the Orbiter and Radio Metric Systems (ORMS) group at JPL in the late 1980's and has been constantly upgraded ever since. It is referred to as GIPSY in the remainder of this document.

GIPSY is a general satellite tracking and orbit determination software system composed of several modules that can be used either independently from each other as stand-alone programs or in combination with each other as subroutines in the setup of a complete strategy constructed towards a specific application (e.g.: GNSS/LEO Precise Orbit Determination, Precise Point Positioning, geodetic applications such as the high-precision determination of geophysical quantities, etc. . .).

GIPSY/OASIS stands for ”GPS Inferred Positioning System/Orbit Analysis and Simulation Software”. As indicated by its name, the software is more specifically designed for high-precision geodetic applications based on GPS data processing and GPS-aided Precise Orbit Determination (POD). Therefore, many parameters commonly required for GPS POD are conveniently defaulted in the software's various modules.

Used in the context of orbit determination based on GPS tracking data, the software package models the GPS observations (both pseudo-range and carrier-phase) accounting for the various perturbations affecting the orbits of the satellite(s) of interest (gravity, tidal effects, solar radiation pressure…) and subsequently estimates corrections to that model. In practice, observation data and a priori orbits are input and combined with geophysical models, atmospheric models, Earth reference system and a priori station information to obtain a file containing both the parameter partials and their nominal values. GIPSY is designed to find the best agreement between the model and the observation in a least-squares sense. To do so, a square-root information filter (SRIF) is iterated on the data, removing outliers and corrupted data until a user-defined convergence criterion is reached.

Orbit determination in GIPSY relies on the reduced-dynamic strategy described in Chapter 5. As a consequence, the software supports a full range of strategies from kinematic to dynamic. The software first computes a dynamic reference solution prior to the filtering/smoothing process and the effects of unknown forces and dynamic mis-modeling are compensated for using process noise. The various steps involved in the estimation procedure outlined above are detailed below. They follow the different stages of the general statistical parameter estimation summarized in Chapter 4.

A recapitulative flow chart is provided below.

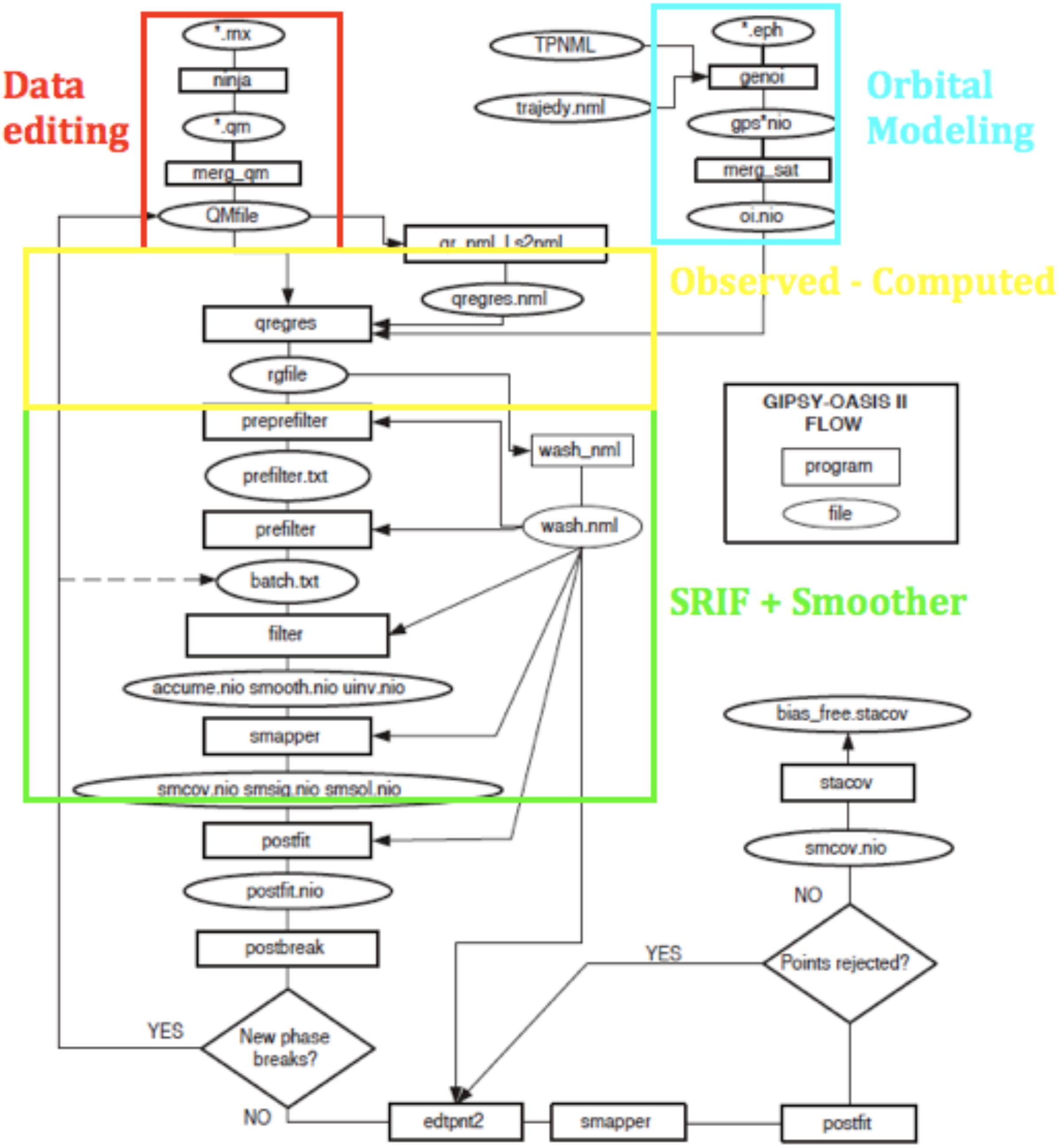

Figure 6.1: Flow chart of the GIPSY/OASIS II software package [116]

6.1.2 Data editing

The tracking data are pre-processed through the GIPSY front-end utilities. In this project, only GPS data were considered. The GPS observations are input as RINEX files that are read by GIPSY's editor, rearranged and converted into a concatenated binary file which is used throughout the estimation process. During the pre-processing stage, the outliers, cycle slips and phase breaks inherent to GPS measurements are automatically detected. Outliers are deleted while cycle slips may be repaired and phase breaks are flagged and recorded for the remainder of the estimation process. Additional phase breaks may be introduced in the observations as needed. In addition, the carrier-phase observations are decimated and the pseudo-range measurements are carrier-smoothed using the Hatch filtering process. Hatch filtering is a code-smoothing technique using integrated carrier phase observations. The Hatch filter can be described as a recursive filter using both the current measurements and previous estimates to provide more precise range measurements without any dynamic model.

6.1.3 Orbital modeling

Prior to the main filtering/smoothing stage, the ephemerides of the satellite(s) of interest are processed through an iterative batch processor - the trajedy module - in order to obtain the initial state vector(s) that will serve as the nominal orbit(s) in the full-up filter solution. The observations are the input ECI ephemeris records, containing both the positions and velocities of the satellite(s) from another (less accurate) source. In the case of GPS POD, the GPS broadcast ephemerides are used. In order to ensure that the quality of the final solution reflects the fact that it fits well both the input orbit and the tracking data, all the parameters are estimated as unconstrained in this batch processor. The parameters iterated upon include the satellite positions and velocities as well as other dynamic parameters, such as the parameters associated with solar radiation pressure force modeling in the case of GPS POD (see Chapter 7). The orbit integrator also provides the dynamic parameter partials and state transition matrices to be used in the subsequent filter/smoother.

Orbital modeling is considered complete and successful once a convergence criterion is reached or when the best fit between the initial ephemerides and the integrated orbit is reached. If the user-specified convergence tolerances are not met after a user-specified number of iterations through the batch processor, the satellite under conside-ration is removed from the solution. When multiple satellites are considered, as is the case for the GPS constellation POD, each satellite is treated individually. High-fidelity dynamic models are used in this process since they guarantee a better representation of the satellite states. In the case of GPS POD, the force model specifications include the activation of the Earth, Sun, Moon and planets point mass models, Solar Radiation Pressure and a 12x12 Earth gravity model.

6.1.4 Measurement and Earth modeling

When GPS tracking data are used, the observables are the ionosphere-free pseudorange (P_c) and carrier phase (L_c). The computed measurements relating the receiving station (or Earth-orbiting spacecraft) i and the transmitting GPS satellite j are written:

$$\begin{cases} P_i^j &= \rho_i^j + c\left(\delta t^j - \delta t_i\right) + \rho_{iono} + \rho_{tropo} + \rho_{multipath} + \varepsilon \\ L_i^j &= \rho_i^j + c\left(\delta t^j - \delta t_i\right) - \rho_{iono} + \rho_{tropo} + \rho_{multipath} + \lambda\, N + \varepsilon \end{cases} \tag{6.1}$$

In Eqs. 6.1, ρ_i^j denotes the geometrical range between the transmitter j and the receiver i. The second terms on the right-hand side of both equations relate to the clock errors affecting the transmitter and receiver, respectively. The third and fourth terms represent the contribution of the atmosphere to the error on the observables. Note that despite the fact that the ionosphere-free dual-frequency linear combination is used for the carrier phase observable, it mitigates the ionosphere effect only to first order. Therefore a residual, much smaller, second-order, ionosphere-related error still affects the received signals. This effect is accounted for through a model as mentioned in section 7.2.5. The parameter N in the carrier phase observation equation denotes the ambiguity term and λ is the wavelength of the carrier. The ε parameters represents the errors on the observations.

The measurement and geometric modeling are carried out by the module qregres. The role of this module is to form the observation residuals $\vec{y}_i$ and the matrices $\tilde{H}$ that contain the partial derivatives relating the observables to the parameters to be estimated. The module owes its name to the fact that the components of the $\tilde{H}$ matrices are referred to as the regression partials in GIPSY. The mathematical description of the observable modeling and derivation of the regression partials can be found in [118].

A number of dynamical, geometrical and geophysical models are available for use in this module. State-of-the-art tidal models are for instance included to model the deformations undergone by the Earth and by each station of the network as well as the orientation and rotational behavior of the Earth. In addition, up-to-date site-specific metadata are employed in the measurement modeling such as receiver and transmitter antenna calibration files, information on the precise location of the antenna reference points, receiver type, etc....

It is important for the purpose of our study to stress the fact that polar motion rates are not currently available for adjustment as stochastic processes in GIPSY.

6.1.5 Estimation process: filter and smoother

The core filtering/smoothing/mapping stage in GIPSY is encompassed in a high-level module called wash. This module is made of two main sub-modules: filter and smapper (a contraction for smoother and mapper). GIPSY uses a SRIF and associates it with a UDU factorized smoother. Both algorithms ensure the computational stability of the estimation process and are extensively described in [17] and [182]. Their formulation in GIPSY is presented in sections 4.4 and 4.5. The filtering process is highly flexible with regard to process noise settings and update time mechanisms. The filter, smoother and mapper routines are described in detail in user's guides. The information that follows can be partly found there and in [116].

The objective of the filter is to process the data points contained in the file output by the qregres module, treating estimable parameters as biases or stochastic processes.. The stochastic processes are parameterized by specifying so-called stochastic event times and stochastic attributes.

A stochastic event is defined as an epoch at which a stochastic process needs to be time-updated. The stochastic attributes of a Gauss-Markov process provide the information needed to map the solution from one epoch to another. These attributes include the correlation time of the process, its steady-state sigma and type (e.g. white noise or random walk), if any. A priori information such as the data weights and the nominal uncertainties on the state vector's initial conditions must also be input to the filter module.

The actual filter is preceded by two pre-filtering phases to assist the user in preparing the input file to the filter. The two pre-filtering processes distinguish between the stochastic events that are data-dependent and those that are data-independent before merging them into batches of various durations. Complex time update mechanisms and process noise resets allow the user to use different stochastic process models for each parameter if desired. Gregorius provides a detailed explanation of the mechanisms governing the inclusion of process noise in GIPSY in his handbook [86]. The sketch displayed in Fig. 6.2 and excerpted from [116] represents the various types of stochastic processes available to describe the behavior of a parameter and shows when each type of parameters gets updated over the estimation arc.

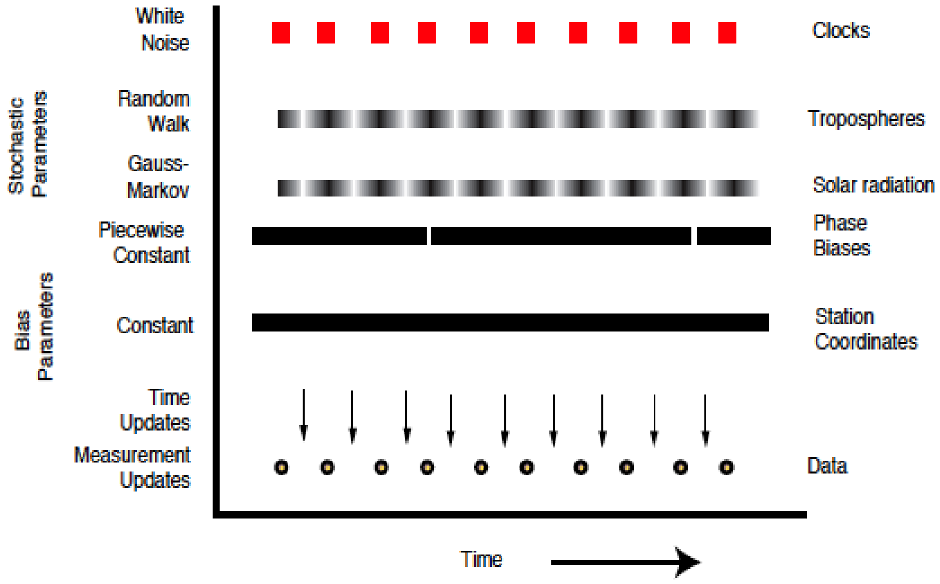

Figure 6.2: GIPSY stochastic update mechanism [116]

The filtering process can be repeated several times to enhance the solution. The stopping criterion in the iterative process can either be defined by the user or based on the number of phase breaks and/or residual outliers detected after each pass through the filter. Once the filtering process ends, the smapper module maps the final variance-covariance and sensitivity matrices as well as the solution at each epoch of the arc. Whenever stochastic processes are present, the filter solution is also smoothed to yield the final solution.

6.2 Modifications performed

6.2.1 Motivation for upgrades

The modifications implemented in the GIPSY software aimed at enabling and facilitating the estimation of the Earth's rotation parameters as stochastic processes at high rates and WITH enhanced accuracy.

The first step consisted of adding the capability to determine and report the ERP at high temporal resolution. This required the implementation of a new file format. Indeed, the historical format for the files containing the earth rotation information is limited to a total of 335 entries spanning a maximum of 36 epochs. For this reason, this format is neither adapted to long estimation arcs, nor suitable to the reporting of high-rate Earth rotation parameters. A new format, referred to as the GEOP format, for GIPSY Earth Orientation Parameters, was created. In contrast to the historical Earth orientation files that consist of a Fortran namelist, the ERP are represented as time series of virtually unlimited length in the new format. The software package was consequently extensively modified to provide interfaces to and enable the use of this new format. The upgrade included changes to existing routines as well as the creation of new utilities.

The second step consisted in replacing the deprecated IAU80/IAU76 precession-nutation model by the most recent models recommended by the IERS in their 2010 Conventions (see the IERS Technical Note 36 [152]). The details of these new models and their implementation have been covered in Chapter 2 and are not repeated here.

6.2.2 Testing procedure

A variety of tests were performed to ensure the backward compatibility of the modified GIPSY version with the operational version of the software. These tests accounted for the different machine architectures and compilers used by the ORMS group at JPL. They spanned the diversity of applications covered by GIPSY and included:

- *The independent testing of individual modules*

  Because all the modules were affected by the changes, each of them was tested individually based on multiple scenarii to evaluate responses to all options and the validity of error messages.

- *A GPS POD test case*

  Precise Orbit Determination of the entire GPS constellation was performed using the Long Arc GPS Processing software (see section 6.3.1).

  The setup of the GPS POD strategy is detailed in Chapters 5 and 8 of this dissertation and is not repeated here.

- *Precise Point Positioning test cases*

  In this configuration, each station is processed independently. The nominal GPS orbits and clocks are kept fixed as well as the nominal timing (UT1, LOD) and polar motion information. The only parameters adjusted in the filter and fitted to the GPS tracking data are the site-specific tropospheric parameters, the station coordinates and clocks as well as the phase biases. The gd2p software, presented in section 6.3.2, is used for this application.

- *A Low-Earth Orbiter (LEO) POD test case*

  The orbit of the low-Earth orbiting altimetry satellite OSTM/Jason-2 was estimated using the gd2p software based on a test case provided by Dr. Shailen Desai.

  In this configuration, nominal LEO ephemerides are input and used as observations in

GIPSY's trajedy module to refine the initial guess and force parameters. Three types of solutions are successively computed, each of them relying on the quality of the preceding one as part of the automation of the filtering strategy. To begin with a purely dynamic solution is solved for. Building on the solution obtained through the dynamic tracking of the satellite, a reduced-dynamic solution is estimated. Finally, ambiguity resolution is performed based on the reduced-dynamics solution and the final solution is obtained (see [11] for instance).

- *The comparison to an independent software implementation*

  To further validate the implementation of the IAU2000A/2006 nutation-precession model, it was tested against the SOFA implementation. Numerical examples proposed by Capitaine and Wallace in [195] and by SOFA in their Earth Attitude Toolbox [114] were also used.

6.3 Wrappers to GIPSY/OASIS II

Two software packages essentially acting as wrappers to the GIPSY software were extensively used to generate the results presented in this dissertation. They are briefly presented below.

6.3.1 The Long Arc GPS Processing software

The Long Arc GPS Processing software (Longarc) is a package developed by the ORMS group at JPL and is constantly evolving. It provides an interface to GIPSY by automating the implementation of various procedures relevant to GPS POD. Longarc enables the use of multiple consecutive days of data to estimate the quantities of interest over many satellite revolutions. All the strategies developed and analyzed in Chapter 5 were implemented in Longarc by means of customized input configuration files.

6.3.2 The gd2p software

The gd2p software is a Perl program that wraps GIPSY for diverse geodetic applications among which static and kinematic precise point positioning, low-Earth orbiter POD and troposphere estimation. The name stands for ”GPS data to position”. Similarly to the Long Arc GPS Processing software, gd2p is designed to automate procedures related to high-precision scientific applications of GPS. This software was used for the tests involving LEO POD and PPP as mentioned above (see [11], [12]). In addition, the gd2p software actively participates in the station selection process through its use for the generation of the engineering files that report the condition and quality of the data collected at all sites over given periods of time. More information on these metadata is given in section 7.3.

Chapter 7

Strategy Implementation

7.1 Introduction

This chapter is concerned with the actual implementation in GIPSY of strategies designed based on considerations covered in Chapter 5. The force, observation and geophysical modeling employed for each candidate procedure are covered, along with the geometry of the problem and its optimization.

A description of the two main coordinate systems mentioned in this chapter and throughout this thesis, namely the HCL and the UVW coordinate systems, is provided in Appendix B.

7.2 Modeling and Parameterization

7.2.1 Satellite dynamics

Prior to the large-scale filtering process, a batch processor is run to adjust the satellite initial states using JPL's final Flinn orbits and clocks as nominals as explained in section 6.1.3.

Various reduced-dynamic strategies have been tested in the quest for the one that best recovers polar motion. These strategies differ in the way they deal with the compensation of surface force mismodeling through the use of process noise, as well as in the length of the estimation arcs used. The orbit determination portion of each of the three strategies considered in this thesis is briefly described below and summarized in Table 7.1.

- **the FlinnR-like strategy or 30-hour strategy**

This strategy constitutes the nominal approach for the JPL IGS Analysis Center's contribution to the IGS final combined orbit and clock products. It has been used at JPL for several years to generate the so-called FLINN (or Flinn, for Fiducial Laboratories for International Natural science Network) products. Consequently, the FlinnR-like strategy served as a reference in this study and was not modified at all, except for the fact that the pole coordinates were estimated as stochastic parameters, modeled as random-walk processes, instead of being adjusted as biases over each estimation arc as is the case in the regular FlinnR strategy.

In this configuration, the estimation arc is 30 hours long and centered on 12PM UTC each day. Each orbital arc thus spans 2.5 orbit revolutions of the GPS satellites only; as a result the strategy is not well suited for inclusion of the 1-cpr custom acceleration terms introduced in section 5.4.

The position and velocity vectors of all the satellites are estimated with constraints in the filter.

Likewise, the overall scale factor and Y-bias component of the solar radiation pressure force are solved for as constants with their a priori values constrained. Additionally, process noise is incorporated into the strategy to compensate for the slowly-varying unmodeled perturbations caused by solar radiation pressure. Thus, on the one hand, an empirical acceleration along the Y-axis is estimated as colored noise to account for the contribution of the Y-bias. On the other hand, because the SRP forces are usually planar in the XZ plane, the X- and Z-components of the solar scale parameter are also modeled as Gauss-Markov processes.

The next two strategies are said to be of the Longarc-type due to the fact that the orbital arcs span multiple days in these cases.

- **the 3-day strategy**

This strategy is explicitly designed to target the one-cycle-per-revolution (1-cpr) orbit error. Various arc lengths have been tested but 3-day arcs yield the best solution obtained to date in terms of polar motion recovery, as shown in section 7.5.3 below.

In contrast to the FlinnR-like strategy, all dynamic parameters are freely estimated in the case of the 3-day strategy case. The set of dynamic parameters adjusted as constants with very loose a priori values include the satellite states as well as the SRP solar scale factor and Y-bias force components.

The 1-cpr custom acceleration is modeled in HCL coordinates according to section 5.4.2. For this reason, this estimation strategy is also referred to as the HCL strategy in the rest of this dissertation whenever the impact of the orbit determination arc length on the solution is assessed (e.g. in sections 7.5.3, 9.1.3 and 9.3.4). Each of the components of the 1-cpr custom acceleration is set up as a random-walk process updated every 12 hours. Furthermore, an alternate stochastic parameterization is used to account for eclipsing satellites or satellites in penumbra which are potentially troublesome for the estimation process.

- **the 9-day strategy**

This last strategy is a variation on the 3-day strategy presented above in which the 1-cpr custom accelerations are expressed in the UVW coordinate system rather than in the usual HCL coordinate system. In addition, a second custom acceleration with a 6-hour period is estimated to accommodate the orbit error that manifests with a twice-per-revolution (2-cpr) frequency. The parameterization is identical to that of the 3-day strategy for the 1-cpr accelerations, apart from the axes chosen to describe the force. It is however a bit different for the 2-cpr force components since the magnitude of the 2-cpr orbit error is typically much smaller than that of the 1-cpr error.

The UVW coordinate system is particularly well suited for the formulation of the solar radiation pressure force acting on the GPS satellites. In that coordinate system, the dominant component of the pressure exerted by solar radiation lies along the U-direction. Because the SRP force is usually planar in the UW plane, the once-per-revolution acceleration is estimated using the same four terms as in the case of the 3-day strategy; they are simply expressed along the U- and W- axes instead of the cross-track and in-track axes used in the 3-day strategy.

This strategy is implemented for arcs spanning 9 days (i.e. 18 GPS orbit re-volutions). It is adapted from a strategy currently used by the ORMS group at JPL to accurately determine the terrestrial reference frame based on GPS only (see [102], [100] and [197] for instance). Using 9-day arcs allows the retrieval of weekly solutions and supposedly yields better quality estimates. The motivations for the use of long estimation arcs are listed in Chapter 5. The interest in testing this strategy in the context of polar motion reco-very is justified by the strong correlation existing between the quality of the reference frame determination and the quality of the ERP solution. Acquiring the capability of applying a homogeneous, single strategy (as far as the force and geophysical models are concerned) for both estimation procedures would ensure the consistency of the two solutions and should, in turn, strengthen the overall GPS POD solution.

Table 7.1, placed on the next page, summarizes the force modeling used in each estimation strategy.

Strategy name	**FlinnR-like**	**3-day**	**9-day**
Orbit Arc Length	30 hours (central day)	3 days (central day)	9 days (central week)
Nominal Orbits and Clocks	JPL FLINN final products		
Gravitational Forces	Point mass model for the Sun, Moon and planets and JGM-3 Earth gravity model		
Solar Radiation Pressure	GSPM04 model overall solar scale, bias, constrained Y-bias, bias, constrained X/Z solar scale components, colored noise constant acceleration along Y-axis, colored noise	GSPM04 model overall solar scale, bias, unconstrained Y-bias, bias, unconstrained	
Custom Acceleration	N/A	1-cpr in HCL frame	1-cpr+2-cpr in UVW frame
Earth's Albedo	Nominal		
Yaw Rate	Nominal + Estimated		
Antenna Thrust	Nominal		

Table 7.1: Dynamical Modeling

7.2.2 Time, position and atmospheric modeling

The receiver and transmitter clocks are modeled as white noise processes with updates at every measurement epoch. Clock biases are therefore estimated every 5 mi-nutes. This treatment implicitly eliminates clocks from the GPS measurement equations and is more advantageous than explicit double-differencing in that respect [116]. Note that one clock must be adopted as reference.

The coordinates of the stations forming the ground network are adjusted as constants in the filter. 25% of the stations are currently held fixed to their a priori positions ($\sigma = 3$ nm for all 3 coordinates). The remainder of the sites are allowed to move away from their a priori location through the use of a 1σ constraint of 3 meters in all directions. A short study was conducted to assess the impact of the proportion of fiducial sites on the quality of the overall solution (orbits, clocks, pole coordinates and station positions) as well as on the processing time. It was concluded that constraining a quarter of the sites to their nominal positions yields solutions of a satisfactory quality. The results of this investigation are presented in Appendix D.

Accurate troposphere modeling is essential in the context of high-precision polar motion estimation since atmospheric effects impact the rotation of the Earth as stated in Chapter 3. As a consequence, a short averaging interval is needed to capture rapidly-varying atmospheric conditions and thereby avoid the propagation of troposphere mis-modeling effects into the pole coordinate estimates. As usual with GPS data processing, there are two parts to the atmospheric modeling.

On the one hand, the wet component of the tropospheric path delay is compensated for by means of process noise. The behavior of the troposphere at each station is modeled through three parameters: the zenith wet delay and two horizontal gradient parameters accounting for azimuthal inhomogeneity. The reader is referred to [7] for information on the modeling of the troposphere and associated path delay estimation. The troposphere parameter estimation settings are directly inherited from the original Flinn estimation procedure. All parameters are modeled as random-walk processes updated every 5 minutes. The constraints imposed on their a priori and steady-state variances are the ones suggested by Bar-Sever et al. in [7]. The GMF (Global Mapping Function) troposphere mapping function is used to map the a priori and estimated zenith wet delays to any elevation angle. The mapping is determined based on the day of year and site coordinates using data output by the European Centre for Medium-Range Weather Forecasts (ECMWF) numerical weather model. The mathematical description of the GMF is detailed in [23].

On the other hand, a priori dry zenith delays are computed for each station using the empirical Global Pressure and Temperature model (GPT) described by Boehm et al. in [22]. Hence, they are not estimated. Indeed, the dry component of the troposphere error is large (about 2 meters) but is well modeled from pressure measurements. In addition, small residual errors in that component will be largely accommodated by the estimation of the wet parameters.

7.2.3 Geophysical modeling

The geophysical modeling as well as the parameterization of the process noise involved are kept the same for all three candidate estimation strategies discussed above.

The pole coordinates are modeled as largely unconstrained random-walk processes updated every 15 minutes (see section 7.4). The steady-state standard deviation is set to the linear equivalent distance of ~50 $m.s^{-1/2}$ at the surface of the Earth. The rates of the pole coordinates are not included in the estimation process, so that only an offset in each pole coordinate is actually estimated. This is because, as mentioned in section 6.1.4, the rates of the Earth's rotation parameters are not available for estimation as stochastic processes in GIPSY yet. The various analyses carried out to validate the time series of estimates obtained however tend to prove that this limitation does not impact the quality of the polar motion estimates, thanks to the shortness of the estimation interval selected for the polar motion parameters.

The geophysical models that the estimation procedure relies on are listed in Table 7.2. Only the models relevant to the precise determination of sub-daily polar motion are mentioned. Their significance is briefly stressed in the paragraphs following.

Feature	Description	Notes
Geopotential		
Gravity field	JGM3 model 12×12	upgrade to GGM02C may prove useful
Tides		
Solid Earth	IERS2010	
Ocean	IERS2010	
Pole	IERS2010	
Ocean loading	FES2004 model	
Effects of Ocean Tides on Polar Motion	extended Ray model IERS2010	based on TOPEX/Poseidon satellite altimeter data
Earth Orientation		
Precession	IAU2006A model	P03 model
Nutation	IAU2006A model	IAU2000A model + adjustments
Polar motion	EOPC04	reference solution for pole coordinates
Rotation	EOPC04	reference solution for UT1-UTC
		for information on nominal EOP series, see Appendix F
Terrestrial Reference Frame	ITRF2005	a priori coordinates for ground network

Table 7.2: Geophysical models and reference solutions employed for polar motion estimation

Gravitational perturbations are accommodated by modeling the geopotential as well as the contributions of other celestial bodies, modeled as point masses. Due to the high altitude of the GPS constellation, modeling the Earth's gravity field up to degree and order 12 is sufficient to obtain accurate solutions and is the standard for GPS-based geodetic applications.

Accounting for tidal effects is critical for high-precision geodetic applications in general and for precise polar motion determination at sub-daily resolution in particular. As a matter of fact, tides cause periodic variations in the station coordinates with frequencies similar to those governing the tide generating potential. Tidal ocean loading can be viewed as a secondary effect of ocean tides that causes site displacements of up to a few centimeters, mainly in the vertical direction. The impact of the pole tide is also significant as resulting site displacements can amount to a couple of centimeters. Pole tides are as a matter of fact directly related to polar motion since they are generated by its centrifugal effect, as explained in [144]. The effects of body tides are the largest in the semi-diurnal and diurnal frequency bands. In addition, diurnal and sub-diurnal variations in polar motion due to ocean tides amount to hundreds of micro-arcseconds. Ocean tides are discussed in more details in Chapter 3.

The IERS Technical Note 36 [152] describes the causes and quantifies the effects of all types of tidal perturbations. Mathematical formulations for the excitation processes, geophysical and geometrical effects as well as applicable corrections are also provided.

The model for ocean tide contributions to polar motion is of particular interest for the performance analysis conducted in Chapter 9. Diurnal and sub-diurnal variations in the ERP (both polar motion and UT1-UTC) are corrected for by means of an ocean tide model recommended by the IERS in their 2010 Conventions. The model implemented includes 71 tidal constituents and relies on an ocean tide height model estimated from altimetry data collected during the TOPEX/Poseidon mission. It is noteworthy that, in Chapter 9, this model is temporarily disabled to ease the quality control of the solutions generated and to verify the extent to which each estimation strategy manages to recover tidally-induced variations in polar motion.

Similar phenomena are observed from the loading of the Earth by the massive atmosphere. In this case, the crustal deformations are shown to be of the order of 2.5 cm in the vertical direction and of up to 1 cm horizontally [144]. The effects of atmospheric pressure loading are however ignored in this research. Atmospheric loading effects that are not corrected for are expected to manifest as systematic effects in the estimation solutions. The magnitude of the errors induced in the pole coordinate estimates is unknown at this stage. The addition of atmospheric loading effects to the geophysical modeling part of the estimation procedure constitutes one of the future tasks outlined in the final chapter of this dissertation.

7.2.4 Antenna calibration

Among the numerous errors that contaminate pseudo-range or carrier-phase measurements, the contribution from phase center variations and phase center offsets has become one of the most critical for high-precision, GPS-based geodesy.

Once a GPS observation is corrected for the receiver and transmitter clock biases as well as for phase biases and path delays, the residual observable corresponds to the range between the electrical phase center of the receiving antenna and that of the GPS satellite transmitter antenna in view. The phase center of a GPS antenna is not a physical point, but rather a virtual floating point whose exact location depends on the direction of the incoming satellite signal and the interaction of that signal with nearby reflectors. As a result, the actual location of this reference point can vary by several centimeters depending on the elevation and azimuth angles of the line of sight.

The total phase center contribution to the measured range is made of two components: an offset and angle-dependent variations. The phase center offset is defined as the vector between the antenna reference point (the actual external point that can be physically measured to) and the mean phase center. The phase center variations (PCV) are line-of-sight-dependent variations in the location of the actual phase center.

To guarantee the high accuracy of its delivered products, the IGS has created cali-bration files (or maps) for the receivers as well as the antenna arrays onboard satellites. The former ones are referred to as the IGS robot antenna calibrations (also referred to as robot maps hereinafter) and the latter are simply called IGS transmitter antenna calibrations. Both sets of antenna calibrations are coupled so that their joint use should increase the precision of the estimated products. Robot maps are available through the IGS and are produced by absolute calibration of GPS receiver antennas. There exist as many robot maps as different antenna types, so that the phase center corrections are the same for all the stations that have the same type of antenna (and radome), regardless of their surroundings or location.

A second class of transmitter antenna calibrations has been created at JPL using data collected by the GRACE (Gravity Recovery And Climate Experiment) twin satellites ([98], [99]). The transmitting antenna calibrations used for this research are the so-called block-averaged GRACE maps. They contain values of the phase center variations ave-raged per GPS block (Block II/IIA and Block IIR). The procedure employed to generate the calibration files is described in [97] for example. When applied in this research, the GRACE-based transmitter antenna calibrations are associated with the IGS receiver antenna calibrations.

Likewise, a second class of receiving antenna calibrations, referred to as the Mesa maps, is available. This set of calibrations was created in 1992 to support the TOPEX/Poseidon mission and is specific to ground choke-ring antenna. The antenna phase, amplitude and group delay measurements used to produce the calibration file were taken at the JPL Mesa West Antenna Range. The apparatus, measurement procedure and data analysis of the Mesa experiment are synthesized in two inter-office memoranda ([68], [67]). When used, these calibrations are paired with the GRACE-based maps.

7.2.5 Miscellaneous advanced features

In addition to the dynamic, geometric and geophysical modeling specified above, several other corrections are considered and applied to guarantee a level of accuracy adequate for geodetic purposes. The most important categories of corrections and the effects they aim at mitigating are listed below.

- Higher-order ionosphere correction

Higher-order ionospheric effects are of concern for the determination of high-precision pole coordinates since they impact both the satellite and receiver positions at the centimeter level. Correcting for the second-order terms is particularly important when investigating the sub-daily variability of polar motion since the errors on the obser-vables are characterized by a strong diurnal signature. The periodic nature of the error originates in the diurnal variations affecting the integrated electron density above the GPS receivers, as shown by Kedar et al. in [120].

- Yaw rate estimation

In each strategy, a constant yaw rate is solved for. The estimation of that parameter is key to the precision of the final solution when eclipsing satellites are present in the estimation arc. Adjusting yaw rate in the estimation procedures accounts for the fact that the GPS satellite yaw attitude during eclipse or penumbra deviates from its nominal value. Ignoring that effect influences both the measurement model and the orbit and results in a degraded accuracy level of the solution [116]. Note that estimating the yaw rate parameter is sometimes insufficient. Indeed, in a few cases, the solution is compromised due to eclipse or penumbra periods occurring during the estimation arc. In those instances, the decision was taken to remove the satellites in shadow from the solution and to entirely re-process the troublesome arc.

- Antenna thrust modeling

The antenna thrust model completes the set of non-conservative force models which comprises block-specific SRP models [8] and an Earth albedo model that compensates for thermal radiation caused by sunlight reflected by the Earth's surface. Antenna thrust effects denote erroneous biases in the radial component of the GPS satellite orbits due to electromagnetic radiation resulting from the GPS signal emission. This effect has been modeled by Ziebart et al. [208]. It is corrected for in the estimation strategies tested for this work although the impact on the determination of polar motion is very likely negligible.

- Resolution of phase ambiguities

A short study showed that resolving phase ambiguities is essential to the correct recovery of the variations in polar motion induced by ocean tides in the semi-diurnal band. If there was already evidence in the literature that fixing the phase ambiguities always strengthens the overall solution, it is clear on Fig. 7.1 that bias-fixing is needed to accurately determine polar motion variations with a period identical to that of the GPS satellite orbits. This effect can be observed independently of the dynamical strategy used; which is why we only show the results obtained from a spectral analysis of the time series output using one of the candidate strategies.

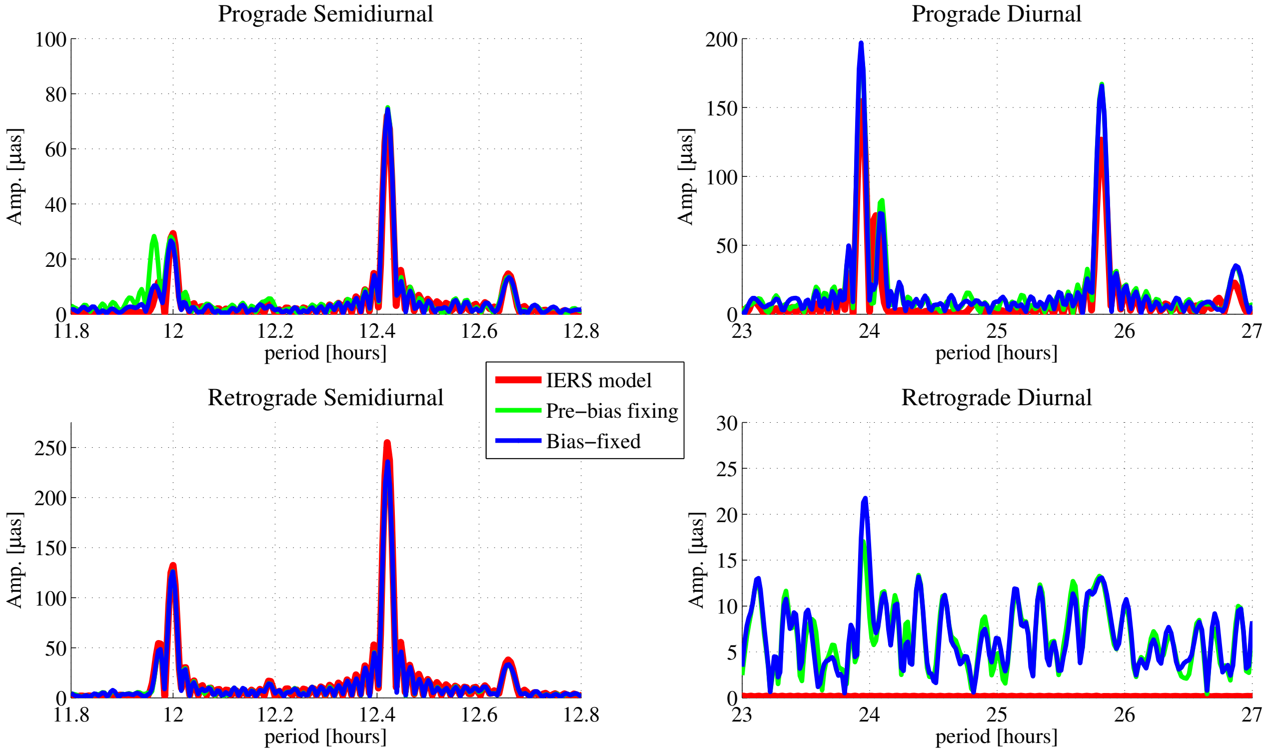

Figure 7.1: Impact of ambiguity resolution on prograde and retrograde spectra of tidally-induced polar motion

- General relativistic effects

The effects of general relativity on the observations are accounted for, which is the default for high-precision GPS-based geodetic applications in GIPSY.

7.2.6 Data sampling, weighting and inclusion

The observations, collected every 30 seconds in the RINEX files, are, by default, decimated to every 5 minutes for the phase measurements and smoothed for the code measurements prior to the fitting. A short study was conducted to determine the impact of the data rate on the estimated pole coordinate series. The results are presented in Appendix E. The data pre-processing stage is discussed in section 7.3.

All the measurements associated with post-fit residuals exceeding a specified threshold are recorded (and not filtered, c.f. section 7.3). The post-fit residual window for the phase measurements is set to 2.5 cm while the window for the code measurements is set to 250 m. Note that in all the analyses performed on the estimation output series, every arc for which the RMS orbit overlap relative to the previous arc or the RMS of the difference with the IGS final orbits exceeded 10 cm in at least one direction of motion was removed from the final solution.

Because carrier-phase measurements are always more accurate than pseudo-range observations, the former are assigned higher data weight relative to the latter in the filter. Thus the a priori uncertainties on the phase and code measurements are set to 1 cm and 1 m respectively.

A cut-off elevation angle of 7° is used for the receivers. This corresponds to the standard value used for JPL's contributions to the IGS solutions. It is expected that the atmospheric effects should be modeled accurately enough. The cut-off elevation angle was kept fixed throughout the studies but it might be interesting to investigate the impact of this factor on the quality of the polar motion solution and more specifically on the recovery of non-tidal variations in polar motion forced by atmospheric effects.

7.3 Ground network selection process

The selection process is composed of two main steps. All the stations available on each day of the estimation arc are first vetted through a quality check. Then, a quasi-minimum energy algorithm is applied to the stations that passed the first round of the selection (see [198] for instance).

7.3.1 Data quality control

Prior to the selection of a set of stations, all the tracking data available over the duration of the specified estimation arc are pre-processed. The data are edited once and for all before the estimation procedure starts. Indeed, to save computational time, the post-fit data editing and phase break detection features available in GIPSY are disabled. To compensate for this fact, the pre-processing stage is made particularly robust in the Longarc software.

The data sanity check consists in the integrity check of the individual RINEX files, the removal of outlier measurements, the detection, flagging and repair of phase breaks and cycle slips and the recording of diverse statistical metrics in so-called engineering files. This quality control is achieved through the precise point positioning of each of the sites by means of the gd2p utility (see section 6.3.2). The broad variety of quality indices include, but are not limited to, the number of phase and pseudo-range measurements, detected phase breaks, outliers (as well as their size), the RMS value of post-fit residuals or the deviations of the site location estimates relative to their nominal values.

Based on the statistics provided in the engineering files, thresholds on the number of measurements, detected phase breaks and overall shift in station position are computed. Other thresholds, such as the maximum acceptable number of missing epochs and the maximum authorized length of data gaps, are invariant. The defined thresholds are applied to the engineering file of each site. All the sites that do not meet all the requirements specified over at least one day of the considered arc are discarded in the subsequent selection process.

In practice, to save some time, databases of engineering and so-called cleaned measurement files covering multiple years are created beforehand and are readily available. Moreover, as implemented for this research, the only quality criteria are the number of phase and range measurements. Besides, the maximum number of missing clock epochs are strictly enforced for the selection of the site that will serve as the reference clock in the estimation procedure. The set of passing criteria is voluntarily limited to avoid the degradation of the global station distribution. Indeed, good quality stations tend to be located in the northern hemisphere with clusters in North America and Western Europe. It was for example noticed that enforcing a balance in the number of stations located in the Northern and Southern hemispheres tends to be counterproductive. Paradoxically, adding the displacement of a site from its ITRF-defined location as a passing criterion in the station selection process is not necessarily optimal either, since it clearly hits the geographical distribution of the final network. The implementation of various cases and various sets of constraints stresses the delicate nature of ground network optimization.

7.3.2 Optimization algorithm

Among the sites that passed the quality control stage, 60 are picked by applying a quasi-minimum algorithm. Note that this number is reduced to 40 in the case of a 9-day solution for computational load and timing reasons. The purpose of the quasi-minimum algorithm is to create a list of the specified number of stations in such a way that they are as evenly spread over the world as possible on a given day (selected to be the central day of the arc). To do so, it will find the unique set of stations that minimizes some potential (referred to as the station energy) on that day. The energy is defined as the sum of the inverse of the distance separating each pair of stations. It is then normalized using the average station radius from the Earth's center. The ground network energy is minimized by swapping stations and the algorithm eventually converges towards the optimal set of stations after iterating on successive configurations. The algorithm is initialized with the reference clock station.
Indeed, the reference clock station is picked first, followed by the subset of fiducial sites. The selection criteria applied are more stringent in these special cases and additional thresholds are imposed. The number of missing epochs, along with the bias and drift of the clock solution, are considered when picking the reference station. The fiducial network is chosen to be optimally globally distributed and composed of the sites displaying the least root-mean-squares deviations from their reference positions.

To guarantee that the reference frame realized by the ground network will be consistent with and tied to the ITRF, a specified ratio of stations belonging to the official ITRF2005 realization of the frame is specified. Throughout this work, the ratio was set to 1, so that all the stations have to be part of ITRF2005. This decision readily results in an imbalanced distribution of stations between the two hemispheres given that the ITRF2005 contains only 70 sites in the Southern hemisphere for 268 in the Northern hemisphere [1]. The impact of the evolving network from solution to solution needs to be assessed further.

The statistics on the entire network of about 200 stations considered for the analysis are displayed on a map on the right-hand side of Fig. 7.2. Next to it, to the left, a typical ground network is shown.

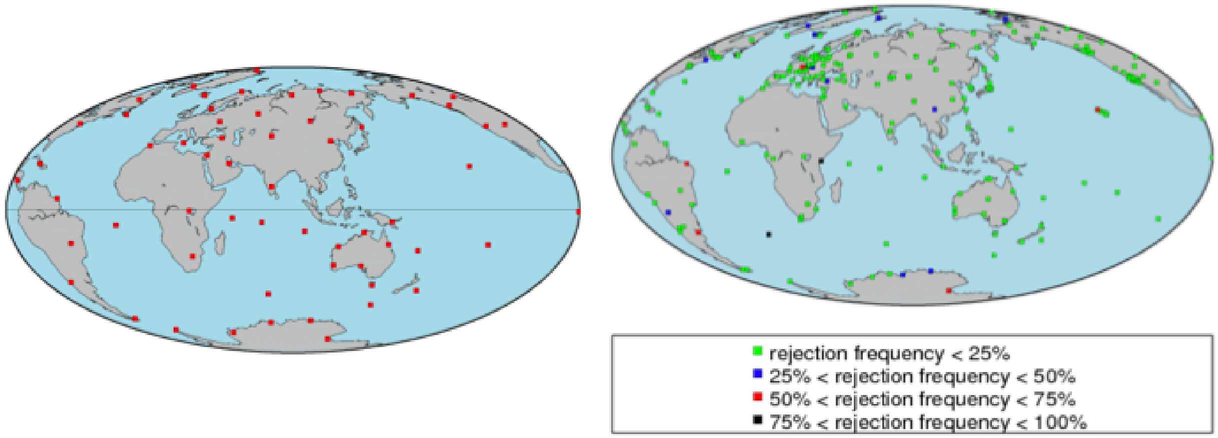

Figure 7.2: Network selection. a) Typical network b) Network status over year 2004

On Fig. 7.2a) the color code (green, blue, red and black) illustrates the statistical percentage of rejection of each site over the entire year in 25% increments.

7.4 Pole coordinates estimation interval selection

The choice of a 15-minute interval is partly dictated by the fact that the pole coordinates are modeled as piecewise constant over the update interval. In order to accurately capture the time evolution of those parameters, a short interval is needed. The impact of the batch length on the recovered pole coordinates was initially studied in the simple analysis described below.

A simple simulation was run in MATLAB considering two different sampling intervals. In one case, the x-axis component of the polar motion vector was modeled as piecewise constant over 15-minute intervals. For the second test case, the sampling rate was reduced to 2 hours. Because the sub-daily variations of polar motion are excited primarily by ocean tides, the study focused on the impact of the interval length on the recovery of the correct tidal amplitudes based on a reference model. Hence, for these simulations, a time series of the x-pole coordinates was created based on the IERS-recommended model for tidally-induced polar motion. The time series generated spanned one year starting on January 1, 2004.

Amplitude spectra were generated from the piecewise constant representation of the simulated and sampled time series. As expected, long averaging intervals fail to properly reproduce the model. The amplitude of the principal spectral lines, which are the ones of greatest interest, are particularly affected by the scaling induced by the combination of sampling and averaging steps.

Figure 7.3 shows the sub-sampling of the modeled X_p time series. The piecewise constant modeling is shown in Fig. 7.4. Fifteen-minute intervals are plotted in blue while the red curves correspond to a two-hour update interval. To enhance the readability of these two plots, the length of the time series represented is limited to 14 days. It is sufficient however to visualize the half-daily and daily patterns enveloped in a 14-day beating characteristic of the semi-diurnal, diurnal and fortnightly tides.

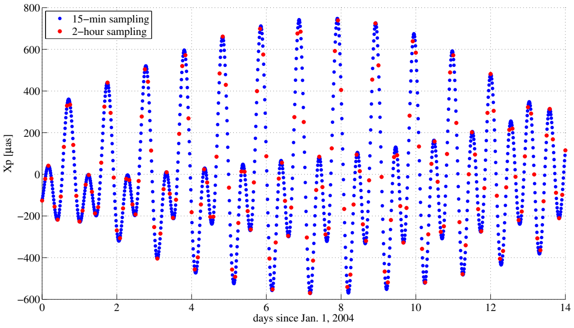

Figure 7.3: Sampling of the modeled X_p series

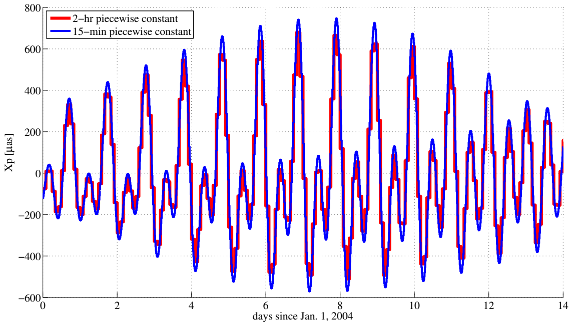

Figure 7.4: Piecewise constant modeling

The amplitude spectra obtained by the application of a fast Fourier transform are plotted in Fig. 7.5. Only the semidiurnal and diurnal parts of the spectra are displayed.

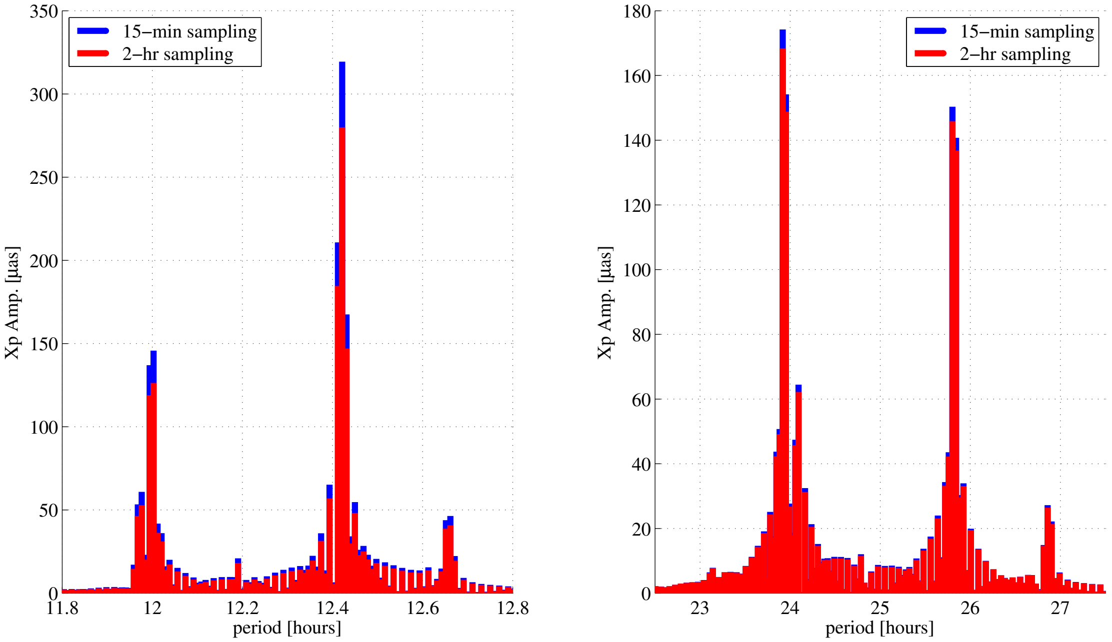

Figure 7.5: Impact of sampling interval on X_p semidiurnal and diurnal amplitude spectra: Simulation results

Based on the simulation results, update times shorter than 15 minutes would, in theory, be even more appropriate to fully recover polar motion variations over short periods. However, we found out that when the pole coordinate update interval reaches the limit of the sampling period, the polar motion solution diverges suddenly and immediately. This does not interfere with the quality of the other estimated parameters. It is believed that the system becomes suddenly unobservable since it is impossible to determine the coordinates of any ground location at the exact same epoch and rate that the observations are processed. In this case, the pole coordinates can be seen as coordinates of a site on the Earth; as a consequence, they cannot be estimated when their update frequency is equal to the data sampling rate.

Figure 7.6 confirms that when 5-minute process noise batches are used to estimate the pole coordinates, the semi-diurnal and diurnal spectra are corrupted, with a maximum amplitude of $8.6.10^4\mu$as at a period of 24h. Figure 7.6 shows the results obtained when processing actual GPS data over one year, the pole coordinate update times ranging from 5 minutes to 2 hours based on the legend included on the right-hand side subplot. Note that this experiment was setup using the

FlinnR-like strategy based on a 40-station network and without bias-fixing.

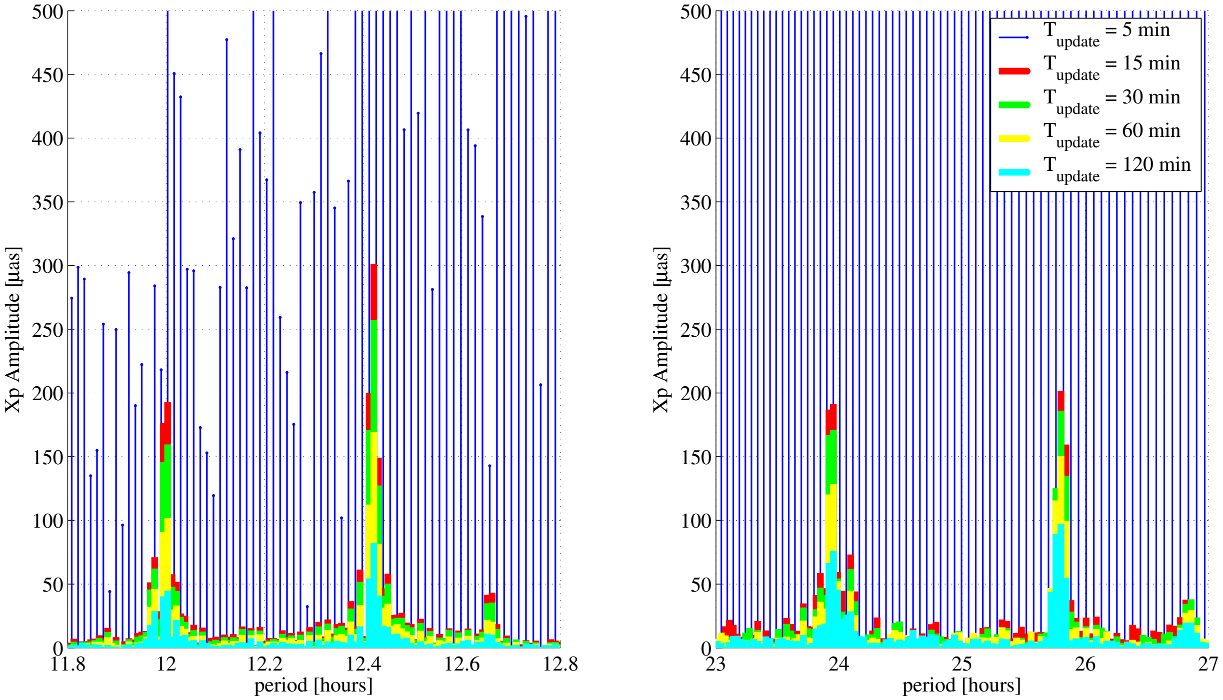

Figure 7.6: Impact of sampling interval on X_p semi-diurnal and diurnal amplitude spectra: Actual results

A correlation analysis showed that when the update period of the pole coordinates parameters become equal to the data sampling rate, the states of all the GPS satellites become highly correlated with the pole coordinates. This is illustrated in Fig. 7.7, a graphical representation of the correlation matrix computed at the end of the orbit determination arc. The correlation coefficients are indicated by the colorbar. Fig. 7.8, also displayed below, is a close-up of Fig. 7.7 that focuses on the specific correlations between polar motion and all of the other parameters appearing in the estimation procedure. This phenomenon has also been observed for other values of the data rate as discussed in Appendix E. Hence, we deduce that the sampling rate of the observations imposes a limit on the maximum frequency update of the pole coordinates.

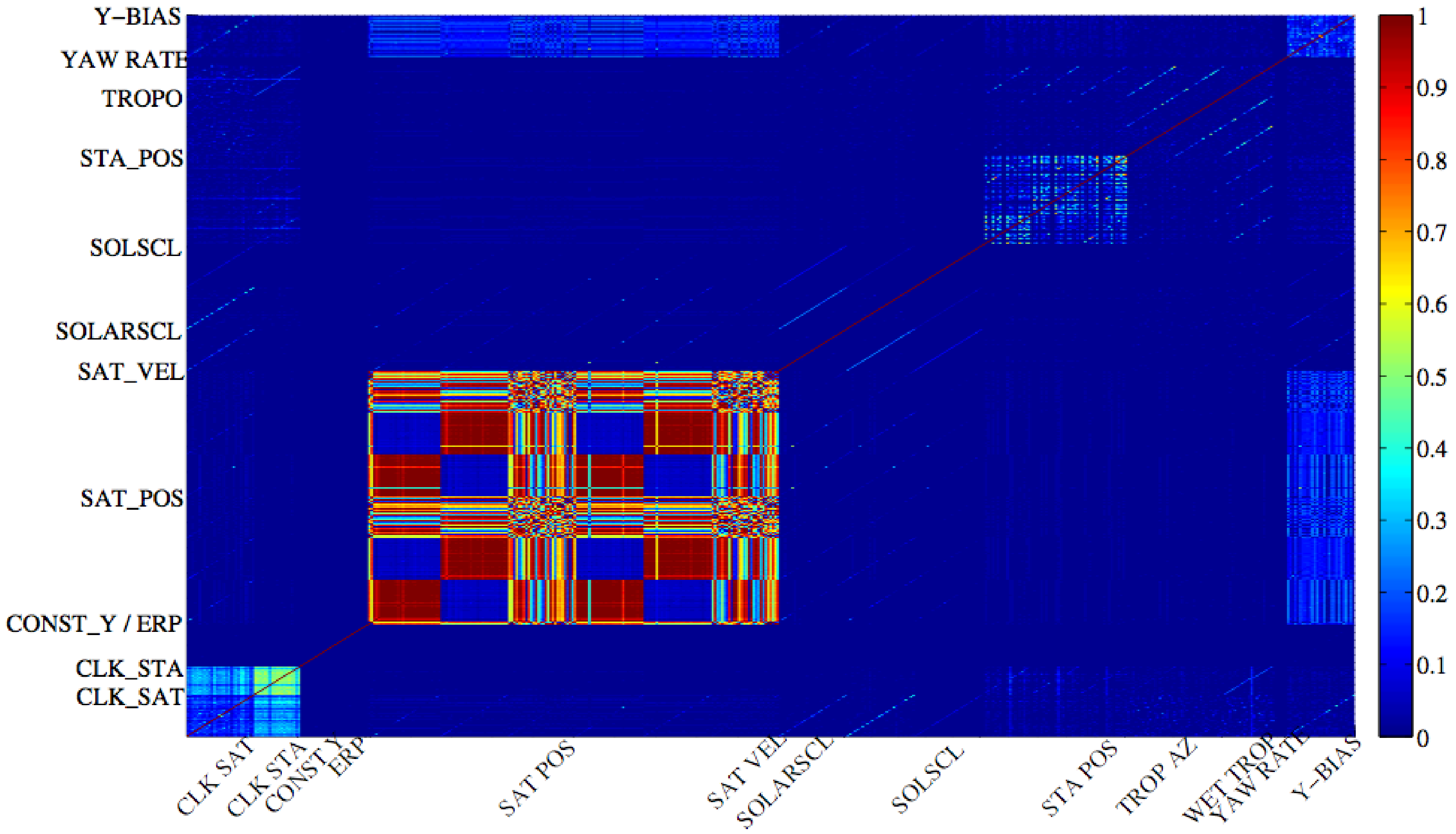

Figure 7.7: Correlation matrix for T_{update} = *data rate* = 5 *minutes*

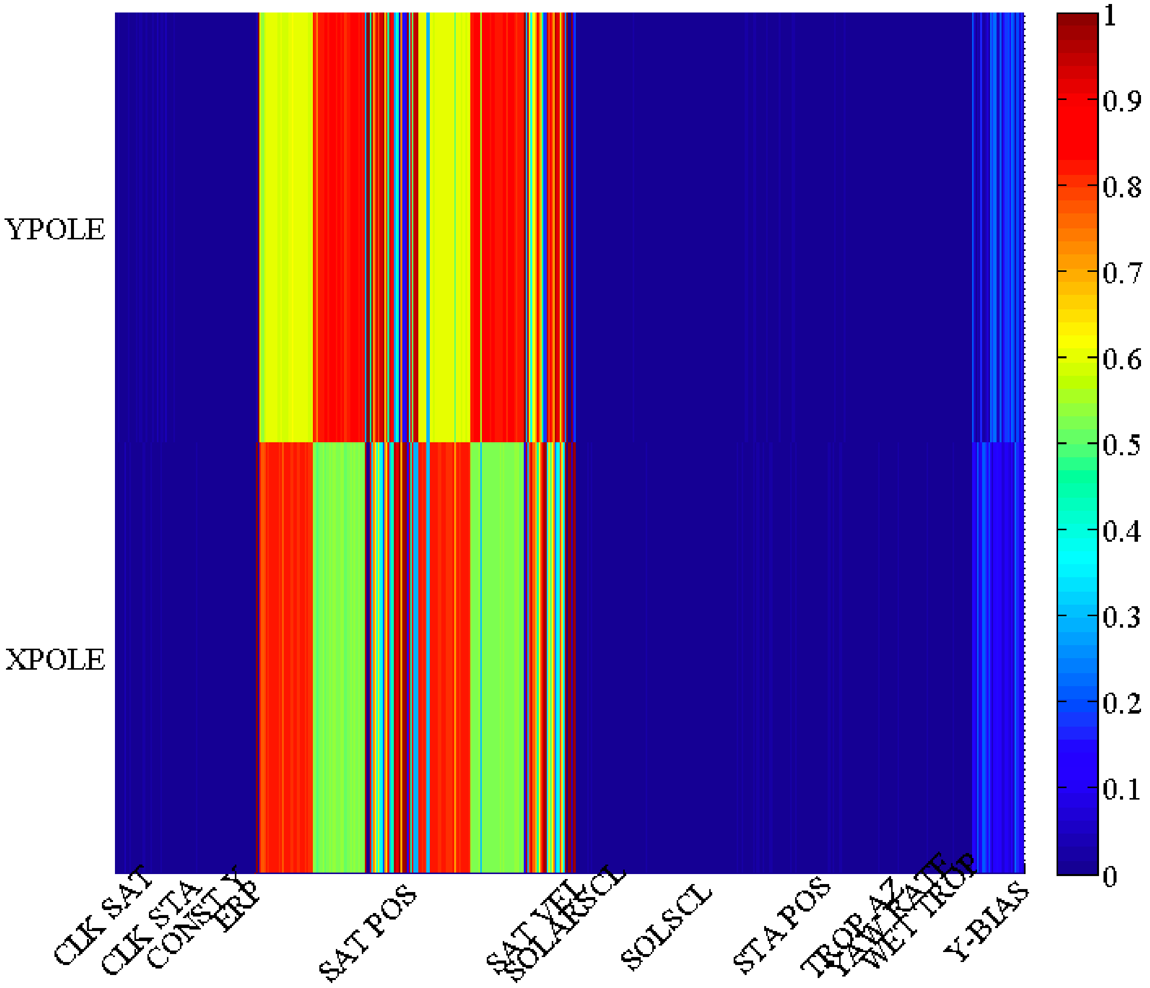

Figure 7.8: Zoom on polar motion related correlation coefficients

7.4.1 Comparative study

A full year of data was processed using the 30-hour strategy setup and varying the pole coordinates estimation interval between 7 minutes and 15 minutes. The upper limit of this interval was chosen based on Fig. 7.6 while the lower bound is dictated by the data rate (see Appendix E). The decision to focus on the 30-hour strategy for this study is purely for the sake of minimizing the computational time and load. Pole overlaps were computed and the amplitude spectra of the prograde and retrograde formal errors were generated to evaluate the level of noise and detect any systematic error, respectively. Pole overlaps are computed by taking the difference between two consecutive pole coordinate solutions coinciding by 6 hours in the case of the Flinn-like strategy and 2 days in the case of the Longarc-type strategies. Note that in the latter case, the overlaps are computed over 24 hours. Preliminary results based on the error analysis of the polar motion time series are presented here while the impact of the pole coordinate estimation interval on the recovery of geodetic signals is treated in Chapter 9.

Table 7.3 contains the yearly RMS value of the pole overlaps for all 4 test cases. The number of samples entering the statistics shown in the table is not the same in each case due to the way the overlaps are computed. The size of the overlaps visibly drops as the estimation interval lengthens.

		Pole Overlaps [μ**as**]	
		$\mathbf{X}_p$	$\mathbf{Y}_p$
Pole coordinates Update interval	**7 min**	456.4	420.3
	10 min	382.9	233.6
	12 min	345.3	299.1
	15 min	332	263.9

Table 7.3: Impact of polar motion update frequency on the RMS value of pole overlaps

Figure 7.9 shows the prograde and retrograde spectra of the pole coordinates formal errors depending on the length of the batch. Both spectra are identical, which means that systematic errors affecting the pole coordinate determination are the same for both coordinates. The magnitude of the systematic errors peaks for both components at periods corresponding to half the arc length and the arc length for reasons explained in section 7.5. The amplitude of the semi-diurnal spectral line increases as the estimation interval shortens whereas the diurnal peak simultaneously tends to get smaller. For a 15-minute update interval, the peaks almost have the same magnitude in both the diurnal and the semidiurnal frequency bands.

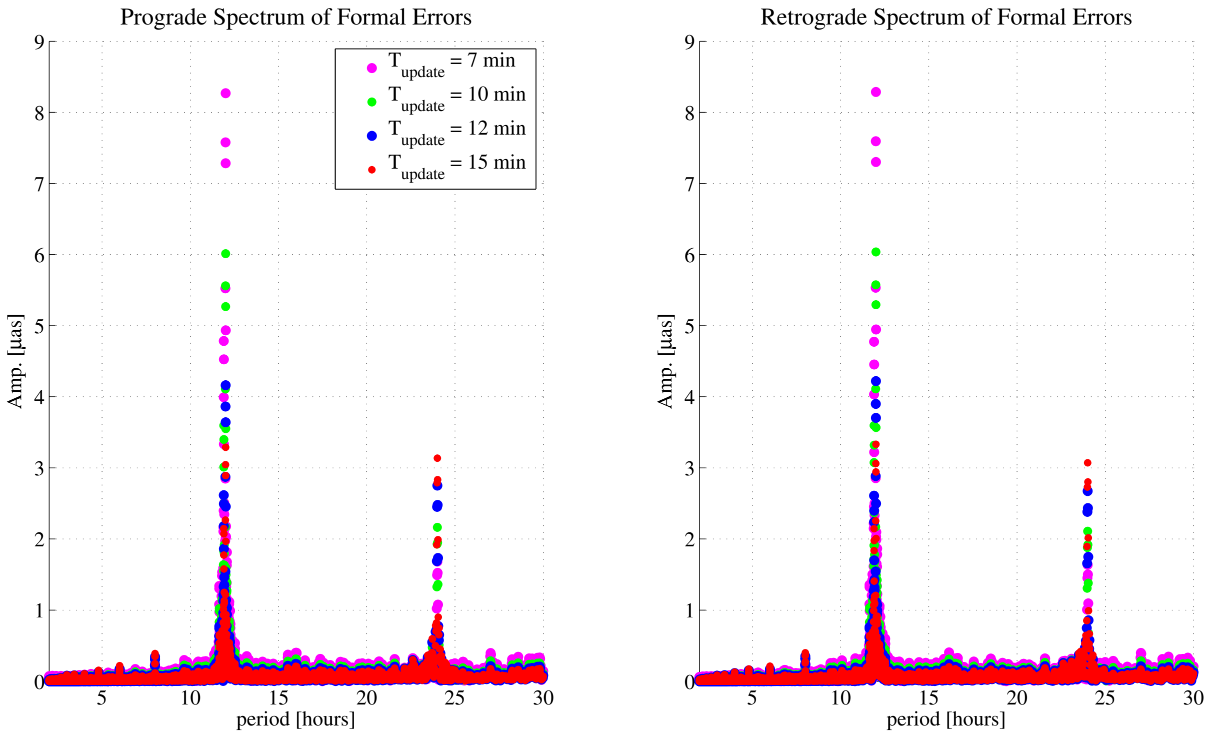

Figure 7.9: Impact of polar motion update frequency on pole coordinate systematic errors spectrum

Considering the results shown above, 15-minute intervals are considered optimal for the recovery of polar motion using GPS data. Therefore, this number is used as the default in the remainder of this dissertation unless stated otherwise. However, depending on the geophysical process under investigation and the level of accuracy desired, the pole coordinate update period can be varied based on the study on data rates conducted in Appendix E and accounting for the fact that the update frequency should always remain lower than the data sampling rate.

7.5 Arc length selection

7.5.1 Considerations relevant to dynamical modeling

The significance of long arcs is discussed in section 6.3.1. To summarize, the longer the estimation arc, the better constrained the satellite dynamics are but the more complex the force model gets. It is therefore expected and verified that systematic errors are amplified as the length of the arc increases.

7.5.2 Considerations related to the estimation of polar motion

The length of the estimation arc has a natural filtering ability with respect to retrograde diurnal polar motion according to Eubanks [70]. Using multi-day estimation arcs should theoretically be equivalent to applying a band-rejection filter with a bandwidth roughly inversely proportional to the duration of the arc and centered on −1 cycle per day to the estimated polar motion signal.

The bandwidth of such filter corresponds to the region of the polar motion spectrum absorbed by the estimation analysis. It can be related to the Rayleigh criterion for the separation of two spectral lines. This criterion states the minimum resolvable frequency difference. Thus, the minimum time period Δt required to resolve any two frequencies f_1 and f_2 is written:

$$\Delta t = \frac{1}{f_1 - f_2} \tag{7.1}$$

Starting from Eq. 7.1 and considering two periods T and $T + \delta T$, the bandwidth of periods that can be fully de-correlated over the time span Δt is given by:

$$\delta T > \frac{T^2}{T + \Delta t} \tag{7.2}$$

Applying Eq. 7.2 in the context of orbit determination of interest, T represents the diurnal period, Δt the estimation arc length and δT the bandwidth of the band-rejection filter mentioned at the beginning of this section. Clearly, as noted by Eubanks, the bandwidth is nearly inversely proportional to the arc length and the filter belongs to the band-rejection category due to the strict inequality in Eq. 7.2.

It is not exactly clear where the retrograde diurnal signal is being absorbed in that context.

7.5.3 Comparative study

A full year of data was processed using the HCL estimation strategy described in the second bullet of section 7.2.1 and varying the arc length between 30 hours and 9 days. Similar to what was done to study the impact of the update interval, overlaps were computed and the periodograms of the prograde and retrograde formal errors were generated to evaluate the magnitude of random and systematic errors affecting the polar motion solution. Note that some systematic errors are immune to a characterization by both an overlap and a formal error study. Again, preliminary results based on the error analysis of the polar motion time series are discussed here while the impact of the orbit determination arc length on the recovery of geodetic signals is treated in Chapter 9.

Table 7.4 gathers the RMS values of the pole overlaps over the entire year processed.

		Pole Overlaps (6h) [μas]		**Pole Overlaps (24h)** [μas]	
		X_p	Y_p	X_p	Y_p
Estimation Arc length	**30 hours**	349.4	319.7	N/A	N/A
	3 days	99.9	109	129.4	129.7
	5 days	173.8	166.6	173.2	166.2
	7 days	197.9	162.7	196.6	188.5
	9 days	237.2	206.4	288.7	245.4

Table 7.4: Impact of arc length on RMS value of pole overlaps over one year

Table 7.4 and Figure 7.10 both indicate that 3-day arcs show the least noise and the fewest systematic errors. This error analysis also reveals the limitations of the 1-cpr custom acceleration parameterization and estimation for 30-hour and 9-day arcs. The 9-day arc solution in particular is remarkably noisy and plagued by systematic errors, which stresses the difficulty in achieving accurate force modeling over long periods.

Figure 7.10 shows the periodograms of the formal errors in each case.

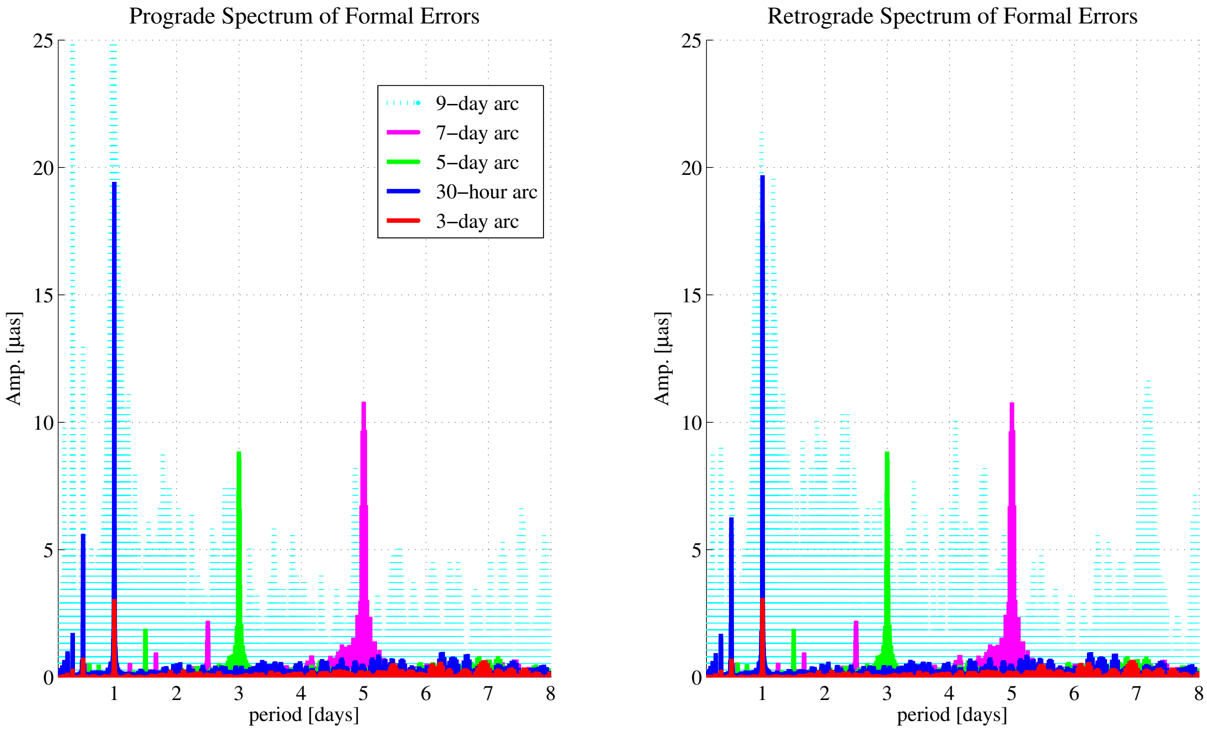

Figure 7.10: Impact of arc length on pole coordinate systematic errors spectrum

As visible on the amplitude spectra, the amplitude reaches its maximum at periods matching the actual solution arc length (which is equal to N-2 days where N is the length of the orbit determination arc) in all cases. This phenomenon is related to discrepancies in the realization of the terrestrial reference frame from one arc to the next, discrepancies that arise from changes in the global distribution of stations. Peaks of lower magnitude also occur at periods equal to half the arc length everytime. These peaks could also be due to orbit error discontinuities. It would be interesting to investigate whether these peaks would disappear if the same network was used from one solution to the next. This could be the object of a small-scale study in the future.

An extensive analysis of the three complete solutions and the evaluation of their quality are reported in the next two chapters.

Chapter 8

Performance Analysis

8.1 Introduction

This chapter describes the various tests performed to evaluate the quality of each category of time series obtained through the different estimation procedures. In the chapter that follows, each strategy is further analyzed in terms of its capability to recover geodetic signals such as ocean tides, oceanic and atmospheric circulations and the effects of earthquakes. This chapter focuses on the overall quality of each of the solutions by analyzing not only the pole coordinate solutions but also the orbit, clock and station coordinate solutions. Results from covariance analyses, overlap analyses and several other post-processing studies are shown. Preliminary conclusions are drawn regarding the superiority of one of the candidate strategies over the two others.

8.1.1 Experimental data set

To evaluate the performances of each of the strategies implemented, GPS observations covering one year were reprocessed. The year 2004 was chosen. The initial attempt was to reprocess two years of data centered around the Sumatra earthquake event that occurred on December 26, 2004. For computational reasons, the focus was then set on the first year of the two-year data set. The decision to process a full year of data was initially driven by the requirements imposed on duration in order to perform meaningful tidal analyses. Indeed, based on the Rayleigh criterion applied to the P1/K1 and S2/K2 pairs of tides, at least six months of data are needed to separate each of the eight principal ocean tides. A collection of more recent data was analyzed less extensively; the corresponding results, presented in [174], are included in Appendix G for completeness.

A 60-station ground network was used, except for the 9-day arc strategy, for which the number of sites was reduced to 40. 25% of the stations were fixed to their a priori coordinates over each estimation arc. These numbers were originally picked at random but a short study, presented in Appendix D, was later conducted based on a month of data. The objective of this study was to evaluate the impact of the number of stations and percentage of stations fixed on the station distribution, computational time and precision of the pole coordinate estimates. The analysis demonstrated that using 60 stations and fixing a quarter of the sites to their nominal coordinates was satisfactory in terms of timing, accuracy and precision. Details on the network selection process are gathered in section 7.3.

To obtain series spanning the entire year, 30-hour arcs are shifted by one day while N-day long arcs ($N \geq 3$) are shifted by $N-2$ days. For runs based on the FlinnR-like and 3-day strategies, the central day of the 30-hour and 3-day arcs, respectively, are accumulated to form the final year-long time series. Likewise, the overall solution is composed of the central week of each individual solution when the 9-day strategy is employed.

Arcs that simultaneously exhibit orbital overlaps and differences with the IGS final orbits larger or equal to 10 cm together with suspiciously large pole overlaps are first reprocessed excluding the satellites in shadow and penumbra from the constellation. If the reprocessed arcs still do not comply with the passing criteria, they are eliminated from the solution, as mentioned in Chapter 7. This editing technique is potentially not restrictive enough in the case of the 9-day strategy since the value for one of the internal metrics can be reasonable even when the values for the other two metrics are exceeding the set thresholds. When applicable, the number of arcs ignored in the calculation of the performance metrics is indicated in the remainder of the thesis.

8.1.2 Performance metrics

The quality of a solution can be assessed in three ways:

1. by evaluating its internal consistency,

2. by comparing it to a solution obtained independently, i.e. using different software packages, strategies and possibly different geodetic techniques in this case,
3. by inter-comparison of solutions generated using the same software and data but different estimation strategies.

The first approach requires the definition of internal performance metrics while external metrics are employed for the other two approaches.

The overall quality of the solution needs to be assessed in order to verify that the orbits, clocks and coordinates of the pole and ground stations are all determined in a consistent manner. In this chapter, individual analyses of each component of the solutions are conducted. Table 8.1, placed at the end of this chapter, lists the metrics traditionally employed to assess the quality of each type of solution. The chapter that follows, Chapter 9, covers the performance evaluation of the solutions in terms of their ability to capture various kinds of geodetic signals.

8.2 Orbit Determination solution

8.2.1 Internal metrics: orbit overlaps

The consistency of the orbit solution is first verified by computing orbit overlaps. In the case of the FlinnR-like strategy, two adjacent estimation arcs overlap for 6 hours only. To mitigate edge effects that would potentially give a pessimistic measure of the orbit precision, 30 minutes are removed at both ends of the 6-hour overlap period, so that the internal orbit overlaps are actually computed over a period of 5 hours.

In contrast, arcs covering three days or more are designed to overlap over two days. To ensure a relatively fair comparison, the orbit overlaps are computed in two ways in the latter case.

1. Overlaps are first computed over a period of 5 hours starting at the beginning of the total overlap period to imitate what is done for the FlinnR-like orbits.
2. Overlaps are also calculated over a period of 24 hours central to the 2-day overlap

period.

The first situation represents a worst case for arcs longer than 3 days because the bow-tie effect tends to be aggravated over long arcs. The second method, on the contrary, typically yields an optimistic measure of the precision of the solution.

Sketches in Figs. 8.1a and 8.1b summarize the different time spans considered for the calculation of the overlaps for each of the three strategies.

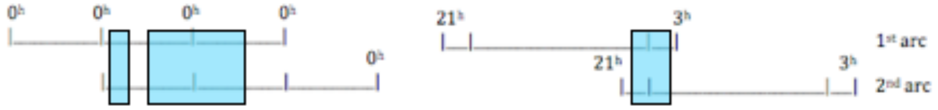

Figure 8.1: Orbit overlaps. a) for arc length ≥ 3 days b) for arc length < 3 days

Overlaps are computed for all three components of the satellite position vectors expressed in the HCL coordinate system. The results are reported in Table 8.2. The values correspond to the yearly average of the daily root-mean-squares overlap values and standard deviation about these mean values. An overall overlap value is also indicated and referred to as the 1D-RMS value.

			Nominal	**30-hour**	**3-day**	**9-day**
Orbit Overlaps [cm]	**H**	**5h**	2.76	2.55±0.62	1.86±0.64	1.70±0.47
		24h	N/A	N/A	1.04±0.67	2.01±0.79
	C	**5h**	2.89	1.99±0.41	3.67±1.81	2.73±1.73
		24h	N/A	N/A	1.40±0.78	2.98±1.37
	L	**5h**	3.33	2.25±0.54	5.15±1.77	3.25±3.39
		24h	N/A	N/A	1.91±0.53	4.2±3.2
	1D-RMS	**5h**	3	2.30±0.44	3.88±1.32	2.71±2.1
		24h	N/A	N/A	1.53±0.43	3.26±1.97

Table 8.2: Inter-comparison of orbit solutions based on overlap RMS values

It is noteworthy that only 52 values contributed to the overlap calculation in the case of the 9-day strategy due to the use of 9-day arcs shifted by 7 days. In contrast, the yearly average shown for the 30-hour (FlinnR-like) and 3-day strategies included 365 overlap values. Rather unexpectedly, 24-hour overlaps are significantly larger than 5-hour overlaps in the case of the 9-day strategy. The reason has yet to be determined. In addition, if the outlier flagging mechanism solely depended on the 10-cm threshold set on orbit overlaps, 3 arcs (i.e. 3 weeks) would have to be removed from this solution; which explains the larger values in the cross-track and in-track directions. In comparison, the other two solutions are free of such outliers, although a couple of days necessitated the removal of all the satellites in shadow.

Based on the analysis of Table 8.2, it is difficult to distinguish whether one of the strategies yields orbits that are more internally consistent than the other two. Indeed, if both Longarc-type strategies provide orbits that are more precise in the radial direction than the FlinnR-like strategy; the opposite is true in the other two directions of motion. Besides, if the orbits output by the 9-day strategy appear more consistent than those obtained by means of the 3-day parameterization, this statement needs to be qualified considering the degradation of the measure for longer overlap periods as well as the lower number of samples used in the statistical analysis, both occurring in the former case. Overall, given that orbit overlap values routinely amount to about 3 centimeters for the operational Flinn products (as reported in the ”Nominal” column of Table 8.2), the determination of polar motion as a stochastic process and at high temporal resolution apparently leads to a slight deterioration in the POD accuracy, except when the FlinnR-like strategy is used.

Prior to the computation of the overlaps, a 7-parameter Helmert transformation was applied to the second of the two adjacent orbit solutions to remove any inconsistency in the realization of the reference frame. Because a fixed-network is used, the day-to-day inconsistencies in the realization of the reference frame should be minor. In practice, the discrepancies between pairs of orbit solutions (transformed vs. original, i.e. not transformed) average to a maximum of 4 mm in the cross-track and in-track directions over one year as demonstrated in Table 8.3. These small misalignments translate into systematic errors in the polar motion solution as discussed in section 7.5.3.

			30-hour	**3-day**	**9-day**
Orbit Overlaps [cm]	**H**	**Transformed**	2.62	1.24	2.24
		Original	2.64	1.24	2.23
	C	**Transformed**	2.04	1.46	3.27
		Original	2.39	1.63	3.67
	L	**Transformed**	2.32	1.98	5.26
		Original	2.72	2.15	5.39
	1D-RMS	**Transformed**	2.34	1.59	3.80
		Original	2.59	1.71	3.98

Table 8.3: Impact of 7-parameter transformation on overlap RMS values

8.2.2 External metrics: comparison to IGS orbits

As an external metric for accuracy, the orbit solutions are compared with standard, independent solutions for each day of the year processed. The IGS final orbits served as reference orbits for this work. Prior to the computation of the differences between the two orbit solutions, any reference frame inconsistency is eliminated through a 7-parameter transformation. On each day, the estimated orbits are transformed into the same reference frame the IGS final orbits are in.

The results of the comparison are gathered in Table 8.4. As in Table 8.2, the values presented correspond to the average daily RMS value over one year and the dispersion around it.

		Nominal	**30-hour**	**3-day**	**9-day**
Difference with IGS [cm]	**H**	3.7	3.2±0.74	2.88±0.49	3.16±0.71
	C	4.12	3.66±0.48	3.60±0.40	4.81±1.61
	L	4.49	3.64±0.48	3.72±0.36	5.38±3.78
	1D-RMS	4.12	3.52±0.48	3.43±0.30	4.45±2.23

Table 8.4: Inter-comparison of orbit solutions based on difference to IGS final orbits

Based on Table 8.4, the 3-day strategy appears to yield the most consistent orbits. In contrast, the orbits obtained using the 9-day estimation procedure are the furthest from the IGS solution. This can be partially explained by the fact that 10 weeks of estimates would be excluded from the calculations based on the passing criterion specific to the difference with the IGS solution.

8.2.3 Impact of arc length on orbit accuracy

To evaluate the impact of the arc length on the precision and accuracy of the orbit solution, the HCL strategy, nominal for 3-day arcs and also referred to as the 3-day estimation strategy in section 7.2.1, was tested with various arc lengths, from 30 hours to 9 days. One day had to be excluded from the 30-hour arc solution. It is noteworthy for the interpretation of the results shown in Table 8.5 that, as the length of the arc increases, fewer samples enter the overlap statistics.

		30 hours	**3 days**	**5 days**	**7 days**	**9 days**
Orbit Overlaps [cm]	**H**	1.50	1.23	1.17	1.40	1.87
	C	1.75	1.46	2.39	2.94	3.92
	L	2.10	1.98	3.2	3.98	5.60
	1D-RMS	1.80	1.59	2.4	2.97	4.09
Difference with IGS [cm]	**H**	3.13	2.92	2.53	2.56	2.63
	C	3.81	3.62	3.80	4.04	4.37
	L	3.64	3.74	3.58	3.72	3.97
	1D-RMS	3.54	3.45	3.35	3.50	3.73

Table 8.5: Impact of arc length on OD solution

The large overlap value for the 9-day arc case is caused by the presence of an outlier in the series. From that standpoint the evolution of the comparison to the IGS final orbit may be more meaningful. The 3-day solutions appear to have a better internal precision than the other solutions but the 5-day solutions seem the most consistent when the IGS final orbits are employed as the true solutions.

8.2.4 Impact of pole coordinate estimation interval on orbit accuracy

Analogously, the update frequency of the pole coordinates is studied with regards to the orbit determination solution accuracy and precision levels. To this end, the setup established in section 7.4.1 was employed. The statistical results for both the orbit overlaps and the comparison to the IGS final solutions are displayed in Table 8.6.

		7 min	**10 min**	**12 min**	**15 min**
Orbit Overlaps [cm]	**H**	2.37	2.37	2.37	2.37
	C	2.17	2.16	2.15	2.16
	L	2.41	2.40	2.40	2.39
	1D-RMS	2.32	2.31	2.31	2.31
Difference with IGS [cm]	**H**	3.08	3.08	3.08	3.08
	C	3.78	3.78	3.77	3.77
	L	3.66	3.66	3.65	3.65
	1D-RMS	3.52	3.52	3.51	3.51

Table 8.6: Impact of pole coordinate update interval on OD solution

It can be concluded from the analysis of the table above that the impact of the pole coordinate estimation interval on the quality of the orbit solution is not statistically significant.

The results obtained in terms of internal orbit overlaps and from the comparison with the IGS orbits give some confidence that the solutions are of acceptable quality. The pole coordinates series are analyzed next.

8.3 Polar Motion Solution

8.3.1 Covariance analysis

A covariance analysis was carried out on the time series of pole coordinate estimates. The time series of pole coordinate estimates and their associated uncertainties obtained with each of the candidate strategies are plotted in Figs. 8.2 a), b) and c) on the next page. In addition and analogously to the orbit solutions, the internal precision of each pole coordinate solution was assessed by means of so-called pole overlaps computed in the same fashion as their orbital equivalent. Figures 8.3 a) through c), placed on the next page, display overlaps for both pole coordinates along with the correspon-ding $\pm 3\sigma$ boundaries. Pole overlaps for arcs longer than 30 hours are computed over 24 hours in an attempt to mitigate the severe edge effects observed on the 9-day solutions. The overlap values obtained for this strategy remain nonetheless very large as shown in Table 8.7. Computing the pole overlaps over a full day for every arc also serves the purpose of increasing the number of samples for use in the statistical analyses.

Figure 8.2: Time series of GPS-based pole estimates and 3σ boundaries. a) 30-hour strategy b) 3-day strategy c) 9-day strategy

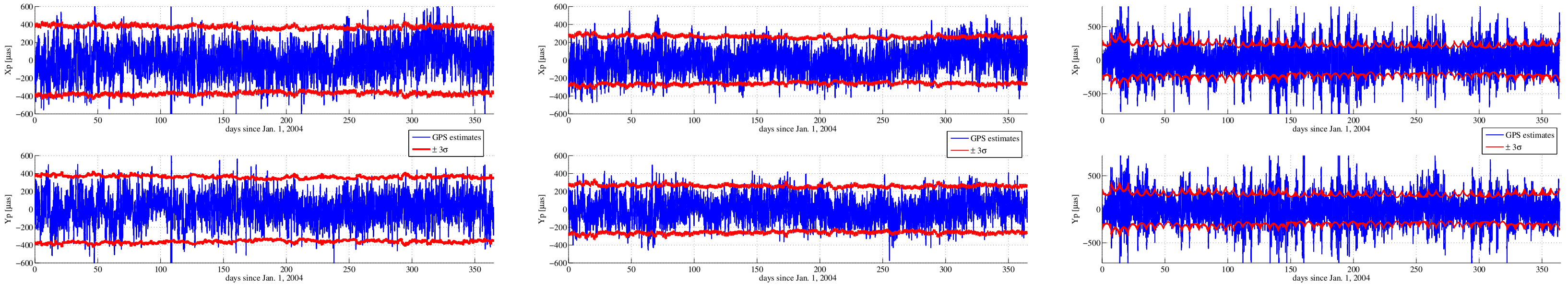

Figure 8.3: Time series of pole overlaps and 3σ boundaries. a) 30-hour strategy b) 3-day strategy c) 9-day strategy

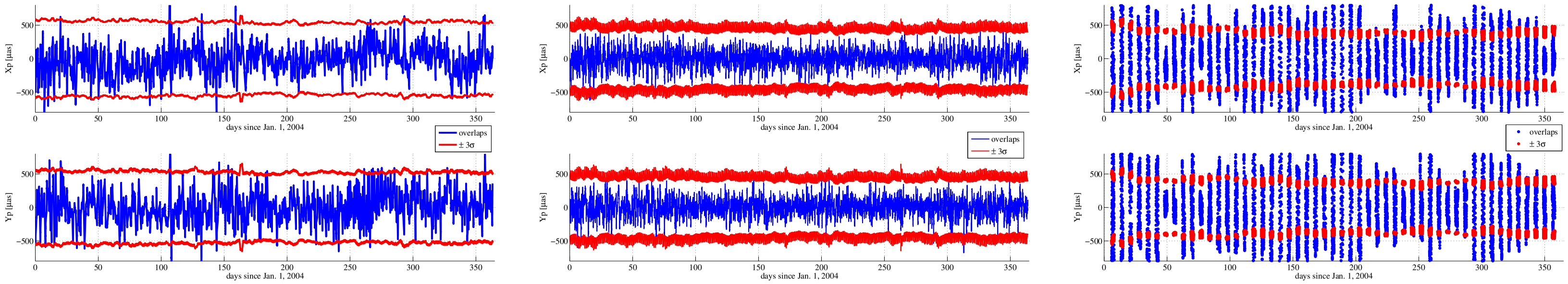

The uncertainty curves overlaid on Figs. 8.2 and 8.3 are calculated from the formal errors of the two adjacent solutions considered by following the law of error propagation written here as a reminder.

Considering f, a function of two arguments a and b, the uncertainty of f given the variance-covariance matrices associated with the estimation of the parameters a and b is written:

$$\sigma^2_{f(a,b)} = \left(\frac{\partial f(a,b)}{\partial a}\right)^2 \sigma^2_a + \left(\frac{\partial f(a,b)}{\partial b}\right)^2 \sigma^2_b + 2\,\frac{\partial f(a,b)}{\partial a}\,\frac{\partial f(a,b)}{\partial b}\,\mu_{ab} \tag{8.1}$$

In Eq. 8.1, the parameters σ^2 denote the variances of the variables and μ represents the covariance between the two variables.

Overall the pole coordinates are well determined when the 30-hour and 3-day arc strategies are used. The signal-to-noise ratios (SNR), computed as the ratios of the RMS of the GPS-based pole estimates to the RMS of the internal pole overlaps, are however extremely low for all three cases and barely exceed one in the case of the 3-day arc strategy only. This is explained by the fact that the estimates under investigation actually correspond to residuals with respect to the nominal polar motion series. The low SNR values essentially suggest that the recovery of geodetic signals of low amplitude buried within those residuals may be challenging. The overall poor performance of the 9-day arc strategy is mostly due to the presence of a large retrograde signal in the diurnal band as confirmed by Table 9.3 and discussed in section 9.1.1. All the results commented here are summarized in Table 8.7.

	30-hour		**3-day**		**9-day**	
	X_p	Y_p	X_p	Y_p	X_p	Y_p
Bias [μ**as**]	15.55	62.19	7.72	77.91	-39.72	12.06
RMS of GPS-based pole estimates [μ**as**]	171.8	154.2	137.8	126.8	225.9	222.5
RMS of internal pole overlaps [μ**as**]	225.1	241.8	129.4	129.4	493.6	500.1
% estimates within 3σ **boundaries**	97	97.9	94.3	95.9	74.2	74.1
% overlaps within 3σ **boundaries**	98.6	97.2	99.9	99.9	58.4	59.5

Table 8.7: Results from time series analysis

Note that all the time series are actually affected by a small bias that was removed prior to plotting them. The mean value of each pole coordinate series is reported in Table 8.7. The offset on the y-coordinate tends to be more marked than that affecting the x-coordinate. Over the course of this research, the magnitude of these biases was discovered to be very sensitive to any change in the estimation procedure, from differences in the force modeling to the use of different antenna calibrations, data rates, length of orbit determination arc, pole coordinate estimation interval, station distribution, etc..., which significantly complicates tracking its origin. It was also realized that the choice of nominal series is of the greatest importance with regard to these biases, as clearly noticeable in Appendix F. In particular, the use of Bulletin B values is not recommended since the pole coordinates reported there are affected by a very large bias, especially in the y-direction, as reported by Thaller et al. in [183], among others. The more recent EOPC04 series, generated by the IERS Central Bureau, should be preferred. The differences between the two operational ERP series are documented by Luzum et al. in [134], along with the methods and sources employed in both cases. A re-alignment campaign was recently conducted by the IERS to correct, or at least minimize, the inconsistency between the IERS y-pole coordinate and the ITRF. These consistency issues between the EOP series and the reference frames were monitored by Gambis and Bizouard in [78]. A discussion of the procedures setup for the reprocessing and recombination of the ERP series can be found in [33] or in [20] and [19] with a focus on the EOPC04_05 and EOPC04_08 series, respectively. Since the short-period variations of polar motion are the focus of this research, these biases are not an issue and their cause was not investigated further.

8.3.2 Spectral analysis

The time series were analyzed in the frequency domain as well as a preliminary feasibility study of the detection of short-period, small-amplitude signals. The perio-dograms produced can be viewed on Fig. 8.4. The top subplot shows the amplitude spectrum of the prograde residual polar motion while the bottom window displays the amplitude spectrum of the residual retrograde component of polar motion. The series are said to be residual series for they represent series of estimates corrected for ocean tide effects and relative to the nominal EOPC04 solution. As this work concentrates on the study of ultra-rapid and rapid polar motion, the axes of abscissae start at a period of 2 hours and end at 20 days.

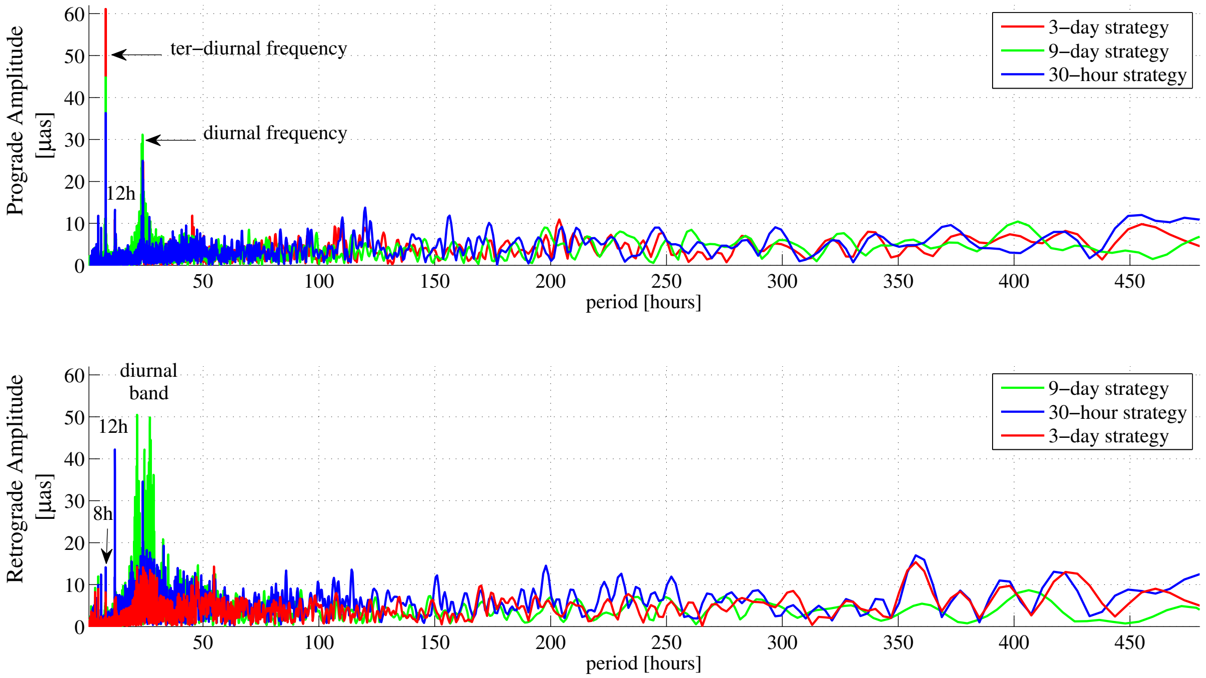

Figure 8.4: Prograde and retrograde spectra for ultra-rapid and rapid polar motion

Two spectral lines clearly stand out from the periodograms corresponding to the prograde component of polar motion. The first spectral line appears at periods of 8 hours while the second one falls on the diurnal frequency. Indeed, on the one hand, the three spectra reach their maxima at the period of 8 hours. While the existence and exact origin of ultra-rapid oscillations in polar motion at the corresponding frequency are still under investigation [Gross, personal communication, 2010], such peaks have already been observed in some GPS as well as VLBI reprocessing campaigns [95]. According to Brzeziński, these ter-diurnal variations are most likely caused by the S3 atmospheric tide and the observed effects of this tide are believed to be entirely of thermal origin [28]. On the other hand, the peaks visible at periods of 24 hours could be related to the S1 tide, to Sun-synchronous errors or just reflect mis-alignments in the daily realization of the reference frames (this argument being valid for the 30-hour and 3-day strategies only). In the case of these two strategies, the 24-hour period peak could also be due to a natural daily modulation in the errors which are the lowest at the center of the arc. The diurnal retrograde line is clearly due to a defect of nutation handling. In addition to the ter-diurnal and diurnal polar motion, two other distinct, although comparatively smaller, peaks are observed at periods of about 5-6 hours and 12 hours respectively. The 12-hour spikes are specific to the 30-hour strategy and are for the most part due to the lack of a dynamic model compensating for the mis-modeling in the SRP perturbation (see section 9.1.2). The peaks around 6 hours could possibly be related to the S4 signal, although this should be investigated further.

8.3.3 Comparison with VLBI time series

The comparison of the time series obtained based solely on GPS observations with VLBI-derived polar motion series is important because it may reveal systematic errors specific to the GPS data processing as well as errors common to both techniques that may, in turn, be interpreted as physical model errors.

- VLBI data set

The time series used for this study are estimates obtained by processing observations collected during the intensive VLBI campaign CONT'05. These estimates were graciously provided by Dr. Thomas Artz, of the University of Bonn, along with series corresponding to the CONT'02 and CONT'08 sessions. These VLBI continuous campaigns were focused on the analysis of highly temporally-resolved ERP. The VLBI data acquisition, processing and analysis corresponding to the three experiments are described by Artz et al. in [6]. The VLBI campaign considered here spanned a total of 15 days starting on September 12, 2005. The ground network was composed of 11 stations. The pole coordinates were estimated hourly and modeled as piecewise linear over the estimation interval, following the random-walk model. Bulletin A values were used as nominals for the pole coordinate solution. The exact same geophysical models were used in the GPS reproduction of this campaign whenever it was possible to allow a more direct and meaningful comparison between the GPS- and VLBI-derived polar motion estimates. The results of this small-scale investigation are presented in the next paragraph.

- Result analysis

The time series of the VLBI- and GPS-derived estimates are displayed on Fig. 8.5 together with the associated estimated uncertainties. The edge effect dependence on the arc length is clearly visible on the subplots corresponding to the six GPS-based solutions. Note that no bias was removed prior to plotting the data. On the contrary, the mean value of the estimates was added to the $\pm 3\sigma$ uncertainty envelopes in order to preserve the offset while shifting the uncertainty band.

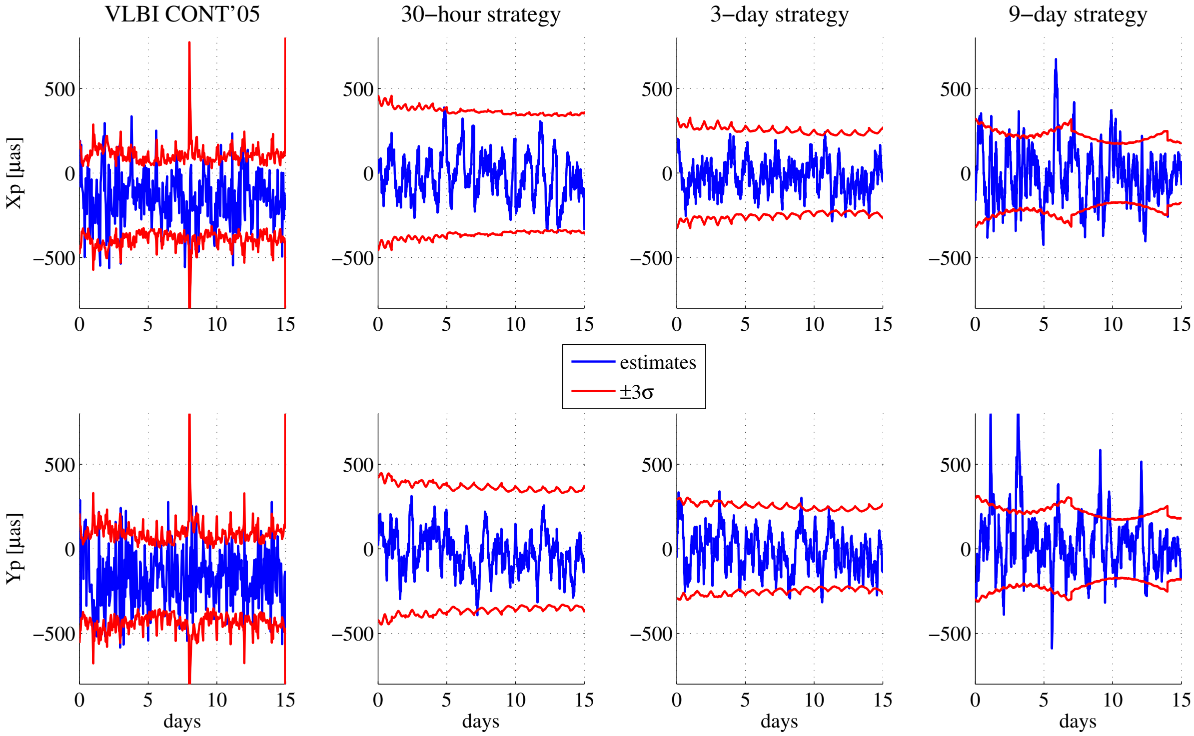

Figure 8.5: Comparison with VLBI: Pole coordinates time series

The VLBI series of estimates and formal errors are much noisier than their GPS-derived equivalent. It is explained in part by the fact that the estimates were filtered by fitting cubic polynomials over 3-day arcs as mentioned by Artz et al. in [6]. As a consequence, the plots show the postfit residuals with respect to that polynomial in the case of the VLBI-derived solution. Moreover, continuity at the arc boundaries was enforced either during the processing or during the

post-processing stage of the VLBI-derived series [6]. In contrast, the GPS-derived series did not undergo any particular treatment prior to their analysis. In particular, continuity constraints were never applied between adjacent arcs to avoid jeopardizing the independence of the solutions and for practical, computational reasons.
The 3-day strategy appears to produce the solution closest in amplitude to the VLBI-based solution. Once again, the 9-day solution contains the most outliers.

A spectral analysis was carried out since the GPS-based solutions exhibit apparent periodic variations. Figure 8.6 compares the amplitude spectra of the 4 solutions for the prograde and retrograde components of polar motion for periods spanning two days.

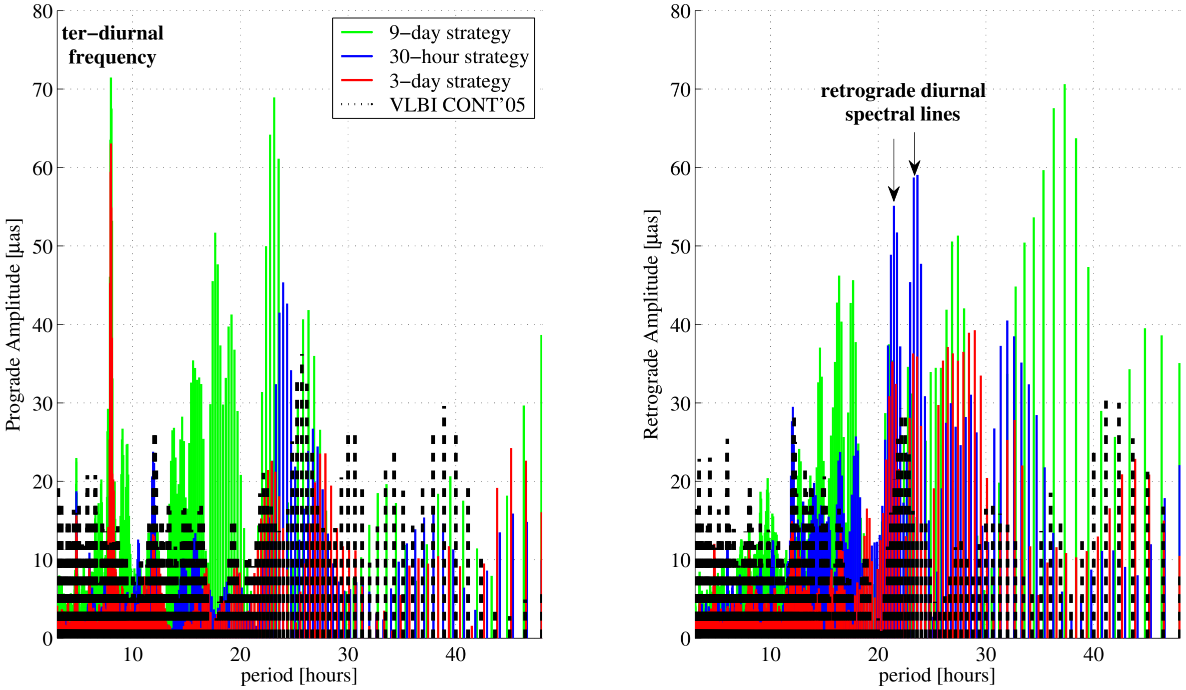

Figure 8.6: Comparison with VLBI: Prograde and Retrograde Spectra

The major difference in the prograde semi-diurnal frequency band consists in the peak manifesting at periods of 8 hours. This spectral line corresponds to the ter-diurnal frequency and is believed to be of geophysical origin as mentioned in the preceding section. Similar peaks have been reported in GPS polar motion analysis and were actually observed by Artz et al. based on the VLBI observations collected during the intensive campaigns of 2002 and 2008 [6]. Therefore, these powerful peaks may not constitute artifacts of the GPS strategies. The retrograde diurnal band is dominated by two clusters of spectral lines. These lines are caused by nutation handling. Although every estimation procedure performs nutation handling by fixing nutation to the IAU2000A model, the VLBI strategy includes additional corrections that help mitigate the contamination of the polar motion solution by a residual nutational signal, as reported in [6]. This explains why the lines seen in the VLBI analysis are of much smaller magnitude than those seen in the GPS-derived spectra. Table 8.8 mentions the root-mean-squares values of the residuals in the prograde and retrograde frequency bands for a direct comparison of the total frequency content.

	Prograde Signal	**Retrograde Signal**
VLBI CONT'05	113.5	112.5
30-hour strategy	72.6	100.5
3-day strategy	70.4	75.8
9-day strategy	116.1	120.6

Table 8.8: RMS value of prograde and retrograde residuals. Units are μas.

Despite providing an independent means for judging the quality of the polar motion solution, the significance of a comparison with a VLBI-derived time series in terms of accuracy is somewhat questionable. Indeed, the VLBI community itself uses GPS-based series as a rule for the accuracy of their pole coordinate estimates. In fact, as reported in their publication, the authors of [6] compared their solution to a special solution based on the CODE contribution to the first reprocessing campaign of the IGS – solution whose setup is described in [179] – as part of the quality assessment of their estimates. Differences of up to 200 μas between the two solutions were reported.

Looking at the spectra of formal errors on the diagrams below, the VLBI solution appears to be corrupted by more systematic errors than the GPS solutions. This prevents any deduction regarding GPS-specific artifacts.

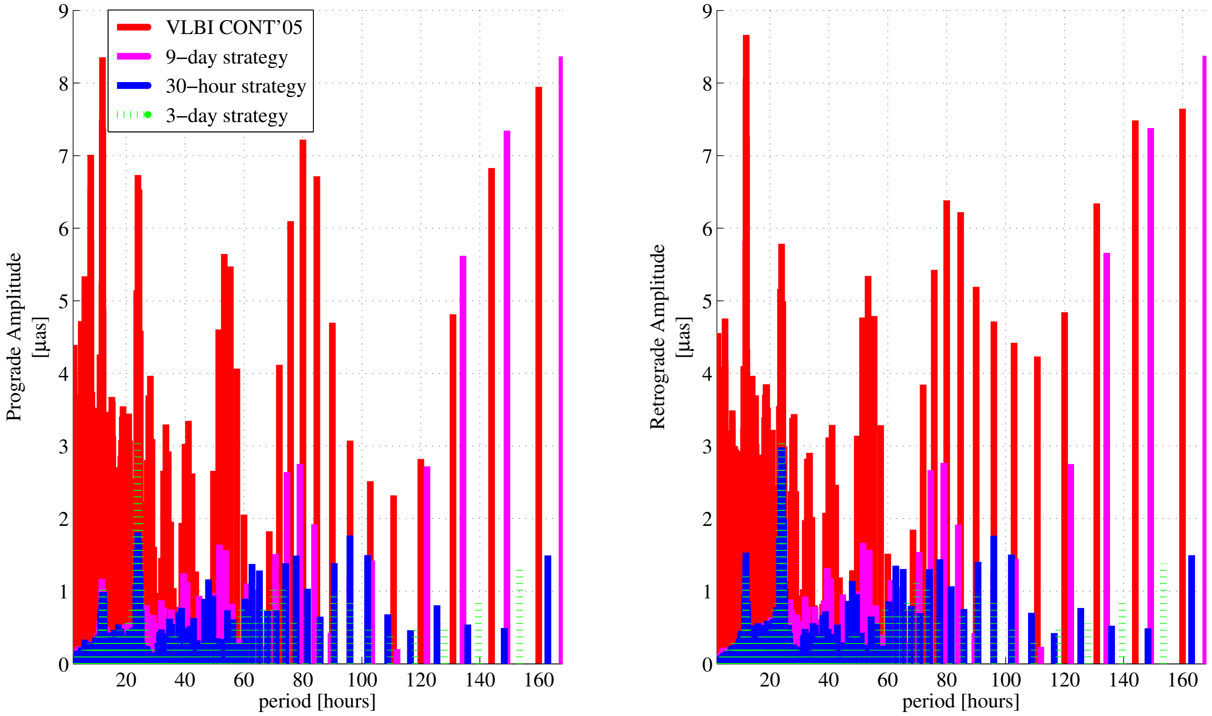

Figure 8.7: Amplitude spectra of VLBI and GPS systematic errors

8.3.4 Error analysis

The last step in the general performance evaluation of the polar motion solutions consists in the analysis of potential systematic errors that could be specific to a strategy. Systematic errors are typically revealed by computing the periodograms of the solutions' formal errors as established in the above section. Figure 8.8 shows the amplitude spectra of the prograde and retrograde uncertainties associated with each strategy. The 8-day limit imposed on the axes of abscissae is justified by the fact that the main spectral lines are found in that frequency range.

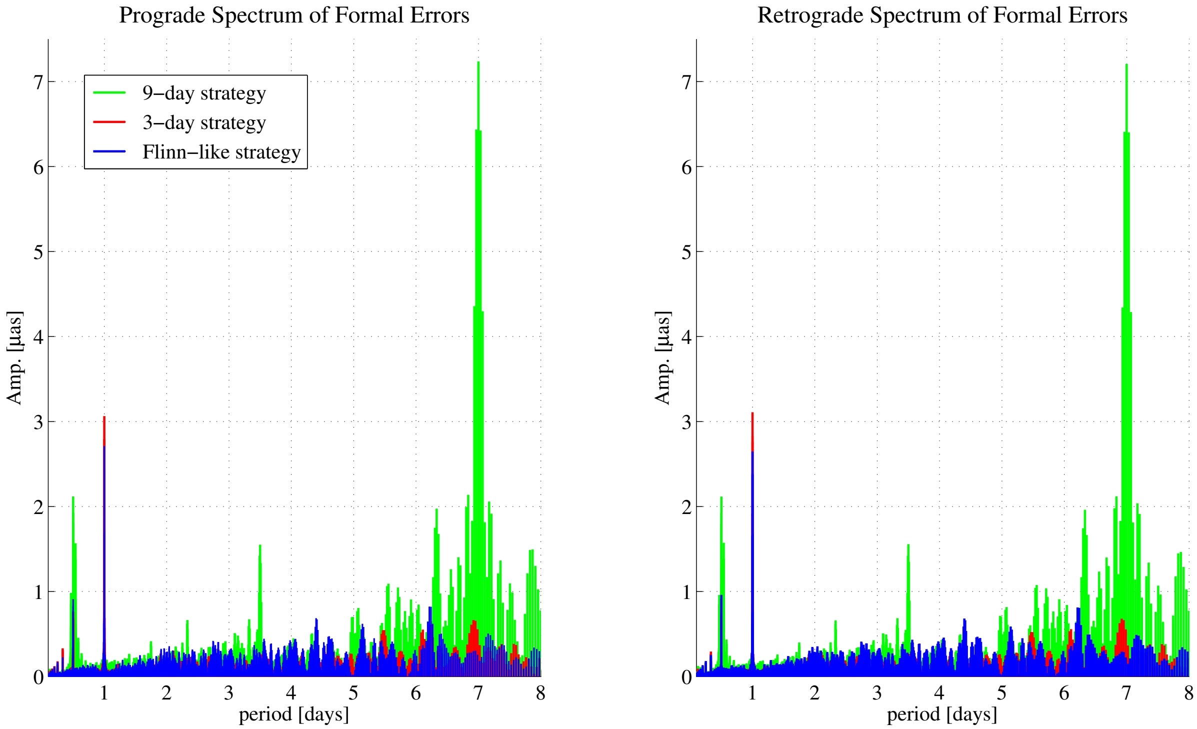

Figure 8.8: Amplitude spectra of systematic errors for all three candidate strategies

Peaks in the amplitude of the systematic errors clearly appear at periods matching the solution length, as well as periods of half the solution length, in all three cases. As a reminder, the length of the actual solution is equal to the arc length minus two days for Longarc-type strategies and to 24 hours for the 30-hour strategy. These errors are mostly related to the stability of the day-to-day realization of the terrestrial reference frame and the natural modulation of errors, as seen before. Yet, changes in the frame do not explain the significant peak occurring at periods of 12 hours in the case of the 9-day strategy. Artifacts in the dynamical modeling are likely contributors to the semi-diurnal spectral line, this period being commensurate with the GPS satellite orbit period. The magnitude of the systematic errors is overall negligible in comparison to the total amplitude of polar motion and the prograde and retrograde components are affected in the same manner, which implies that the pole coordinates are equally impacted. The spectra corresponding to the use of the 9-day arc strategy exhibit many more spectral lines than the other two. This potentially indicates artifacts specific to the dynamical strategy used in this case. Conversely, the periodograms associated with the 3-day arc strategy appear to be the least noisy and only have two major peaks, at periods of 12h and 24h. This last result is somewhat expected based on the fact that the reference frame realized by the ground network is more stable in this case, as deduced from Table 8.3.

It is remarkable that the systematic errors related to discrepancies in the daily (or weekly, depending on the type of solution considered) realization of the terrestrial reference frame or to inter-arc discontinuities of other origins could be mitigated by smoothing the pole coordinate time series. Indeed, the alignment of independent solution is not forced here. This smoothing practice is however discouraged by the IGS for their analysis centers, as detailed by Ray in [155]. No smoothing was performed on the solutions provided through this research, which does result in systematic errors but ensures that none of the potentially real signal is lost.

8.4 Other metrics

8.4.1 Station coordinate repeatability

Statistics on the station positions are presented in Table 8.9. The values represent the mean repeatability in longitude, latitude and height of the station network and the mean dispersion around the average values.

The fiducial nature of the network is attested by the small variations in all station positions. No reference frame transformations were applied prior to computing the statistics.

	30-hour	**3-day**	**9-day**
Latitude	2.7 ± 0.4	2.4 ± 0.2	1.8 ± 0.6
Longitude	1.5 ± 0.2	1.1 ± 0.4	2.2 ± 0.7
Height	2.8 ± 0.3	2.6 ± 0.3	3.8 ± 1.1

Table 8.9: Coordinate repeatability. Units are mm

Based on Table 8.9, the 3-day strategy yields the best results again although no strategy really stands out from this simple test. It is noteworthy that fewer samples contributed to the statistics computed on the 9-day strategy than to the statistics calculated based on the other two strategies.

8.4.2 Satellite clock overlaps

Satellite clock overlaps are computed next and displayed in Table 8.10. The values correspond to the mean RMS value of the clock overlaps for all the satellites over the entire year processed and standard deviation about this mean value. To ease the comparison, the time unit has been converted to equivalent distance unit.

30-hour	**3-day**	**9-day**
1.21 ± 0.30	1.24 ± 0.6	2.17 ± 0.7

Table 8.10: Intercomparison of satellite clock solutions. Units are cm

8.4.3 Post-fit residuals

The fit of the solution is verified by computing statistics on the post-fit resi-duals. Data noise was set to 1 m on the range measurements and 1 cm on the phase observations. Table 8.11 gathers the mean RMS value of the residuals on both types of measurements as well as the standard deviation around that mean value.

	30-hour	**3-day**	**9-day**
Phase [cm]	0.69 ± 0.06	0.70 ± 0.01	0.69 ± 0.03
Range [cm]	54.31 ± 2.24	55.05 ± 2.3	56.79 ± 3.81

Table 8.11: Inter-comparison of fit to the observations.

All strategies yield solutions that fit the data similarly.

8.5 Impact of transmitter and receiver antenna calibrations

As mentioned in section 7.2.4, two types of antenna calibration files are available to model the phase center offsets and variations of the transmitter antennas, the so-called GRACE maps and the IGS transmitter calibrations. All the results presented so far were obtained using the GRACE-based calibrations. However, these suffer from known deficiencies that do not affect the IGS transmitter calibrations. Indeed, the latter are generated in such a way that unknown effects or errors are absorbed when they are used in combination with the IGS receiver calibrations. Besides, the second set of ground antenna calibrations, the Mesa maps, is also of interest as a replacement for the IGS receiver maps. In this case, the ground network selection and hence, potentially the global distribution of stations, are affected since these calibrations are valid for choke ring antennas only.

A study was conducted to evaluate the impact of the transmitter calibrations on the final orbit determination and polar motion solutions. Likewise, the influence of the two available sets of receiver calibrations was evaluated. In both cases, the 3-day strategy was employed based on the higher performances it exhibited relative to the other two strategies. Similarly to Tables 8.2 and 8.4, Table 8.12 displays the results in terms of orbit overlaps and comparison to the IGS final orbits. It should be noted that one day was removed from the Mesa/GRACE solution and that all the satellites in shadow had to be excluded from the estimation procedure in the IGS/IGS configuration on 10 occasions.

		IGS/GRACE	**IGS/IGS**	**Mesa/GRACE**
Orbit Overlaps [cm]	**H**	1.24	1.22	1.25
	C	1.46	1.45	1.44
	L	1.98	2.0	1.99
	1D-RMS	1.59	1.59	1.59
Difference with IGS [cm]	**H**	2.92	2.43	2.86
	C	3.62	2.64	3.58
	L	3.74	2.93	3.75
	1D-RMS	3.45	2.67	3.42

Table 8.12: Impact of antenna calibrations on OD solution

The orbit overlaps study reveals that the level of precision of the orbits is strictly equivalent in all three cases. Besides, as expected, the changes in the calibration of the antennas mainly affect the results relative to the difference with the IGS orbits when both the receiver and transmitter IGS maps are used. The difference between coupling the GRACE transmitter calibrations with either the Mesa or the IGS receiver calibrations is negligible on the orbit determination level.
Table 8.13 reports the results of this comparative study based on the pole coordinate time series analysis. The values referred to as GPS estimates and overlaps correspond to the RMS values over one year of those quantities.

	IGS/GRACE		IGS/IGS		Mesa/GRACE	
	X_p	Y_p	X_p	Y_p	X_p	Y_p
Bias	7.7	77.9	4.1	22.8	13.9	-32.5
Estimates	137.8	126.8	150.7	129.8	216	182.1
Overlaps	129.4	129.4	132.6	128.4	191.6	161.1

Table 8.13: Impact of antenna calibrations on polar motion estimates. Units are μas.

Changing the antenna calibration files significantly impacts the magnitude of the bias, especially for the y-coordinate. Based on the two tables above, the substitution of GRACE maps by the IGS version of the transmitter calibrations visibly improves the quality of the solution as determined by the signal-to-noise ratio (RMS of GPS-derived estimates vs. RMS of internal pole overlaps). Even the bias affecting the y-coordinate is significantly reduced in this case. The solution using MESA antenna calibrations appears to be the outlier of the three solutions. The meaningfulness and reality of the signal estimated in each case need to be evaluated to determine if the use of Mesa calibrations is suitable to the recovery of polar motion. This is done in Chapter 9. A priori, the Mesa/GRACE configuration seems to dramatically deteriorate the quality of the pole solution.

8.6 Impact of selected coordinate system for the once-per-revolution custom accelerations

As described in Chapter 7, the once-per-revolution non-specific acceleration terms can be parameterized either in the HCL coordinate system or in the UVW coordinate system, both described in Appendix B. To study the impact the coordinate system chosen to express the 1-cpr force may have on the solution, the 3-day arc strategy was slightly modified. The cosine and sine terms of the accelerations were estimated along the U- and W-axes rather than in the cross-track and in-track directions. Note that one day was eliminated from the solution in which the acceleration is expressed in the UVW coordinate system.

This small-scale study was motivated by the realization that the 1-cpr cross-track accelerations are significantly correlated with the pole coordinates as shown on Fig. 8.9 a). While changing the coordinate system removes these correlations as observed on Fig. 8.9 b), it clearly aggravates the correlations among other parameters as visible on Figs. 8.10 and 8.11. The sets of figures shown below are color-coded graphical representations of the correlation matrices extracted from the variance-covariance matrix computed at the last epoch of the arc on the same day picked at random. For enhanced visibility, absolute values of the correlation coefficients were used. The color bars on the right hand side of each subplot indicate the correlation coefficient values. Besides, on Figs. 8.10 and 8.11, the x- and y-label ticks point to the index in each correlation matrix of the last parameter belonging to the specified group of parameters.

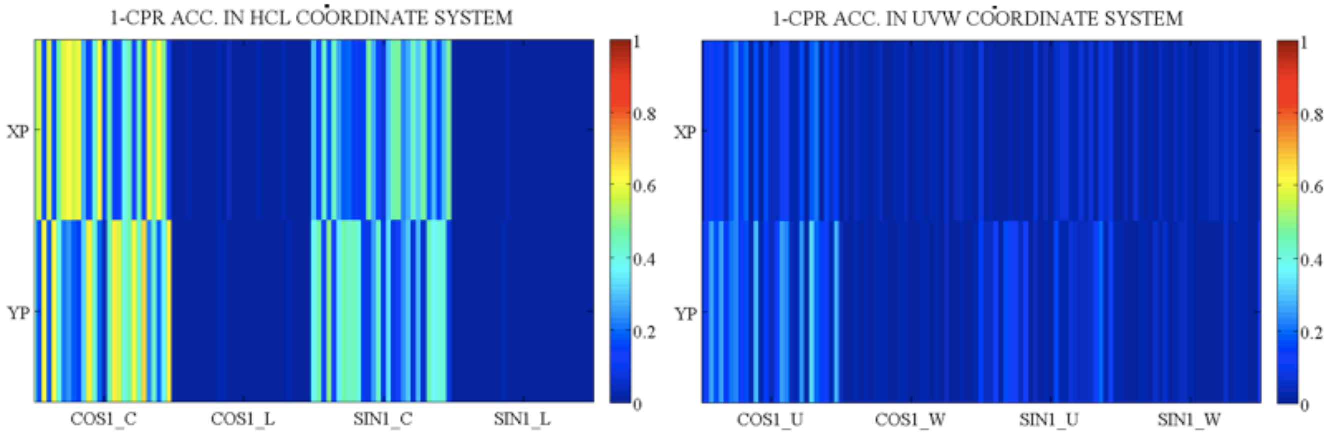

Figure 8.9: Correlation between Xp, Yp and 1-cpr acc. along a) C/L b) U/W axes

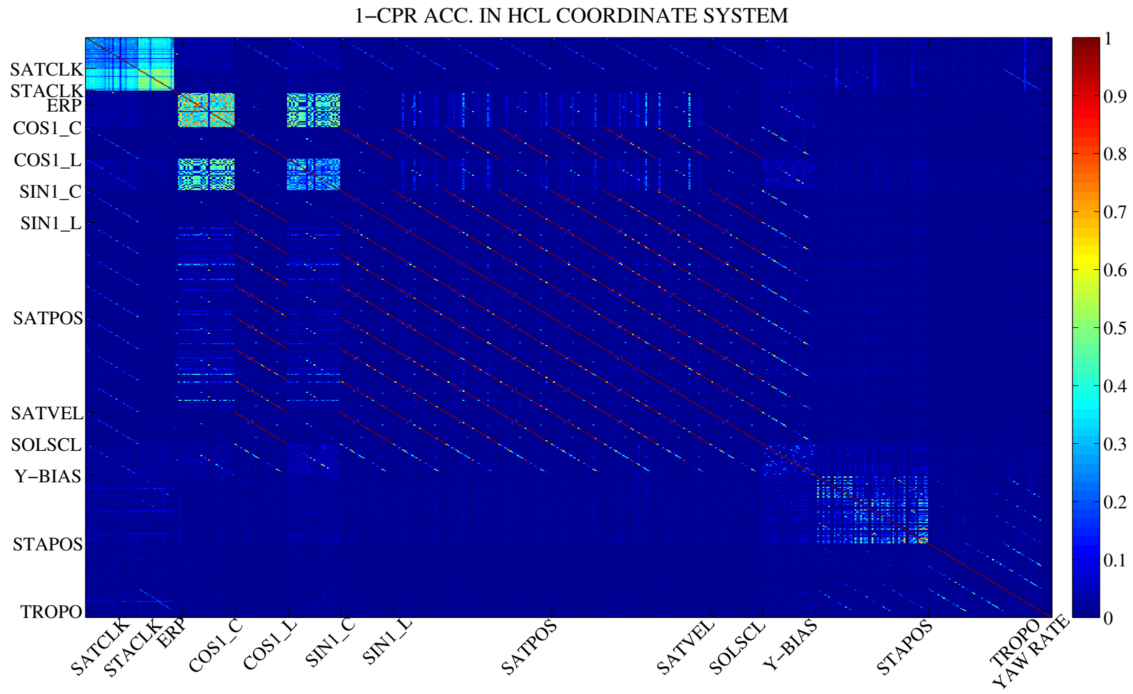

Figure 8.10: Correlation matrix: 1-cpr acceleration expressed in the HCL system

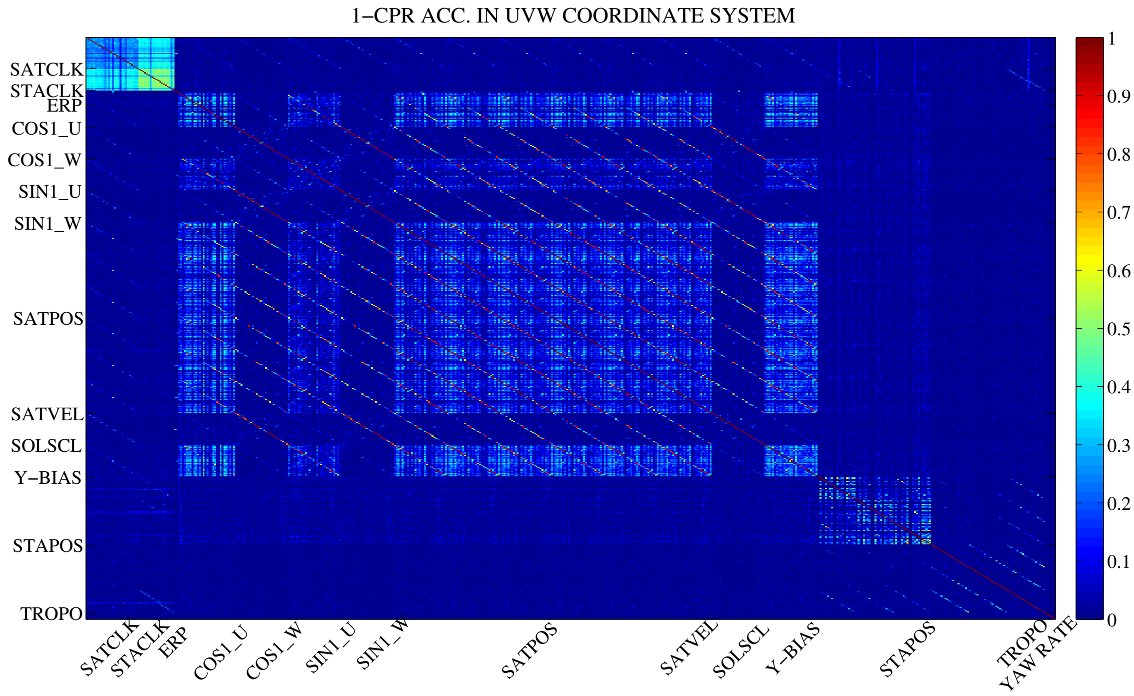

Figure 8.11: Correlation matrix: 1-cpr acceleration expressed in the UVW system

Overall expressing the 1-cpr custom acceleration in the UVW coordinate system proves detrimental in terms of polar motion recovery. In spite of the improvement visible in the orbit solution and reported in Table 8.14, the signal-to-noise ratio is significantly reduced as seen in Table 8.15. It should be mentioned that the UVW approach as implemented in the GIPSY software package provides a shadow factor and turns off the accelerations when the Sun is blocked. This difference in the parameterization of the force model could provide some insight into the results shown here. This needs to be investigated further.

		HCL frame	**UVW frame**
Orbit Overlaps [cm]	**H**	1.24	0.80
	C	1.46	1.23
	L	1.98	1.27
	1D-RMS	1.59	1.12
Difference with IGS [cm]	**H**	2.92	2.61
	C	3.62	3.45
	L	3.74	3.45
	1D-RMS	3.45	3.20

Table 8.14: Impact of coordinate system for 1-cpr acceleration formulation on OD solution

	HCL frame		**UVW frame**	
	X_p	Y_p	X_p	Y_p
Bias [μ**as**]	7.7	77.9	13.5	46.3
RMS of GPS estimates [μ**as**]	137.8	126.8	162.4	139.4
RMS of internal overlaps [μ**as**]	129.4	129.4	293.2	298.4

Table 8.15: Impact of coordinate system for 1-cpr acceleration formulation on polar motion estimates

8.7 Preliminary conclusions

The results shown in this chapter are encouraging although the noise levels currently achieved on the polar motion estimates remain high. The POD accuracy is not significantly altered when targeting polar motion recovery and all the solutions appear to be consistent with each other. Clearly, the 3-day strategy performs the best in terms of internal precision and comparison to external solutions in all domains. The results obtained using the 30-hour strategy are satisfactory as well. On the contrary, issues arise when the 9-day strategy is employed. In particular, a powerful retrograde diurnal signal, most likely reflecting a lack of nutation handling, is observed when the 9-day parameterization is used. However, this last strategy cannot be discarded before the geophysical meaningfulness and value of the solutions produced are estimated. Therefore, the quality of the estimates is further assessed by their ability to retrieve geodetic signals of various types.

Table 8.1: Metrics used in the Performance Analysis

Target	Metrics	Significance	Comments
Overall Solution	postfit residuals	used to assess the fit of the estimation	
	station coordinates repeatability	used to assess the quality of the reference frame realization	strong indicator of the consistency and quality of the solution
	impact on the tropospheric delay	detection of potential absorption of mis-modeling noise	currently not considered
	station clock overlaps	detection of potential correlation with troposphere parameters	currently not evaluated
OD Solution	orbit overlaps	orbit consistency and internal precision	potentially optimistic indicator of accuracy
	comparison with IGS final orbits	performance wrt. standard products	indicative of orbit accuracy
	satellite clock overlaps		
Polar Motion Solution	comparison to ocean tide model	independent validation based on altimetry data and theory	ocean tide model turned off to perform the assessment
	pole overlaps	precision and internal consistency	establishment of noise level
	comparison with VLBI estimates	performance relative to other space geodetic techniques	
	comparison to IERS combined solution		final modifications to GIPSY required

Chapter 9

Recovery of Geodetic Signals

The investigations presented in this chapter are aimed at providing the ultimate vali-dation of the estimation procedures. The studies carried out target the recovery of geodetic signals of various types and gradually decreasing in magnitude and hence, in likelihood of detectability. To do so, the series of estimates were analyzed both in the time and in the frequency domains using a set of geophysical models and independently obtained geodynamic solutions. The chapter is structured as follows. Tidally-driven polar motion variability is examined first. The capture of non-tidal variations forced by large-scale oceanic and atmospheric rapid processes follows. Ultimately, the application of the techniques implemented and tested throughout this work to the detection of the signature of an earthquake is discussed. Because this research is focused on the determination of ultra-rapid and rapid variations in polar motion, the studies presented concentrate on the frequency band ranging from 0.5 cpsd to 0.05 cpsd. The case of non-tidal ultra-rapid polar motion is treated separately.

9.1 Recovery of tidal variations

For the purpose of tidal analyses, the GIPSY software package was reconfigured by turning the model predicting the influence of ocean tides on polar motion in the semi-diurnal and diurnal frequency bands off. This model is included by default in the processing and was used in all the test cases presented thus far. It is referred to as the IERS model hereinafter, since it is officially recommended for use in the IERS Conventions [152]. It is noteworthy that the effects of tides on polar motion cannot be isolated. Indeed, the GPS-derived series of pole coordinates contain the tidal contribution as well as a variety of additional, non-tidally induced effects.

9.1.1 Time-domain tidal analysis

The series of estimated pole coordinates are directly compared to simulated time series generated using the coefficients of the sub-daily model supplied by the IERS. Because the ocean tide model considered is based on satellite altimetry data, such a comparison is particularly appropriate for an independent validation of the sub-daily GPS-derived estimates.

The time series of the differences between the model for tidally-induced polar motion and the GPS estimates for all three candidate strategies are shown in Figs. 9.1 a), b) and c). Envelopes of 3σ formal errors are overlaid on the plots. Besides, pole overlaps were computed and plotted in the same fashion as when the model for tidal polar motion was accounted for in Chapter 8. These overlap values and corresponding uncertainty limits are represented in Fig. 9.2 a), b) and c). Similarly to Figs. 8.2 and 8.3, a mean offset was removed from the estimates before performing the comparison and computing the overlaps, respectively.

Figure 9.1: Time series of difference between GPS-derived pole estimates and IERS2003 model with 3σ boundaries. a) 30-hour strategy b) 3-day strategy c) 9-day strategy

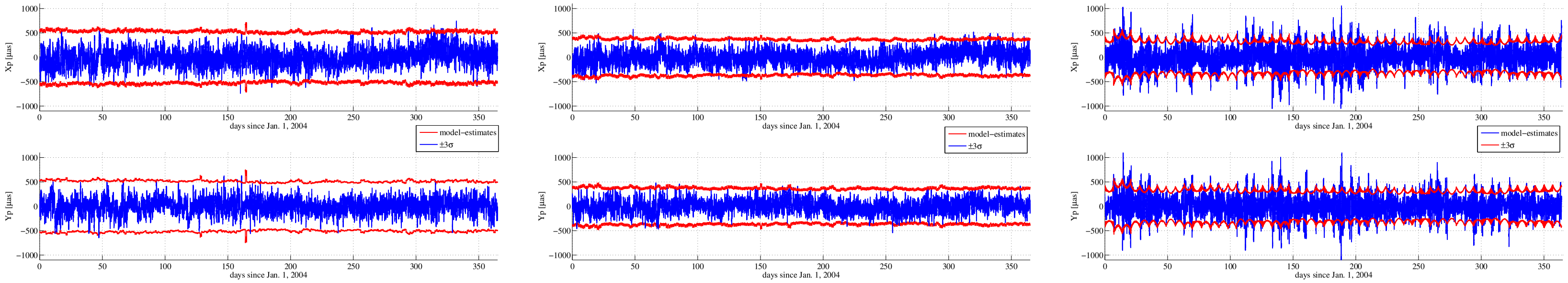

Figure 9.2: Time series of pole overlaps and associated 3σ boundaries. a) 30-hour strategy b) 3-day strategy c) 9-day strategy

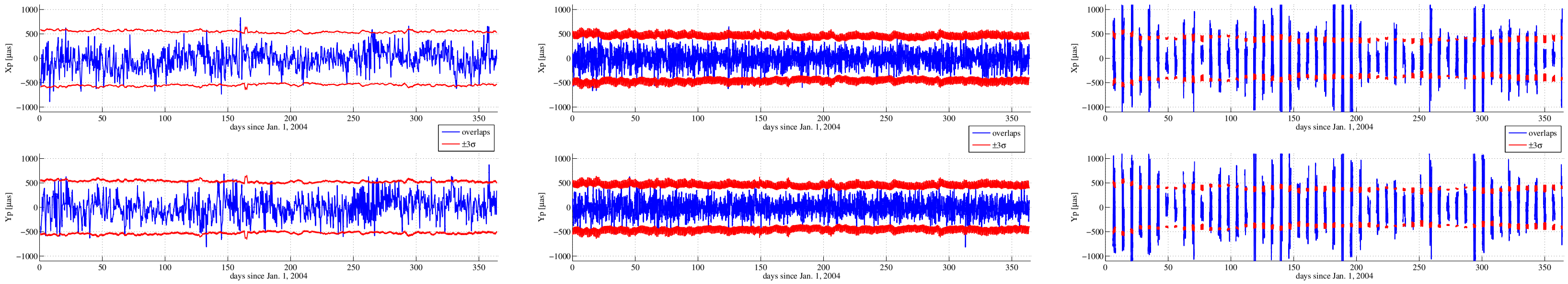

As reported in Table 9.1, the estimates comply with the model within three times the formal errors over 99% of the time in the case of the 30-hour and 3-day strategies. Likewise, the overlaps are constrained by the 3σ uncertainty boundaries more than 99% of the time using the 3-day arc parameterization. The FlinnR-like strategy yields uncertainties that may be slightly optimistic. The 9-day arc strategy gives the poorest results. The pole overlap values exceed the formal errors about 40% of the time and the difference with the theoretical confidence interval on the difference with the model is exceeded by up to 15%. In terms of signal-to-noise ratio, considering the root-mean-squares value of the GPS estimates and comparing them to the root-mean-squares value of the internal overlaps, the 3-day strategy performs much better than the other two again. The 9-day strategy has a signal-to-noise ratio lower than 1 in that case whereas when the tide model is switched off, the signal-to-noise ratio is larger than 1 for both the 30-hour and the 3-day cases. Overall, the overestimation visible in the RMS of the GPS-derived estimates of the pole coordinates reflects the fact that the series also contain signal induced by non-tidal variations, model errors and strategy artifacts.

	30-hour		**3-day**		**9-day**	
	X_p	Y_p	X_p	Y_p	X_p	Y_p
Bias [μ**as**]	16.1	65.3	11	85	-37.3	12.7
RMS of IERS model [μ**as**]	317	242.4	317	242.4	317	242.4
RMS of GPS estimates [μ**as**]	367.2	295.1	340.6	264.2	400.9	330.5
RMS of difference with model [μ**as**]	173.5	156.3	139	129	228.6	219.6
RMS of internal overlaps [μ**as**]	294.6	230	155.4	156.8	492.1	488.4
% overlaps within 3σ **boundaries**	95.7	97.7	99.7	99.5	59.8	61.3
% difference with model within 3σ	99.6	99.8	99.1	99.6	86.5	87.7

Table 9.1: Results from time series analysis

To determine in which direction of propagation polar motion carries the most content, the solutions are each decomposed into their prograde and retrograde components. Thus, prograde and retrograde time series are reconstructed by inverse Fourier transform starting from the corresponding amplitudes and phases obtained by least-squares adjustment using the Lomb-Scargle periodogram method. The results obtained are gathered in Table 9.2.

	30-hour		**3-day**		**9-day**	
	Pro	**Retro**	**Pro**	**Retro**	**Pro**	**Retro**
RMS of IERS model	190.8	207.9	190.8	207.9	190.8	207.9
RMS of GPS estimates	212.9	256.2	214.4	216.7	229.8	286.6
RMS of difference wrt. model	86.9	138.8	89	98.6	104.9	197.7
RMS of internal overlaps	98.5	167.1	76.5	127.3	109.3	472.2

Table 9.2: Results from time series analysis. Units are μas

The figures shown in Table 9.2 demonstrate the major contribution of the re-trograde component to the overall noise level, in particular when the 9-day strategy is used.

To verify the good agreement between the estimates and the modeled series in the time domain, the correlation coefficients relating the two classes of series were calculated. Table 9.3 indicates how correlated the estimated series are with the sub-daily model for each candidate strategy.

	$\mathbf{X}_p$	$\mathbf{Y}_p$	**Prograde**	**Retrograde**
30-hour	0.88	0.85	0.91	0.84
3-day	0.91	0.87	0.91	0.89
9-day	0.82	0.75	0.89	0.72

Table 9.3: Coefficients of correlation between modeled values and estimates

As seen in the table above, the correlation with the model is always better for the x-coordinate and, as expected, for the prograde variations. Note that, even though constituents of the retrograde signal in the diurnal frequency band could be artificially filtered out from the solutions considering that they are forced to 0 in the model, they were not. It was however verified that removing all the frequency content in the diurnal retrograde band slightly improves the fit to the model, especially for the 9-day strategy.

The interpretation of the results gathered in Table 9.1 remains challenging at this point because multiple sources contribute to the estimated polar motion series besides the ocean tides that are accounted for in the model. To further evaluate the compliance with the sub-daily model, tidal analyses were conducted in the frequency domain.

9.1.2 Frequency-domain tidal analysis

The tidal analyses carried out in the frequency domain concentrate on the eight major daily and half-daily ocean tides. As mentioned in section 3.2.2, there are four main tides in the diurnal frequency band, K1, O1, P1 and Q1. Four other tides dominate the semi-diurnal band of the polar motion spectrum, namely K2, M2, N2 and S2. The origin of each of these tides is briefly stated in Table 3.1.

Amplitude spectra were computed by means of the Lomb-Scargle periodogram technique [205] to compensate for data gaps. They are shown below.

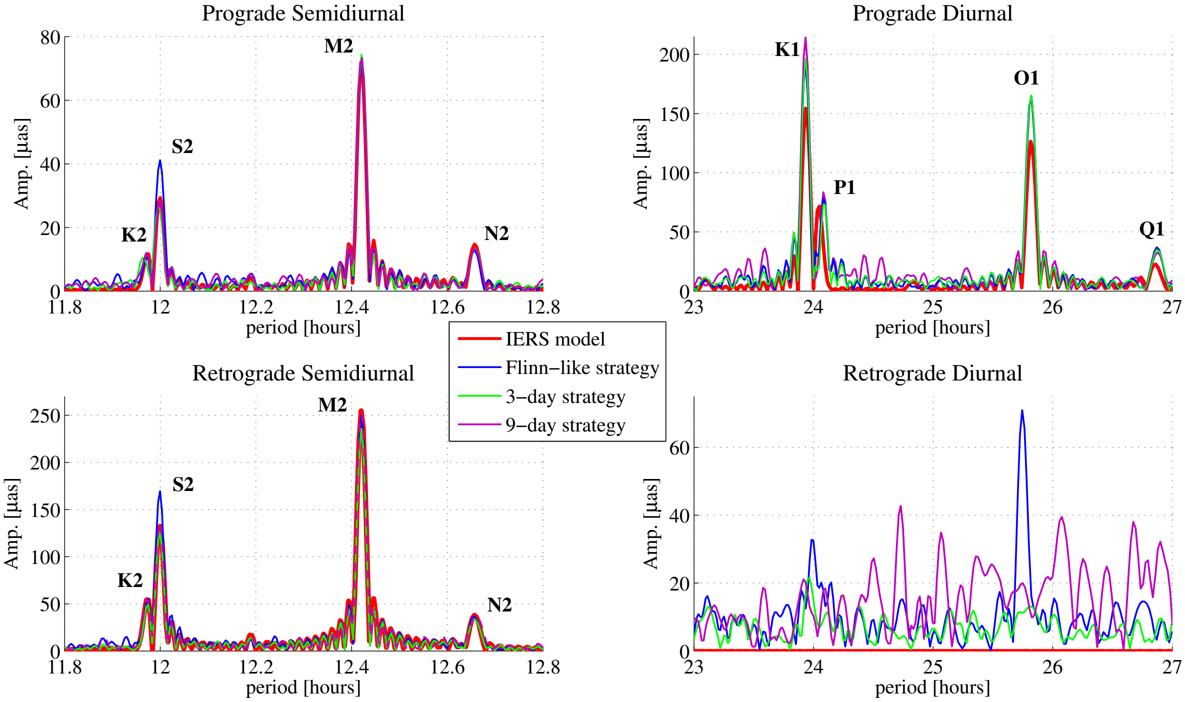

Figure 9.3: Amplitude spectra of the modeled and GPS-derived series

Since the P1 and K1 gravitational tides respectively correspond to annual prograde nutation and precession [206], errors in the nutation and precession models, respectively, are likely to contribute to any signal in the retrograde components of these two tides.

The fit to the model was more precisely assessed by concentrating on the eight major tides cited above. Their amplitudes and Greenwich phase lags were estimated from a least-squares adjustment using the ERP estimates as pseudo-observations weighted by their formal errors. The tidally-driven variations in polar motion are represented as shown in Eqs. 9.1.

$$\begin{cases} \delta X_p = \sum\limits_{tides,k} \left[S_{k,x} \sin\left(\varphi_k(t)\right) + C_{k,x} \cos\left(\varphi_k(t)\right) \right] & (9.1a) \\ \delta Y_p = \sum\limits_{tides,k} \left[S_{k,y} \sin\left(\varphi_k(t)\right) + C_{k,y} \cos\left(\varphi_k(t)\right) \right] & (9.1b) \end{cases}$$

$$\varphi_k(t) = \sum_{j=1}^{6} N_{kj}\, F_k(t) \qquad (9.1c)$$

In the set of equations above, $C_{k,x}$, $C_{k,y}$, $S_{k,x}$ and $S_{k,y}$ are cosine and sine amplitudes for the k^{th}

tides in the x- and y-direction. The angular variable $\varphi(t)$ denotes the astronomical fundamental argument, obtained through a linear combination of the Delaunay arguments $F_k(t)$ with coefficients N_{kj}.

Phasor diagrams were produced from the least-squares fit to the modeled and the three different estimated time series. They are shown in Fig. 9.4. The amplitudes are expressed in microarcseconds and the phases, graduated on the outer circles, are given in degrees. The legend is indicated in the caption.

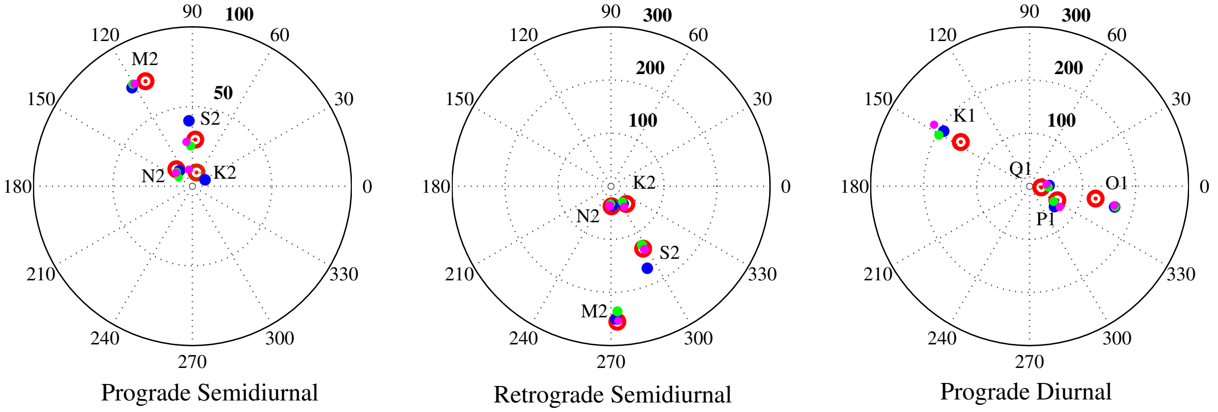

Figure 9.4: Phasor diagrams obtained by unconstrained least-squares adjustment. red: IERS model, blue: 30-hour strategy, green: 3-day strategy and magenta: 9-day strategy

Among other features, the phasor diagrams reveal that the 30-hour strategy ge-nerally yields tidal estimates that are slightly out-of-phase with respect to the model, which is valuable to the interpretation of the retrograde diurnal spectra given in section 9.1.3. Still, the computation of the phasor diagrams needs to be refined for more accuracy. Indeed, the spectral resolution is not high enough to properly solve for the sidebands of the tides. As a result, they may contaminate the estimates of the major tide amplitudes and phases through aliasing effects. To account for the sidebands the least-squares adjustment algorithm was modified to include equality constraints. The constraints applied are defined and justified by Gipson in [85]. They arise from the hypothesis that the relative sizes of the excitations are proportional to the relative sizes of the amplitudes of the tidal response. Essentially, the ratios of the sine and cosine coefficients of the sidebands and their associated major tide are forced to equate the ratios of the corresponding amplitudes in the tide generating potential.

Hence, the constraints enforced are written:

$$\begin{cases} \dfrac{a_i}{a_j} = \dfrac{A_i}{A_j} \\[2ex] \dfrac{b_i}{b_j} = \dfrac{A_i}{A_j} \end{cases} \tag{9.2}$$

In Eqs. 9.2, a and b are the cosine and sine amplitudes. The indices i and j refer to the sideband i^{th} of the j^{th} tide, respectively. A denotes the tidal height.

Results obtained from the constrained least-squares fits are plotted on the phasor diagrams shown below. Units are degrees for the phases and microarcseconds for the amplitudes. A drawback of constrained least-squares fitting when implemented in the post-processing stage is that all information on the formal errors is lost. Therefore, no confidence levels can be calculated. The implementation of the constrained least-squares algorithm followed the procedure outlined in [128].

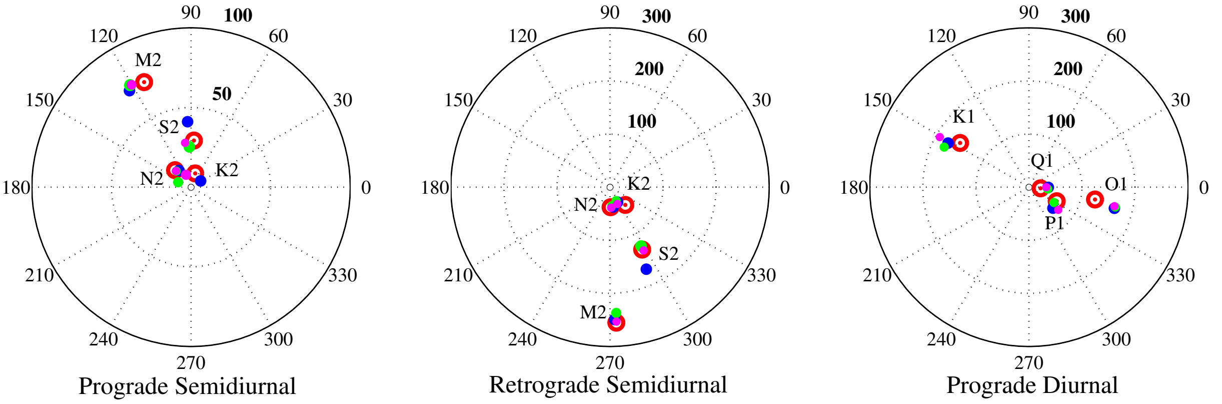

Prograde Semidiurnal

Retrograde Semidiurnal

Prograde Diurnal

Figure 9.5: Phasor diagrams obtained by least-squares adjustment with equality constraints. red: IERS model, blue: 30-hour strategy, green: 3-day strategy and magenta: 9-day strategy

Considering the results presented so far, the K1, K2 and O1 tides consistently display the poorest fit to the model. This can be partly explained by the commensurability of the periods of the K1 and K2 ocean tides with the GPS constellation repeat period and GPS satellite orbital period, respectively. The reason for the O1 tide misfit could originate in the large peak that occurs at the same frequency in the retrograde diurnal spectrum, as visible in Fig. 9.3. Ray also suggests that the current model could be inaccurate at that frequency [156]. Besides, the K1 and O1 tidal frequencies are the most affected by the effects of libration on polar motion. According to the model recommended in the IERS Conventions 2010, the amplitudes of the libration effects on polar motion for these two tidal frequencies are 16.48 μas and 13.12 μas, respectively [152]. Hence, the inclusion of the libration model is expected to reduce the differences between the tidal polar motion model and the estimates. It is interesting to note that the S2 tide is much better fitted using the Longarc-type strategies, namely the 3-day and 9-day strategies, than it is using the 30-hour strategy. Because S2 is the principal solar tide with a period of 12 hours, it is believed that the SRP-related mis-modeling errors at this frequency are not accommodated as well when no 1-cpr acceleration is estimated. The fit error affecting S2 is likely to correspond to the propagation of the mis-modeling errors in the polar motion estimates.

The fit to the polar motion sub-daily model is more easily assessed through the use of a unique metric. The performance index employed in this case is the root-mean-squares value of the differences between the modeled and the estimated amplitudes.

This criterion, introduced by Rothacher et al. in [162], is calculated following Eq. 9.3.

$$RMS = \sqrt{\frac{\sum_{j=1}^{n}\left(\Delta {a_j}^2 + \Delta {b_j}^2\right)}{2n}} \tag{9.3}$$

In Eq. 9.3, a and b denote the cosine and sine coefficients characterizing the tide with index j while n represents the number of tides considered.

For comparison, the RMS values of the modeled amplitudes in the semi-diurnal and diurnal tidal bands are given below:

- RMS = 77.59 microarcseconds for the semi-diurnal tides
    - RMS = 29.00 microarcseconds for the prograde semi-diurnal component,
    - RMS = 105.83 microarcseconds for the retrograde semi-diurnal component
- RMS = 81.47 microarcseconds for the prograde diurnal tides.

In addition to facilitating the strategy performance evaluation, Table 9.4 summarizes the impact of the constraints on the sidebands. The first line of the table indicates the RMS value of the differences between the actual model and the simulated model. The simulated model was obtained by propagating the coefficients of the model provided by the IERS in [144] over the same period of time as that spanned in the other tests and by applying an identical treatment to the resulting time series afterwards. The RMS values of the differences with the model are given in microarcseconds.

Strategy	Semi-diurnal		Diurnal	
	Unconstrained	Constrained	Unconstrained	Constrained
Simulated model	4.33	3.4	12.6	10
30-hour strategy	10.6	10.7	20.6	6.8
3-day strategy	6.9	6.5	21.5	5.4
9-day strategy	3.4	3.3	25.7	11.1

Table 9.4: Tidal analysis - Comparison to IERS ocean tide model. Units are μas

A conspicuous improvement is noticed in the diurnal band when the constraints are applied, as already visible on Fig. 9.5. The 9-day strategy is the most efficient for the recovery of the model in the semi-diurnal band. The recovery of polar motion in the diurnal band however is more troublesome for this strategy than for the other two. Overall, the 3-day strategy, once the sidebands are accounted for in the analysis, recovers the semi-diurnal and diurnal with similar levels of accuracy and performs the best.

9.1.3 Impact of arc length

A test was conducted to observe the actual impact of the arc length on the amplitude spectra of ultra-rapid polar motion. This was accomplished by varying the arc length several times in the HCL strategy, following the procedure established in section 7.5.3. Results are presented in the form of amplitude spectra in Fig. 9.6.

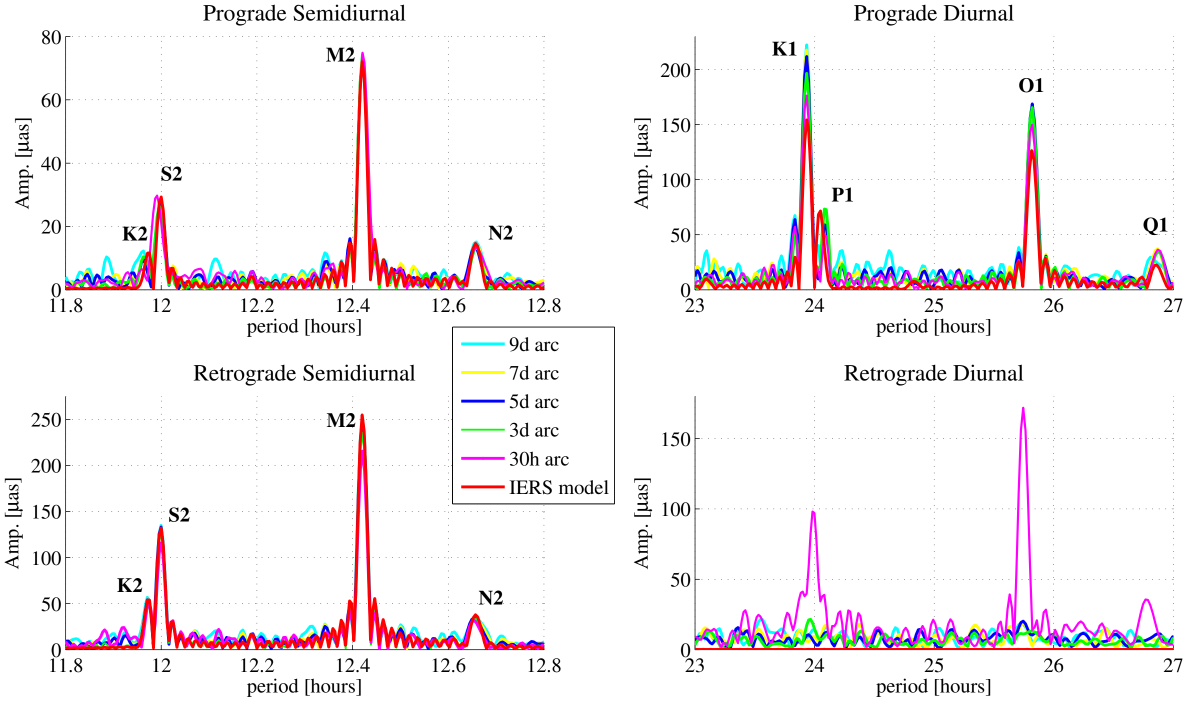

Figure 9.6: Impact of arc length on amplitude spectra

As seen on the figure above, the power in the spectra tends to increase with the arc length, especially in the prograde diurnal band. The peak occurring at the O1 tidal frequency in particular reaches significant amplitudes for the longer arcs. All four parts of the spectra are affected by a lengthening of the arc. The peaks appearing in the subplot corresponding to the retrograde diurnal band for the 30-hour-arc test case bring evidence that they are specific to the 30-hour arc length since they also appear when the FlinnR-like strategy is used. These spectral maxima correspond to tidal peaks that are slightly shifted with respect to the true tidal frequencies due to either leakage or aliasing effects. They are most likely an artifact of the use of 30-hour arcs. These results suggest that the spectral maxima observed in the case of the 30-hour arcs for both the 30-hour and the HCL estimation strategies could be independent of the dynamic modeling used. It is however not excluded that other dynamic modeling might work better when this specific arc length is employed.

The interpretation of Fig. 9.6 is far from straightforward because peaks could arise from multiple sources. They could be noise, the manifestation of systematic effects due to strategy artifacts or model errors and even real signal. The complementary analyses performed in section 9.3 helped determine how much of the signal can be deemed real. In the meantime, the impact of the arc length on the signal-to-noise ratio was studied by computing the RMS values of the estimates and the internal overlaps for each test case. The x- and y-pole coordinates were recombined into prograde and retrograde polar motion for more insight. The outcome of this analysis is presented in Table 9.5.

	Prograde Component		**Retrograde Component**	
	RMS estimates	**RMS overlaps**	**RMS estimates**	**RMS overlaps**
30 hours	207.9	142.8	254.3	210.5
3 days	214.4	76.5	216.7	127.3
5 days	226.0	91.7	232.1	157.7
7 days	233	115.1	235.5	161.4
9 days	252.2	139.9	247.4	177.3

Table 9.5: Study of Signal-to-Noise Ratio as a function of arc length. Units are μas

The results corresponding to the 9-day case point to a problem inherent to the dynamic modeling and force parameterization adopted in the 9-day strategy. Indeed, the noise level observed here is far inferior to the noise level estimated in Table 9.2 for the 9-day strategy. Based on this study, the length of the arc cannot be held responsible for the low signal-to-noise ratio or insufficient nutation handling seen for this strategy.

9.1.4 Impact of update interval

The potential impact of the pole coordinate update interval was investigated next. The setup employed in section 7.4.1 was duplicated. Again, Fig. 9.7 shows amplitude spectra corresponding to the prograde and retrograde components of polar motion in the semi-diurnal and diurnal tidal bands.

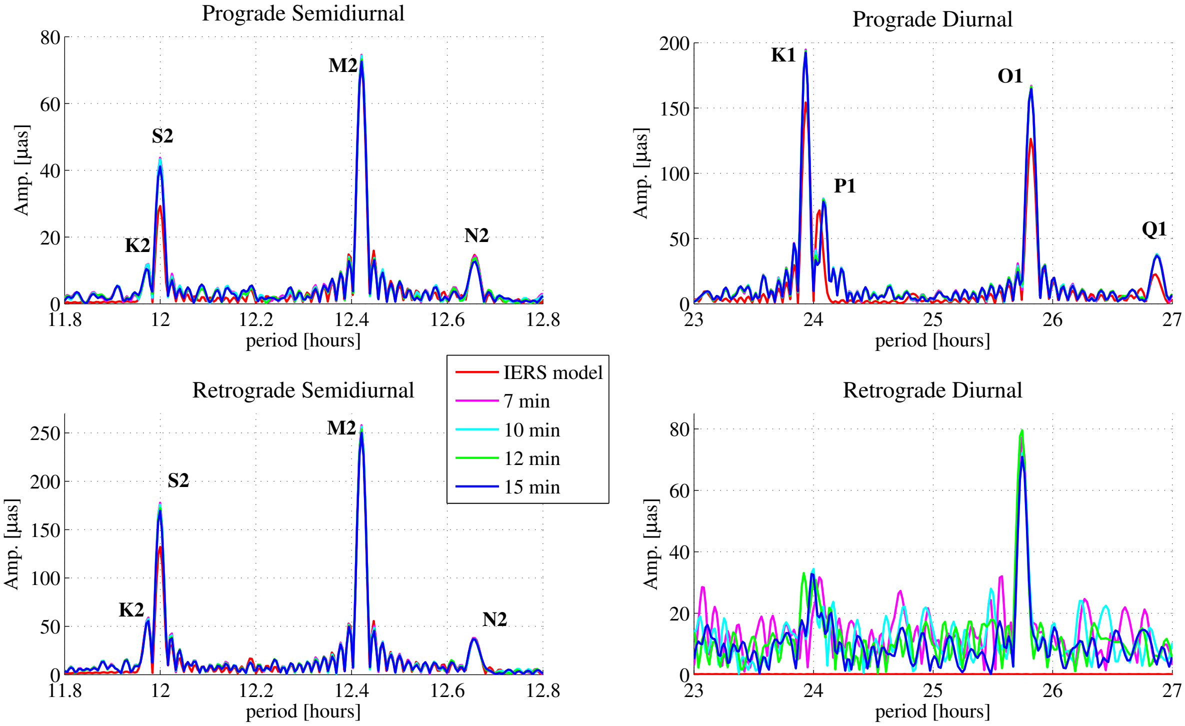

Figure 9.7: Impact of arc length on amplitude spectra

It can be concluded that the length of the pole coordinate estimation interval within these reasonable bounds has a negligible influence on the ability of the strategy to recover the variations in polar motion driven by the ocean tides. Neither the amplitudes nor the phases are affected, except in the retrograde diurnal band and, even then, only to a small extent.

9.1.5 Impact of transmitter and receiver antenna calibrations

The influence of the transmitter and receiver antenna calibrations was assessed using the same combinations of maps as in section 8.5. The performance metrics used previously are computed to get the results shown in Table 9.6.

	IGS/GRACE		IGS/IGS		Mesa/GRACE	
	X_p	Y_p	X_p	Y_p	X_p	Y_p
Bias	11	85	-58.9	9	30.2	-26.6
IERS model	317	242.4	317	242.4	317	242.4
GPS estimates	340.6	264.2	346.7	264.9	383.7	283.9
Difference wrt. model	139	129	155.4	133.1	223.7	199.2
Internal overlaps	155.4	156.8	161.5	157.8	211	183.9
Correlation with model	0.91	0.87	0.89	0.87	0.81	0.74

Table 9.6: Impact of antenna calibrations on pole estimates. RMS values are in μas.

These results confirm the "optimality" of the IGS/GRACE configuration and argue against the use of the Mesa receiver antenna calibrations, for which the noise level is the highest and the correlation with the model the lowest.

9.1.6 Impact of the selected coordinate system for the once-per-revolution custom accelerations

Imitating what was done in section 8.6, the impact the selection of the coordinate system used to express the 1-cpr custom forces might have on the recovery of tidal polar motion was evaluated. As visible in Table 9.7, the UVW parameterization suffers from a much higher noise floor than the HCL parameterization. This shortcoming of the UVW reference frame formulation is not reflected in the coefficients determining the correlation between the model and the estimates.

	HCL frame		UVW frame	
	X_p	Y_p	X_p	Y_p
Bias [μ**as**]	11	85	81.6	80.4
RMS of IERS model [μ**as**]	317	242.4	317	242.4
RMS of GPS-derived pole estimates [μ**as**]	340.6	264.2	370.1	287.7
RMS of difference with model [μ**as**]	139	129	162.9	144.8
RMS of internal pole overlaps [μ**as**]	155.4	156.8	275.7	281.1
Correlation with model	0.91	0.87	0.90	0.86

Table 9.7: Impact of parameterization of 1-cpr acceleration on pole estimates

9.2 Polar Motion deconvolution

Once the tidally-coherent components of the signal removed by means of the IERS model discussed earlier, the residual time series contain not only the effects of atmospheric tides, oceanic and atmospheric normal modes but also non-tidal signals caused by the interactions between the different sub-systems of the Earth. Unfortunately, the residuals are also contaminated by any artifact specific to the estimation strategies as well as by model errors. As a consequence, as much of the remaining signal as possible needs to be identified in order to infer a more precise noise level. To this end, the GPS-derived polar motion time series are typically compared with combined Atmosphere and Ocean Effective Angular Momentum Function ([A+O]EAMF) series. This method was used to check how well the general circulations of the atmosphere and the oceans could be recovered. The challenges associated with this comparison are addressed in the sections below. Upon completion of this task, the portions of the signals correlated with the series generated from geophysical sources were filtered out. Based on the final estimated noise level, insight was gained into the types of geophysical events or processes detectable in the residual time series. The trustworthiness of the models and reality of the signals detected are also discussed.

The first step that needs to be taken to enable a direct comparison of EAMF series and the estimates of polar motion is to convert the latter into the excitation formalism. This is done through polar motion deconvolution.

9.2.1 Concept and associated Transfer Functions (TF)

Due to the presence of resonant modes in the rotation of the Earth, the observed variations in the pole coordinates result from the convolution of geophysical excitations with the free modes of polar motion (the Chandler and Nearly Diurnal Free wobbles). Equation 9.4 describes the convolution of the excitations with the Chandler wobble.

$$\vec{p}(t) = \exp(\mathrm{i}\sigma_{cw}\, t) \left[\vec{p}(t_0) - \mathrm{i}\sigma_{cw} \int_{t_0}^{t} \vec{\chi}(\tau) \exp(\mathrm{i}\sigma_{cw}\, \tau)\, \mathrm{d}\tau\right] \tag{9.4}$$

It is the general solution of the ordinary differential equations governing the relationship between polar motion and excitation:

$$\vec{p}(t) + \frac{\mathrm{i}}{\sigma_{cw}} \dot{\vec{p}}(t) = \vec{\chi}(t) \tag{9.5}$$

where σ_{cw} denotes the angular frequency of the Chandler wobble and is expressed in complex form as:

$$\sigma_{cw} = \frac{2\pi}{T_{cw}} \left(1 + \frac{\mathrm{i}}{2Q_{cw}}\right) \tag{9.6}$$

In Eq. 9.6, T_{cw} is the period of the Chandler wobble and Q_{cw} is a quality factor accounting for dissipation [199]. The transfer function including the contribution of the free core nutation is shown in Eq. 9.7.

In that context, polar motion deconvolution denotes the process by which the geodetic excitation vector at each epoch is inferred from the polar motion observations. The reason why observed polar motion needs to be deconvolved and converted to equivalent excitation vectors instead of proceeding the other way around (i.e. converting the geophysical excitation vector into polar motion) is detailed by Chao in [45]. The former procedure is commonly referred to as the "direct approach" in the literature whereas the latter is known as the "integrated approach".

Brzeziński extended Eqs. 9.5 to include the resonant effects of the free core nutation at nearly diurnal frequencies using Sasao and Wahr's dynamical theory ([166]). These equations are known as the "broadband Liouville equations of polar motion" and are reviewed in [29]. They are formulated in the frequency domain and are reproduced below.

$$\vec{p}(\sigma) = \frac{\sigma_{cw}}{\sigma_{cw} - \sigma}\left[\vec{\chi}^{p}(\sigma) + \vec{\chi}^{m}(\sigma)\right] + \frac{\sigma_{cw}}{\sigma_{fcn} - \sigma}\left[a_p\,\vec{\chi}^{p}(\sigma) + a_m\,\vec{\chi}^{m}(\sigma)\right] \tag{9.7}$$

with:

$$\sigma_{cw} = \frac{2\pi}{T_{cw}}\left(1 + \frac{\mathrm{i}}{2\,Q_{cw}}\right) \text{ and } \sigma_{fcn} = -\frac{2\pi}{T_{fcn}}\left(1 - \frac{\mathrm{i}}{2\,Q_{fcn}}\right) \tag{9.8}$$

In Eq. 9.8, σ_{fcn} represents the rotational rate of the nearly diurnal free wobble. The values employed for the period of the Chandler wobble T_{cw} and the associated dissipation factor Q_{cw} are the values given in [93]. The values for the equivalent quantities in the case of the nearly diurnal free wobble are picked from [32]. The values used are reproduced below:

$$T_{cw} = 433 \text{ days} \ , \ T_{fcn} = 1 - \frac{1}{431} \text{ days} \tag{9.9}$$

$$Q_{cw} = 179 \ , \ Q_{fcn} = 30,000 \tag{9.10}$$

Besides, the a_p and a_m parameters are constants specific to the mass and motion terms, respectively. Their numerical values are equal to 9.2e-2 and 5.5e-4, respectively, accor-ding to [32]. When the FCN resonant effect is accounted for, the pressure (superscript p above) and motion (superscript m above) terms need to be multiplied with their associated transfer function separately. Their contributions are then summed, still in the frequency domain. For this reason, performing comparisons between geophysical and geodetic excitations in the nearly diurnal frequency band in the time domain gets complicated and is typically avoided.

9.2.2 Discretization of the polar motion ordinary differential equations

In practice, the polar motion ODEs need to be discretized. Several algorithms have been proposed over the years and build on each other. They are reviewed in this subsection.

First, starting from Eqs. 9.4 and replacing the continuous functions $\vec{p}(t)$ and $\vec{\chi}(t)$ by their equivalent discrete forms and the integral over time by the corresponding discrete sum, Wilson and Haubrich expressed the excitation vector at epoch t in terms of polar motion observations (or estimates in our case) at epochs t and $t-1$. Their discrete solution, developed in [201], is reproduced in Eq. 9.11.

$$\vec{\chi}(t) = \frac{\mathrm{i}}{\sigma_{cw}\,\Delta T}\left[\vec{p}(t) - \exp(\mathrm{i}\,\sigma_{cw}\,\Delta T)\,\vec{p}(t-\Delta T)\right] \tag{9.11}$$

In Eq. 9.11, ΔT and t denote the sampling interval of the observations and the sampling epoch, respectively.

Improving upon Eqs. 9.11, Wilson [199] established discrete polar motion equations that enable the recovery of variations in the excitation vector at epochs placed exactly in between samples of polar motion estimates, as shown below.

$$\vec{\chi}(t) = \mathrm{i}\,\frac{\exp(-\mathrm{i}\pi\,F_{cw}\,\Delta T)}{\sigma_{cw}\,\Delta T}\left[\vec{p}\left(t + \frac{\Delta T}{2}\right) - \exp(\mathrm{i}\sigma_{cw}\,\Delta T)\,\vec{p}\left(t - \frac{\Delta T}{2}\right)\right] \tag{9.12}$$

Wilson and Chen [200] modified Eqs. 9.12 to correct numerical errors arising for short periods. They empirically designed two different digital filters characterized by their transfer functions. The first one consists in a single-stage filter, the transfer function of which is written below.

$$TF_{single-stage} = 1.5151\,\frac{-\mathrm{i}\,\sigma_{cw}\,\Delta T\,\exp[\,\mathrm{i}\pi\,(F_{cw}-f)\,]\,[\,2.3 + \exp(\mathrm{i}\,(\sigma_{cw}-2\pi f)\,\Delta T)\,]}{[\,1 - \exp(\mathrm{i}\,(\sigma_{cw}-2\pi f)\,\Delta T)\,][4.0 + \exp(\mathrm{i}(\sigma_{cw}-2\pi f)\Delta T)\,]} \tag{9.13}$$

The second filter is a revised version of the first one and is a two-stage filter. The phase error introduced by the single-stage filter case relative to the geophysical transfer function is corrected by running a zero-phase forward and reverse digital filter on the output of the single-stage filter. The transfer function of the zero-phase filter is given in Eq. 9.14 and reproduced from [200] again. This last version is the one used to obtain the results shown in the results section that follows.

$$TF_{two-stage} = \frac{c_1\,\exp(-\mathrm{i}\,\sigma_{cw}\,\Delta T) + c_2\,\exp(-\mathrm{i}\,2\pi f\,\Delta T) + c_3\exp[\,\mathrm{i}(\sigma_{cw} - 4\pi f)\,\Delta T\,]}{1 - c_4\exp[\,\mathrm{i}(\sigma_{cw} - 2\pi f)\Delta T\,]} \tag{9.14}$$

where the numerical values of the c_i parameters are:

$$c_1 = 0.9304\ ;\ c_2 = 0.5024\ ;\ c_3 = 0.01861\ ;\ c_4 = -0.4541 \tag{9.15}$$

Figure 9.8 is a diagram of the transfer functions associated with the Chandler wobble resonance. The top portion of the plot displays the magnitude of the transfer function while the bottom part shows its phase. The digital transfer functions obtained for the three different deconvolution schemes reviewed above are compared with the geophysical transfer function (shown in red). The geophysical transfer function is given by Eq. 9.16, in which f represents the frequency.

$$TF_{ideal}(f) = \frac{\sigma_{cw}}{\sigma_{cw} - 2\pi f} \tag{9.16}$$

The blue curve corresponds to the implementation of the transfer functions derived by Wilson in [199] based on his discrete approximation of the polar motion differential equations, shown in Eq. 9.12. The green curves are obtained by coding up the so-called single-stage filter transfer function numerically designed by Wilson and Chen to improve on the accuracy of Wilson's original transfer function at high frequencies. Finally, the magenta curve corresponds to the revised version of the single-stage filter detailed in [200] as well. The accuracy of the last implementation is notably better than that of the other two in terms of both phase and magnitude, as visible on Fig. 9.9.

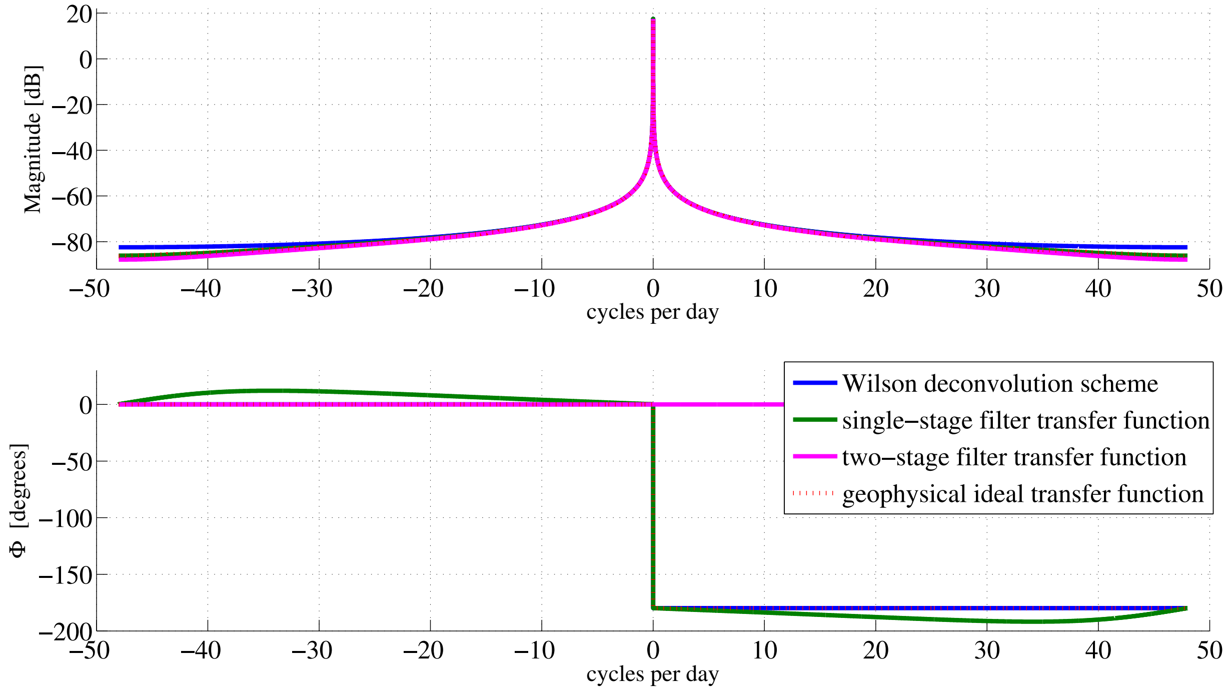

Figure 9.8: Numerical transfer functions

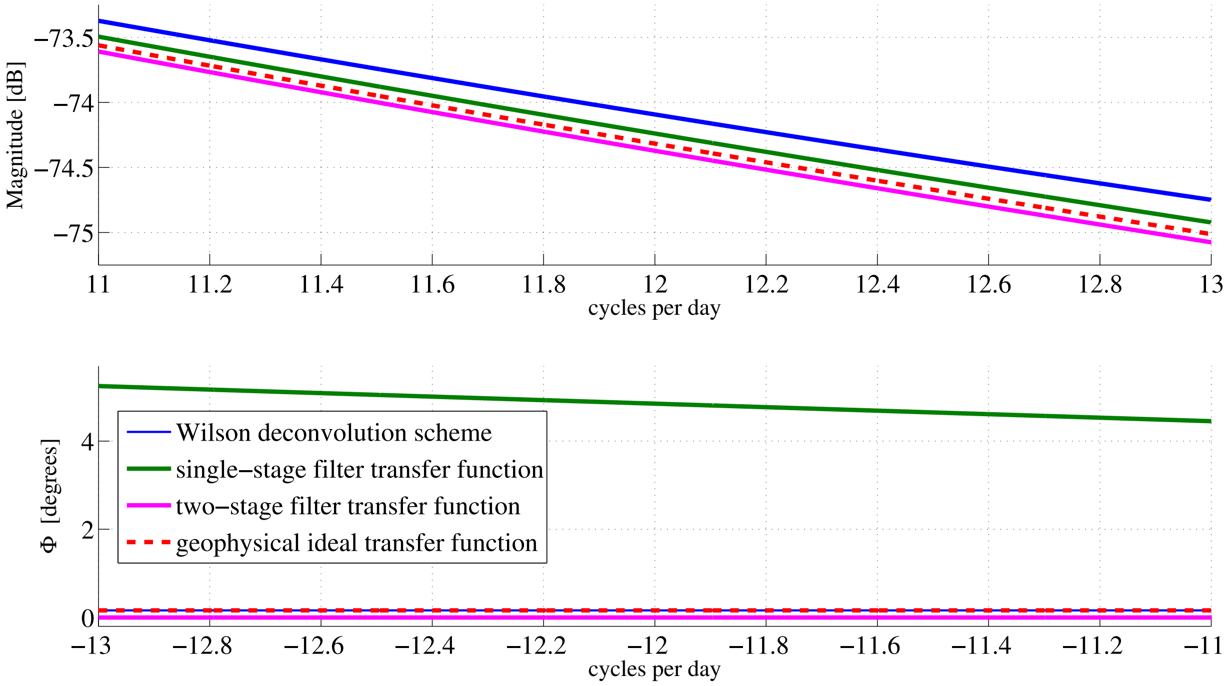

Figure 9.9: Zoom on numerical errors

9.2.3 Implementation of the deconvolution procedure

The rigorous procedure followed to deconvolve the estimated pole coordinates in the frequency band characteristic of rapid polar motion is outlined below. Four steps are identified and it is noteworthy that, with the exception of step (3), the real and imaginary parts of polar motion are treated separately.

(1) Cubic hermitian interpolation

To begin with, the nominal EOPC04 polar motion series are updated to include the estimated corrections. Cubic splines are employed to interpolate the reference solution based on the offsets and rates of the pole coordinates. The choice of this interpolation scheme is natural since geophysical processes are characterized by their smoothness and continuity over time (with the exception of singular events such as earthquakes). No averaging scheme is used in the process of updating the reference solution. Both the pole solutions and the geophysical excitation series are de-trended as an initial step.

(2) Sampling of the GPS products

Once interpolated and updated, the GPS-derived series are decimated to match the sampling rate of the geophysical excitation functions, the time-lag introduced by the deconvolution process is accounted for in doing so.

(3) High-frequency polar motion deconvolution

The deconvolution of the pole coordinates estimates is then performed by means of Wilson and Chen's two-stage filtering procedure. Edge effects are removed at both ends of the time span. The algorithm is depicted in a following paragraph.

(4) Butterworth bandpass filtering

A Butterworth bandpass filter with cut-off periods of 2 and 20 days is then applied to both the geophysical and geodetic (observed) time series to retain the forcing frequencies related to rapid polar motion only. The orders of the low- and high-pass Butterworth filters used in combination with each other to form a bandpass are chosen based on trial and error.

9.2.4 Current limitations in the deconvolution method

As seen above, the path taken for the deconvolution of the pole coordinate series consists in approximating the continuous differential equations by the corresponding difference equations. This method offers the advantage of being readily applicable to the analysis of discrete time series of estimates. However, a strong shortcoming resides in the neglect of the formal errors associated with the pole coordinate estimates. Indeed, accounting for the presence of noise on the measurements (i.e. the polar motion estimates can be viewed as pseudo-observations in this case) or the statistical properties of that noise is impossible. Moreover, digital deconvolution renders the series much noisier than they originally are, according to [45]. So-called regularization and corrective smoothing procedures have been investigated by Zotov in [209] but the studies focused on the recovery of long-period polar motion, as a result these techniques may not be suitable for high-frequency polar motion.

A more appropriate way to proceed would be to employ a statistical method. A Kalman filter combined with the auto-regressive modeling of the excitations is the common alternate approach to the use of a digital filter. This solution however requires additional efforts to establish an adequate model for the excitation data. The main difficulty resides in the parameterization of the process noise. Setting up the stochastic deconvolution procedure, one needs to decide on realistic covariance levels for the excitation processes, as well as on which processes to include. The tuning of this estimation strategy is the key to balance the precision of the excitation estimates with their time resolution.

Kalman filter deconvolution algorithms have been implemented in the frequency domain by Gross and Chao who reported their findings in [91] and later in the time-domain by Morabito, Eubanks and Steppe in [146]. The latter designed the process noise matrix based on the power spectra of the excitation functions. In both cases, the deconvolution was restricted to long-period polar motion. The concept of statistical deconvolution was revisited by Brzeziński in a series of two papers [24] and [25]. He concluded on the impracticality and challenging nature of the method.

9.3 Recovery of non-tidal oceanic and atmospheric variations

The purpose of this section is to contrast geophysical effective angular momentum functions (EAMF) against geodetic excitation functions derived from the GPS-derived pole coordinates. In this context, the estimated quality of the solutions depends on how much of the short-period fluctuations contained in the equatorial geophysical EAMF can be related to rapid variations in the deconvolved polar motion estimates. The intention is not to explain nor discuss in depth the geophysical processes occurring within the different subsystems of the Earth or their interactions. Such scientific considerations are beyond the scope of this work. For an overview of these, the reader is referred to specialized treatises of geophysics.

9.3.1 Atmospheric and oceanic effects on polar motion

As mentioned in Chapter 3, global oceanic and atmospheric circulations have been shown to give rise to non-tidal variations in polar motion. Water mass redistribution within the oceans plays a major role in the variations of polar motion through forcing from ocean bottom pressure changes. Additionally, oceanic currents affect polar motion variability via the production of relative angular momentum. It is believed that the oceanic excitation of polar motion occurs over periods longer than one day [186]. Atmospheric winds and global air pressure changes are responsible for a portion of the observed rapid polar motion as well. In particular, atmospheric forcing of polar motion is expected at diurnal and semi-diurnal frequencies due to thermally-driven atmospheric tides. The oceanic and atmospheric effects are somewhat coupled since the non-tidal changes in water heights and currents are partly induced by winds and atmospheric pressure changes.

The general circulation of the atmosphere and oceans are monitored by the IERS Special Bureau for Atmosphere (SBA) and Special Bureau for Oceans (SBO), respectively. A comparison of EAMF series using different data sets for the atmosphere and the oceans reveal that the effects of atmospheric forcing on rapid polar motion are better known than those of oceanic forcing, as illustrated in [84]. In addition, atmospheric effects on the rotational behavior of the Earth have been more widely studied than their oceanic equivalent. This stresses the complexity of global ocean modeling.

In addition to the purely oceanic forcing, the oceanic response to the atmospheric pressure load is known to somewhat modify the excitation of the Earth's rotation induced by fluctuations of the air pressure. This effect is taken into account by means of corrections introduced in the atmospheric effective angular momentum function series computed. Due to the lack of knowledge regarding the reaction of the oceans to the atmospheric forcing, hypotheses are made. Three types of responses characterizing the interaction between the atmosphere and the oceans exist. They are briefly discussed here.

(1) the inverted-barometer (IB) hypothesis or static ocean assumption

This hypothesis is only valid for periods longer than a few days, which corresponds to periods for which the ocean has time to readjust and perfectly compensate for the atmospheric pressure loading. The limit for the validity of this hypothesis is typically set to 10 days, but it is still deemed valid for periods longer than 2 days [Gross, personal communication, 2011]. It is therefore traditionally used in practice for rapid polar motion investigations.

(2) the dynamic-barometer response

Oceanic dynamic-barometer corrections have been derived and calculated by Dickman. The motivation behind the study presented in [64] is stated to be the failure of the IB hypothesis to account for the oceanic currents driven by the atmospheric pressure loading. Stieglitz and Dickman showed in [181] that slightly better correlations between geophysical and geodetic excitations were obtained using this type of oceanic response. However, they are the only researchers, to the best of our knowledge, to have computed and used such a model [Gross, personal communication, 2011]. The reason why the use of this model has remained experimental is undetermined. The extent to which the use of the other two hypotheses are limiting factors to the accuracy of the comparison between the observed and geophysical excitations is not quantified.

(3) the non-inverted barometer (Non-IB) approximation

This approximation constitutes the extreme opposite to the IB hypothesis. The oceans are treated as perfectly rigid and assumed not to yield to air pressure loading at all. At very short time scales (diurnal and below), when the ocean has almost no time to react to ultra-rapid variations in the atmospheric pressure, the atmosphere and oceans can be assumed to be decoupled [Brzeziński, personal communication, 2011].

9.3.2 Data sets

The time series of estimates considered for this study are a priori corrected for the sub-daily, tidally-induced polar motion effects by means of the IERS-recommended model implemented in GIPSY. They are the same series as the ones analyzed in Chapter 8. Among the various EAMF series published, the operational oceanic angular momentum (OAM) and atmospheric angular momentum (AAM) series supplied by the GFZ and ECMWF centers, respectively, were used as references. The ECMWF AAM series used are involved in weather forecasts and have a daily latency; the OAM series supplied by GFZ are updated daily and have a five-day latency. This choice was dictated by the high temporal resolution of the series (6 hours) and the availability of OAM and AAM series consistent with each other. In addition, there are no discontinuities or duplicates in the data sets and the series benefit from good data coverage. A review of the series available from different centers and the possible combinations recommended for consistency is provided by Chen and Shen in [50]. The meteorological data assimilation systems and models used by the ECMWF and GFZ centers to produce the solutions used as nominals here are detailed in [66]. The geophysical excitation series include the effects of rotational deformation, elastic deformation and decoupling of core motion from the mean mantle as highlighted in Eqs. 3.32. The oceanic model used by the GFZ center for geosciences is the Ocean Model for Circulation and Tides developed by Thomas [184]. It is forced by the operational ECMWF analysis data from which the AAM series used as nominals are derived, which guarantees the consistency of the two types of series (see [82] for information on the ECMWF atmospheric data sets). Atmospheric forcing includes wind stress, surface pressure as well as heat and freshwater fluxes [83], [81]. Ideally, the effects of all the fluid layers of the Earth should be accounted for in the comparison. Even so, this research was restricted to the study of the atmospheric and oceanic forcings of polar motion. Daily-resolved hydrological angular momentum function values are available through the GFZ IERS Analysis Center but their quality has sometimes been questioned. Cryospheric AMF are not available yet but could be provided soon according to Dickman [EGU 2011].

9.3.3 Results obtained for rapid polar motion

The agreement between the geophysical and geodetic excitation series in the rapid polar motion period range (i.e between 2 and 20 days) is tested by computing their coefficients of correlation. The statistical significance of these quantities is established since Stieglitz and Dickman verified the statistical significance of the correlation between atmospheric angular momentum variations and polar motion at the 99.7 % level by means of Monte Carlo simulations. The null hypothesis tested in their Monte Carlo experiments was stated by them in these terms: ”the observed correlation between geodetic and atmospheric excitation is not statistically distinguishable from correlations between geodetic excitation and noise or between atmospheric excitation and noise” [181].

The results yielded by each strategy are gathered in Table 9.8. The independent contributions of the oceans and the atmosphere are also computed for information.

	30-hour		**3-day**		**9-day**	
	χ_1	χ_2	χ_1	χ_2	χ_1	χ_2
ρ(aam+oam,est)	0.79	0.80	0.82	0.82	0.80	0.82
ρ(aam,est)	0.29	0.45	0.28	0.45	0.29	0.45
ρ(oam,est)	0.35	0.32	0.39	0.33	0.37	0.34

Table 9.8: Correlation between the geophysical and geodetic excitations

A spectral analysis was conducted to ease the visualization. Amplitude spectra for both coordinates of the excitation vectors are displayed in Fig. 9.10.

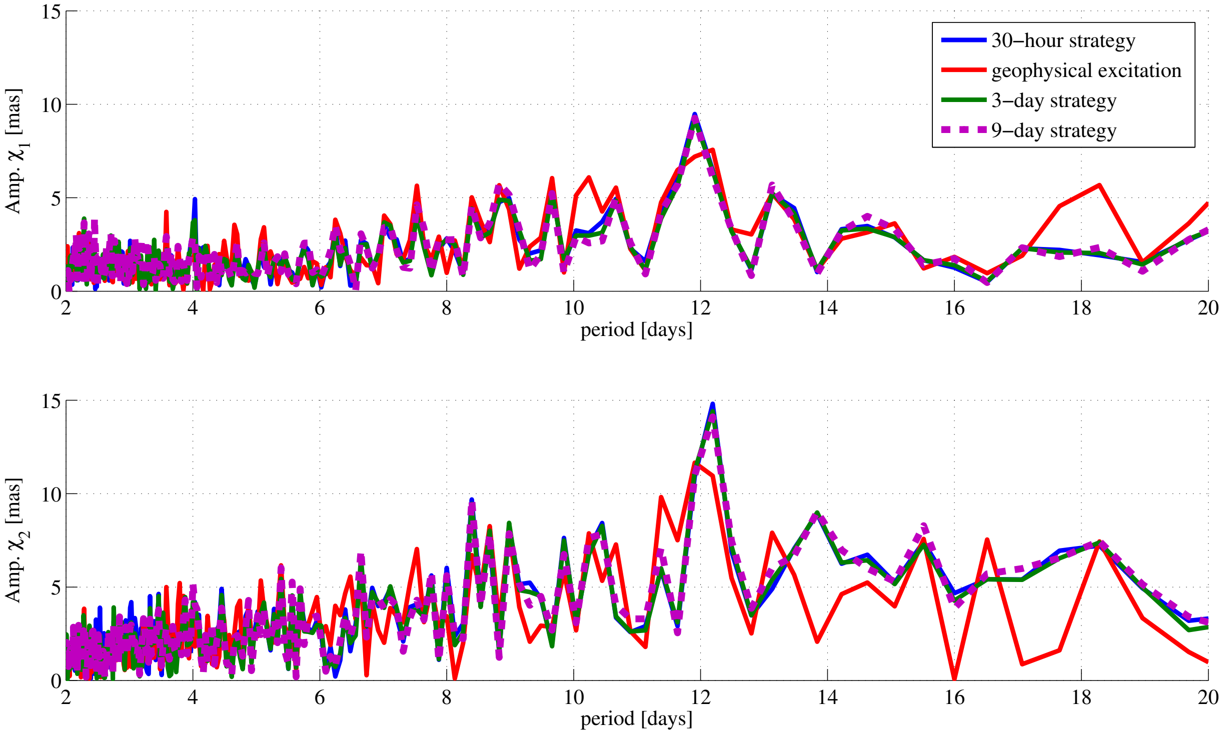

Figure 9.10: Excitation spectra - Rapid polar motion frequency band

The peak appearing for periods of 12 days could not be identified. To the best of the author's knowledge there are no specific geophysical signals occurring around that period. The coherence between the geophysical excitation function vector and the geodetic excitation vector is computed for each of the candidate strategies based on the multi-taper coherence method (see [151] for instance). The results obtained in terms of squared coherence and phase lag are plotted on Fig. 9.11. The curves almost coincide for the three strategies, confirming what is observed on the amplitude spectra shown above.

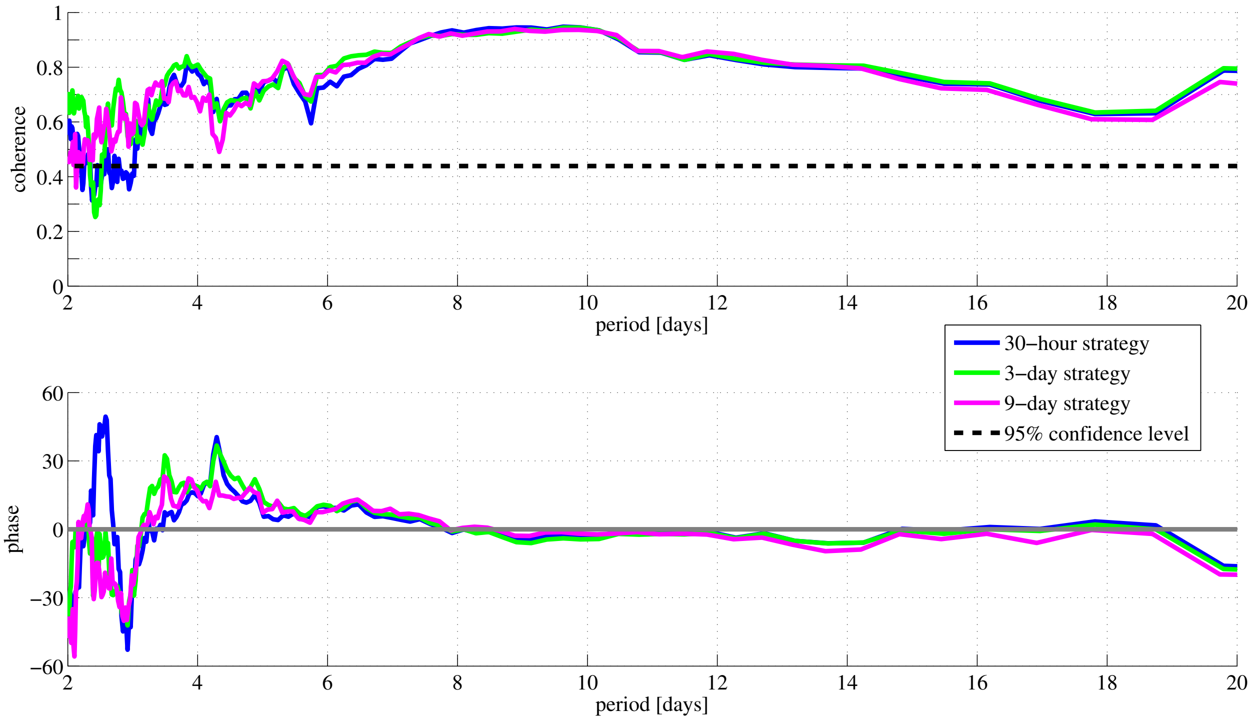

Figure 9.11: Magnitude squared coherence function relative to geophysical EAMF series

The set of results presented above confirm the good quality of the polar motion solutions. The spectral and coherence analyses highlight the fact that the strategy differ in their ability to recover non-tidal variations in polar motion excitation at very high frequencies only. The correlations achieved with the geophysical excitations are very satisfactory for all three estimation strategies.

9.3.4 Impact of arc length

The impact of the arc length on the recovery of polar motion was assessed by checking the correlation for the different test cases depicted in section 7.5.3. The results are recorded in Table 9.9.

	ρ(aam+oam,est)		ρ(aam,est)		ρ(oam,est)	
	χ_1	χ_2	χ_1	χ_2	χ_1	χ_2
30 hours	0.76	0.80	0.29	0.46	0.31	0.32
3 days	0.82	0.82	0.28	0.45	0.39	0.33
5 days	0.83	0.82	0.29	0.45	0.38	0.34
7 days	0.82	0.82	0.29	0.46	0.37	0.33
9 days	0.82	0.82	0.29	0.45	0.38	0.34

Table 9.9: Impact of arc length on correlation with ECMWF EAMF series

Table 9.9 implies that the impact of the arc length on the correlation between the geophysical excitation functions and their geodetic equivalent is not statistically significant.

9.3.5 Impact of update interval

As done before, the effects of the pole coordinate update frequencies on the agreement between the geophysical and geodetic excitation series were quantified using the same technique as in section 7.4.1. The results are visible in Table 9.10. The conclusion can be drawn that the pole coordinate estimation interval does not have a statistically significant influence on the recovery of rapid polar motion either. In fact and even though the differences between the test cases are negligible, the 15-minute test case exhibits the highest correlations with the geophysical series. The reason why no results are shown for the 7-minute case is that comparing both series would require interpolating one or the other, thus adding more noise and inaccuracies into the results of the comparison.

	ρ(aam+oam,est)		ρ(aam,est)		ρ(oam,est)	
	χ_1	χ_2	χ_1	χ_2	χ_1	χ_2
7 min	N/A	N/A	N/A	N/A	N/A	N/A
10 min	0.75	0.79	0.28	0.46	0.33	0.32
12 min	0.77	0.79	0.29	0.45	0.33	0.32
15 min	0.78	0.80	0.29	0.46	0.35	0.32

Table 9.10: Impact of the pole coordinate estimation interval on the correlation with ECMWF EAMF series

9.3.6 Impact of transmitter and receiver antenna calibrations

Changes in antenna calibrations hardly impact the agreement between the geophysical and geodetic excitations at all. The use of IGS receiver maps and the GRACE-based transmitter calibration files still results in the highest correlations, as seen in Table 9.11.

	ρ(aam+oam,est)		ρ(aam,est)		ρ(oam,est)	
	χ_1	χ_2	χ_1	χ_2	χ_1	χ_2
IGS/GRACE	0.82	0.82	0.28	0.45	0.39	0.33
IGS/IGS	0.81	0.81	0.29	0.45	0.37	0.33
Mesa/IGS	0.78	0.79	0.26	0.43	0.40	0.32

Table 9.11: Impact of antenna calibrations on the correlation with ECMWF EAMF series

9.3.7 Impact of the selected coordinate system for the once-per-revolution custom accelerations

The choice of reference system for the parameterization of the 1-cpr accelerations does not matter either in terms of rapid polar motion recovery, as verified in Table 9.12.

	ρ(aam+oam,est)		ρ(aam,est)		ρ(oam,est)	
	χ_1	χ_2	χ_1	χ_2	χ_1	χ_2
HCL frame	0.82	0.82	0.28	0.45	0.39	0.33
UVW frame	0.82	0.81	0.29	0.46	0.36	0.32

Table 9.12: Impact of coordinate system used to express the 1-cpr acceleration on the correlation with ECMWF EAMF series

The fact that all the series are more or less equivalent when investigating rapid polar motion could reflect the weakness of the Butterworth bandpass filtering. A more finely tuned filter might yield slightly different results; this could require switching to an entirely different type of filter, as suggested in Chapter 10.

Before the case of ultra-rapid polar motion is discussed, some of the assumptions implicitly made for the investigation of rapid polar motion and invalid at nearly diurnal frequencies are reviewed and revised.

9.3.8 Review of the ”long-period” assumptions made

Some strong low-frequency assumptions are made in the derivation of the ordinary differential equations governing the relationship between geophysical excitation and polar motion. As a consequence, they lose their validity in the nearly diurnal and diurnal frequency bands. These long-period assumptions are reviewed and commented here. To begin with, the EAMF series provided by the ECMWF and GFZ assume the decoupling of the mantle and core. However, the inertial coupling between core and mantle is known to become very important in the vicinity of the diurnal retrograde frequency, since the FCN resonance occurs then. In this case, even when the broadband Liouville equations are used in replacement of Wilson’s polar motion equations, the assumptions introduced in the computation of the geophysical EAMF may invalidate any result obtained in the nearly-diurnal frequency band. Furthermore, the closed-system assumptions do not hold anymore for nearly diurnal frequencies. The angular momentum of the system is not conserved anymore because the gravitational torque is not negligible. Indeed, the retrograde frequency band ranging from 16h to 48h corresponds to nutation, as stressed in Fig. 2.3.

9.3.9 Current limitations to the evaluation of ultra-rapid polar motion

Beside the assumptions discussed above, several other obstacles hinder the ana-lysis of the geodetic and geophysical excitation series in the search for ultra-rapid polar motion signals. On the one hand, geophysical EAMF data are officially not considered trustworthy at periods of the order of 1 day due to a significant drop in coherence both between the series generated by different centers and between the model-based atmospheric torques and the torques evaluated by differentiation of the EAM data (e.g. [29] or [55]). In addition, the non-tidal OAM series with subdiurnal resolution still have an experimental character due to deficiencies in the knowledge of oceanic processes at this resolution. Likewise, the AAM series including the IB hypothesis might not be reliable at high frequencies based on the divergence of opinions regarding the type of hypothesis to be considered as far as the oceanic response to atmospheric forcing at such short periods is concerned. On the other hand, the fact that most oceanic and atmospheric circulation models are forced every 6, 12 and 24 hours only constitutes a serious limitation to the investigation of very-high-frequency variations. In particular, confirming the presence of ter-diurnal variations in the geophysical data would be interesting but is currently unachievable with 6-hour resolved EAMF series. Likewise, the detectability of the semi-diurnal atmospheric tides, another interesting feature of ultra-rapid polar motion, cannot currently be assessed. Ultimately, even though the transfer functions included in Eq. 9.17 exhibit a resonance at the FCN frequency, their use requires taking an integration approach, which, according to Chao, can be misleading [45].

$$\vec{p}(\sigma) = T_p(\sigma)\,\tilde{\vec{\chi}}^{p}(\sigma) + T_m(\sigma)\,\tilde{\vec{\chi}}^{m}(\sigma) \tag{9.17}$$

with

$$\begin{cases} T_p(\sigma) = \sigma_{cw}\left(\dfrac{1}{\sigma_{cw}-\sigma} + \dfrac{a_p}{\sigma_{fcn}-\sigma}\right) \\[2ex] T_m(\sigma) = \sigma_{cw}\left(\dfrac{1}{\sigma_{cw}-\sigma} + \dfrac{a_m}{\sigma_{fcn}-\sigma}\right) \end{cases} \tag{9.18}$$

Overall, the interpretation of the results would be very complicated and most likely compromised by the combination of the model deficiencies and inaccurate methods mentioned.

9.4 Removal of identified non-tidal variations from estimated series

9.4.1 Dual-channel Wiener filtering: concept and implementation

Because the geophysical angular momentum is not entirely transferred to the rotational vector of the Earth, as determined by Stieglitz and Dickman by means of Monte Carlo simulations, simply substracting the geophysical excitation series from the geodetic data may not be the most effective way of removing the geophysical contribution from the observed excitations [181]. Wiener filtering was proposed as an alternative in the aforementioned journal article.

Wiener filters are designed to yield the best approximation to a desired output upon convolution with the input time series. The objective is therefore to minimize the mean square error between the desired output and the actual output, as expressed by Eq. 9.19.

$$\begin{gathered} J = \textstyle\sum_{i=0}^{n+l} \left[z_i - y_i\right]^2 \Delta t \\ \text{where } y_i = \textstyle\sum_{j=0}^{l} f_j \, x_{i-j} \, \Delta t \end{gathered} \tag{9.19}$$

In the equation above, x, y and z represent the input to and desired output as well as actual output of the filter, respectively. The filter is characterized by its coefficients f and is of length $l + 1$. n denotes the number of data points in the input and desired output series and Δt is the sampling period of the data. In practice, the performance criterion is equal to the trace of the mean square error matrix and depends entirely on the auto-correlation function of the desired output, cross-correlation of the input and desired output and on the filter coefficients to be estimated. The normal equations corresponding to this type of statistical filter are obtained by minimizing Eq. 9.19 with respect to the filter coefficients and are written:

$$\Phi_{zx}(j) = \sum_{i=0}^{l} f_i \, \Phi_{xx}(j - i)\Delta t \text{ with } j = 0, \ldots, l \tag{9.20}$$

In Eq. 9.20, Φ_{zx} denotes the cross-correlation between the desired output and input time series while Φ_{xx} represents the auto-correlation of the input signal. These normal equations are solved recursively following algorithms developed and discussed by Robinson in [158].

A clear illustration of the concept of the dual-channel Wiener filter is given in [35]. The block diagram is reproduced below using the notations introduced above.

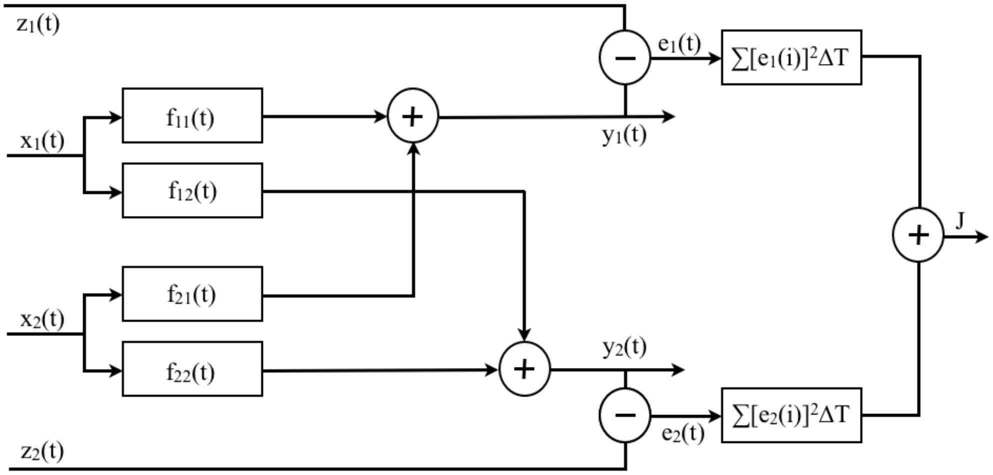

Figure 9.12: Block diagram of the dual-channel Wiener filter, adapted from [35]

The multi-channel Wiener filter algorithm was coded up following the procedure outlined by Robinson in [158]. The implementation was validated thanks to the test cases provided in that book.

9.4.2 Application to the study of rapid polar motion

As mentioned earlier, the Wiener filtering of geodetic excitation time series was first suggested by Stieglitz and Dickman in [181]. Di Leonardo et al. justified its application to the study of rapid polar motion both qualitatively and quantitatively in [61]. They also demonstrated the efficiency of the technique at removing the correlated portion of their estimated series from atmospheric effective angular momentum series. For this research, their method was extended to include the effects of the variations in the oceanic angular momentum vector.

In this configuration, the desired outputs are the geodetic time series while the inputs are the sum of the oceanic and atmospheric effective angular momentum functions series. The use of a two-channel filter offers the advantage of accounting for possible cross-excitations. In contrast, the use of two distinct regular Wiener filters would require the separate treatment of each coordinate.

The excitation residuals obtained by applying the two-channel Wiener filter implemented to the geodetic excitations output by the three candidate estimation strategies are shown below. Ideally, the time series should be dominated by changes in continental water storage, ice mass, atmospheric loading, core/mantle coupling, unidentified other sources of rapid polar motion. In reality, model errors and strategy artifacts are also represented in the residuals.

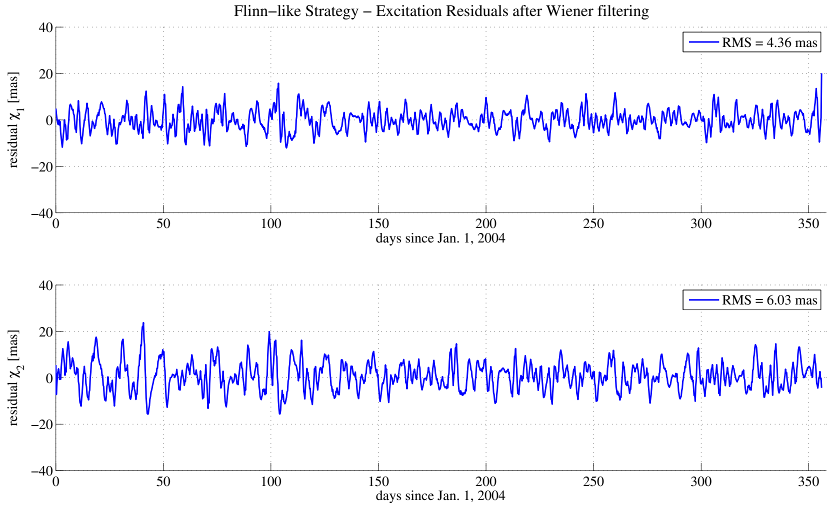

Figure 9.13: Excitation residuals - 30-hour strategy

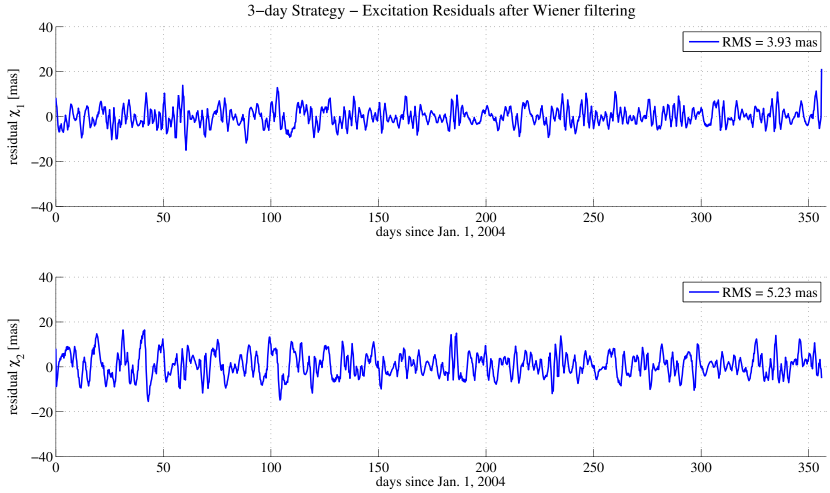

Figure 9.14: Excitation residuals - 3-day strategy

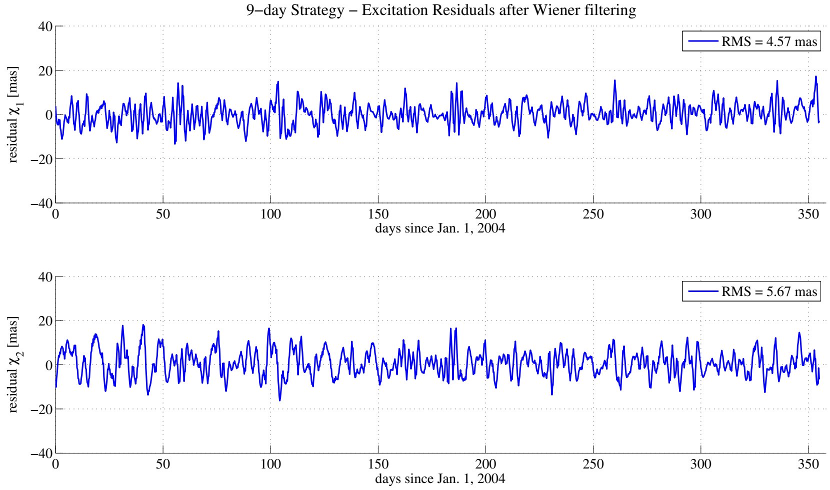

Figure 9.15: Excitation residuals - 9-day strategy

The time series of residuals displayed in Figs. 9.13, 9.14 and 9.15 clearly exhibit periodic patterns. Therefore, they were converted into their prograde and retrograde counterparts and corresponding amplitude spectra were plotted for further investigation. The spectra are shown in Fig. 9.16.

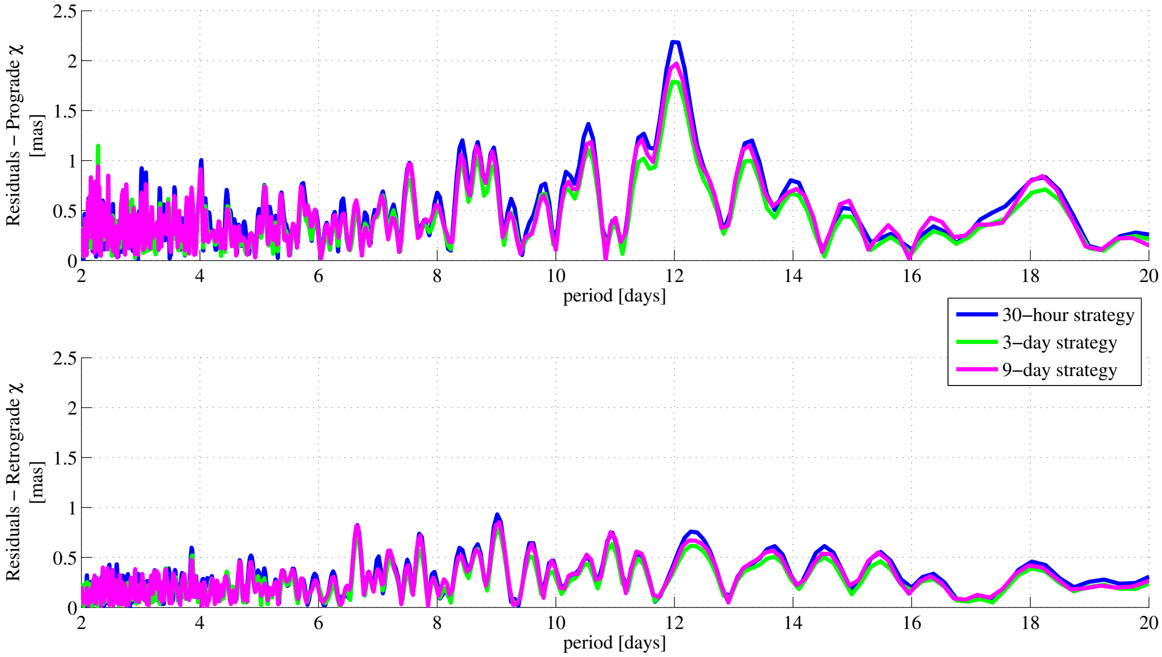

Figure 9.16: Amplitude spectra of excitation residuals for rapid polar motion

Peaks tend to be concentrated in the period band ranging from 7 to 14 days and in the prograde direction. Their exact origin is not determined but, in addition to all the potential sources already identified, they could indicate the limits of the Butterworth bandpass filtering process employed as well as small biases introduced in other stages of the deconvolution procedure. It is striking that a clear peak stands out in the prograde spectrum for periods of 12 days. Such a spectral line was already visible in the geophysical excitation obtained from the GFZ and ECMWF EAMF series in Fig. 9.10. No geophysical origin could be determined for this peak which should be investigated further.

The inability to compute confidence levels to conclude on the statistical signi-ficance of the spectral lines due to the absence of any uncertainty information proves to be detrimental in this case.

Switching to a statistical deconvolution scheme would definitely help determine the meaningfulness of the most powerful spectral lines.

9.5 Application to earthquake detection

9.5.1 Theoretical impact of earthquakes on polar motion

Earthquakes have been investigated for a long time as a potential source of excitation of the Chandler wobble. The interest in understanding and observing the impact of such geophysical events on the rotation of the Earth and the displacement of the Earth's figure axis was rekindled in the aftermath of the great Sumatra-Andaman islands earthquake of December 26, 2004. The reader interested in studies conducted on this event is referred to papers by Gross and Chao (see [92]) and Kouba (see [122]) for instance. Gross and Chao modeled the changes in ERP caused by the earthquake and compared their findings to an experimental data set while Kouba looked for observational evidence in the official IGS final ERP solutions. In spite of active on-going research in that field, the effects of earthquakes on polar motion have never been detected in reduced, space-geodetic observations. This is easily explained by the very low signal-to-noise ratios currently reached at the level of data reduction needed to separate the potential signature of an earthquake from the remainder of the geophysical processes, model errors and other artifacts contained in the geodetic observations (which only sense globally integrated geophysical signals).

The subject matter has been theoretically studied and modeled since the early 1970s. Earthquakes are thought to manifest as step functions in the excitation domain and as "kinks", i.e. sudden changes in the direction of velocity in the polar motion domain, manifesting as breaks in smoothness over long periods [154]. Due to the effect of the convolution with the Chandler wobble, the maximum change in direction is expected to be observed 7 months (i.e. half the Chandler wobble period) after an earthquake hits. Figure 9.5.1 illustrates the theoretical effects of earthquakes in both the polar motion and the excitation domains. The plot on the right-hand side reflects the fact that the effects of an earthquake on polar motion are permanent and accumulate with the impacts of other earthquakes over time.

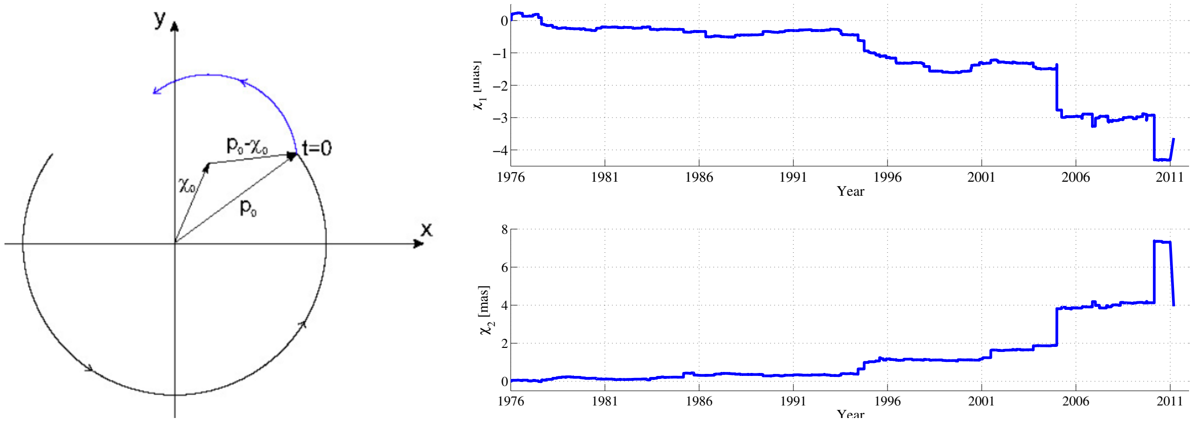

Figure 9.17: Modeled and simulated effects of earthquakes on the: a) polar motion vector, from [26] b) polar motion excitation vector since 1976 (data provided by Dr. Richard Gross and updated to include the 2011 Honshu earthquake)

The potential impact of an earthquake on the ERP variability is the result of a complex mechanism and is linked to three factors: the magnitude of the earthquake, its location and the focal mechanisms at play [92]. As stated by Gross and Chao, earthquakes do not load the Earth and are assumed to be instantaneous events, so that there is no relative angular momentum associated with such natural hazards [92]. Under these conditions, the equatorial effective angular momentum functions associated to the earthquake become, using the nomenclature introduced in Chapter 3:

$$\tilde{\tilde{\chi}}(t) = \frac{1}{1 - \frac{k_2}{k_s}} \frac{\vec{c}(t)}{(C_m - A_m)} \tag{9.21}$$

9.5.2 Application of this research to the 2011 M9.0 Japan earthquake

The earthquake considered for this short study hit Japan on Friday, March 11, 2011 at 05:46:23 UTC and was of moment magnitude 9.0, according to the United States Geological Survey (USGS) online publications. Based on the results of simulations run by Gross, presented in [90] and listed in Fig. 9.18, among the most recent major earthquakes monitored during the GPS era (except for the last two events mentioned), this particular earthquake has the highest likelihood of observability. Note that the 1σ uncertainties shown on the figure below were not calculated through the work presented here but are the uncertainties claimed by Dr. Richard Gross. It is promising to remark that our residuals are of the same order of magnitude and almost match the value of 5 mas for both pole coordinates.

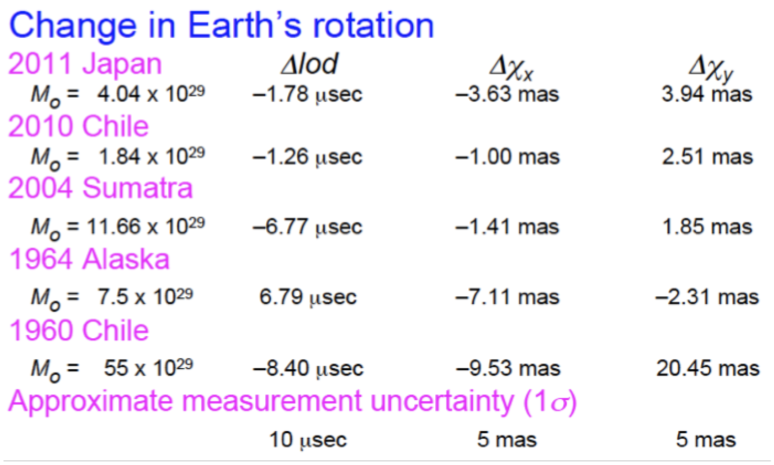

Change in Earth's rotation

	Δlod	$\Delta\chi_x$	$\Delta\chi_y$
2011 Japan			
M_o = 4.04 x 10^{29}	–1.78 μsec	–3.63 mas	3.94 mas
2010 Chile			
M_o = 1.84 x 10^{29}	–1.26 μsec	–1.00 mas	2.51 mas
2004 Sumatra			
M_o = 11.66 x 10^{29}	–6.77 μsec	–1.41 mas	1.85 mas
1964 Alaska			
M_o = 7.5 x 10^{29}	6.79 μsec	–7.11 mas	–2.31 mas
1960 Chile			
M_o = 55 x 10^{29}	–8.40 μsec	–9.53 mas	20.45 mas
Approximate measurement uncertainty (1σ)			
	10 μsec	5 mas	5 mas

Figure 9.18: Modeled change in Earth's rotation due to recent major earthquakes - slide provided by Dr. Richard Gross. The units of the scalar moment M_o are dyne-cm.

The data set considered for this case study span 6 months starting on January 1, 2011 and ending on June 9, 2011. The arc centered on the date of the earthquake was removed from the analysis. Since the 3-day strategy was the only one giving acceptable results, only one set of results are presented in this section. The data were not filtered during the post-processing stage in order to eliminate any error potentially resulting from the use of a bandpass Butterworth filter. Moreover, because the effect of the earthquake on the Earth's excitation vector can be modeled as a step function, filtering the data is not absolutely necessary in this case. The correlation coefficients reported in Table 9.13 tend to indicate that the unfiltered geophysical and geodetic excitation series are still fairly well correlated with each other. In particular, the χ_2 coordinate of the geodetic and geophysical excitation vectors are correlated at the conspicuous level of 60% in the case when only the contribution of the atmosphere is analyzed.

ρ(aam+oam,est)		ρ(aam,est)		ρ(oam,est)	
χ_1	χ_2	χ_1	χ_2	χ_1	χ_2
0.51	0.69	0.27	0.60	0.27	0.27

Table 9.13: Correlation coefficient between geodetic and ECMWF EAMF series

Large biases affect the geodetic excitation data along both the x- and y-directions, and, to a much smaller extent, the geophysical data as well. The biases affecting the polar motion excitation vector coordinates are shown in Fig. 9.19. The geodetic excitation series are plotted in blue while the red curves correspond to the geophysical excitation series. The bias on the χ_2 coordinate of the deconvolved polar motion series is particularly large.

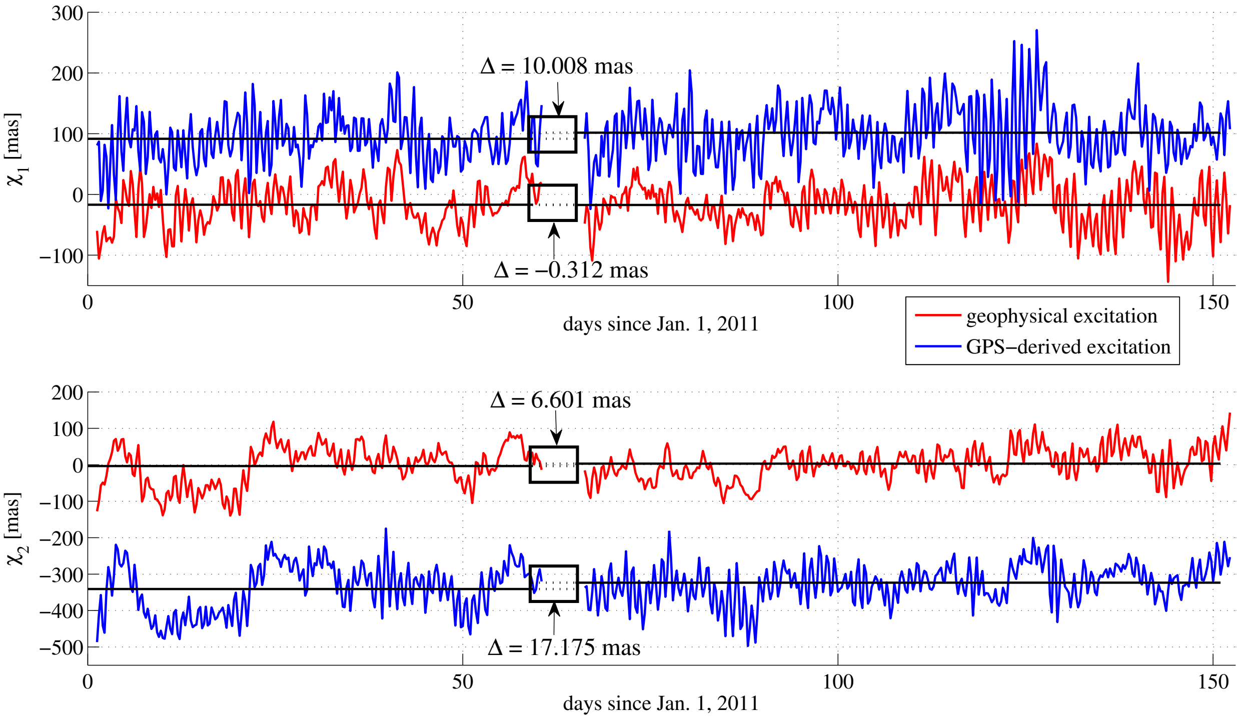

Figure 9.19: Excitation: 3-day strategy

The origin of the offsets observed still remains unexplained and unfortunately prevents the use of the dual-channel Wiener filter discussed earlier. Indeed, applying the Wiener filter would necessitate detrending the series, which would directly conflict with the objective of the study, i.e. investigating whether or not a (statistically significant) change in bias occurs between the segments processed before and after the earthquake. For this reason, the entire time series of EAMF was substracted from the deconvolved estimates of polar motion. While not ideal for reasons explained in [181], this technique is commonly used (see [92] for example) and it is believed that, under the circumstances of interest, proceeding that way should not affect the change in bias. An interesting feature of the four curves plotted on Fig. 9.19 lies in the fact that both the geodetic and geophysical excitation series exhibit changes in their means when comparing the segment spanning the pre-earthquake period with the one covering the period immediately following the earthquake. The differences in offsets amount to -0.3 mas and 6.6 mas in the case of the geophysical excitations for the χ_1 and χ_2 coordinates, respectively. The means of the geodetic χ_1 and χ_2 coordinates change by 10 mas and 17.17 mas, respectively.

To gain insight into the relative contributions of the atmospheric and oceanic forcings to the total bias in the geophysical excitation series, the changes in means observed for each individual forcing source were computed. The values are denoted $\Delta mean$. The results are shown in Table 9.14.

	Δmean [A+O]EAMF	**Δmean** Oceans	**Δmean** Atmosphere
$\boldsymbol{\chi_1}$	-0.31	5.92	-6.23
$\boldsymbol{\chi_2}$	6.60	-7.48	14.08

Table 9.14: Statistics on the EAMF series before and after the earthquake. Units are mas.

It is clear that both subsystems contribute to the overall bias. Their contributions tend to be in opposite directions and even almost cancel each other out as far as the χ_1 component is concerned. The results are somewhat intriguing and raise many questions that remain open. To analyze their implications, it seems critical to understand if the biases observed are directly related to the earthquake or can be considered a natural phenomenon. Indeed, this finding could question the validity of the assumption that the effects of the earthquake on the oceans and the atmosphere are only transient. Therefore, the interpretation of Table 9.14 requires extreme caution. To the best of the author's understanding, the effective angular momentum function values do not include the effects of the earthquake on the solid Earth's moment of inertia. In addition, according to both Gross and Wahr [personal communications, 2011], the effects of the giant tsunami triggered by the earthquake should not be included in the general circulation models (GCM) that simulate the oceanic forcing, with the possible exception of GCM that assimilate data. Even in this special case, in which the data would sense the tsunami due to the displacement of the sea floor at its origin, the impact on the computed OAM should be short-term. A possible response of the atmosphere to the tsunami due to the coupling between the two fluid layers is also deemed unlikely. It is noteworthy that a tectonic contribution to the atmospheric angular momentum was mentioned back in 1992 by Preisig when he investigated the relationships between polar motion, earthquakes and atmospheric angular momentum in [154]. In this paper, Preisig provided evidence of a strong correlation between peaks in the AAM excitation and the occurrence of great earthquakes in 6 cases out of the 8 studied.

In this context, one may wonder if removing the entire geophysical series from the geodetic series may not be detrimental to the study after all. In the absence of any alternative solution, the time series of residuals obtained are shown in Fig. 9.20.

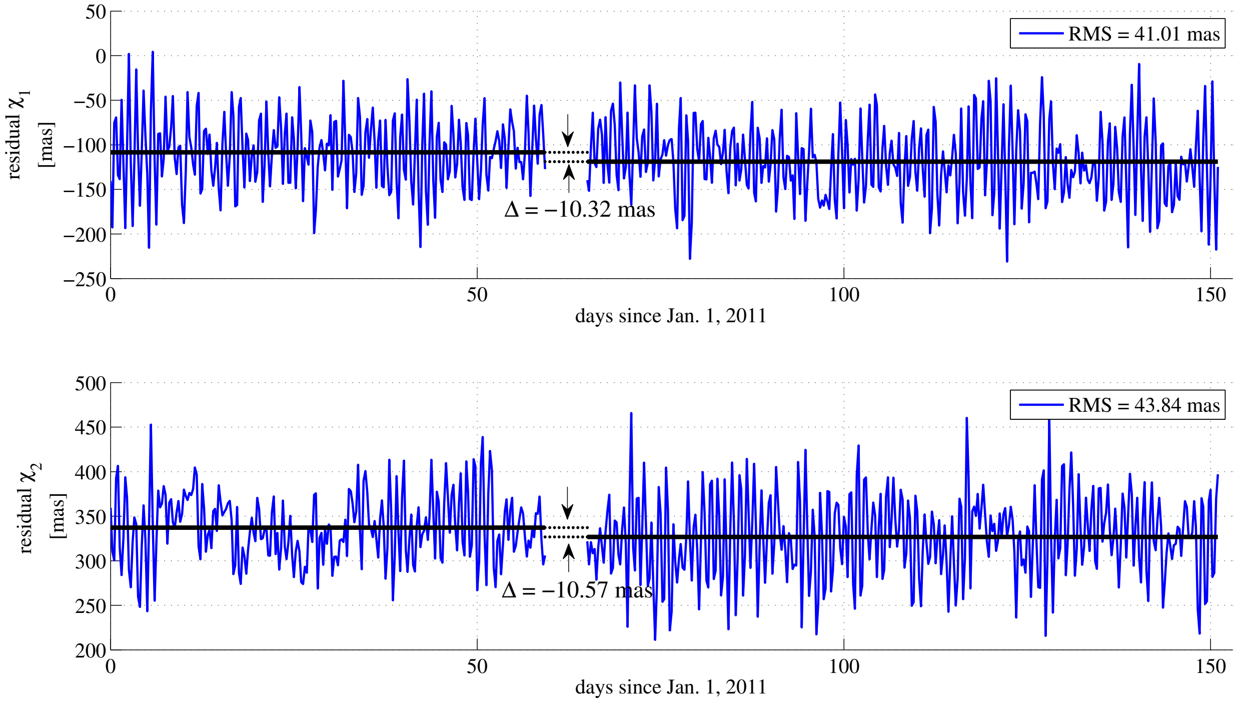

Figure 9.20: Excitation residuals

Statistics were computed on the excitation residuals and are presented in Table 9.15. The differences in the means of the segments corresponding to the periods prior to the earthquake and following the earthquake are denoted Δmean. The values specific to the geophysical, geodetic and residual excitation series are reported. The standard deviation figures are calculated from the residual time series and over the entire time span. Likewise, the standard error of the mean statistics computed are associated to the full time series of excitation residuals.

	Δmean Geophysical	**Δmean** Geodetic	**Δmean** Residuals	**Standard Deviation** Residuals	**Standard Error of the Mean**
χ_1	-0.31	10.01	-10.32	41.49	1.72
χ_2	6.60	17.17	-10.57	43.98	1.82

Table 9.15: Statistics on excitation series before and after the earthquake. Units are mas.

The fact that the change in mean is about the same for both coordinates of the excitation vector and do not match the direction of the modeled change for one of the coordinate appears suspicious. Moreover, the scatter around the mean seems too large for the experiment to be conclusive. The standard error of the mean statistics may also be too optimistic given that signatures of systematic processes are still visible in the residual signals. Overall, the results are probably not statistically significant due to the apparent residual periodic patterns.

9.5.3 Conclusions relevant to earthquake detection

The analysis that was carried out over a relatively short period of time in an attempt to detect the 2011 Japan earthquake is not conclusive as yet but the preliminary results obtained seem promising nevertheless. It is believed that increasing the period covered by the study should help answer and clarify some of the questions and concerns raised. The main concern is the separation between tectonic excitation signals and general circulation signals in the oceanic and atmospheric effective angular momentum function series. In addition, more insight into the precise computation of the EAMF series for the oceans and the atmosphere by the ECMWF and GFZ center for geosciences is needed. To identify the cause of the change in bias observed in the geophysical excitation series before and after the earthquake, the current OAM series could be replaced by OAM series that are known not to assimilate data, as recommended by Gross [personal communication, 2011]. As far as the estimation strategy and post-processing stage implementations themselves are concerned, areas of improvement, mentioned throughout this chapter, have been identified. It is expected that some progress can rapidly be made in some of them. Interesting follow-on studies are discussed in Chapter 10.

Chapter 10

Conclusions and Future Work

In the final chapter of this dissertation, the main contributions of this work to the field are reviewed and conclusions are drawn regarding the procedure to adopt for the determination and analysis of polar motion at sub-hourly frequencies. Recommendations for future research work are outlined and briefly justified.

10.1 Conclusions

The main contribution of the research presented in this dissertation has been to advance the state of the art in the field of high-frequency polar motion estimation using GPS ground data only. The best level of accuracy (identified with the difference between the IERS model and the GPS-derived estimates) reached is of the order of 80 μas, which is the root-mean-squares value of the prograde and retrograde components (see Table G.5). The best level of precision attained (calculated based on the root-mean-squares value of pole overlaps) is of the order of 95 μas due to significant noise contaminating the retrograde component of polar motion (see Appendix G). As a reminder, although distinguishing between precision and accuracy in the state-of-the-art performances reported in the literature is challenging and while the exact process employed to measure the corresponding levels is seldom detailed, the nominal values for the accuracy and precision of polar motion estimates are considered to range between 50 μas and 250 μas. For this reason, it is believed that the 3-day strategy designed and tested in this dissertation provides competitive products. Besides and to the best of our knowledge, the temporal resolutions considered during this thesis are unprecedented and the highest ever reported. It is also the first time that JPL's GIPSY/OASIS software package is used to estimate polar motion as a stochastic process and to generate series of pole coordinates at high temporal resolution. This was accomplished by contributing to the development and upgrade of the existing GIPSY/OASIS and Long Arc GPS Processing software packages for their use towards the study of rapid and ultra-rapid polar motion, as well as through the implementation of a set of tools specific to the analysis of pole coordinate time series.

The GPS-based estimates of the pole coordinates were shown to have sufficient precision and sensitivity to provide useful and meaningful geophysical information. As a matter of fact, the ability to recover ultra-rapid tidally-driven signals as well as non-tidal variations induced by oceanic and atmospheric forcing was demonstrated. Some progress was also made towards the detectability of earthquake-triggered variations in polar motion. Overall, the results presented raise very interesting and challenging questions that could have new and potentially important implications for the geophysics community.

Along the course of this thesis, the trade-space between the need for polar motion solutions accurate enough for high-precision geodetic applications and requirements on the overall GPS POD was extensively investigated. Thanks to this careful analysis, insight was gained not only into the impact of the pole coordinate estimation update frequency and length of the orbit determination arc, but also into the effects of the network geometry (ground station number/parameterization/selection, antenna calibration), the force modeling (frames used, custom acceleration use/parameterization...) and the observation sampling rate. The strengthes and limitations of each of the candidate strategies in that respect are qualitatively and quantitatively described throughout the dissertation. It was shown that good-quality polar motion estimates can be obtained without sacrificing much (if any) accuracy in the POD solution.

Overall, guidelines for the estimation of pole coordinates at high temporal resolution emerged from the variety of test cases studied. The findings are summarized below in the form of recommendations :

(1) it is recommended to use the 3-day strategy that always provides the best levels of accuracy and repeatability of the pole coordinate solutions;

(2) as usual, transmitter and receiver antenna calibrations should be used to increase the overall accuracy of the solution and the combination of GRACE-based and IGS robot maps is preferable over other combinations considered here in the case of polar motion determination;

(3) the real need for ambiguity resolution to ensure the generation of useful geodetic products was demonstrated;

(4) the estimation of 1-cpr accelerations is highly recommended to enhance the ability to recover tidal variations with semi-diurnal periods;

(5) it is recommended to adapt the observation sampling rate to the pole coordinate estimation interval needed for the potential detection of the geophysical process of interest;

(6) the data rate itself should be selected according to the periods of the geophysical phenomena of interest and based on the Nyquist frequency. The default 5-minute observation sampling interval should be chosen whenever possible (see Appendix E).

10.2 Future work

The topic of high-frequency polar motion, and more generally high-frequency ERP, is rich in possibilities for further exploration. Some directions for future work and areas of interest for further investigation are given in the paragraphs that follow. The ideas listed are sorted based on their estimated latency for implementation. The tasks that are expected to be the fastest to complete are mentioned first. They are followed by suggestions that may be challenging to concretize due to current model inadequacies or current lack of scientific knowledge.

10.2.1 Implementation of new and additional models

Some models that have been validated recently and recommended for use by the IERS with regards to polar motion determination should be added to GIPSY. Models that already exist but are currently missing from the software should be included too. A non-exhaustive list is given below:

- Libration model

The libration model, which accounts for the small torque acting on the tri-axiality of the Earth, should be implemented in the software package. Libration affects the precise recovery of tidally-induced polar motion in the diurnal band for instance. Although one order of magnitude smaller than the effects of ocean tides, the predicted effects of libration on polar motion are still important to consider at the level of accuracy reached.

- Atmospheric loading model

As mentioned in Chapter 7, atmospheric loading effects are not included in the estimation procedure, which is known to result in systematic effects corrupting the pole coordinate estimates. A model similar to the tidal ocean loading model exists and should be implemented in the software.

- Inclusion of hydrological, cryospheric, core EAMF into the deconvolution procedure and upon availability

The field of angular momentum modeling and computation is always evolving. Thus, variations in the cryospheric angular momentum due to global changes in ice mass should be available in the next few years from GRACE data, although their computation is currently deemed challenging. In addition, variations in the land hydrology, although problematic to include into the deconvolution procedure, should be accounted for. Experimental 3-hour series reportedly exist [82] but do not seem to be publicly available. Very recently, atmospheric data with hourly-resolution were provided by the ECMWF (as the 4DVar analysis products, for Four-Dimensional Variational Assimilation products) in support of the VLBI CONT'08 campaign as publicized in [170]. Testing these very high resolution EAMF series would be interesting, especially with the objective of investigating very-short-period geophysical phenomena occurring simultaneously to earthquakes (e.g. toroidal oscillations with periods of a few minutes) or to investigate further the ter-diurnal signal observed by GPS as well as VLBI in some of the CONT campaigns (see 8.3.3).

10.2.2 Further tuning of the strategies and refinement of post-processing

Based on the preliminary results shown in Chapter 9, it is believed that the estimation strategies could be tailored or revised to specifically target earthquake detection. All the research reported here provides the foundation upon which to build to accomplish this task. Indeed, we now have some confidence in the ability to recover small-amplitude variations in polar motion. The refinement of the candidate strategies would also be a consequence of the implementation of the various models mentioned above.

In the context of the detection of earthquake-triggered geophysical effects, the study of high-frequency normal modes of the Earth and, more specifically, of the Slichter triplet should be considered a priority among the follow-on studies. This would very likely require the estimation of gravitational coefficients of degree 1 which are related to the deformation of the figure of the Earth [Desai, Haines and Wahr, 2011, personal communication].

Potential polar motion signal in periods ranging from 1 day to 2 days, i.e. periods in-between the ultra-rapid and the rapid polar motion characteristic ranges, should also be investigated. The geophysical origin of the signal observed in the retrograde diurnal frequency band need to be considered as well since it is definitely possible that nutation handling might not be the only cause for the presence of some signal in that band. It could be the sign of nutation/retrograde polar motion of geophysical origin in that band [Wahr, 2011, personal communication].

Moreover, the so-called "tag-up" approach implemented by the JPL ORMS group to generate the FLINN solutions should be applied and tested in the context of high-frequency stochastic estimation of polar motion [Desai, 2011, personal communication]. This approach consists in producing a free network solution first before fixing it to a well-known, well-defined realization of the ITRF. This initial solution would supply an optimal subnetwork of stations that would remain fixed in the second stage of the estimation of the high-frequency pole coordinate series.

Furthermore, before completely discarding the 9-day strategy, it might be of interest to look at the correlation between the orbital elements and the retrograde diurnal polar motion component by means of error propagation and fast Fourier transforms. Comparing the outcome to the same quantity computed for the other two candidate strategies might help to track down what part of the dynamic modeling causes the tremendous noise level in the retrograde diurnal frequency band. The strategy should also be used with a parameterization of both the once-per-rev and twice-per-rev custom accelerations in the HCL reference frame rather than in the UVW reference frame used thus far.

Besides, the post-processing of the estimates could be enhanced in three main ways. To begin with, the series analysis could probably benefit from the definition of a criterion specific to the pole coordinate estimates and enabling the detection of outliers independently of the POD solution. Next, the spectral analyses could be made more robust and perhaps more accurate by comparing the results obtained using different methods. In particular, considering performing evolutive time analysis and using multitaper methods that provide minimum leakage of the spectral estimates and enable the determination of confidence intervals on the spectral lines seems worthwhile [4]. Last, the Butterworth bandpass filter used as part of the comparison with geophysical excitation series in the rapid polar motion band could be substituted for a Vondrák filter. The latter technique is widely used by the geodetic community and is deemed more adapted to the study of the Earth Rotation Parameters. It offers the advantage of retaining a high level of fidelity to the raw series while smoothing them to a user-specified level ([188], [189]).

10.2.3 Implementation of capability to estimate ERP rates

The capability to estimate the rates of all ERP as stochastic processes could prove beneficial on at least three different levels. First, it is believed that a new method of nutation handling could potentially be derived from the estimation of the rates of the pole coordinates. Indeed, based on the results presented throughout this document, the correlation between the satellite orbital elements and sub-daily polar motion could probably be handled better, especially in the case of very long-arc strategies. This needs to be accomplished by somehow resolving the singularity arising from the definitions of polar motion and nutation. To this end, the rates of the pole coordinates could be estimated instead of the corresponding offsets. The rationale behind this idea is that rates of the pole coordinates are correlated to rates of the nutation parameters, which, unlike the nutation parameters, are not correlated with the satellite orbital elements.

Moreover, generating three types of solutions based on the estimation of pole offsets only, pole rates only and the combination of both could help distinguish systematic errors and would provide insight on the sensitivity of each quantity to force and observation modeling. The performances of these different approaches could be contrasted against one another and provide valuable information for the refinement of the estimation strategies.

Ultimately, adding this capability to the software would enable the simultaneous estimation of LOD (and hence UT1-UTC) and polar motion, which is important to study spin-wobble coupling, predicted by Dahlen ([54]) due to the influence of oceans and neglected by assumption in this dissertation.

10.2.4 Statistical polar motion deconvolution

Statistical deconvolution of the pole coordinates series could be attempted by means of a Kalman filter, as mentioned in Chapter 9. The challenges associated with this task are described in section 9.2.4.

Bibliography

[1] Z. Altamimi, X. Collilieux, and C. Boucher. Strengthes and Limitations of the ITRF: ITRF2005 and Beyond. Geodetic Reference Frames, pages 73–79, 2009.

[2] Z. Altamimi, D. Gambis, and C. Bizouard. Rigorous combination to ensure ITRF and EOP consistency. In Journées Systèmes de Référence Spatio-temporels 2007, volume 1, page 151, 2008.

[3] P. Andersen. Measuring rapid variations in Earth orientation, geocenter and crust with satellite laser ranging. Journal of Geodesy, 69(4):233–243, 1995.

[4] Y. Aoyama and I. Naito. Atmospheric excitation of the Chandler wobble, 1983–1998. Journal of Geophysical Research, 106:8941–8954, 2001.

[5] K. Arfa-Kaboodvand et al. Interpretation of high frequency polar motion and length of day variations. IERS Technical Note 28, pages 15–25, 2000.

[6] T. Artz, S. Bockmann, A. Nothnagel, and P. Steigenberger. Subdiurnal variations in the Earth's rotation from continuous Very Long Baseline Interferometry campaigns. Journal of Geophysical Research, 115(B5):B05404, 2010.

[7] Y. Bar-Sever, P. Kroger, and J. Borjesson. Estimating horizontal gradients of tropospheric path delay with a single GPS receiver. Journal of Geophysical Research, 103(B3):5019–5035, 1998.

[8] Y. Bar-Sever and D. Kuang. New Empirically Derived Solar Radiation Pressure Model for Global Positioning System Satellites. IPN Progress Report, pages 42–159, 2004.

[9] Y. Bar-Sever and K. Russ. New and Improved Solar Radiation Models for GPS Satellites Based on Flight Data. Technical report, California Institute of Technology Pasadena/Jet Propulsion Lab, 1997.

[10] R. Barnes et al. Atmospheric angular momentum fluctuations, length-of-day changes and polar motion. Proceedings of the Royal Society of London. Series A, Mathematical and Physical Sciences, 387(1792):31–73, 1983.

[11] W. Bertiger et al. Jason-2 Precision Orbit Determination Status, 2008. OST/ST Meeting, Nice France.

[12] W. Bertiger et al. Single receiver phase ambiguity resolution with GPS data. Journal of Geodesy, 84(5):327–337, 2010.

[13] G. Beutler. Methods of Celestial Mechanics: Physical, mathematical and numerical principles, volume I. Springer Verlag, 2005.

[14] G. Beutler, L. Mervart, and A. Verdun. Methods of Celestial Mechanics: Application to planetary system, geodynamics and satellite geodesy, volume II. Springer Verlag, 2005.

[15] G. Beutler et al. The International GPS Service (IGS): an interdisciplinary service in support of Earth sciences. Advances in Space Research, 23(4):631–653, 1999.

[16] G. Beutler et al. Polar Motion with Daily and Sub-Daily Time Resolution. In Polar Motion: Historical and Scientific Problems, ASP Conference Series, volume 208, 2000.

[17] G. Bierman. Factorization Methods for Discrete Sequential Estimation. Mathematics in Science and Engineering, 1977.

[18] G. Bierman. Square-root information filtering and smoothing for precision orbit determination. Algorithms and Theory in Filtering and Control, pages 61–75, 1982.

[19] C. Bizouard and D. Gambis. The combined solution C04 for Earth Orientation Parameters consistent with International Terrestrial Reference Frame 2008.
`http://hpiers.obspm.fr/iers/eop/eopc04`.

[20] C. Bizouard and D. Gambis. The combined solution C04 for Earth orientation parameters consistent with International Terrestrial Reference Frame 2005. Geodetic Reference Frames, pages 265–270, 2009.

[21] C. Bizouard and L. Seoane. Atmospheric and oceanic forcing of the rapid polar motion. Journal of Geodesy, 84(1):19–30, 2010.

[22] J. Böhm, R. Heinkelmann, and H. Schuh. Short note: A global model of pressure and temperature for geodetic applications. Journal of Geodesy, 81(10):679–683, 2007.

[23] J. Böhm et al. Global Mapping Function (GMF): A new empirical mapping function based on numerical weather model data. Geophysical Research Letters, 33(7), 2006.

[24] A. Brzeziński. Polar motion excitation by variations of the effective angular momentum function: considerations concerning deconvolution problem. Manuscripta Geodaetica, 17:3–20, 1992.

[25] A. Brzeziński. Polar motion excitation by variations of the Effective Angular Momentum Function, II: Extended model. Manuscripta Geodaetica, 19(3):157–171, 1994.

[26] A. Brzeziński. Review of the Chandler wobble and its excitation. In Proceedings of the Workshop: Forcing of polar motion in the Chandler frequency band: a contribution to understanding interannual climate variations, held in Luxemburg, Grand Duchy of Luxemburg, 21-23 April 2004, pages 109–120. Ministère de la Culture, de l'Enseignement Supérieur et de la Recherche, Cahiers du Centre Européen de Géodynamique et de Séismologie, Volume 24, 2005.

[27] A. Brzeziński. A simple digital filter for the geophysical excitation of nutation. Journal of Geodesy, 81(6):543–551, 2007.

[28] A. Brzeziński. On the influence of diurnal atmospheric tides on Earth rotation. In Journées Systèmes de Référence Spatio-temporels 2007, volume 1, page 180, 2008.

[29] A. Brzeziński, C. Bizouard, and S. Petrov. Influence of the atmosphere on Earth rotation: what new can be learned from the recent atmospheric angular momentum estimates? Surveys in Geophysics, 23(1):33–69, 2002.

[30] A. Brzeziński and N. Capitaine. The use of the precise observations of the Celestial Ephemeris Pole in the analysis of geophysical excitation of Earth rotation. Journal of Geophysical Research, 98(B4):6667–6675, 1993.

[31] A. Brzeziński, J. Nastula, and B. Kolaczek. Seasonal excitation of polar motion estimated from recent geophysical models and observations. Journal of Geodynamics, 48(3-5):235–240, 2009.

[32] A. Brzeziński, R. Ponte, and A. Ali. Nontidal oceanic excitation of nutation and diurnal/semidiurnal polar motion revisited. Journal of Geophysical Research, 109(B11):B11407, 2004.

[33] A. Brzezinski et al. Commission 19: Rotation of the Earth. Proceedings of the International Astronomical Union, 4(T27A):37–49, 2008.

[34] B. Buffett, P. Mathews, and T. Herring. Modeling of nutation and precession: Effects of electromagnetic coupling. Journal of Geophysical Research, 107(B4):2070, 2002.

[35] B. Buttkus. Spectral analysis and filter theory in applied geophysics. Springer Verlag, 2000.

[36] L. Campbell et al. Experiences in implementation and use of the Square Root Information Filter/Smoother for orbit determination. In Proceedings of the 27th IEEE Conference on Decision and Control, pages 831–839, 1988.

[37] N. Capitaine. Comparison of Old and New concepts: the Celestial Intermediate Pole and Earth Orientation Parameters. Observatoire de Paris, Paris, France, 18–19 April 2002, page 35, 2002.

[38] N. Capitaine. Orientation et rotation de la Terre – Modélisation astronomique. Ecole d'été du GRGS, 1-5 septembre 2008, 2008.

[39] N. Capitaine. Nomenclature and numerical standards for IAU models and IERS Conventions for Earth rotation. In Journées Systèmes de Référence Spatio-temporels 2008, 2009.

[40] N. Capitaine, M. Folgueira, and J. Souchay. Earth rotation based on the celestial coordinates of the celestial intermediate pole. Astronomy and Astrophysics, 445(1):347–360, 2006.

[41] N. Capitaine and P. Wallace. Implementation of the IAU 2000 definition of UT1 in astronomy. Proceedings of the International Astronomical Union, 5(H15):212–212, 2009.

[42] N. Capitaine, P. Wallace, and J. Chapront. Expressions for IAU 2000 precession quantities. Astronomy & Astrophysics, 412:567–586, 2003.

[43] N. Capitaine et al. IERS Technical Note 29. Proceedings of the IERS Workshop on the Implementation of the New IAU Resolutions, 2002. http:///www.iers.org/iers/publications/tn/tn29.

[44] P. Cerveira, R. Weber, and H. Schuh. The instantaneous Earth rotation – still inaccessible? Vermessung & Geoinformation, 2007.

[45] B. Chao. On the excitation of the Earth's polar motion. Geophysical Research Letters, 12(8):526–529, 1985.

[46] B. Chao. Excitation of the Earth's polar motion rotation by Atmospheric Angular Momentum variations, 1980-1990. Geophysical Research Letters, 20(2):253–256, 1993.

[47] B. Chao. Earth Rotational Variations Excited by Geophysical Fluids. IVS 2004 General Meeting Proceedings, 2004.

[48] B. F. Chao. Space Geodesy Monitors Mass Transports in Global Geophysical Fluids. EOS, Transactions, American Geophysical Union, 81(22):247–249, 2000.

[49] B. Chao et al. Libration in the Earth's rotation. Geophysical Research Letters, 18(11):2007–2010, 1991.

[50] W. Chen and W. Shen. Rotational Evaluations of Global Geophysical Fluid Models and Improvement in the Annual Wobble Excitation. 2011. `http://acc.igs.org/erp/pole-excite-models_iugg11.pdf`.

[51] J. Chen et al. A new assessment of long-wavelength gravitational variations. Journal of Geophysical Research, 105:16, 2000.

[52] T. Chin, R. Gross, and J. Dickey. Modeling and forecast of the polar motion excitation functions for short-term polar motion prediction. Journal of Geodesy, 78(6):343–353, 2004.

[53] O. Colombo. The dynamics of Global Positioning System orbits and the determination of precise ephemerides. Journal of Geophysical Research, 94(B7):9167–9182, 1989.

[54] F. Dahlen. The passive influence of the oceans upon the rotation of the Earth. Geophysical Journal of the Royal Astronomical Society, 46(2):363–406, 1976.

[55] O. De Viron and V. Dehant. Earth's rotation and high frequency equatorial angular momentum budget of the atmosphere. Surveys in Geophysics, 20(6):441–462, 1999.

[56] O. De Viron, S. Marcus, and J. Dickey. Diurnal angular momentum budget of the atmosphere and its consequences for Earth's nutation. Journal of Geophysical Research, 106(B11):26747–26, 2001.

[57] O. De Viron et al. Diurnal and subdiurnal effects of the atmosphere on the Earth rotation and geocenter motion. Journal of Geophysical Research, 110, 2005.

[58] S. Desai. Ocean tides from TOPEX/Poseidon altimetry with some geophysical applications. PhD thesis, University of Colorado at Boulder, 1996.

[59] S. Desai. Observing the pole tide with satellite altimetry. Journal of Geophysical Research, 107(C11):3186, 2002.

[60] S. Desai et al. Recent Developments in the Processing of Global GPS Data at the Jet Propulsion Laboratory. In AGU Fall Meeting Abstracts, volume 1, page 05, 2007.

[61] S. Di Leonardo and S. Dickman. Isolation of atmospheric effects on rapid polar motion through Wiener filtering. Geophysical Journal International, 159(3):863–873, 2004.

[62] J. Dickey. Earth rotation. In Global Earth Physics: A Handbook of Physical Constants, page 356, 1995.

[63] S. Dickman. The rotation of the ocean-solid earth system. Journal of Geophysical Research, 88(B8):6373–6394, 1983.

[64] S. Dickman. Determination of oceanic dynamic barometer corrections to atmospheric excitation of earth rotation. Journal of Geophysical Research, 103(B7):15127–15, 1998.

[65] S. Dickman. Evaluation of Effective Angular Momentum Function formulations with respect to core-mantle coupling. Journal of Geophysical Research, 108(B3):2150, 2003.

[66] H. Dobslaw et al. Seasonal polar motion excitation from numerical models of atmosphere, ocean, and continental hydrosphere. Journal of Geophysical Research, 115(B10):B10406, 2010.

[67] C. Dunn and L. Young. TOPEX GPS Antenna Phase Calibration. Inter-office Memorandum 335.9-92-016, Jet Propulsion Laboratory, April 1992.

[68] C. Dunn and L. Young. TOPEX POD Network Antenna Phase Calibration. Inter-office Memorandum 335.9.027-92, Jet Propulsion Laboratory, September 1992.

[69] S. Englich et al. Determination of Earth rotation variations by means of VLBI and GPS and comparison to conventional models. Vermessung & Geoinformation, pages 104–112, 2007.

[70] T. Eubanks. Variations in the orientation of the Earth. In Contributions of space geodesy to geodynamics: Earth dynamics, page 1, 1993.

[71] T. Eubanks et al. A spectral analysis of the Earth's angular momentum budget. Journal of Geophysical Research, 90(B7):5385–5404, 1985.

[72] T. Eubanks et al. Causes of rapid motions of the Earth's pole. Nature, 334:115–119, 1988.

[73] A. Freedman. Measuring Earth Orientation with the Global Positioning System. Journal of Geodesy, 65(1):53–65, 1991.

[74] M. Fritsche et al. Impact of higher-order ionospheric terms on GPS estimates. Geophysical Research Letters, 32(23):L23311, 2005.

[75] L. Fu and A. Cazenave. Satellite altimetry and Earth sciences: A handbook of techniques and applications. Academic Press, 2000.

[76] T. Fukushima. A new precession formula. The Astronomical Journal, 126:494, 2003.

[77] D. Gambis. Monitoring Earth orientation using space-geodetic techniques: state-of-the-art and prospective. Journal of Geodesy, 78(4):295–303, 2004.

[78] D. Gambis and C. Bizouard. Consistency analysis between EOP series and reference frames. In Proceedings of the IERS Workshop on Combination Research and Global Geophysical Fluids, IERS Technical Note, volume 30, pages 57–62, 2003.

[79] D. Gambis et al. General combination of EOP series. IERS Technical Note, 30, 2003.

[80] D. Gambis et al. Combination of Earth Orientation Parameters and terrestrial frame at the observation level. Geodetic Reference Frames, pages 3–9, 2006.

[81] GFZ Helmholtz Centre Potsdam. EAM functions from the GFZ German Research Center for Geosciences. `http://www.gfz-potsdam.de/portal/gfz/Struktur/Departments/Department+1/sec13/services/eam_functions`.

[82] GFZ Helmholtz Centre Potsdam. ECMWF atmospheric data sets. `http://www.gfz-potsdam.de/portal/gfz/Struktur/Departments/Department+1/sec13/services/description_ECMWF`.

[83] GFZ Helmholtz Centre Potsdam. Physics of the OMCT model. `http://www.gfz-potsdam.de/portal/gfz/Struktur/Departments/Department+1/sec13/services/OMCT_Physics`.

[84] F. Gőttl and F. Seitz. Contribution of non-tidal oceanic mass variations to polar motion determined from space geodesy and ocean data. Observing our Changing Earth, pages 439–445, 2008.

[85] Gipson, J.M. Very Long Baseline Interferometry determination of neglected tidal terms in high-frequency Earth orientation variations. Journal of Geophysical Research, 101(B12):28051, 1996.

[86] T. Gregorius. Gipsy-Oasis II, How it works. NASA Jet Propulsion Laboratory, California Institute of Technology, Pasadena, USA, 1996.

[87] R. Gross. Correspondence between theory and observations of polar motion. Geophysical Journal International, 109:162–170, 1992.

[88] R. Gross. Earth rotation variations-long period. Treatise on Geophysics, 3, 2007.

[89] R. Gross. Chilean Quake May Have Shortened Earth Days, March 2010. `http://www.nasa.gov/topics/earth/features/earth-20100301.html`.

[90] R. Gross. Understanding Earth rotation, 2011. Presentation given at KASI Headquarters, Daejeon, Republic of Korea, 2011 Winter School on Space Geodesy.

[91] R. Gross and B. Chao. Excitation study of the LAGEOS-derived Chandler wobble. Journal of Geophysical Research, 90(B11):9369–9380, 1985.

[92] R. Gross and B. Chao. The rotational and gravitational signature of the December 26, 2004 Sumatran earthquake. Surveys in Geophysics, 27(6):615–632, 2006.

[93] R. Gross, I. Fukumori, and D. Menemenlis. Atmospheric and oceanic excitation of the Earth's wobbles during 1980–2000. Journal of Geophysical Research, 108(B8):2370–2385, 2003.

[94] B. Guinot. Basic Problems in the Kinematics of the Rotation of the Earth. In Time and the Earth's Rotation, volume 82, pages 7–18, 1979.

[95] R. Haas and J. Wünsch. Sub-diurnal earth rotation variations from the VLBI CONT02 campaign. Journal of Geodynamics, 41(1-3):94–99, 2006.

[96] B. Haines et al. Determining precise orbits for Topex/Poseidon within one day of real time: Results and Implications. In Proceedings of the AAS/AIAA Space Flight Mechanics Meeting, Breckenridge, CO, 1999.

[97] B. Haines et al. Using GRACE as an Orbiting Fiducial Laboratory for GPS. In AGU Fall Meeting Abstracts, page 07, 2006.

[98] B. Haines et al. GRACE-Based Estimates of GPS Satellite Antenna Phase Variations: Impact on Determining the Scale of the Terrestrial Reference Frame. In AGU Fall Meeting Abstracts, volume 1, page 01, 2007.

[99] B. Haines et al. Space-based satellite antenna maps; Impact of different satellite antenna maps on LEO and Terrestrial Results, 2008. IGS Workshop, Miami.

[100] B. Haines et al. Strategies for Defining the Terrestrial Reference Frame from GPS Alone. In AGU Fall Meeting Abstracts, volume 1, page 04, 2009.

[101] B. Haines et al. Strategies for Defining the Terrestrial Reference Frame from GPS Alone. In AGU Fall Meeting Abstracts, volume 1, page 04, 2009.

[102] B. Haines et al. Strategies to Improve GPS-Based Determination of the Terrestrial Reference Frame, 2009. NASA Sea Level Workshop, Austin.

[103] J. Hefty and J. Vondrák. Periodic fluctuations at frequency of the nearly diurnal free wobble in Ondřejov PZT observations. Studia geophysica et geodaetica, 33(2):117–132, 1989.

[104] J. Hefty et al. Analysis of the first year of Earth rotation parameters with a sub-daily resolution gained at the CODE processing center of the IGS. Journal of Geodesy, 74(6):479–487, 2000.

[105] T. Herring, B. Buffett, P. Mathews, and I. Shapiro. Forced nutations of the Earth: Influence of inner core dynamics 3. Very Long Interferometry data analysis. Journal of Geophysical Research, 96(B5):8259–8273, 1991.

[106] T. Herring, R. King, and S. McClusky. GAMIT. GPS analysis at MIT, Release, 10, 2003.

[107] T. Herring, P. Mathews, and B. Buffett. Modeling of nutation-precession: Very Long Baseline Interferometry results. Journal of Geophysical Research, 107(10.1029), 2002.

[108] J. L. Hilton et al. Report of the International Astronomical Union Division I Working Group on Precession and the Ecliptic. Celestial Mechanics and Dynamical Astronomy, 94(3):351–367, 2006.

[109] K. Hocke and N. Kämpfer. Gap filling and noise reduction of unevenly sampled data by means of the Lomb-Scargle periodogram. Atmos. Chem. Phys, 9:4197–4206, 2009.

[110] B. Hofmann-Wellenhof, H. Lichtenegger, and J. Collins. GPS Theory and Practice. 5th revised edition, Springer-Wien, New York, 2001.

[111] R. Ibanez-Meier et al. Estimation of Subdaily Polar Motion with the Global Positioning System During the Epoch'92 Campaign. Geophysical Reseach Letters, 1994.

[112] IERS. IERS Rapid Service/Prediction Center for Earth Orientation. `http://maia.usno.navy.mil`.

[113] IERS. IERS Conventions Center, 2003. `http://tai.bipm.org/iers/conv2003/conv2003_c5.html`.

[114] International Astronomical Union - Standards Of Fundamental Astronomy. SOFA Tools for Earth Attitude, August 2007. `http://www.iausofa.org/publications/sofa_pn.pdf`.

[115] C. Jekeli. Geometric reference systems in geodesy. 2006.

[116] Jet Propulsion Laboratory. Introduction to GIPSY/OASIS II - Class Handouts, 2007.

[117] H. Jochmann. Basic Relations for Studying the Influence of Geophysical Processes on the Earths Rotation: The Angular Momentum Approach. Surveys in Geophysics, 30(1):1–37, 2009.

[118] JPL Internal Document. GPS POD System Software Design Document.

[119] G. Kaplan. The IAU resolutions on astronomical reference systems, time scales, and Earth rotation models. Arxiv preprint astro-ph/0602086, 2006.

[120] S. Kedar et al. The effect of the second order GPS ionospheric correction on receiver positions. Geophysical Research Letters, 30(16):1829, 2003.

[121] A. Kleusberg and P. Teunissen. GPS for Geodesy. Berlin; New York: Springer, 1996.

[122] J. Kouba. Comparison of polar motion with Oceanic and Atmospheric Angular Momentum time series for 2-day to Chandler periods. Journal of Geodesy, 79(1):33–42, 2005.

[123] J. Kovalevsky and P. Seidelmann. Fundamentals of Astrometry. Cambridge University Press, 2004.

[124] J. Kryński. Major concepts of recent Celestial and Terrestrial Reference Systems. Annual of Navigation, pages 5–20, 2004.

[125] K. Lambeck. Methods and geophysical applications of satellite geodesy. Reports on Progress in Physics, 42:547–628, 1979.

[126] K. Lambeck. Geophysical geodesy: The slow deformations of the earth. Oxford Sci. Publ., Oxford, UK, 1988.

[127] K. Lambeck. The Earth's variable rotation: geophysical causes and consequences. Cambridge Univ Pr, 2005.

[128] C. Lawson and R. Hanson. Solving least squares problems. Society for Industrial Mathematics, 1995.

[129] S. Lee, B. Schutz, and P. Abusali. Hybrid precise orbit determination strategy by global positioning system tracking. Journal of Spacecraft and Rockets, 41(6):997–1009, 2004.

[130] S. Lichten. Estimation and filtering techniques for high-accuracy gps applications. *The Telecommunications and Data Acquisition Progress Report 42-97*, pages 1–20, 1989.

[131] S. Lichten and J. Border. A demonstration of high precision gps orbit determination for geodetic applications. *Telecommunications and Data Acquisition Progress Report*, 91:1–22, 1987.

[132] J. Lieske et al. Expressions for the precession quantities based upon the IAU/1976/system of astronomical constants. *Astronomy & Astrophysics*, 58:1–16, 1977.

[133] S. Luthcke et al. The 1-centimeter orbit: Jason-1 precision orbit determination using GPS, SLR, DORIS, and altimeter data. *Marine Geodesy*, 26(3):399–421, 2003.

[134] B. Luzum et al. Recent improvements to iers bulletin a combination and prediction. *GPS Solutions*, 4(3):34–40, 2001.

[135] R. Madden, H. Lejenäs, and J. Hack. Semidiurnal variations in the budget of angular momentum in a general circulation model and in the real atmosphere. *Journal of the Atmospheric Sciences*, 55(15):2561–2575, 1998.

[136] L. Mansinha and D. Smylie. Earthquakes and the Earth's Wobble. *Science*, 161(3846):1127, 1968.

[137] P. Mathews and P. Bretagnon. Polar motions equivalent to high frequency nutations for a nonrigid earth with anelastic mantle. *Astronomy and Astrophysics*, 400(3):1113–1128, 2003.

[138] P. Mathews, B. Buffett, T. Herring, and I. Shapiro. Forced nutations of the Earth: Influence of inner core dynamics 1. Theory. *Journal of Geophysical Research*, 96(B5):8219–8242, 1991.

[139] P. Mathews, B. Buffett, T. Herring, and I. Shapiro. Forced nutations of the Earth: Influence of inner core dynamics 2. Numerical results and comparisons. *Journal of Geophysical Research*, 96(B5):8243–8257, 1991.

[140] P. Mathews, T. Herring, and B. Buffett. Modeling of nutation and precession: new nutation series for nonrigid Earth and insights into the Earth's interior. *Journal of Geophysical Research*, 107(B4):2068, 2002.

[141] D. McCarthy. IERS Technical Note 13. *Observatoire de Paris. Central Bureau of IERS. Paris*, 1992.

[142] D. McCarthy. IERS Technical Note 21. *IERS Conventions*, 1996, 1996.

[143] D. McCarthy and N. Capitaine. Practical consequences of resolution b1. 6" iau2000 precession-nutation model," resolution b1. 7" definition of celestial intermediate pole," and resolution b1.8 "definition and use of celestial and terrestrial ephemeris origin". *Observatoire de Paris, Paris, France, 18-19 April 2002*, page 9, 2002.

[144] D. McCarthy and G. Petit. IERS Conventions (2003). *US Naval Observatory*, 2003.

[145] P. Mendes Cerveira et al. Earth rotation observed by very long baseline interferometry and ring laser. *Pure and Applied Geophysics*, 166(8):1499–1517, 2009.

[146] D. Morabito, T. Marshall, and J. Steppe. Kalman filtering of Earth orientation changes. In The Earth's rotation and reference frames for geodesy and geodynamics: Proceedings of the 128th Symposium of the International Astronomical Union, held in Coolfont, West Virginia, USA, 20-24 October 1986, page 257. Springer, 1988.

[147] H. Moritz and I. Mueller. Earth rotation: theory and observation. Ungar, 1987.

[148] W. Munk and G. MacDonald. The rotation of the Earth. Cambridge University Press Cambridge, 1960.

[149] J. Nastula et al. High resolution Earth Rotation Parameters determined during the CONT02 campaign. In IVS 2004 General Meeting Proceedings, volume 412, 2004.

[150] H. J. Neuberg, J. and W. Zurn. On the Complex Eigenfrequency of the" Nearly Diurnal Free Wobble" and its Geophysical Interpretation. Variations in Earth rotation, page 11, 1990.

[151] D. Percival and A. Walden. Spectral analysis for physical applications: multitaper and conventional univariate techniques. Cambridge University Press, 1993.

[152] G. Petit. IERS Conventions (2010). Technical report, DTIC Document, 2010.

[153] R. Ponte and D. Stammer. Role of ocean currents and bottom pressure variability on seasonal polar motion. Journal of Geophysical Research, 104(C10), 1999.

[154] J. Preisig. Polar motion, atmospheric angular momentum excitation and earthquakes-correlations and significance. Geophysical Journal International, 108(1):161–178, 1992.

[155] J. Ray. Analysis Effects in IGS Polar Motion Estimates, 2008. `http://acc.igs.org/erp-index.html`.

[156] R. Ray. Thoughts on the Diurnal/Semidiurnal EOP Model. `www.bipm.org/utils/en/events/iers/Ray_Richard.pdf`.

[157] B. Richter, J. Engels, and E. Grafarend. Transformation of amplitudes and frequencies of precession and nutation of the earths rotation vector to amplitudes and frequencies of diurnal polar motion. Journal of Geodesy, 84(1):1–18, 2010.

[158] E. Robinson. Multichannel time series analysis with digital computer programs. Holden-Day San Francisco, 1967.

[159] M. Rochester. Causes of fluctuations in the rotation of the Earth. Philosophical Transactions of the Royal Society of London. Series A, Mathematical and Physical Sciences, 313(1524):95–105, 1984.

[160] M. Rochester, O. Jensen, and D. Smylie. A Search for the Earth's Nearly Diurnal Free Wobble. Geophysical Journal of the Royal Astronomical Society, 38(2):349–363, 1974.

[161] M. Rothacher et al. Estimation of nutation using the Global Positioning System. Journal of geophysical research, 104(B3):4835–4859, 1999.

[162] M. Rothacher et al. High-frequency variations in Earth rotation from Global Positioning System data. Journal of Geophysical Research, 106(B7):13711–13738, 2001.

[163] D. Rowlands et al. Short-arc analysis of intersatellite tracking data in a gravity mapping mission. Journal of Geodesy, 76(6):307–316, 2002.

[164] C. Rutherford Appleton Laboratory. The Astronomical Almanac for the Year 2011: Data for Astronomy, Space Sciences, Geodesy, Surveying, Navigation and other applications. US Naval Observatory, 2010.

[165] D. Salstein et al. Atmospheric excitation of Earth rotation/polar motion at high temporal resolution. In Journées Systèmes de Référence Spatio-temporels 2007, volume 1, page 177, 2008.

[166] T. Sasao and J. Wahr. An excitation mechanism for the free core nutation. Geophysical Journal of the Royal Astronomical Society, 64(3):729–746, 1981.

[167] J. Scargle. Studies in astronomical time series analysis. II- Statistical aspects of spectral analysis of unevenly spaced data. The Astrophysical Journal, 263:835, 1982.

[168] J. Scargle. Studies in astronomical time series analysis. III- Fourier transforms, autocorrelation functions, and cross-correlation functions of unevenly spaced data. Astrophysical Journal, 343(Part 1), 1989.

[169] H. Schaub and J. Junkins. Analytical mechanics of space systems, volume 1. AIAA, 2003.

[170] M. Schindelegger et al. High-resolution atmospheric angular momentum functions related to earth rotation parameters during cont08. Journal of Geodesy, 85(7):425–433, 2011.

[171] G. Seeber. Satellite geodesy. Walter de Gruyter, 2003.

[172] P. Seidelmann. Explanatory Supplement to the Astronomical Almanac. Univ. Science Books, 2005.

[173] P. Seidelmann and J. Kovalevsky. Application of the new concepts and definitions (ICRS, CIP and CEO) in fundamental astronomy. Astronomy and Astrophysics, 392(1):341–351, 2002.

[174] A. Sibois et al. GPS-based estimation of polar motion parameters at sub-hourly frequency, 2011. General Assembly of the EGU Poster Session: Observing and understanding Earth rotation variability and its geophysical excitation.

[175] N. Sidorenkov. The Interaction Between Earth's Rotation and Geophysical Processes. Wiley-VCH, 2009.

[176] M. Smith and F. Dahlen. The period and Q of the Chandler wobble. Geophysical Journal of the Royal Astronomical Society, 64(1):223–281, 1981.

[177] Special Bureau for the Core. Free Core Nutation (FCN). `http://sbc.oma.be/freecornu.html`.

[178] T. Springer. Modeling and validating orbits and clocks using the Global Positioning System. PhD thesis, Astronomical Institute, University of Berne, Berne, Switzerland, 1999.

[179] P. Steigenberger et al. Reprocessing of a global GPS network. Journal of Geophysical Research, 111(B5):B05402, 2006.

[180] P. Steigenberger et al. Subdaily Earth rotation observed by GPS and VLBI. In Geophysical Research Abstracts, volume 10, 2008.

[181] T. Stieglitz and S. Dickman. Refined correlations between atmospheric and rapid polar motion excitations. Geophysical Journal International, 139(1):115–122, 1999.

[182] B. Tapley, B. Schutz, and G. Born. Statistical Orbit Determination. Academic Press, 2004.

[183] D. Thaller et al. Combined Earth orientation parameters based on homogeneous and continuous VLBI and GPS data. Journal of Geodesy, 81(6):529–541, 2007.

[184] M. Thomas. Ocean induced variations of Earths rotation–Results from a simultaneous model of global circulation and tides. PhD thesis, University of Hamburg, Germany, 2002.

[185] C. Thornton and J. Border. Radiometric tracking techniques for deep-space navigation. Wiley-Interscience, 2005.

[186] C. Tierney et al. Short-period oceanic circulation: Implications for satellite altimetry. Geophysical Research Letters, 27(9):1255–1258, 2000.

[187] D. Vallado, J. Seago, and P. Seidelmann. Implementation Issues Surrounding the New IAU Reference Systems for Astrodynamics. Paper AAS, pages 06–134, 2006.

[188] J. Vondrak. A contribution to the problem of smoothing observational data. Bulletin of the Astronomical Institutes of Czechoslovakia, 20:349–355, 1969.

[189] J. Vondrak. Problem of smoothing observational data II. Bulletin of the Astronomical Institutes of Czechoslovakia, 28:84–89, 1977.

[190] J. Wahr. The forced nutations of an elliptical, rotating, elastic and oceanless Earth. Geophysical Journal of the Royal Astronomical Society, 64(3):705–727, 1981.

[191] J. Wahr. The effects of the atmosphere and oceans on the Earth's wobbleI. Theory. Geophysical Journal of the Royal Astronomical Society, 70(2):349–372, 1982.

[192] J. Wahr. The effects of the atmosphere and oceans on the Earth's wobble and on the seasonal variations in the length of day-II. Results. Geophysical Journal of the Royal Astronomical Society, 74(2):451–487, 1983.

[193] J. Wahr. Geophysical aspects of polar motion, variations in the length of day, and the lunisolar nutations. In Space Geodesy and Geodynamics, pages 281–313, 1986.

[194] J. Wahr. The Earth's rotation. Annual Review of Earth and Planetary Sciences, 16(1):231–249, 1988.

[195] P. T. Wallace and N. Capitaine. Precession-nutation procedures consistent with IAU 2006 resolutions. Astronomy & Astrophysics, 459(3):981–985, 2006.

[196] R. Weber, M. Rothacher, and G. Beutler. Contribution of GPS to monitor earth orientation parameters. High frequency to subseasonal variations in Earth Rotation. IERS Technical Note, 28:43–51, 2000.

[197] J. Weiss et al. Improving GPS-Based Determination of the Terrestrial Reference Frame. 2010.

[198] J. Weiss et al. Near real time GPS orbit determination: Strategies, performance, and applications to OSTM/Jason-2. In 2010 AAS GNC Conference, Breckenridge CO, Feb, pages 6–10, 2010.

[199] C. Wilson. Discrete polar motion equations. Geophysical Journal of the Royal Astronomical Society, 80(2):551–554, 1985.

[200] C. Wilson and J. Chen. Discrete polar motion equations for high frequencies. Journal of Geodesy, 70(9):581–585, 1996.

[201] C. Wilson and R. Haubrich. Meteorological excitation of the Earth's wobble. Geophysical Journal of the Royal Astronomical Society, 46(3):707–743, 1976.

[202] C. Wunsch and D. Stammer. Atmospheric loading and the oceanic inverted barometer effect. Reviews of Geophysics, 35(1):79–107, 1997.

[203] C. Yoder, J. Williams, and M. Parke. Tidal variations of Earth rotation. Journal of Geophysical Research, 86(B2):881–891, 1981.

[204] T. Yunck. Orbit Determination. Global Positioning System: Theory and Applications, page 559, 1996.

[205] M. Zechmeister and M. Kurster. The generalised Lomb-Scargle periodogram. Astronomy and Astrophysics, 496(2):577–584, 2009.

[206] V. Zharov and D. Gambis. Atmospheric tides and rotation of the Earth. Journal of Geodesy, 70(6):321–326, 1996.

[207] Y. Zhou et al. Oceanic excitations on polar motion: a cross comparison among models. Geophysical Journal International, 162(2):390–398, 2005.

[208] M. Ziebart, S. Edwards, S. Adhya, and P. Cross. High Precision GPS IIR Orbit Prediction using Analytical Non-conservative Force Models. Proceedings of ION GNSS 2004, Long Beach, CA, USA, pages 1764–1770, 2004.

[209] L. Zotov. Excitation function reconstruction using observations of the polar motion of the earth. Proceedings of the Journées Systèmes de Référence Spatio-Temporels, pages 237–240, 2005.

Appendix A

Computation of the Delaunay arguments

The Delaunay arguments involved in the mathematical description of ocean tides are computed as shown in the set of equations below. The formulas are excerpted from [144].

Mean anomaly of the Moon:

$$l = 134^{\circ}.96340251 + 1717915923.2178''\,t + 31''.8792\,t^2 + 0''.051635\,t^3$$
$$-0''.00024470\,t^4$$

Mean anomaly of the Sun:

$$l' = 357^{\circ}.52910918 + 129596581''.0481\,t - 0''.5532\,t^2 - 0''.000136\,t^3$$
$$-0''.00001149\,t^4$$

F = L - Ω where L is the mean longitude of the Moon:

$$F = 93^{\circ}.27209062 + 1739527262''.8478\,t - 12''.7512\,t^2 - 0''.001037\,t^3$$
$$+0''.00000417\,t^4$$

Mean elongation of the Moon from the Sun:

$$D = 297^{\circ}.85019547 + 1602961601''2090\,t - 6''.3706\,t^2 + 0''/006593\,t^3$$
$$-0''.00003169\,t^4$$

Mean longitude of the ascending node of the Moon:

$$\Omega = 125^\circ.04455501 - 6962890''.5431\,t + 7''.4722\,t^2 + 0''.007702\,t^3 \\ -0''.00005939\,t^4$$

θ = Greenwich Mean Sidereal Time (GMST) + π = rotation angle:

$$\chi = 15 \times (67310.54841 + (876600 \times 3600 + 8640184.812866)\,t + 0.093104\,t^2 - 6.2e^{-6}\,t^3) + 648000.0$$

In these equations, t is measured in Julian centuries of 36525 days of 86400 seconds of Dynamical Barycentric Time since J2000.0.

Appendix B

Satellite-centered coordinate systems

Two rotating coordinate systems attached to the spacecrafts are commonly used to describe forces acting upon the satellites, in particular the solar radiation pressure force. They are the HCL and UVW coordinate systems.

B.1 The HCL coordinate system

As indicated by the acronym that stands for Height/Cross-track/Long-track, the three axes of this coordinate system are in the radial, cross-track and in-track direction.

- The radial direction is defined positive towards the spacecraft.
- The positive cross-track axis is collinear to the cross product between the spacecraft velocity vector and the radial axis.
- The L-axis completes the right-handed system.

The HCL coordinate system is also commonly referred to as the RIC coordinate system.

B.2 The UVW coordinate system

The UVW coordinate system is defined in [9] as follows:

- U is pointing along the Sun-spacecraft direction,

- V is pointing along the cross product between the U direction and the spacecraft-geocenter direction,
- W completes the system.

The UVW coordinate system is sometimes named the EPS (Earth-Probe-Sun) coordinate system (e.g. in [86]).

Appendix C

Relationship between theoretical and reported pole coordinates

The relationship between the theoretical and reported pole coordinates was analytically developed by Gross in [87]. The derivation relies on kinematics and in particular on the use of the rotation matrices appearing in the general transformation between inertial and terrestrial coordinates formulated in Eq. 2.10. As mentioned in Chapter 2, the (x_p, y_p) values reported by the IERS refer to the CIP while the perturbations in the location of the Earth's rotation axis with respect to the equilibrium state and denoted (m_1, m_2) in Chapter 3 are connected to the figure axis of the Earth. Therefore, relating the two couples of variables necessitates mapping coordinates from the intermediate reference frame to the terrestrial reference frame. Hence, the transformation equation can be written as shown in Eq. C.1.

$$\vec{r}_i(t) = A^T \, \vec{r}_t(t) \tag{C.1}$$

where $A = U\,XY$ is the transformation matrix, composed of U, the transformation matrix associated with the proper rotational motion of the Earth and XY, the matrix associated with polar motion. The matrix XY itself is the product of the matrices associated with the rotations of angles x_p and y_p, respectively. Note that the XY matrix was referred to as the W matrix in Chapter 2. The notation is changed in this Appendix to avoid confusion with another matrix traditionally depicted as W and defined in Eq. C.9 below.

The proper rotation matrix of the Earth is defined in terms of the hour angle H as:

$$U = \begin{bmatrix} \cos(H) & -\sin(H) & 0 \\ \sin(H) & \cos(H) & 0 \\ 0 & 0 & 1 \end{bmatrix} \tag{C.2}$$

The polar motion matrix is defined in terms of the pole coordinates as:

$$XY = \begin{bmatrix} \cos(x_p) & 0 & -\sin(x_p) \\ 0 & 1 & 0 \\ \sin(x_p) & 0 & \cos(x_p) \end{bmatrix} \begin{bmatrix} 1 & 0 & 0 \\ 0 & \cos(y_p) & \sin(y_p) \\ 0 & -\sin(y_p) & \cos(y_p) \end{bmatrix} \tag{C.3}$$

Taking the time derivative of Eq. C.1 yields:

$$\frac{\mathrm{d}}{\mathrm{d}t}\left[\vec{r}_i(t)\right] = \frac{\mathrm{d}}{\mathrm{d}t}\left[A^T(t)\right]\vec{r}_t(t) + A^T \frac{\mathrm{d}}{\mathrm{d}t}\left[\vec{r}_t(t)\right] \tag{C.4}$$

Multiplying both sides of the equation above by the matrix $A(t)$ defined earlier results in:

$$A(t)\frac{\mathrm{d}}{\mathrm{d}t}\left[\vec{r}_i(t)\right] = A(t)\frac{\mathrm{d}}{\mathrm{d}t}\left[A^T(t)\right]\vec{r}_t(t) + A(t)\,A^T(t)\frac{\mathrm{d}}{\mathrm{d}t}\left[\vec{r}_t(t)\right] \tag{C.5}$$

Making use of the fact that rotation matrices are orthogonal, one can then write:

$$A(t)\frac{\mathrm{d}}{\mathrm{d}t}\left[\vec{r}_i(t)\right] = W^T\vec{r}_t(t) + \frac{\mathrm{d}}{\mathrm{d}t}\left[\vec{r}_t(t)\right] \tag{C.6}$$

The W matrix is defined as:

$$W = A(t)\frac{\mathrm{d}}{\mathrm{d}t}\left[A^T(t)\right] \tag{C.7}$$

It is also defined using the coordinates of the angular velocity vector describing the rotation of the terrestrial frame with respect to the inertial intermediate frame. The rotation vector of the Earth with respect to the space-fixed reference system is defined as:

$$\vec{\omega} = \left[m_1\ m_2\ (1+m_3)\right]\Omega = \left[\omega_x\ \omega_y\ \omega_z\right] \tag{C.8}$$

Therefore:

$$W = \begin{bmatrix} 0 & \omega_z & -\omega_y \\ -\omega_z & 0 & \omega_x \\ \omega_y & -\omega_x & 0 \end{bmatrix} \tag{C.9}$$

Now substituting the vector $\vec{r}_t(t)$ by its mapping to the intermediate reference frame expressed in C.1, one gets:

$$A(t)\,\frac{\mathrm{d}}{\mathrm{d}t}\,[\vec{r}_i(t)] = W^T A(t)\,\vec{r}_i(t) + \frac{\mathrm{d}}{\mathrm{d}t}\,[A(t)\,\vec{r}_i(t)] \tag{C.10}$$

Since the $W(t)$ matrix is by definition a skew-symmetric matrix, Eq. C.10 is equivalent to Eq. C.11.

$$A(t)\,\frac{\mathrm{d}}{\mathrm{d}t}\,[\vec{r}_i(t)] = -W(t)\,[A(t)\,\vec{r}_i(t)] + \frac{\mathrm{d}}{\mathrm{d}t}\,[A(t)\,\vec{r}_i(t)] \tag{C.11}$$

Using Eq. C.7, one obtains:

$$A(t)\frac{\mathrm{d}}{\mathrm{d}t}\,[\vec{r}_i(t)] = \frac{\mathrm{d}}{\mathrm{d}t}\,[A(t)\,\vec{r}_i(t)] + \vec{\omega} \times [A(t)\,\vec{r}_i(t)] \tag{C.12}$$

Equations. C.9 through C.12 are all derived from the laws of rigid body kinematics and the application of the transport theorem (see [169] for example).

Considering the small angles involved in the displacement of the Earth's rotation vector, the matrices associated with polar motion can be linearized to the first order by means of a small angle approximation.

The polar motion matrix, XY, becomes:

$$XY \simeq \begin{bmatrix} 1 & 0 & -x_p \\ 0 & 1 & y_p \\ x_p & -y_p & 1 \end{bmatrix} \tag{C.13}$$

As a result the overall transformation matrix A is reformulated as:

$$A^T \simeq \begin{bmatrix} \cos(H) & -\sin(H) & -x_p\cos(H) - y_p\sin(H) \\ \sin(H) & \cos(H) & y_p\cos(H) - x_p\sin(H) \\ x_p & -y_p & 1 \end{bmatrix} \tag{C.14}$$

Taking the time derivative of Eq. C.14 yields:

$$\frac{\partial A}{\partial t} = \begin{bmatrix} -\dot{H}\sin H & \dot{H}\cos H & \dot{x_p} \\ -\dot{H}\cos H & -\dot{H}\sin H & -\dot{y_p} \\ -\dot{x_p}\cos H - \dot{y_p}\sin H + \dots & \dot{y_p}\cos H - \dot{x_p}\sin H - \dots & 0 \\ x_p\dot{H}\sin H - y_p\dot{H}\cos H & y_p\dot{H}\sin H - x_p\dot{H}\cos H & \end{bmatrix} \tag{C.15}$$

By definition, the time derivative of the hour angle H is equal to:

$$\dot{H} = (1 + z_p)\,\Omega \tag{C.16}$$

where z_p is the third component of the perturbation vector $\vec{p}$ and is associated with the perturbation in the rotational speed of the Earth.

Using the expressions defined above together with Eq. C.7, the matrix W can be calculated as shown in Eq. C.17:

$$W = \frac{\partial A}{\partial t}A^T = \begin{bmatrix} 0 & (1+z_p)\,\Omega & y_p\,\Omega + \dot{x_p} \\ -(1+z_p)\,\Omega & 0 & -\dot{y_p} + x_p\,\Omega \\ -\dot{x_p} - y_p\,\Omega & \dot{y_p} - \Omega.x_p & 0 \end{bmatrix} \tag{C.17}$$

Equating Eq. C.17 and Eq. C.9 yields:

$$\begin{cases} \omega_x = x_p\,\Omega - \dot{y}_p \\ \omega_y = -y_p\,\Omega - \dot{x}_p \\ \omega_z = (1 + z_p)\,\Omega \end{cases} \tag{C.18}$$

Expressing all quantities in the complex plane, one obtains:

$$\begin{cases} \vec{\omega} = \omega_x + \mathrm{i}\,\omega_y = \Omega\,[m_1 + \mathrm{i}\,m_2] = \Omega\,\vec{m} \\ \vec{p} = x_p - \mathrm{i}\,y_p \end{cases} \tag{C.19}$$

Starting from Eqs. C.18 and using the complex formulation shown above results in:

$$\begin{aligned} \Omega\,\vec{m} &= \Omega\,[x_p - \mathrm{i}\,y_p] - \mathrm{i}\,[\dot{x}_p - \mathrm{i}\,\dot{y}_p] \\ &= \Omega\,\vec{p} - \mathrm{i}\,\frac{\mathrm{d}}{\mathrm{d}t}\vec{p} \end{aligned} \tag{C.20}$$

Eventually, the vector $\vec{m}$ is related to the polar motion vector $\vec{p}$ through:

$$\vec{m}(t) = \vec{p}(t) - \frac{\mathrm{i}}{\Omega}\,\frac{\mathrm{d}}{\mathrm{d}t}\vec{p}(t) \tag{C.21}$$

Each coordinate of the $\vec{m}$ vector is related to the pole coordinates over time by:

$$\begin{cases} m_1(t) = p_1(t) + \dfrac{1}{\Omega}\,\dfrac{\mathrm{d}p_2(t)}{\mathrm{d}t} \\ \\ m_2(t) = p_2(t) - \dfrac{1}{\Omega}\,\dfrac{\mathrm{d}p_1(t)}{\mathrm{d}t} \end{cases} \tag{C.22}$$

Appendix D

Study of Ground Network Parameterization

D.1 Methodology

The combined influences of the number of stations composing the ground network and of the ratio of fixed stations among them on the processing time and quality of the pole estimates was evaluated processing 12 test cases over one month of data (July 2004) chosen at random. The test cases fall into three categories: in the first category, the network counts 40 stations only, its size is then increased to 60 stations and to 80 stations finally. In each case, 10%, 25%, 40% and 60% of the sites are alternatively kept fixed. To reduce the computational intensity of the runs involved in this small-scale study, the 30-hour strategy was employed in the estimation procedure. Results are presented below. Prior to the solution analysis, the computational speeds and optimality of the global station distributions are compared.

D.2 Computational Time

Figure D.1 displays the mean duration of a run for each of the test cases. As visible, addind 20 sites to the network dramatically increases the total processing time in each case. Unexpectedly, the runs take longer when 60% of the 80 sites are kept fiducial, although fewer parameters are to be estimated in this case. Computer node-dependent effects should be negligible.

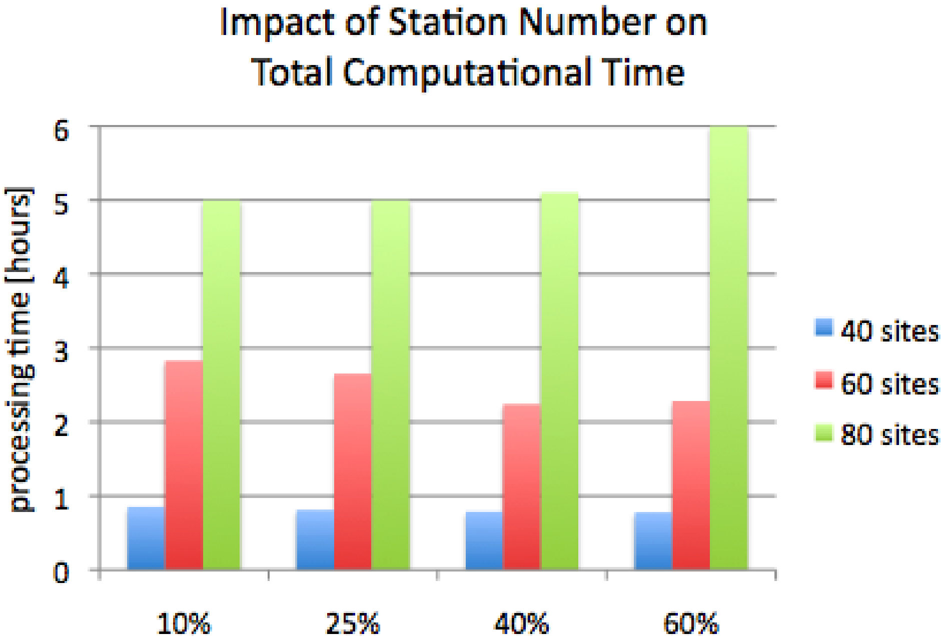

Figure D.1: Processing time vs. Number of sites

D.3 Station Distribution

The geographical quality index of the global distribution of a ground network is called ζ. It is computed in GIPSY as the RMS value of the distance from an arbitrary location on the Earth to the nearest ground site. The optimal value of this criterion corresponds to the case of an evenly distributed ground network and is calculated using Eq. D.1 where N is the number of sites considered (from the GIPSY/OASIS documentation).

$$\zeta_{optimal} \approx \frac{2}{\sqrt{6}} R_e \sqrt{\frac{\pi}{N}} \tag{D.1}$$

Figure D.2 shows the values of the ζ and corresponding $\zeta_{optimal}$ parameters for each station number. The monthly patterns are similar for the three categories of cases, reflecting the quality of the full network of available stations on each day.

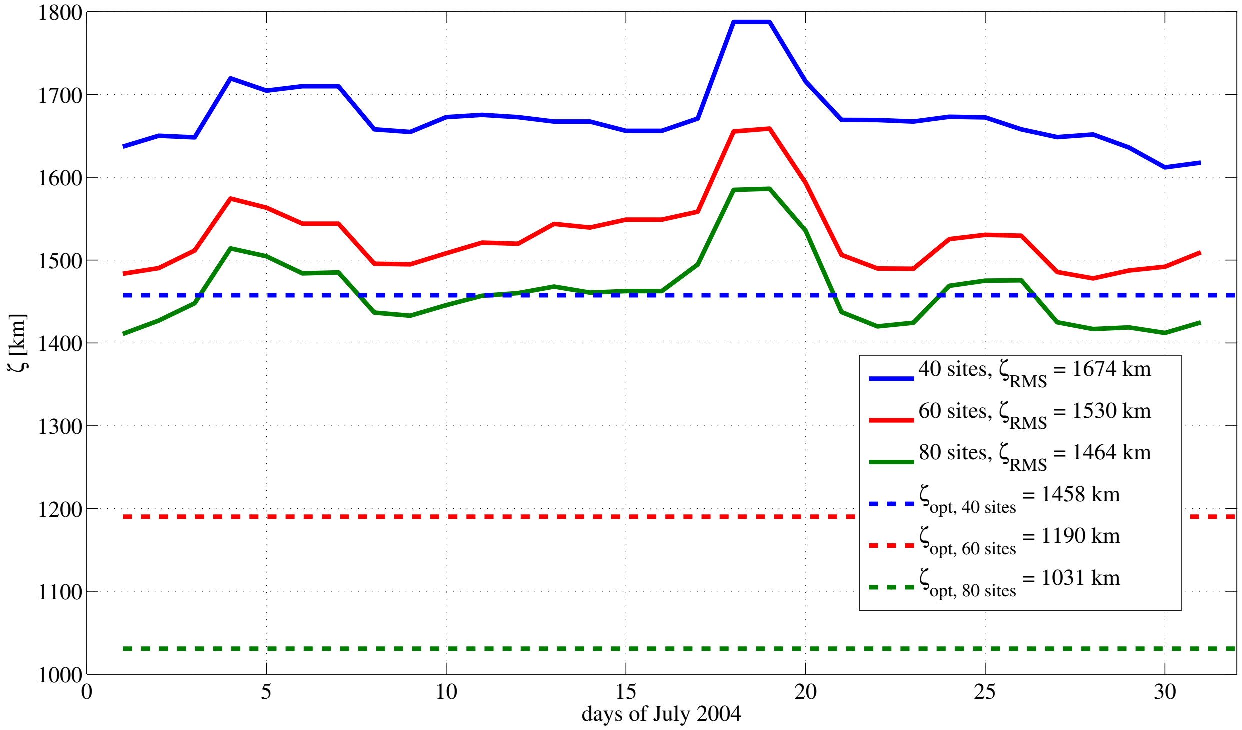

Figure D.2: Geographical quality indicator of station distribution

It is clearly noticeable on Fig. D.2 that, as more stations are added, their distribution over the surface of the globe gets less and less optimal. This is explained by the gradual formation of clusters in the Northern hemisphere and in particular in Western Europe and the U.S.A., as mentioned in section 7.3.

The solution of the estimation procedure is analyzed in the sections that follow.

D.4 General Solution

D.4.1 Orbit and Clock quality

Results obtained when comparing the final orbits with the IGS final orbits as well as in terms of orbital and clock overlaps are shown in Tables D.1 a), b) and D.2, respectively.

	40 sites	**60 sites**	**80 sites**
10%	3.23	3.21	3.24
25%	3.29	3.28	3.29
40%	3.43	3.42	3.44
60%	3.73	3.59	3.63

	40 sites	**60 sites**	**80 sites**
10%	2.0	1.80	1.72
25%	2.25	2.03	2.01
40%	2.62	2.38	2.36
60%	3.48	2.96	2.78

Table D.1: 1D-RMS value in cm of a) Difference with IGS final orbits b) Orbit overlaps

	40 sites	**60 sites**	**80 sites**
10%	41.9	39.2	36.42
25%	43	39.7	36.2
40%	43.6	40.3	37.6
60%	46.5	42.2	38.6

Table D.2: 1D-RMS value of satellite clock overlaps [ps]

The number of stations fixed visibly impacts the precision and accuracy of the OD solution. As expected, the precision of the orbit and clock estimates tend to decrease as the ratio of fiducial sites increases. Besides, increasing the size of the network has a positive influence on the internal consistency of the orbit and clock solutions. Regarding the accuracy of the orbit solutions, it is interested to notice that the 60-station cases always perform slightly better than the 40- and 80-station cases. In particular, when 60% of the sites are fixed, the orbits obtained with a 60-station ground network are significantly closer to the IGS final orbits than they are when the network only counts 40 sites or is augmented to 80 stations (although the difference in the latter case is not really significant).

D.4.2 Station coordinate repeatability

The statistical repeatability of the station locations is an important factor to consider when studying the design and optimization of a ground network. For this reason, Table D.3 records the geodetic repeatabilities in longitude, latitude and altitude of the different solutions considered.

	40 sites				**60 sites**				**80 sites**			
	10%	25%	40%	60%	10%	25%	40%	60%	10%	25%	40%	60%
lat.	4.2	3.1	1.2	2	2.2	2.2	1.3	2.8	1.7	1.9	1.1	0.8
lon.	4.0	3.3	1.3	2	2	2.5	1.3	2.8	1.6	2.4	1.2	1
alt.	5.4	4.9	3.7	3.2	4.9	4.6	3.6	3.3	4.9	4.8	3.7	2.9

Table D.3: Station coordinate repeatability [mm]

As expected, station coordinate repeatability increases with the size of the network. If the station positions seem more stable when the percentage of fiducial sites is high, this statement is not always true. Indeed, rather unexpectedly some anomalies are visible in Table D.3. In particular, the results obtained in latitude and longitude when 25% of the sites of the 60-station and 80-station networks or when 60% of the 60-station network are held fixed seem anomalous.

D.5 Polar Motion Solution

D.5.1 Error analysis

As part of the error analysis, both the random and systematic components of the errors on the pole coordinate estimates are studied by means of pole overlaps computation and spectral analysis of the formal errors, respectively. The results obtained for the pole overlaps are reported in Table D.4. The results are clearly in favor of using as many stations as possible while fixing as few of them as possible. Still, the behaviors of the X_p and Y_p coordinates are not consistent with each other, which makes drawing firm conclusions from this short-period study difficult.

	40 sites		**60 sites**		**80 sites**	
	X_p	Y_p	X_p	Y_p	X_p	Y_p
10%	240.4	213.8	245.7	240.7	201.5	214.4
25%	246.4	227.5	246.6	229.6	220.4	217
40%	237.5	213.8	260.7	223.2	219.3	214.9
60%	220.6	215.3	268.1	235.5	269.1	228

Table D.4: RMS value of pole overlaps [μas]

The amplitude spectra of the formal errors are displayed in Fig. D.3. It is observed that the ratio of stations fixed does not matter until it reaches 10%, at which point the systematic errors slightly increase. The prograde and retrograde spectra being identical, only the prograde ones are shown. Overall the impact of the number of stations and percentage of stations fixed on the magnitude of the systematic errors is negligible. This means that the global distribution of stations should not cause significant systematic errors in the pole solution.

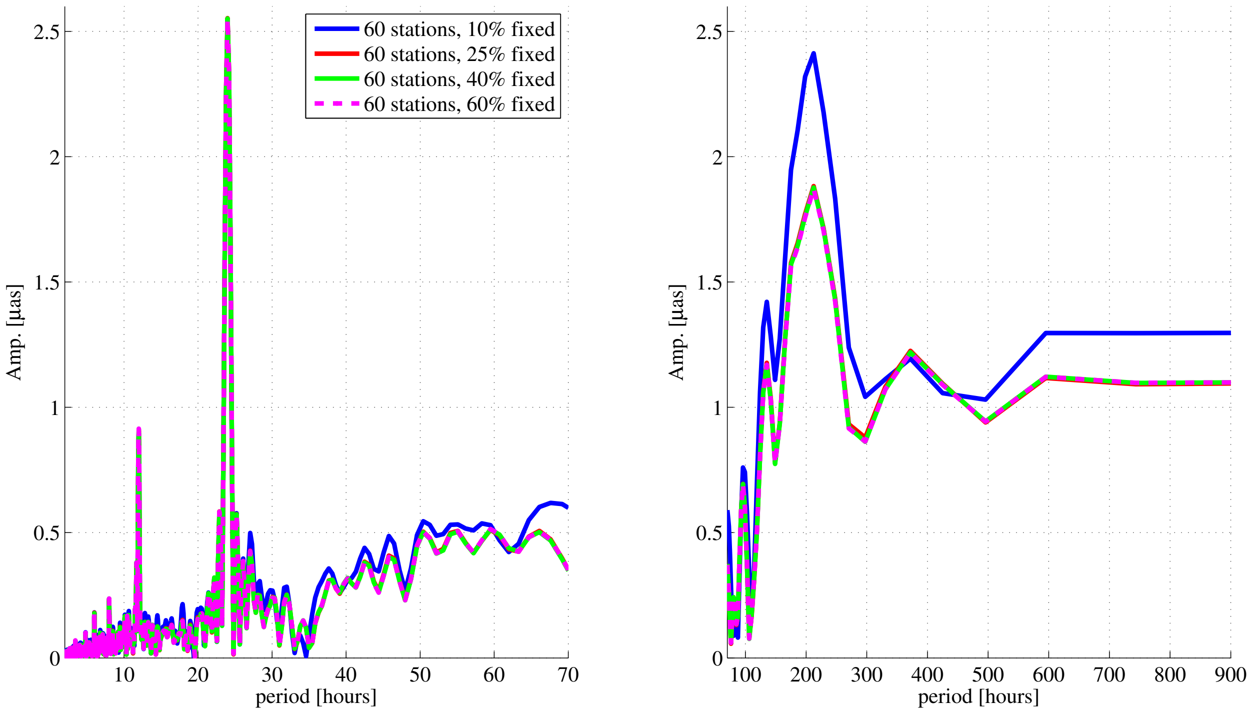

Figure D.3: Spectrum of Prograde Polar Motion Systematic Errors

D.5.2 Impact on recovery of geodetic signals

The time period processed was deemed too short to conduct any meaningful tidal analysis. As a result, the quality of the recovery of tidally-induced polar motion were not tested in this study. The recovery of non-tidal rapid polar motion was assessed in the same manner as that described in Chapter 9 of this dissertation. Thus, Table D.5 displays the percentage of correlation between the geodetic and geophysical excitations, restricting again the geophysical excitation to the participation of oceanic and atmospheric angular momentum variations.

	40 sites		**60 sites**		**80 sites**	
	χ_1	χ_2	χ_1	χ_2	χ_1	χ_2
10%	50.9	79.2	56.4	77.8	47.8	78.2
25%	52.2	82.6	59.4	83.5	62.2	84.6
40%	55.6	83.8	60.1	84.1	59.5	84.6
60%	55.3	83.4	60.4	83.9	61.4	83.6

Table D.5: Correlation coefficients between geodetic and geophysical excitations [%]

No clear pattern can be identified from the results shown above. The behavior of both coordinates seem erratic and the study, from that standpoint, is inconclusive.

D.6 Conclusions

Using a lot more than 60 stations clearly hits the computational intensity and does not necessarily provide better quality solutions. On the contrary, the polar motion solution can be degraded, likely due to the degraded distribution of the stations over the globe. Indeed, as mentioned before, the constraints imposed on the selection of the stations composing the ground network only reinforces the natural imbalance between the number of stations available in the two hemispheres of the Earth and accentuate the formation of cluster of stations in some areas of the globe.

As for the percentage of sites that need to be kept fiducial, it was shown that fixing too many sites can be detrimental to the quality of the orbit determination solution. Unfortunately, the results obtained through the analysis of the pole solution cannot be interpreted as easily as the results related to the orbit and clock solutions.

It is important to bear in mind that these results were obtained processing data over a short period of time and it could be argued that they could be misleading or not very representative of the situation. In any case, this short study reveals that quantifying the impact of the ground network selection process on the quality of the pole coordinate estimates is challenging, if only worthwhile.

Appendix E

Impact of data rate on performance

E.1 Methodology

The impact of the data sampling period on the performance of the overall estimation solution was studied by processing 12 test cases using one month of data (July 2004). The 30-hour estimation strategy was employed for this investigation to save computational resources. Three different data rates were considered: a 1-minute, a 3-minute and the default 5-minute sampling rates. The estimation interval was gradually varied from 3 minutes to 15 minutes in steps of 5, 7, 10 and 15 minutes. Due to the singularity observed when the data rate is set equal to the pole coordinate estimation interval (c.f. section 7.4), the corresponding cases were excluded from the study. It was however confirmed that this singularity manifests every time under that condition. The results shown below encompass the performance evaluation of the overall solution as well as results specific to the pole solution. The general OD solution is analyzed first.

E.2 General Solution

E.2.1 Orbit and Clock quality

The quality of the OD solution is assessed through the usual means of orbit and clock overlaps as well as through the comparison with the IGS final orbits. Table E.1 gathers the results obtained in terms of orbit overlaps. Below it, Table E.2 contains the RMS values of the differences between the estimated orbits and the IGS final orbits. At the end, Table E.3 shows the clock overlap values.

	drate = 1min	**drate = 3min**	**drate = 5min**
3min	3.97	X	X
5min	3.91	3.71	X
7min	3.90	3.70	2.06
10min	3.95	3.67	2.03
15min	3.95	3.68	2.03

Table E.1: 1D-RMS value of orbit overlaps [cm]

	drate = 1min	**drate = 3min**	**drate = 5min**
3min	4	X	X
5min	3.98	3.96	X
7min	3.97	3.95	3.44
10min	4.14	4.13	3.41
15min	3.97	3.93	3.28

Table E.2: 1D-RMS value of difference with final IGS orbit [cm]

	drate = 1min	**drate = 3min**	**drate = 5min**
3min	87.98	X	X
5min	88.16	82.24	X
7min	88.21	82.50	33.28
10min	82.86	74.33	33.41
15min	87.68	82.38	39.66

Table E.3: 1D-RMS value of satellite clock overlaps [ps]

Conspicuous improvements are observed when the default data rate of 5 minutes is used for all three performance metrics. The degradation in the quality of the solution when the observation sampling period is reduced from 3 minutes to 1 minutes is less drastic than when the default data rate is switched to 3 minutes. This observation is particularly true when the internal consistency of the orbit and clock solutions is analyzed.

E.2.2 Post-fit residuals

Since the data rate potentially impacts the size of the post-fit residuals due to varying levels of noise on the observations, RMS values of the post-fit residuals were calculated for each case and are shown in the table below.

	drate = 1min		**drate = 3min**		**drate = 5min**	
	L_C	P_C	L_C	P_C	L_C	P_C
3min	0.61	85.26	X	X	X	X
5min	0.61	85.26	0.61	63.89	X	X
7min	0.61	85.26	0.61	63.89	0.67	56.51
10min	0.58	85.22	0.58	63.86	0.67	56.52
15min	0.60	85.31	0.61	63.89	0.67	56.52

Table E.4: RMS value of post-fit residuals [cm]

As seen in Table E.4, the range residuals are the most impacted by a change in the data rate. The RMS values of the range residuals tend to diminish for lower data rates. The differences in the phase residuals are negligible.

Based on the results obtained concentrating on the general solution, the sampling rate appears to influence rather significantly the quality of the OD solution. A five-minute sampling period yields the solution of the best quality, both in terms of internal consistency, accuracy (considering the IGS final solution to be the reference solution) and fit to the observations.

E.3 Polar Motion Solution

The impact of the data rate on the quality of the polar motion solution was investigated by focusing on the analysis of the errors contaminating each solution as well as on the ability of each solution to capture rapid fluctuations of non-tidal origin in the motion of the Earth's rotation axis.

E.3.1 Error analysis

An error analysis was conducted for which pole overlaps were computed. The corresponding RMS values are given in Table E.5. Note that the 7-minute interval is not well suited for the computation of pole overlaps, so that no values are available for this test case.

	drate = 1min		**drate = 3min**		**drate = 5min**	
	X_p	Y_p	X_p	Y_p	X_p	Y_p
3 min	363	344	X	X	X	X
5 min	322	284	361	458	X	X
7 min	N/A	N/A	351	290	572	449
10 min	515	323	389	312	517	352
15 min	251	227	214	209	247	230

Table E.5: RMS value of pole overlaps [μas]

It is remarkable that the "further away" from the data rate the pole estimation interval is, the lower the overlaps get. This is most likely related to a gradual increase in the correlation between the pole coordinates and the satellite state vectors in the reverse situation, as mentioned in Chapter 7. In that context, the results obtained for the test case characterized by a 1-minute sampling interval and a 10-minute polar motion update frequency are believed to be anomalous. A more extensive analysis could provide further insight into the relationship between the precision of the pole solution and the observation sampling. Merely repeating the same analysis over a longer period of time could prove useful and may be sufficient to distinctly detect a pattern.

E.3.2 Impact on recovery of geodetic signals

The influence of the various combinations of data rates and the pole coordinate update frequencies on the ability of the estimation strategy to recover tidally-induced polar motion as well as non-tidal, oceanic and atmospheric signals is analyzed here. To begin with, tidally-driven, ultra-rapid variations in polar motion are analyzed following the procedure detailed in Chapter 9. Tables E.6 and E.7 contain the results obtained for data rates of 1 minute and 3 minutes, respectively. The corresponding values obtained when the data rate is equal to 5 minutes are gathered in Table E.8.

	3 min		5 min		7 min		10 min		15 min	
	X_p	Y_p	X_p	Y_p	X_p	Y_p	X_p	Y_p	X_p	Y_p
Bias [μas]	-27.4	-86.4	-19.6	-88	-20.3	-83.8	-25.3	-79.4	-23.2	-60.7
RMS of IERS03 model [μas]	327.2	259.2	327.2	259.2	327	259.5	327.2	259.3	327.2	259.3
RMS of GPS estimates [μas]	462.2	368.7	414.4	318.8	389.3	321.9	381.3	305.2	369.6	282.7
Correlation with model [%]	75.9	66.6	81.8	80.8	81.8	84.7	84.9	83.9	87.3	85.2
RMS of difference with model [μas]	304.2	275.8	240.4	187.9	225.8	171.8	203.1	166.3	181.2	149.5
RMS of internal overlaps [μas]	620.2	465.6	585	358	N/A	N/A	499.2	326.4	404.8	288.2

Table E.6: Results from time series analysis for data rate = 1 minute

	5 min		7 min		10 min		15 min	
	X_p	Y_p	X_p	Y_p	X_p	Y_p	X_p	Y_p
Bias [μas]	-49	-42.1	-55.7	-38.5	-48	-44.5	-51.6	-36.5
RMS of IERS03 model [μas]	327.2	259.2	327	259.4	327.2	259.2	327.2	259.3
RMS of GPS estimates [μas]	486.4	393.7	439.3	364.3	402.2	341.7	393.6	300.9
Correlation with model [%]	75.5	65.1	79.9	74.7	84.9	82.1	88.5	82.1
RMS of difference with model [μas]	322.5	298.9	265.9	242.7	213.6	196.5	184.7	172.3
RMS of internal overlaps [μas]	545.3	458.9	514.8	341.4	391.4	307.5	353.1	266.8

Table E.7: Results from time series analysis for data rate = 3 minutes

	7 min		**10 min**		**15 min**	
	X_p	**Y_p**	**X_p**	**Y_p**	**X_p**	**Y_p**
Bias [μas]	-23.5	-86.1	-28.7	-83.1	-27.4	-78.2
RMS of IERS03 model [μas]	327.6	258.7	327.2	259.2	327.2	259.3
RMS of GPS estimates [μas]	459.7	366.3	413.4	350.6	385.6	303.2
Correlation with model [%]	75.8	67.3	78.7	76.8	85.6	83.3
RMS of difference with model [μas]	301.1	271.1	255.5	225	197.9	168.1
RMS of internal overlaps [μas]	585.4	450.7	506.1	352.5	450	266

Table E.8: Results from time series analysis for data rate = 5 minutes

The correlation between the geodetic and geophysical excitation vectors is studied next. Table E.9 shows the percentage to which the deconvolved, estimated polar motion vector is correlated with the ECMWF oceanic and atmospheric EAMF series over the month processed. Again, the pole coordinate update interval of 7 minutes is not adapted to this comparison, so that no results are provided in all corresponding cases.

	drate = 1 min		**drate = 3 min**		**drate = 5 min**	
	χ_1	χ_2	χ_1	χ_2	χ_1	χ_2
3 min	24.5	80.3	X	X	X	X
5 min	76.8	84.9	65.5	86.8	X	X
7 min	N/A	N/A	N/A	N/A	N/A	N/A
10 min	66.1	84	77.9	83.1	58.4	87.8
15 min	74.6	86.1	73.4	83.6	59.4	83.5

Table E.9: Correlation coefficients between geodetic and geophysical excitations [%]

No clear pattern emerges from the analysis of Table E.9. The lack of results for the 7-minute estimation interval prevents drawing any reliable conclusions. If a tendency towards higher correlation coefficients as the pole coordinate update interval increases can be observed, it is really only the case for the 1-minute data rate cases. Besides, the results obtained for the cases related to the use of the default data rate raise a lot of questions and concerns. A more extensive and detailed study will be needed to identify trends more clearly.

E.4 Conclusions

Much like the short study that was conducted to assess the impact of the total number of stations and the ratio of fiducial stations in the ground network in Appendix D, the study presented here is only a month-long, which complicates the result analysis. Concluding anything from this small-scale investigation appears premature and the results shown above should be interpreted with caution. Still, this study tends to show that reducing the data rate can be done and that solutions of acceptable quality can be obtained by doing so as long as the pole coordinate estimation interval is modified accordingly and optimized to suit the observation sampling rate the best.

Appendix F

Operational combined ERP solutions

The purpose of this appendix is to show the differences that exist between the pole coordinate time series published by the IERS. To this end, the official, combined solutions for polar motion reported in Bulletin A, Bulletin B and EOPC04_05 are compared to the EOPC04 series that served as nominals throughout the research presented in this dissertation. Mean differences are of particular interest since they provide insight into the biases observed on the pole coordinate estimates and the magnitude of which depend on the nominal series employed. The figures displayed on the next two pages were provided by Dr. Shailen Desai.

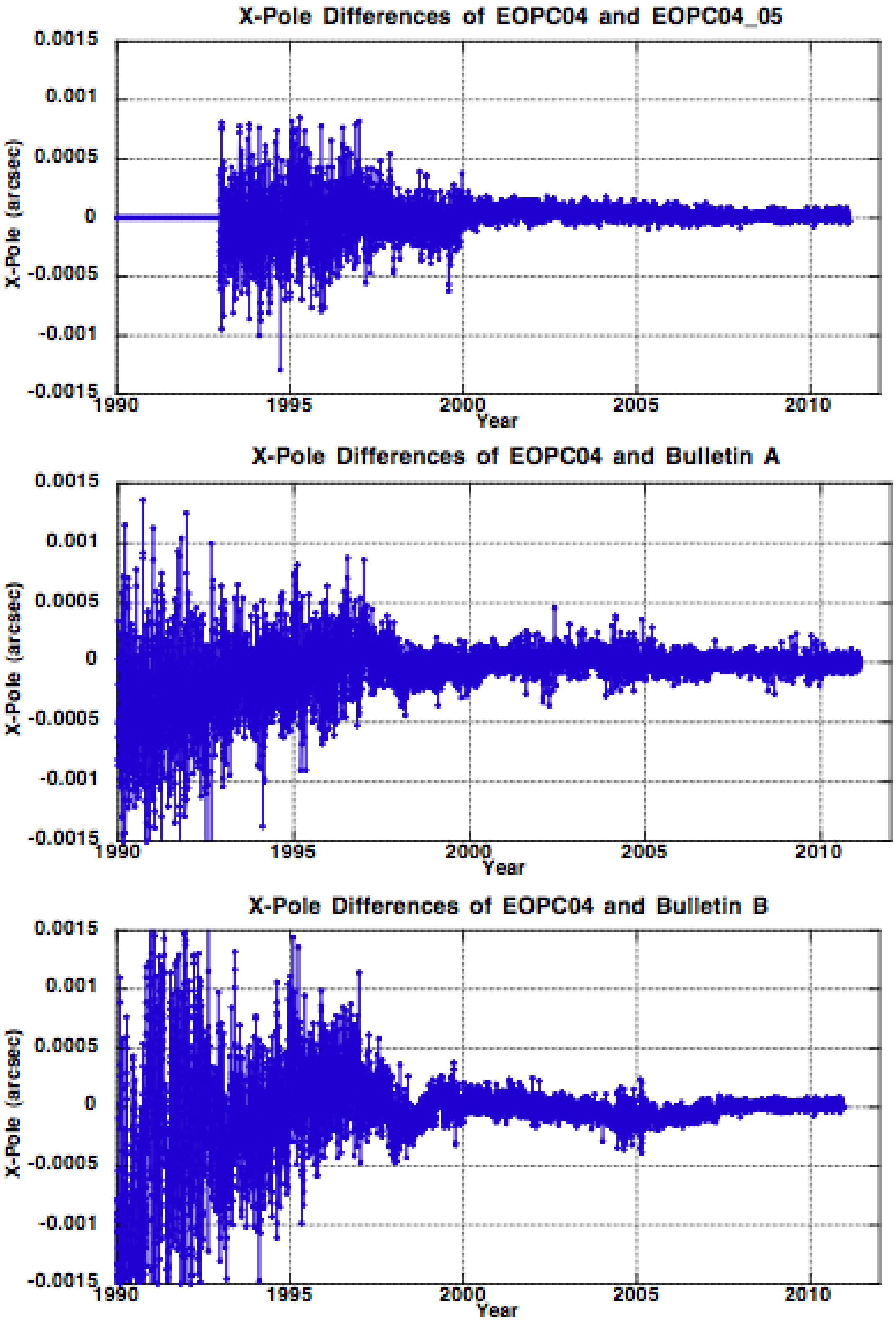

Figure F.1: Differences between values of X_p reported in EOPC04 series vs. EOPC04_05, Bulletin A and Bulletin B from top to bottom

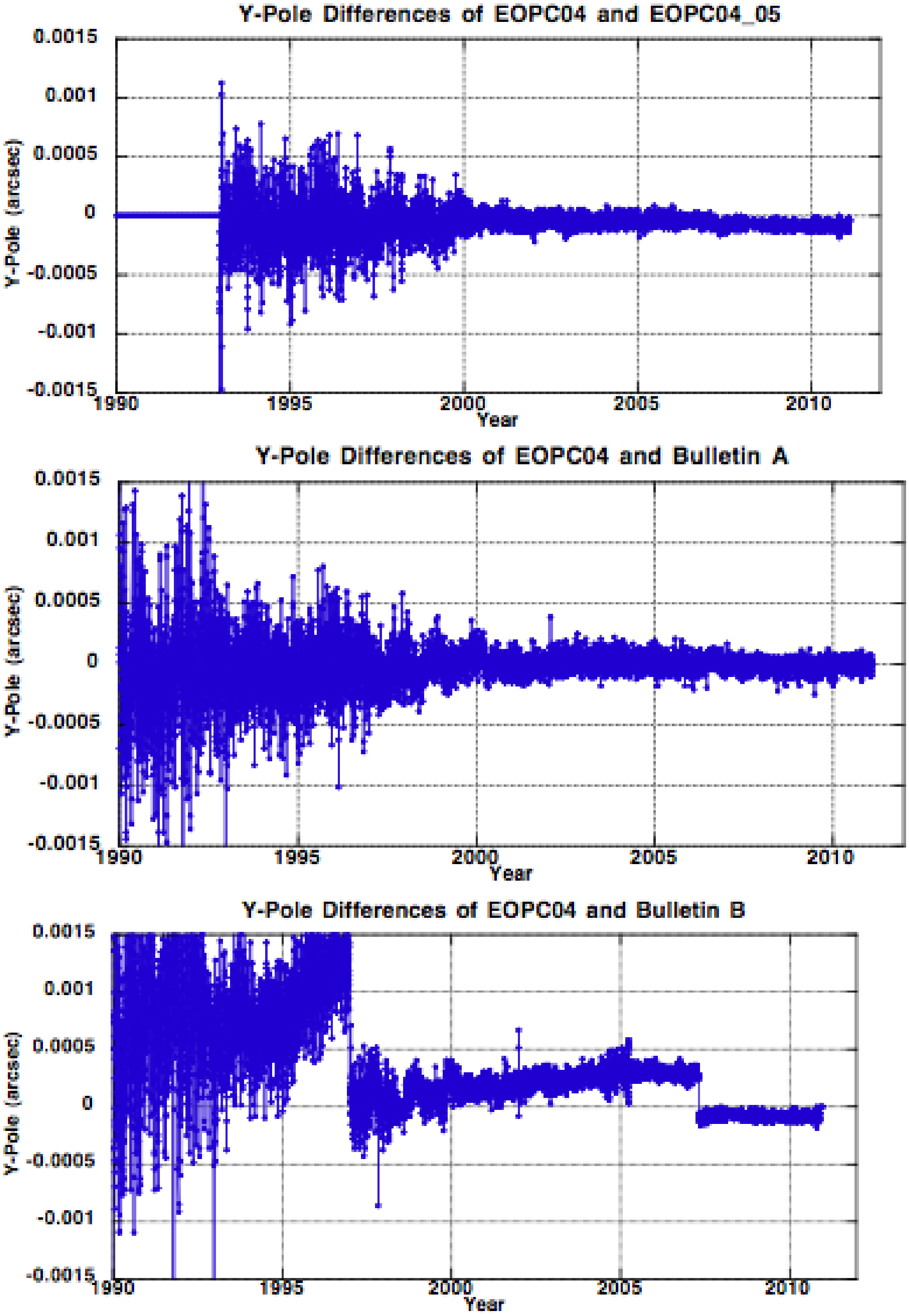

Figure F.2: Differences between values of Y_p reported in EOPC04 series vs. EOPC04_05, Bulletin A and Bulletin B from top to bottom

Appendix G

Reprocessing of the years 2009-2010

This appendix reproduces the results that were presented at the General Assembly of the European Geophysical Union in the Spring 2011. This appendix is included for completeness and for two main reasons. First, the reprocessed period is longer than the one analyzed throughout this dissertation. Second, the time period considered spans the years 2009 and 2010, so that the GPS observations, acquired more recently than the 2004 data set, are believed to be more accurate.

G.1 Experiment setup

Results from a reanalysis of 14 months of data from a global GPS network specifically targeting the recovery of polar motion parameters at high resolution are presented. The reanalysis was performed using the GIPSY/OASIS software package and covers a period of time centered on the date of the M8.8 earthquake that hit Chile on February 27th, 2010. The performances of the three candidate strategies are assessed in terms of the correlation of the estimates with the IERS-recommended model for tidally-induced polar motion variations as well as the correlation of the deconvolved residuals with modeled oceanic and atmospheric circulations in the frequency range characteristic of rapid polar motion.

Table G.1 summarizes the parameterization of the strategies. Note that the no-minal orbits and clocks used for this reanalysis are the latest JPL FlinnR final products. This constitutes the only difference with the results shown in the dissertation. Indeed the latter were obtained using the JPL FlinnP final products.

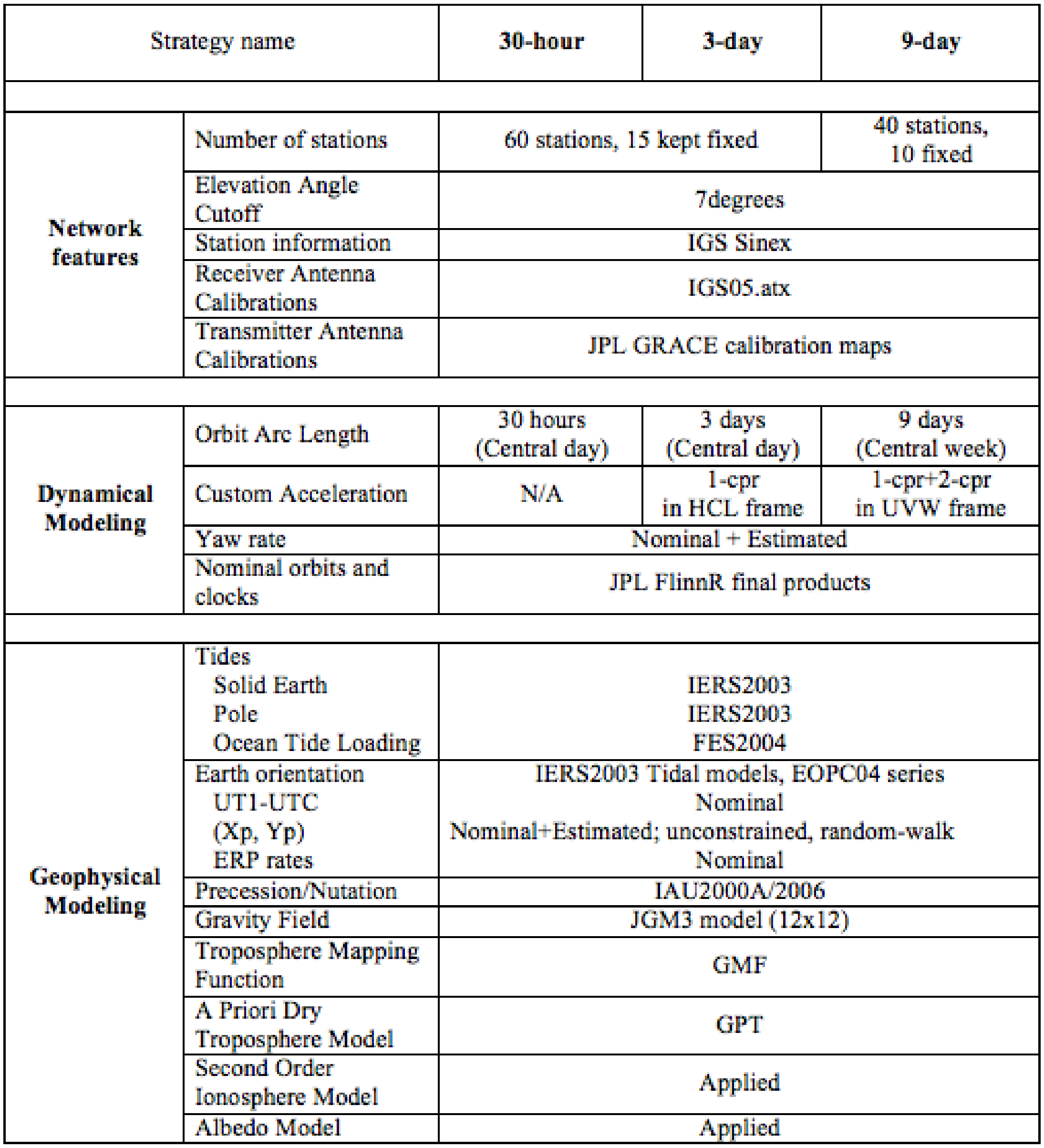

Strategy name		30-hour	3-day	9-day
Network features	Number of stations	60 stations, 15 kept fixed		40 stations, 10 fixed
	Elevation Angle Cutoff	7degrees		
	Station information	IGS Sinex		
	Receiver Antenna Calibrations	IGS05.atx		
	Transmitter Antenna Calibrations	JPL GRACE calibration maps		
Dynamical Modeling	Orbit Arc Length	30 hours (Central day)	3 days (Central day)	9 days (Central week)
	Custom Acceleration	N/A	1-cpr in HCL frame	1-cpr+2-cpr in UVW frame
	Yaw rate	Nominal + Estimated		
	Nominal orbits and clocks	JPL FlinnR final products		
Geophysical Modeling	Tides Solid Earth Pole Ocean Tide Loading	 IERS2003 IERS2003 FES2004		
	Earth orientation UT1-UTC (Xp, Yp) ERP rates	IERS2003 Tidal models, EOPC04 series Nominal Nominal+Estimated; unconstrained, random-walk Nominal		
	Precession/Nutation	IAU2000A/2006		
	Gravity Field	JGM3 model (12x12)		
	Troposphere Mapping Function	GMF		
	A Priori Dry Troposphere Model	GPT		
	Second Order Ionosphere Model	Applied		
	Albedo Model	Applied		

Figure G.1: Estimation strategies

Outliers were detected based on the sizes of the internal orbit and clock overlaps and the amplitude of the pole coordinate estimates over a given arc. These criteria led to the removal of 6 days out of 428 in the case of FlinnR-like strategy, 5 days out of 428 in the case of the 3-day strategy and 6 weeks out of 60 when the 9-day strategy was used. The idea of eliminating all the satellites in shadow and penumbra before reprocessing the troublesome arcs had not been implemented at the time of this analysis.

G.2 Performance analysis of the orbit and clock solutions

The performance of the orbit determination solution was assessed based on the computation of orbit and satellite clock overlaps. The results obtained are displayed in Tables G.2 and G.3. Unlike what was unexpectedly observed with the 2004 data set, the 24-hour overlaps are smaller than the 5-hour overlaps for the two Longarc-type strategies. The 3-day strategy remains the best of the candidates in terms of orbit and clock consistency.

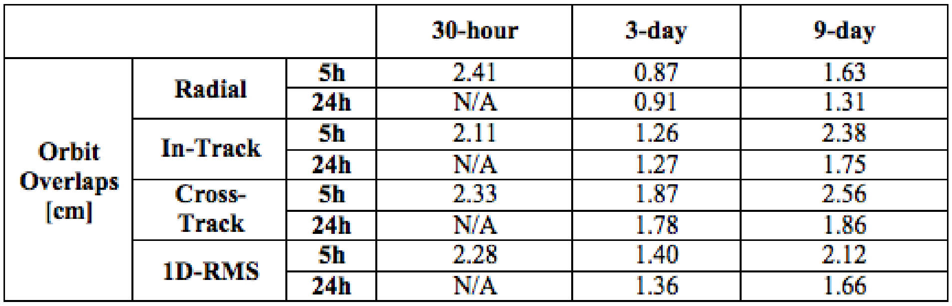

			30-hour	3-day	9-day
Orbit Overlaps [cm]	**Radial**	**5h**	2.41	0.87	1.63
		24h	N/A	0.91	1.31
	In-Track	**5h**	2.11	1.26	2.38
		24h	N/A	1.27	1.75
	Cross-Track	**5h**	2.33	1.87	2.56
		24h	N/A	1.78	1.86
	1D-RMS	**5h**	2.28	1.40	2.12
		24h	N/A	1.36	1.66

Figure G.2: RMS values of orbit overlaps

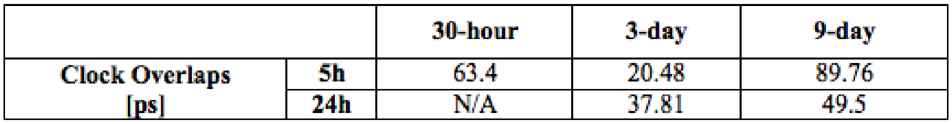

		30-hour	3-day	9-day
Clock Overlaps [ps]	**5h**	63.4	20.48	89.76
	24h	N/A	37.81	49.5

Figure G.3: RMS values of satellite clock overlaps

G.3 Performance analysis of the polar motion solution

The series of pole coordinates estimated were analyzed in the time domain first. The performance analysis was conducted on solutions that had not been corrected for the effects on ocean tides on polar motion. Table G.4 gathers the results obtained. Below it, Table G.5 provides the same information but the pole coordinates have been combined to compute the prograde and retrograde parts of polar motion.

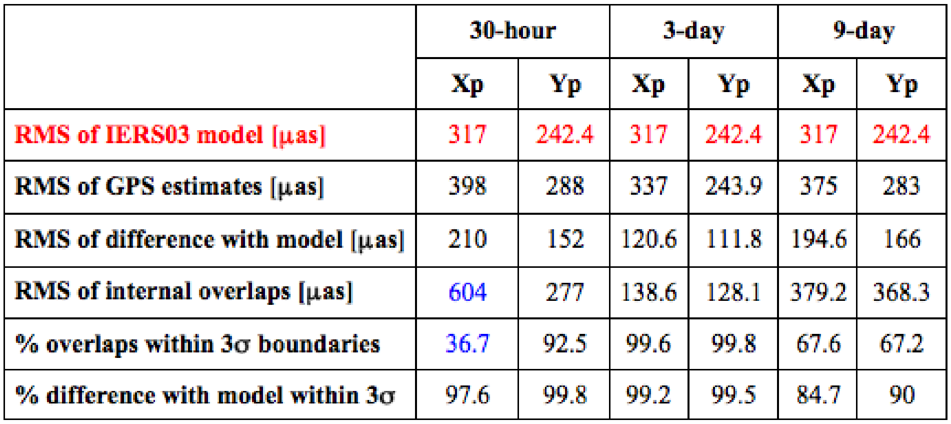

	30-hour		3-day		9-day	
	Xp	Yp	Xp	Yp	Xp	Yp
RMS of IERS03 model [μas]	317	242.4	317	242.4	317	242.4
RMS of GPS estimates [μas]	398	288	337	243.9	375	283
RMS of difference with model [μas]	210	152	120.6	111.8	194.6	166
RMS of internal overlaps [μas]	604	277	138.6	128.1	379.2	368.3
% overlaps within 3σ boundaries	36.7	92.5	99.6	99.8	67.6	67.2
% difference with model within 3σ	97.6	99.8	99.2	99.5	84.7	90

Figure G.4: Results from the time-domain analysis of the polar motion solutions

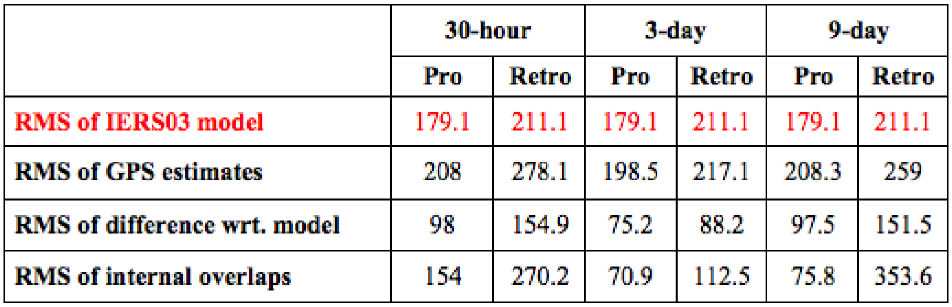

	30-hour		3-day		9-day	
	Pro	Retro	Pro	Retro	Pro	Retro
RMS of IERS03 model	179.1	211.1	179.1	211.1	179.1	211.1
RMS of GPS estimates	208	278.1	198.5	217.1	208.3	259
RMS of difference wrt. model	98	154.9	75.2	88.2	97.5	151.5
RMS of internal overlaps	154	270.2	70.9	112.5	75.8	353.6

Figure G.5: Results from the analysis of the prograde and retrograde polar motion series

As mentioned before, accuracy can be tied to the difference with the IERS model. As a consequence, the level of accuracy reaches about 80 μas in the case of the 3-day strategy when the polar motion vector is decomposed into its prograde and retrograde constituents. The differences with the model arise from three sources: non-tidal variations in polar motion, estimation strategy artifacts and modeling errors. Pole overlaps are computed similarly to orbit and clock overlaps and provide a measure of the precision of the estimates. The metric also relates to the noise level of the series. SNR values are promising, in particular for the prograde component in the case of the 3-day strategy. The results corresponding to the use of the FlinnR-like strategy appear to be anomalous for reasons undetermined yet. The larger differences relative to the model observed for the retrograde component, in comparison to those corresponding to the prograde component, are partly explained by the fact that the retrograde diurnal signals are not blocked nor filtered out neither during the processing nor in the post-processing phase.

G.4 Recovery of tidal variations in polar motion

The ability of each strategy to detect the tidal variations in polar motion was evaluated by computing the correlation coefficients between the values predicted by the IERS model for tidally-induced polar motion and the actual estimates. As seen in the table below, the 3-day strategy performs significantly better than the other two strategies both in the cartesian coordinate system and in the prograde and retrograde domains.

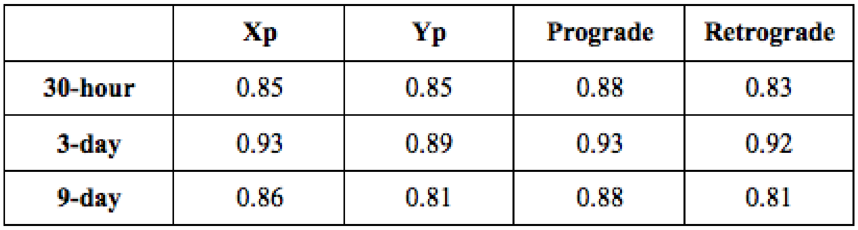

	Xp	**Yp**	**Prograde**	**Retrograde**
30-hour	0.85	0.85	0.88	0.83
3-day	0.93	0.89	0.93	0.92
9-day	0.86	0.81	0.88	0.81

Figure G.6: Coefficients of correlation between modeled values and estimates

G.5 Recovery of non-tidal variations in polar motion

Results regarding the recovery of non-tidal oceanic and atmospheric variations in polar motion are collected in the tables placed below. Once again, the superiority of the 3-day strategy is evident. Conversely, the 9-day strategy yields the worst correlations once again.

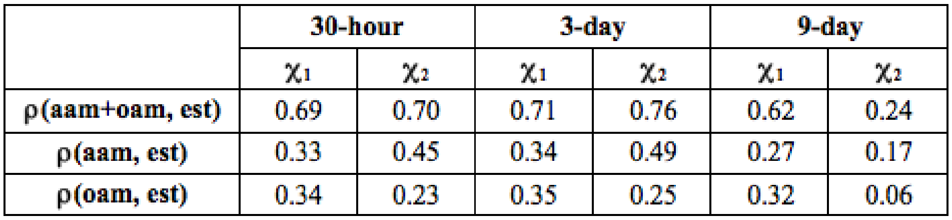

	30-hour		**3-day**		**9-day**	
	χ_1	χ_2	χ_1	χ_2	χ_1	χ_2
ρ(aam+oam, est)	0.69	0.70	0.71	0.76	0.62	0.24
ρ(aam, est)	0.33	0.45	0.34	0.49	0.27	0.17
ρ(oam, est)	0.34	0.23	0.35	0.25	0.32	0.06

Figure G.7: Correlation between the geophysical and geodetic excitations

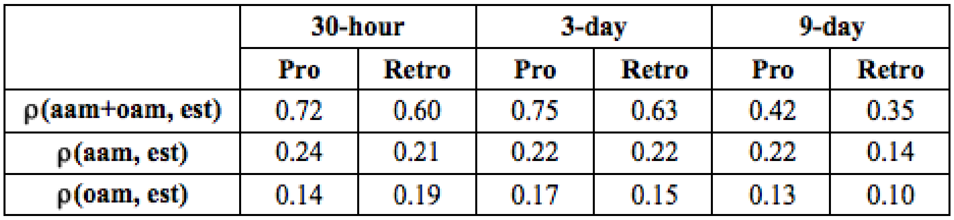

	30-hour		3-day		9-day	
	Pro	**Retro**	**Pro**	**Retro**	**Pro**	**Retro**
ρ(aam+oam, est)	0.72	0.60	0.75	0.63	0.42	0.35
ρ(aam, est)	0.24	0.21	0.22	0.22	0.22	0.14
ρ(oam, est)	0.14	0.19	0.17	0.15	0.13	0.10

Figure G.8: Correlation between the prograde and retrograde geophysical and geodetic excitations

G.6 Conclusion

The analyses conducted on this recent data set confirms the results observed with the 2004 data set and allows us to definitely conclude on the superiority of the 3-day strategy over the other two candidates in all aspects of the parameter estimation. It is verified that the reprocessing of more recent data sets yield pole solutions of a competitive quality relative to the levels of accuracy and precision currently reached by other institutions by means of other software and strategies. Since the estimation interval for the pole coordinates used here is the highest ever reported, we claim to have advanced the state-of-the-art performances for high-frequency polar motion estimation.